Open Research Online

The Open University's repository of research publications
and other research outputs

Electromagnetic reflections inside ice sheets

Thesis

How to cite:

Miners, William Dingle (1999). Electromagnetic reflections inside ice sheets. PhD thesis The Open University.

For guidance on citations see FAQs.

© 1999 The Author

Version: Version of Record

Copyright and Moral Rights for the articles on this site are retained by the individual authors and/or other copyright owners. For more information on Open Research Online's data policy on reuse of materials please consult the policies page.

oro.open.ac.uk

UNRESTRICTED

Electromagnetic Reflections inside Ice Sheets

by
William Dingle Miners

A thesis submitted for the degree of
Doctor of Philosophy to the Open University

Sponsored by: British Antarctic Survey,
Natural Environment Research Council,
Madingley Road, Cambridge, UK

Submitted on
30th September 1998

AUTHOR'S NUMBER: P9277234
DATE OF NUMBER: 16 JANUARY 1999

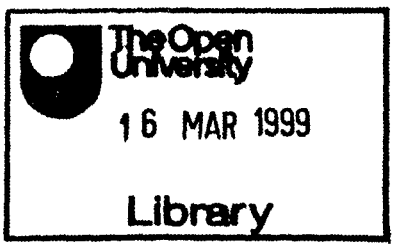

DONATION

X 551.31
C

Abstract

When radio echo sounding polar ice sheets weak stratified reflections are visible deep inside the ice sheets. These reflections are often called internal layers. Previously it has been suggested as a result of glacier flow models that these reflections can be treated as surfaces of equal age. In order for a reflection to be related to a single age feature in an ice sheet a one dimensional wave model must be adequate to model the propagation of a wavelet down to the feature and back to the surface. In this thesis four different one dimensional models are constructed each including different physics. It is shown that for the frequencies of interest to radio echo sounding it is sufficient to use the non-dispersive high frequency values of permittivity and conductivity for the ice in the models.

The models are used on data from two drill sites. The first site is Berkner Island where I constructed an instrument to measure the electrical conductivity of the 181 metre long ice core. The second site is the Greenland Ice Core Project (GRIP) site at Summit of length 3028 metres. For both sites permittivity and conductivity profiles inside the ice sheet are calculated and put into the models with an estimate of the transmitted wavelet to produce expected radio echo profiles at the sites. For Berkner despite altering many parameters no match between model result and radar data was obtained. For GRIP a satisfactory match was obtained between model result and radar data.

It is concluded that the weak, specular (plane like), stratified reflections at depth can be treated as isochrones. The strong reflections at shallow depths are a result of a combination of spherical reflection surfaces and interference between many closely spaced layers and cannot necessarily be treated as isochrones.

Acknowledgments

Firstly I would like to thank Dr Eric Wolff for giving me the opportunity to study this problem. He has been very generous in his help and encouragement while I have been working at the British Antarctic Survey. Many thanks are also due to my other supervisors: Dr John Moore of the Arctic Institute Finland, who supplied very detailed comments on the research and Dr William Fitzgerald of Cambridge University who managed to fit me into a very busy schedule.

I must also thank many others: Dr Rob Mulvaney for his patience with me and my instrument in the field and at BAS; Hugh Corr, who always found time to explain radio echo sounding and electronics; Dr Sebastian Gerland, for his friendship and for providing the excellent density data; Dr Norbert Blindow and Dr Daniel Steinhage, for providing the radio echo data from Berkner; Arne Hildebrand, for explaining the Münster model; Dr Robert Jacobel, for providing the GRIP airborne radio echo data and Dr Ludwig Hempel, for providing the GRIP surface radio echo data.

I would like to express my gratitude to the past and present Directors of BAS for giving permission for the results of this work carried out at BAS to be used in this thesis. I am also extremely grateful to BAS for their financial support.

Many thanks to the other members of the Ice and Atmospheric Chemistry section for making the years fly by: Dr. David Peel, Dr Julie Hall, Dr Anna Jones, Natalie Holman and Bruce Knight.

My final thanks go to my parents and Sharon without whose encouragement and help this thesis would never have been produced.

Contents

List of Figures

Chapter 6: Modelling the Berkner Island Record

Chapter 7: Modelling the GRIP Record

Chapter 8: Summary and Conclusions

List of Tables

Note on units

The field of Optics is complex, and some of the standard texts (Born and Wolff, 1975) are in Gaussian units {centimetres, grams, seconds) so that {$\varepsilon_0 = 1$ and $\mu_0 = 1$) and the conductivity is in units of s^{-1} (1 S m^{-1} becomes 9×10^9 s^{-1}) , for a good discussion on the units see the appendix in Jackson (1975). I will attempt to adhere to the conventions of the angles used in Optical work while using the SI system of units (metres, kilograms, seconds).

Note on computation

The programs were developed using MatLAB (matrix mathematical software on a 90 MHz, Pentium). For the ice cores the programs were taking so long to run that they were transferred to IDL (Interactive Data Language) software running on a 513 MHz Dec Alpha UNIX system.

Glossary

Abbreviations

AGC	Automatic gain control
BAS	British Antarctic Survey
DEP	Dielectric Profiling
ECM	Electrical Conductivity Measurement
EM	Electromagnetic
EPICA	European Project for Ice Coring in Antarctica
FPG	Forschungsstelle für Physikalische Glaziologie, (University of Münster).
FRIS	Filchner Ronne Ice Shelf
GISP2	Greenland Ice Sheet Programme
GPIB	General Purpose Interface Bus
GPR	Ground Penetrating Radar
GRIP	Greenland Ice Core Project
IRH	Internal Reflecting Horizon
MSA	Methane Sulphonic Acid
NSF	National Science Foundation (of America)
RES	Radio Echo Sounding
SEM	Scanning Electron Microscopy
SPRI	Scott Polar Research Institute
TUD	Technical University of Denmark

Definitions

Cold Glacier	All the ice is below the melting point or the melting point is only reached at the bed (Paterson, 1994).
Birefringence	The phenomenon wherein waves whose polarisation differs by 90° propagate at different velocities in an anisotropic medium.
Dispersion	The variation with frequency of the refractive index or wave vector.
Firn	Porous grain-like ice, transitional between snow and glacier ice (Kotlyakov and Smolyarova, 1990). Snow that is over one year old (Shoji and Langway, 1989).
Glacier	A large slowly moving accumulation of ice and firn resulting from consolidation and transformation of atmospheric precipitation provided its perennial balance is positive (Kotlyakov & Smolyarova, 1990).
Glacier Grain	An individual ice crystal in a glacier (Gary et al. 1974).
Grain size	The grain size of the ice is measured from thin sections and in this thesis the size will be expressed as an average area (Gow, 1969; Jacka 1984).
Ice Rise	An ice mass, usually dome-shaped, resting on unexposed rock and surrounded either by an ice shelf, or partly by an ice shelf and partly by sea or ice-free land or both (Gary et al. 1974).
Ice Sheet	A glacier more than 50 000 km^2 in area forming a continuous cover over a land surface or resting on a continental shelf (Kotlyakov & Smolyarova, 1990).
Permittivity	The ratio of the displacement of electric charge to the strength of the electric field.
Polar Glacier	Glaciers which are below freezing point to a considerable depth, and on which there is no melting even in summer (Kotlyakov & Smolyarova, 1990).
Porosity	The porosity of a sample is the volume fraction that is not occupied by ice and is the sum of the open and closed porosity (Schwander, 1989).
Snow Grain	A mechanically separate particle of snow, often but not necessarily a single ice crystal (Gary et al. 1974).

Symbols

Roman

B	Real Magnetic field scalar value
$\boldsymbol{B}$	Real Magnetic field vector
C	Capacitance (Units F Farad) Coulombs per volt, $F=A^2s^4kg^{-1}m^{-2}$
c	speed of light in a vacuum, 3×10^8 m s^{-1}.
D	Displacement field scalar value
$\boldsymbol{D}$	Displacement field vector
E	Real Electric field scalar value
$\boldsymbol{E}$	Real Electric field vector
f	Frequency , (Units Hertz Hz)
f_r	Relaxation frequency of AF-LF dispersion.
G	Conductance, (Units Siemens S) Inverse of resistance, $S=\Omega^{-1}=A^2s^3kg^{-1}m^{-2}$
i	is the imaginary number $\sqrt{-1}$
k	wave number, scalar
$\boldsymbol{k}$	wave number, vector
P	Polarisation scalar value
$\boldsymbol{P}$	Polarisation vector
r_A	the amplitude reflection coefficient at any boundary
r_{AF}	the Fresnel amplitude reflection coefficient (for an interface between two semi infinite media)
r_p	the power reflection coefficient
T	Period of a wave

Greek

ε	Permittivity (Units F m^{-1})
ε_0	Permittivity value in a vacuum: = 8.854×10^{-12} F m^{-1}
$\varepsilon'_{r\infty}$	High frequency relative real permittivity (dimensionless)
λ	wavelength (m)
ρ	density of the firn (kg m^{-3})
σ	Conductivity (Symbol) (Units S m^{-1}) Inverse of resistivity
σ_{dc}	static or direct current (dc) conductivity
σ_∞	High frequency conductivity (Units S m^{-1})
τ_D	Debye relaxation period (Units s)
ω	Radian frequency ($2\pi f$)

Superscripts

*	complex conjugate
/	real part of complex number
//	imaginary part of complex number
~	the tilde denotes a complex variable
$-_T$	line over a character average over a period , in this case T

Subscripts

∞	high frequency value
r	relative value

The first scientific research in ice conductivity of which this author is aware began more than 100 years ago. At present the list of papers devoted to the electrical properties of ice contains several hundred items. It is extremely difficult to conduct a comparative and critical review.

V.F.Petrenko
Electrical Properties of Ice, 1993

The vast expansion of the literature in recent years is making it increasingly difficult for one person to write a comprehensive account of the physics of glaciers.

W.S.B.Paterson,
Physics of Glaciers, 1994

It is necessary to point out that it is impossible to perform a complete review of the results obtained in this field because of their enormous extent.

I.Ohlídal and K.Navràtil,
Scattering of light from multilayer systems with rough boundaries,
In E.Wolff, Progress in optics XXXIV, 1995

..we do not provide any detailed description of the techniques of dielectric measurements themselves, which constitute a highly specialised branch of knowledge. The equipment available now is at a very advanced level of development and it would be futile to try to give justice to this complex field...

A.K.Jonscher,
Dielectric relaxation in solids,
Chelsea Dielectrics Press, London, 1983

The pages that follow are my best attempt...

CHAPTER 1

INTRODUCTION

This chapter is an introduction to the scope of the thesis; the problem to be tackled is stated. The remainder of the chapter explains the present knowledge and the way that this thesis will attempt to answer the problem.

1.1 The problem

Weak, stratified internal reflections are observed when a pulse of electromagnetic energy is transmitted into a cold glacier. Can it be assumed that the ice causing each reflection fell as snow at the same time?

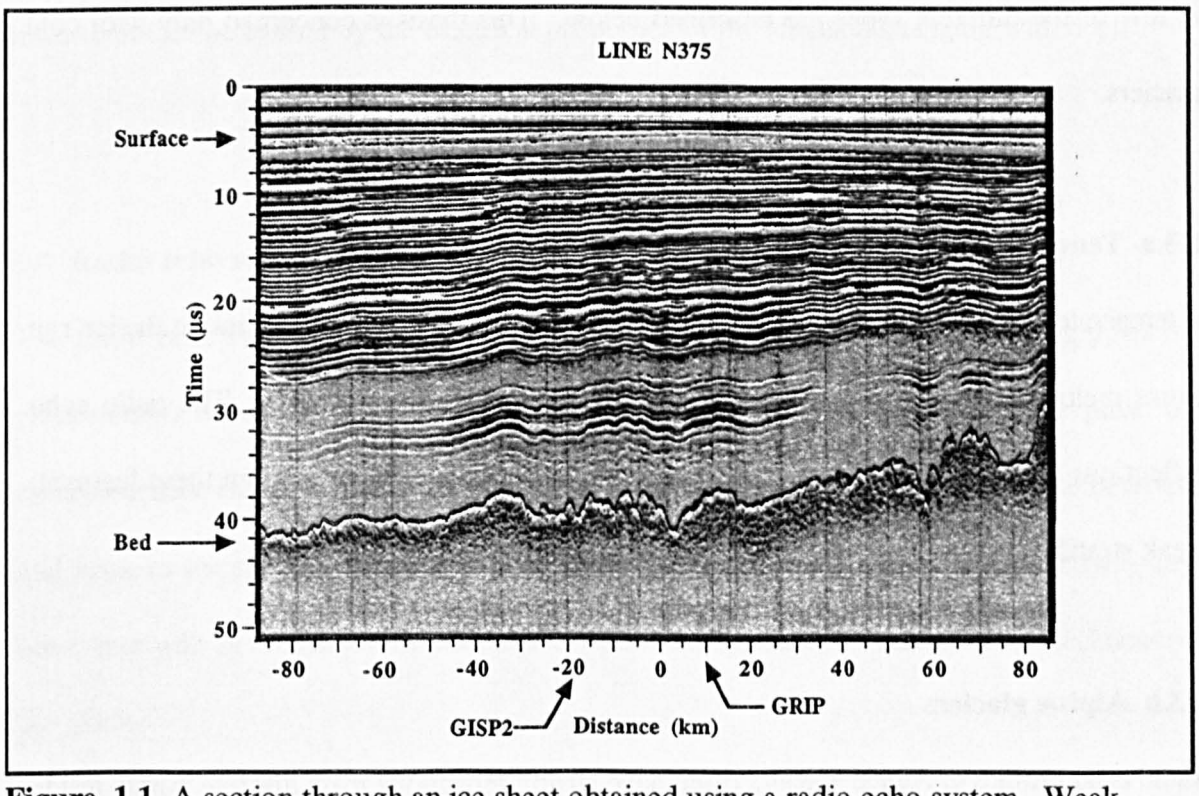

Figure 1.1 A section through an ice sheet obtained using a radio echo system. Weak stratified internal reflections are visible (from Jacobel and Hodge, 1995).

1.2 Why solve this problem?

A surface inside the glacier where the points on the surface all have the same age is called an isochrone. If it can be shown that the internal reflections are isochrones then an age versus depth relation obtained at one location can be traced to other locations. This will enable mapping of the spatial variation in the past accumulation rates giving information about the climate in the past. It will also help scientists who model the flow and development of ice sheets to improve their models and improve the ability of the models to predict the future growth or shrinkage of the Antarctic ice sheet.

1.3 Glaciers

There are many different types of glaciers, each can be classified by location or its properties. A few of the different types are described below. This thesis is concerned only with cold glaciers.

1.3.a Temperate glaciers

A temperate glacier is at its melting point throughout. The presence of water inside the ice can cause meltwater tunnels, solid ice layers and pockets of water or voids. The radio echo reflections seen inside temperate glaciers are strong discrete reflections from these features; weak stratified internal reflections are not commonly seen.

1.3.b Alpine glaciers

Radio echo profiles of Alpine glaciers often have strong reflections from discrete points inside the middle of the glacier, which are due to foreign bodies in the snow such as rock fragments. The rock fragments would have rolled onto the glacier from surrounding mountains or been

plucked from the bedrock. Alpine glaciers often also have all the internal features of temperate glaciers.

1.3.c Cold Glaciers

Cold glaciers are ones for which the temperature is below the melting point over the entire depth, (though there can be melting at the base.) Such glaciers are mainly found in the polar regions such as in central Greenland and Antarctica. In these polar regions the glaciers are very large and are called ice sheets. Weak stratified internal reflections are observed on the radio echo profiles of cold glaciers. Due to the properties and locations of the cold glaciers these reflections cannot be caused by the presence of foreign material with a different permittivity to the ice. In addition the temperatures are too low to cause the melting of the snow on the surface and the ice sheets are too thick to have any rock outcrops. These weak reflections must therefore be caused by the electrical properties of the ice itself changing with depth.

1.4 Radio echo sounding (RES)

The radio echo systems used in the polar regions are designed to deliver a strong pulse of electromagnetic energy in order to produce a reflection at the bedrock. The pulse of electromagnetic energy is transmitted into the glacier. The time taken to travel to the bedrock and back to the surface (the two-way travel time) is recorded. By combining the two-way travel time with an estimate of the speed of the pulse it is possible to calculate the thickness of the glacier.

The historical development of radio-glaciology is covered in the book by Bogorodsky et al. (1985). In the early systems an operator would need to be stationary with an antenna on the

surface of the glacier. The two-way travel time would be determined at one site, the operator would then move along the surface of the glacier and repeat the measurement. By repeated measurements the operator could construct a profile of the changing thickness along the glacier. With advances in electronics, the latest equipment is now faster and more powerful and it is possible to mount the antenna under the wing of an aircraft. With the aircraft flying at a speed of sixty metres per second above a glacier the thickness can be measured, with an accuracy of around one percent, at a horizontal spacing of order ten metres (Corr, pers com).

1.4.a Transmission of the radio echo pulse

There are three different types of transmitting system. The first is burst transmission where an electronic oscillator produces a continuous carrier wave at a centre frequency. A finite duration portion of the carrier wave, typically at least 15 periods, is taken, amplified, and sent to an antenna from which it is transmitted into the ice sheet. The longer the duration of the wavelet the more energy can be transmitted.

The second type is monocycle transmission, where the antenna is subjected to a single spike, or one period of the carrier oscillation. The antenna resonates in response to the arriving energy and will transmit at least one, and possibly up to four or more, periods of the carrier. As less of the carrier wave is transmitted compared to the burst systems, less power is transmitted. These systems are therefore used to collect higher resolution records near the surface. Monocycle systems can either be called surface penetrating radar (Daniels, 1996) or ground penetrating radar (GPR).

The third type are synthetic pulse systems which transmit at a number of different mono-frequencies (Hamran and Aarholt, 1993; Richardson et al. 1997). These require signal

processing involving inverse Fourier transforms to recover the time domain record. This thesis will only consider data from the first two types of system.

1.4.b The reflection of the radio echo pulse at the bedrock

The speed of the electromagnetic pulse inside the glacier is determined by the permittivity of the material through which it is travelling. The permittivity will be explained further in a later chapter. When the down-going pulse encounters a sudden change in the permittivity, a fraction of the energy is reflected back to the surface. The permittivity of ice and rock are very different as can be seen in the table below. At the base of the glacier the transition between the two is abrupt enough to reflect a large fraction of the down-going pulse. These strong reflections caused by the sharp boundary between two materials of very different permittivities have been frequently observed and are well understood.

Table 1.1 Relative real permittivity values (Parkomento, 1967)

Material	Relative real permittivity
Snow	2
Ice	3
Sandstone	5
Granite	12
Water	81

1.4.c Reception of the radio echo signal

The energy reflecting from the bedrock can be detected either at the same or another antenna. It then passes through various electronic devices designed to amplify the signal. More details will be given on these when considering specific systems in later chapters. In the past only analogue methods existed for recording the returning signal. Much of the literature dealing with reflection horizons inside the ice is based on analogue recordings. The analogue records

had a poor resolution making it difficult to identify reflections from any foreign material inside the glacier. The use of digital recording started in the mid seventies (Goodman, 1975).

1.4.d Displaying the radio echo signal

There are two display types that have traditionally been used: A scope and Z scope.

A Scope: Returned power versus time for one burst. Usually the logarithm of the returned power is used, but sometimes the differential of the returned power is used instead. The returned power is usually displayed on an oscilloscope screen which displays delay time since transmission versus logarithmic echo power received.

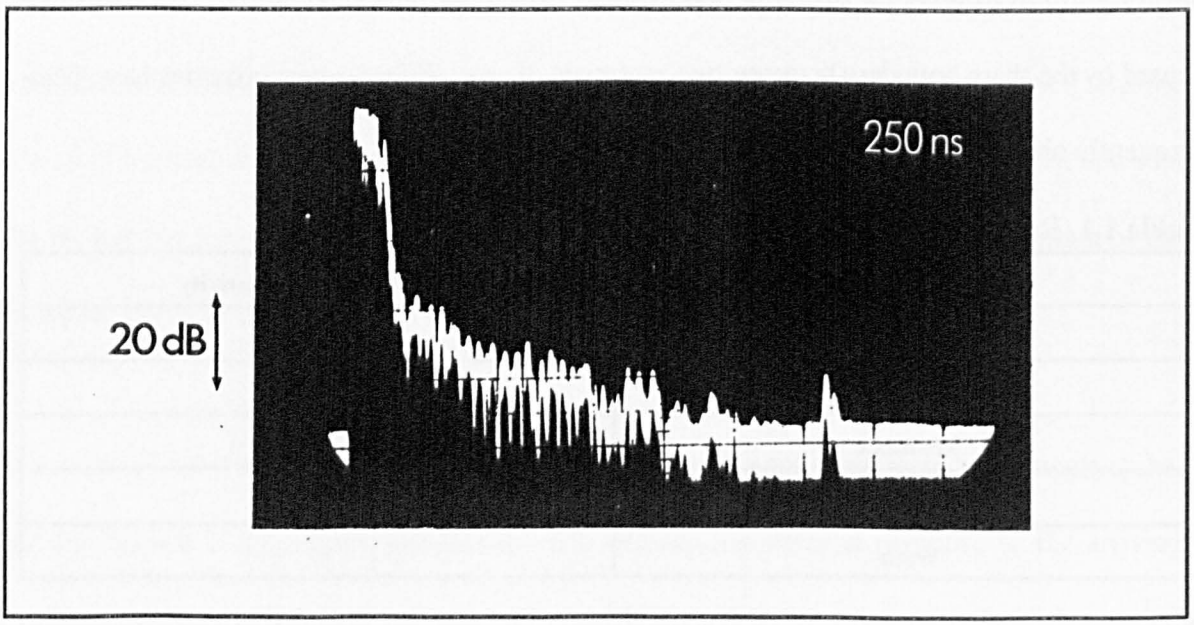

Figure 1.2 An A scope display, taken using a pulse length of 250 ns. The last peak on the right is the reflection from the base of the glacier. (from Millar, 1981 a)

Z Scope: The returning energy is differentiated then the intensity modulated power return is plotted against time along the flight track. This would typically be recorded on 35 mm photographic film.

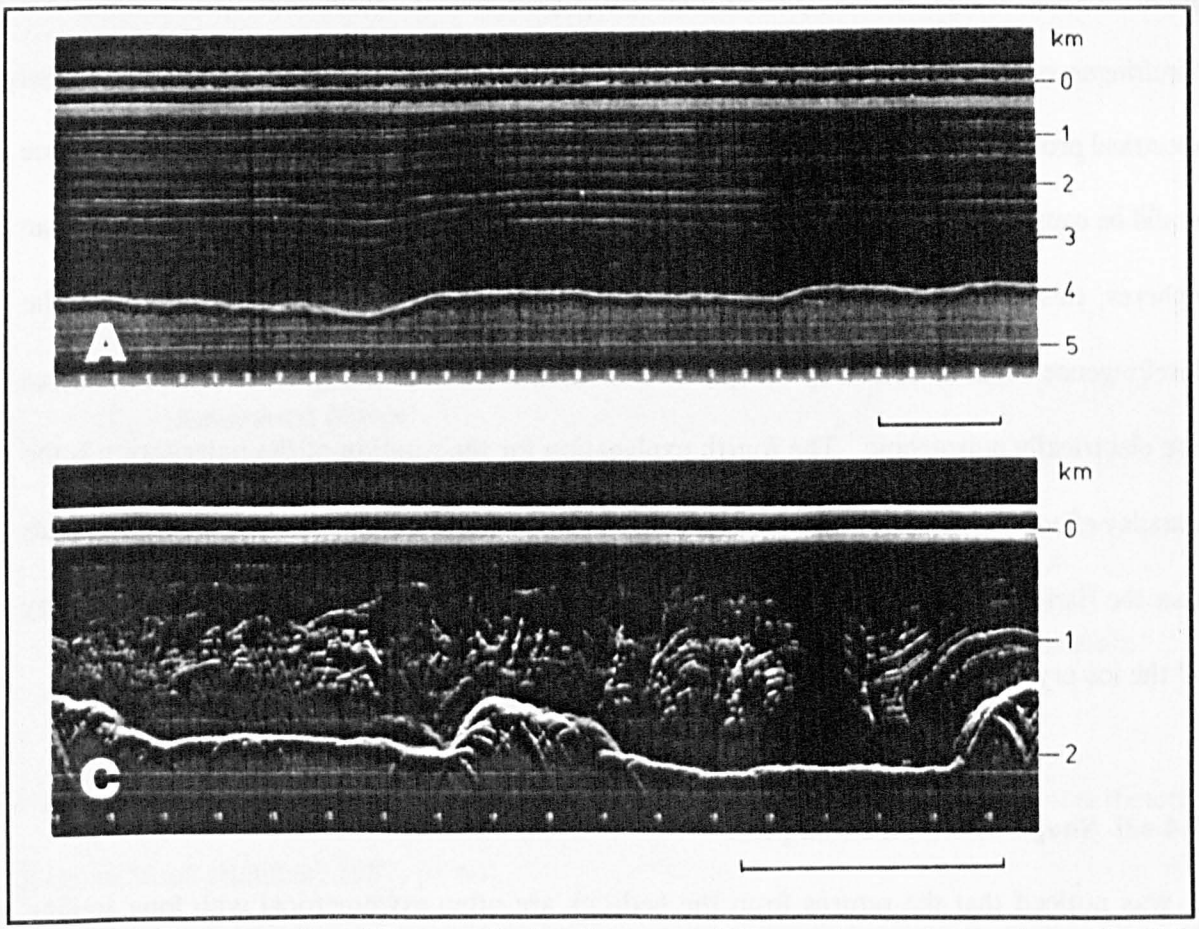

Figure 1.3 Two examples of Z scope display, from two different Antarctic locations, 60 MHz system, 250 ns wavelet length, scale bar = 10 km. The bedrock reflection is the strong reflection at a depth of 2 km. (from Millar, 1981 a).

1.4.e Understanding the bedrock reflection

There are many publications which consider the radio echo reflection from the bedrock. In this section three attributes of the bedrock reflection are considered. These are: polarisation, pulse shape and power.

1.4.e.i Polarisation of the reflected pulse

Early on in the use of radio echo systems it was noticed that the bedrock reflection had a different polarisation to the transmitted pulse (Jiracek, 1967). There are four possible explanations for this, the first three explanations being due to the ice sheet behaving as a birefringent material. In a birefringent material electromagnetic waves travelling with

polarisations that are at 90^0 to each other propagate with different velocities. Firstly, the birefringence could be caused by the ice sheet being a periodically layered media with different electrical properties in each layer (Sivaprasad and Lessow, 1976). Secondly, the birefringence could be caused by the bubbles inside the ice being squeezed so that they are ellipses rather than spheres, this would cause anisotropy when scattering electromagnetic waves. Thirdly, the birefringence could be caused by changes in the orientation of the ice crystals which themselves are electrically anisotropic. The fourth explanation for the rotation of the polarisation is the Faraday effect where a polarised electromagnetic wave propagating in a magnetic field (in this case the Earth's) will be rotated. Hargreaves (1977, 1978) concluded that it was the anisotropy of the ice crystals that was causing the rotation in the polarisation.

1.4.e.ii Shape of the reflected pulse

It was noticed that the returns from the bedrock are often asymmetrical with long trailing edges, which is typical of a diffuse reflector. The connection between the shape of the reflected pulse and the bedrock roughness has been examined by many authors (Robin et al. 1969; Berry, 1973; Oswald, 1975). The statistical distribution and amplitude of the bedrock can be derived from the maximum observed power, the extent of variation of the received power over short distances and the horizontal autocorrelation functions of the received signals.

1.4.e.iii Power of the reflected pulse

For most radar applications the "radar equation" is applicable (Skolnik, 1970). It considers the transmission and reception of continuous waves in air which have been reflected from a point object. In radio echo sounding from the bedrock Skolnik's radar equation cannot be used because: the target is a surface, the medium refracts and the transmitted signal is a pulse. However many authors do use a form of the radar equation which assumes a perfectly

reflecting infinite plane. An equation for the received power (P_R) in radio-glaciology is given by Bogorodsky et al. (1985, pp 48):

$$P_R = \frac{P_T G_t A_r q}{4\pi (2(H+h))^2 L} \qquad (1.1)$$

where

P_T = transmitted power
G_t = transmitting antenna gain
A_r = effective area of the receiving antenna
q = refraction gain, requires refractive index.
H = height of the antenna above the snow surface
h = ice thickness
L = losses during two way transit, includes transmission loss through the surface, absorption inside ice sheet and reflection loss at the base of the ice sheet

It is by using equations such as this that estimates have been made for the reflection coefficient at the bedrock (Bamber, 1987, pp 60).

1.5 The discovery of weak stratified internal reflections

Weak stratified internal reflections were first noticed during a traverse in North West Greenland in the summer of 1964 by the Scott Polar Research Institute (Bailey et al. 1964). The characteristics of the system that they were using, the SPRI Mk II, are outlined in the table below:

Table 1.2 The SPRI Mk II RES (Evans and Smith, 1969)

Carrier frequency	35 MHz
Pulse length	240 ns
Rise time to maximum transmitted power	60 ns
Peak power	500 W
Performance	145 dB (Evans, 1966)

A continuous energy return was recorded in the first few microseconds and attributed to the

many density variations near the surface. The reflections near the surface behaved as if from diffuse Lambert reflectors. Such surfaces have equal brightness from whatever direction they are viewed.

The unexpected result was that for over half the distance travelled weak reflections were recorded after the end of the continuous signal, but before the arrival of the bedrock reflection (Robin et al. 1969). These observed internal reflections had some continuity parallel to the surface and behaved as if originating from specular reflectors (Evans, 1966). For a specular (or polished reflector) the surface ridges and valleys are small compared to λ in the medium in front of the surface. It is these types of internal reflections that will be discussed for the rest of this thesis. Robin et al. (1969) used the radar equation (eqn 1.1) to determine the power reflection coefficient of the internal reflections. Different internal reflections were given power reflection coefficients (r_p) between -43 and -80 dB. After the observations of Robin et al. (1969), internal reflections have been noticed routinely with a variety of radar systems in Greenland, Antarctica and other polar regions.

The present understanding of internal reflections has been reached by four methods which will be considered in the next four sections: firstly, observing the behaviour of internal reflections at different sites and using different radio echo systems (§1.6); secondly by comparing internal reflections with ice cores (§1.7); thirdly by the use of electromagnetic wave models (§1.8), and finally by comparing internal reflections with glacier flow models (§1.9).

1.6 The observed behaviour of internal reflections

In this section the observed behaviour of internal reflections will be considered; firstly their behaviour at different positions in the glacier (§1.6.a) and secondly how altering the radio echo system alters the observed reflections (§1.6.b). Many of the observations have been made with the SPRI Mk 2 system, as previously described in table 1.2. Other observations have been made with the Technical University of Denmark (TUD) system, which has a carrier frequency of 60 MHz, a wavelet duration of 250 ns and a peak power of 10 kW.

1.6.a Characteristics of internal reflections as functions of position in the glacier

The characteristics of internal reflecting horizons (IRH) seen in a profile will alter depending on the position in the ice sheet, this can be seen in table 1.3.

Table 1.3 Changing position

Initial Observation		Subsequent Observation / explanation
Paper and type of RES system	**Observation**	
Robin et al. (1969) SPRI Mk 2	IRH are specular reflections	(Millar, 1981 a) IRH echoes are sharp and symmetrical without a trailing edge.
	IRH can be discontinuous	(Sondergaard, 1975) Passing over the same track with a shorter pulse length improves the resolution and makes the reflection a continuous line. (Jacobel and Hodge, 1995) Accumulation is not spatially constant, so the condition for constructive interference is fulfilled only intermittently.
	Power returned by IRH can fluctuate along the track.	(Millar, 1981 a) Calls this phenomenon fading, From observations of the fading determines the roughness of the surfaces causing the IRH, suggesting IRH are depositional in origin.
	IRH deforms when the ice flows over subglacial ridges.	(Harrison, 1973) Layer of constant thickness remains the same proportional height above the bedrock. (Robin et al. 1977) Conformity of IRH with bedrock relief decreases as ice speed increases.
Robin et al. (1977) SPRI Mk 2	Absence of IRH in the basal part of ice sheets.	(Robin et al. 1977) Likely to be due to variable shear strain in the lowest layers, caused by deformation over rough relief. (Maccagan and Duval, 1982) Due to a temperature effect. (Jacobel and Hodge, 1995) Overall signal strength from weaker IRH is low at these depths and the power returned is only marginally above the noise level. (Jacobel and Hodge, 1995) Accumulation horizons near the base conform to the bedrock topography and steeper inclines in both directions perpendicular to the RES beam make it increasingly difficult to produce constructive interference.
Millar, (1981 a) TUD	No thinning in spacing of layers with depth .	Implies we are not seeing the real layers.
	Rapid decrease in r_p with depth. Once deep inside the glacier r_p reaches a steady value.	Attributed to density fluctuations near surface and loss tangent variation at depth.
Robin and Millar, (1982) TUD	Folding of IRH above a smooth bed	(Robin and Millar, 1982) Due to flow over bedrock obstacles upstream. (Whillans and Johnsen, 1983) Flow over flat surface that has alternate subglacial lakes and rougher high drag regions.
Sandhäger, (1995)	Up arching of IRH below domes.	Attributed to changes in the strain conditions beneath domes (Raymond bumps).

1.6.b Characteristics of internal reflections as functions of radio echo system

A number of experiments have also been conducted to see how an IRH will alter if the RES system is altered. The tables below review some of the results seen in previous publications.

Table 1.4 Changing position of antennas

Paper	Initial observation	Subsequent observation / explanation
Jiracek (1967)	Increasing the separation of the transmitting and receiving antennas produces more IRH near the surface.	This moves the IRH out of the receiver recovery and ringing and allows them to be seen.
	Rotating the receiving antenna causes the position and strength of IRH to alter	Due to anisotropy in the ice. (Maeno et al. 1995) Maximum absorption is related to the direction of the flow vector.
Bogorodsky et al. 1970, Pole Station (Summary in Clough, 1974, pp 86, 95)	IRH down to a depth of 400 - 500 m (5-6 μs) are not depolarised. Echoes from depths 750 - 850 m (9 - 10 μs) are strongly depolarised	(Bogorodsky et al. 1970) Discusses three mechanisms: 1) Anisotropy of permittivity 2) Faraday effect which should be insignificant 3) Due to stressed state of glacier (Hargreaves, 1977). Mathematical description of how the birefringent ice could cause elliptical polarisation as it travels down to the IRH and back to the surface. (Hargreaves, 1978) Observed birefringence is not due to the distortion of the air bubbles in the ice.

Table 1.5 Changing duration of wavelet while keeping same carrier frequency.

Paper and type of system	Initial observation	Subsequent observation / explanation
Robin et al. (1969) SPRI Mk 2	Shorter transmitted wavelet gives a shorter duration of echo from an IRH.	-
Harrison, (1973) SPRI Mk 2	Shorter transmitted wavelet causes vertical displacement of IRH	-
	Shorter transmitted wavelet gives a weaker echo from an IRH	(Harrison, 1973) Integration effect of all the reflections from all the layers inside the pulse length. (Harrison, 1973) Reflecting area of the plane is proportional to the pulse length.
Gudmandsen, (1976) . TUD.	Shorter transmitted wavelet gives more IRH echoes	(Gudmandsen, 1976) Increased resolution for a smaller pulse. (Millar, 1981 a, b) Mean layer echo spacing will be approximately equal to the pulse length. Tried with 60 ns, 250 ns, 1000 ns on the TUD system.

Table 1.6 Changing carrier frequency

Paper and type of system	Initial observation	Subsequent observation / explanation
Millar, (1981 a) TUD	Changing the centre frequency of the system (60 MHz to 300 MHz, while remaining at 250 ns duration) at some sites makes the positions of the reflection alter.	-
	Higher frequency systems have a lack of IRH near the surface.	(Millar, 1981 a) Greater scattering in the ice at higher frequencies.

Jacobel et al. (1993) report that there was a linear relationship between apparent separation of the internal layers and input centre frequency. This result was obtained using a system built by Wright et al. (1990). This system had a very low carrier frequency that could produce a single monocycle at any of the frequencies 1, 2, 4, 8 and 12.5 MHz. However, I suggest that the important point is not the frequency of the monocycle but its duration (the period). This is the effect previously observed by Gudmandsen (1976) when looking at the wavelet length.

1.6.c Conclusions from the observations

From the observations in the above tables it is clear that the position, number and strength of the internal reflections depend on the radio echo system. There are very few occasions where two different systems have been used in the same place and given similar reflections. One such case at the GRIP site will be discussed later.

1.7 Comparing internal reflections with ice cores.

There have been a number of studies that compare an ice core with the radio echo profile obtained near the drill site, see appendix 1. The two main difficulties of such a comparison were discussed by Gudmandsen (1975). The first difficulty is the low resolution of the RES, with a best resolution in the order of metres whereas the ice core data have a resolution in the order of centimetres. Thus an internal reflection will be the response to several permittivity variations within the resolution distance of the RES. The second difficulty is an uncertainty in the depth of the internal reflection.

To calculate the depth of the internal reflection its two-way travel time needs to be known. The two-way travel time determination will be affected by three things (Gudmandsen, 1975): the signal to noise ratio of the received signal, the pulse response of the layers and the time delay in the receiver. Then there is the conversion of the travel time to a depth. This calculation is dependent on how well the velocity-depth relation is known, which in turn depends on the density in the upper part of the ice sheet.

Each of the above factors will be considered in turn in the next few sections, from the point of an observer trying to pick a reflection on the radio echo for which a depth needs to be determined.

1.7.a Signal to noise ratio in the received signal

The returning radio echo is being recorded along with background noise being picked up by the antenna. One problem is determining the onset of the received signal amongst this noise. This can be seen in figure 1.4, where the problem is whether to choose the arrival of the signal as point A or point B, with the position of B being dependent on the amplitude of noise. This

problem is also considered in Harrison, (1972, fig 2.11).

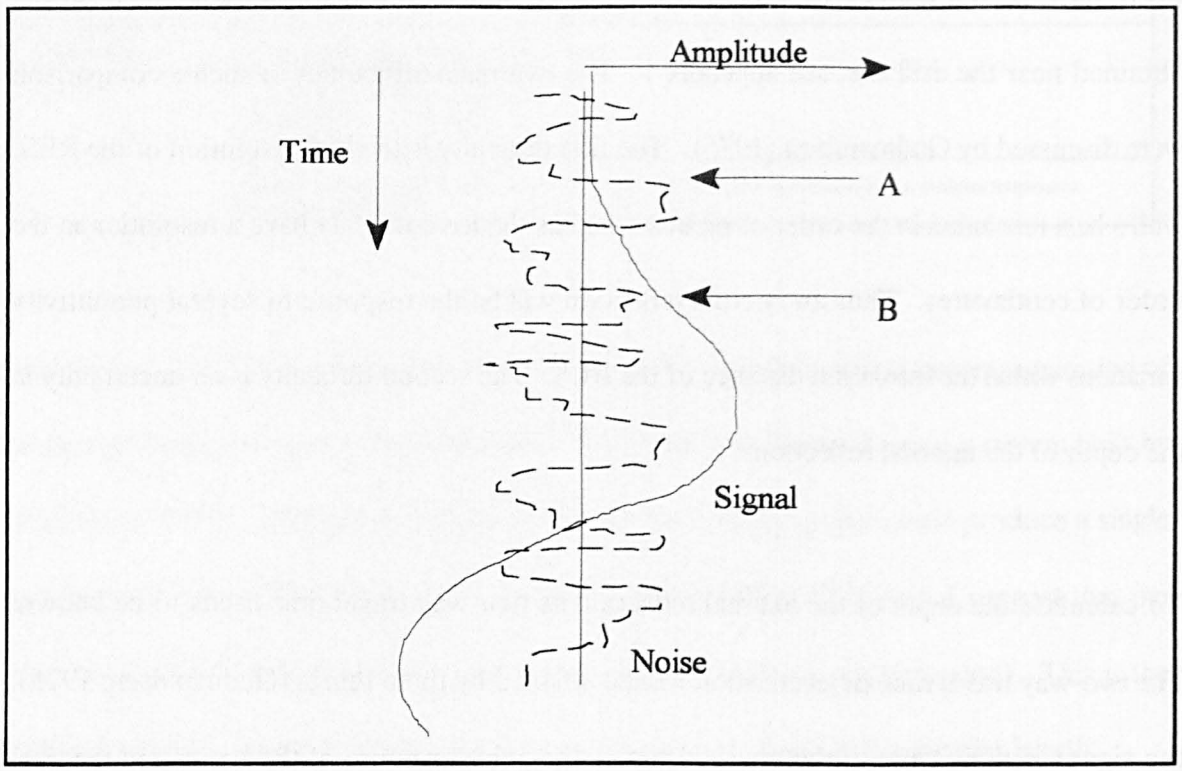

Figure 1.4 Determining the onset of the received signal from the background noise. A is when the initial signal starts to rise, B is when the signal rises above background noise.

1.7.b Pulse response of the layers

When an electromagnetic pulse strikes a stack of layers the observed reflection is a superposition of the reflections from each of the boundaries. It is difficult to decide where one reflection finishes and another begins. This is shown later when considering the reflection of a wavelet from a twenty metre long section of core (§5.6.e). The tail end of reflections from a shallow boundary may mask the beginning of the reflection from a deeper boundary, in a similar manner to the presence of noise.

1.7.c Time delay in the receiver

There will be a time delay in the receiver circuit. If the transmission time is being taken as when the pulse left the antenna this may cause a problem. However it should be possible to

determine the delay experimentally. If the RES is airborne and there is a reflection from the surface which can act as a start time then the delay in the receiver is not important. In some RES systems there can be an amplitude dependent delay in the receiver (Jezek and Roeloffs, 1983).

Another problem in the assigning of a travel time to a reflection is the roughness of the boundary causing the reflection. It has been shown that the duration of reflections from the bedrock will vary with surface roughness (Harrison, 1972; Oswald, 1975). A similar effect may be present for internal reflections.

1.7.d Conversion of travel time to depth.

The time taken to travel through the ice sheet is dependent on the velocity of the electromagnetic wave. The velocity is a function of the permittivity which in turn is a function of the density (see chapters three and four). The firn has a lower density, which means a lower permittivity, which means the electromagnetic wave has a higher velocity. One common correction is to add an additional ten metres to the depth to account for the higher velocity in the firn (Robin et al. 1969).

In appendix 1 are two tables which list the publications that compare the RES at a site with one or more of the measured physical properties of an ice core from the site. It can be seen that many of the early comparisons were hampered by the poor quality analogue A scope RES recordings from the Scott Polar Research Institute and National Science Foundation surveys.

From the ice core comparisons there is evidence that the density, conductivity, and ice fabric all contribute to the formation of the internal reflections.

1.8 Comparing internal reflections with electromagnetic wave models

1.8.a Earliest model

In Robin et al. (1969) the authors hypothesised that layers of high density solid ice lying within the lower density bubbly glacier ice would give the necessary permittivity change to cause the observed reflections. They tested this by considering a monochromatic wave in a transmission line that had a small impedance added. Their equation is valid for thin layers, with a thickness less than a quarter of a wavelength, without interference between the top and bottom reflections. In order to obtain the power reflection coefficients observed in the range of -43 dB to -80 dB, the equation required either large density contrasts ($\Delta\rho > 5$ kg m^{-3}) or thick layers ($d > 0.1$ m). Such density variations are generally not seen deep inside ice sheets (Schytt, 1968).

1.8.b Scalar wave theory

The best early modelling of internal reflections was done using scalar wave theory (also called Radiometry or the Kirchhoff approximation) which deals with unpolarised, incoherent radiation. This theory is able to deal with absorption, reflection from a varying medium and with rough surfaces. It is suitable for modelling the recordings of the early radio echo systems which were only able to detect the intensity of the returning signal. Harrison (1972, 1973) used scalar wave theory to model the expected reflection coefficient of a pulsed radar from a number of distributions of the real permittivity. He assumed that the surfaces were smooth (specular) and that there was no absorption. For the case of an isolated thin layer (when the layer was much smaller than the wavelength), he obtained a result that agrees with that of Robin et al. (1969). The second case he considered was a random variation of the real permittivity with depth. As he did not have any ice core data he had to make various assumptions about the permittivity variation. He concluded that internal reflections are likely

to be due to the vectorial sum of reflections from many closely spaced layers within the pulse resolution length, rather than reflection from a single layer. No subsequent authors have disputed the importance of the reflections from many closely spaced layers. But this may be because most subsequent authors have concentrated on the effect of a single layer in the ice sheet.

Sivaprasad and Lessow (1976) have pointed out alternative methods to the scalar wave theory for considering a pulse propagating in a loss free dielectric slab. However lacking any ice core data they were unable to test their equations.

1.8.c Recognising the importance of the conductivity

Paren and Robin (1975) were the first authors to consider the importance of the conductivity in causing reflections. This was a result of laboratory measurements they had conducted showing the range of conductivity in glacier ice. Their model was a single layer, but included the effect of interference between the reflections from the top and bottom of the layer. They concluded that internal reflections deep inside ice sheets could be due to changes in the conductivity of the ice.

1.8.d Scattering by bubbles

When considering the bubbles inside cold glaciers it is typical to use spherical scattering. As the bubbles (~1 mm) are much smaller than the wavelength of the radio echo (> 6 m) most workers use a theory based on Rayleigh scatterers (Robin et al. 1969; Smith and Evans, 1972; Watts and England, 1976).

Robin et al. (1969) considered the effect of bubbles and concluded: firstly that the loss of

power in the propagating wavelet is negligible; secondly that the frequency content of the propagating wavelet is not affected and thirdly that the energy reflecting from the bubbles is not detectable as an echo.

As long as the average size of the dispersoid is << the wavelength then it is unnecessary to consider the scattering properties of the system but one can more appropriately treat the system in terms of dielectric theory. This is what will be done for the rest of this thesis.

1.8.e Reflections from fabric variations

Harrison (1973) proposed that the variation in ice fabric was one of the dominant causes of internal reflections. Clough (1977) calculated that abrupt changes in the crystal orientation could cause internal reflections if the electrical anisotropy was 1% or greater. The first attempt to model the reflection coefficients from crystal orientation changes by using data from ice cores was by Ackley and Keliher (1979). Their estimate for the effect of fabric is less than the effect for bubbles. Fujita and Mae (1994) allow the fabric to change suddenly from a random orientation to all crystal axes aligned vertically and obtain power reflection coefficients of up to -60 dB.

The most recent development in modelling for internal reflection is the production of synthetic radargrams where the properties of the ice sheet are used to calculate an expected radar response. This is called forward modelling and will be considered in the next section.

1.8.f Forward modelling

I will review two other areas of forward modelling before returning to the forward modelling of radio echo sounding in ice. The first is synthetic seismograms where the propagation of acoustic waves through the ground is considered. The second is radar modelling for ground penetrating radar in soil.

1.8.f.i Synthetic seismograms

The main area where modelling of reflections from varying ground has been done in the past is in seismics, where reflections occur as a result of changes in the acoustic impedance (product of density and wave velocity).

The first synthetic seismogram (Peterson et al. 1955) was possible as the first continuous velocity logs from boreholes started to be available. However the authors had to make assumptions about the variation in the density. They introduced an approximate expression for the reflection coefficient which depended on the change in the logarithm of the acoustic impedance. They found that this expression was valid even for very large changes in the value of acoustic impedance. This gave them a reflection profile that contained only the primary reflections and did not account for the transmission losses.

They found a time delay in the recording system relative to the well log of anything between 17 to 55 milliseconds, due to the mechanical delay in the seismic pulse and delays introduced in the recording system. This was corrected by a bulk time shift of the well log trace. They also talked about the tuning effect that can occur for certain relationships between bed thickness and the length of the incident wavelet.

The next development was to generate a spike reflection profile for the ground that included multiple reflections. The first multiple calculating algorithms in seismics used algebra (Berryman et al. 1958; Baranov and Kunetz, 1960). These were improved by the introduction of matrices by Wuenschel (1960) where he derived Laplace transform solutions for a theoretical seismogram without absorption. He considered the transmission between the layers where he approximates variable velocity zones by homogeneous layers of constant transit time. The synthetic record produced predicts many events that are not actually recorded due to the roughness of the interfaces which scatter energy and decrease the contribution of multiples.

A useful review of synthetic seismograms is by Dennison (1960) who makes the point that while a close match between synthetic and field record may be intellectually satisfying, the real use lies in the ability to study the changes produced in the synthetic by changes in the ground. These include producing a synthetic with and without certain interfaces to see which are responsible for a particular reflection, or producing a synthetic with and without multiples. He concludes that the use of synthetics has emphasised that a good reflection may not be due to a single large velocity contrast.

Subsequent forward modelling in seismics developed by the use of the finite difference time domain technique (Kelly et al. 1976).

1.8.f.ii Ground penetrating radar modelling

There is a growing body of literature on the forward modelling of ground penetrating radar. The first paper in which a synthetic radargram is modelled for soil is Goodman (1994) who considered a 1 m deep portion of ground containing buried pipes using a two dimensional ray tracing model. He writes "properly predicting radar signatures from 1-D structures in the

ground requires higher dimensional modelling to account for the effects of antenna aperture, as well as geometric spreading". One of the results of this thesis will be to see if higher dimensional modelling is necessary when considering the greater depths in ice sheets. Goodman says that forward modelling (prior to his paper) is limited to 1-D structures in the literature, yet he gives no references to any publications.

Another ray tracing calculation is used for a GPR on a temperate glacier (Nicollin and Kofman, 1994). However they make assumptions about the ice properties and do not produce a synthetic radargram. Their result is the reflection power as a function of two way travel time.

Subsequent authors continue to consider two dimensional algorithms for GPR over distances of a few metres, with increasing number of publications using finite difference time domain modelling (Bergmann et al. 1996, 1998).

1.8.f.iii Synthetic radargrams for ice

Moore (1988 a, b) produced the first synthetic radargram for radio echo sounding using ice sheet conductivity measurements. He had 2500 conductivity measurements along a 130 m long core from Dolleman Island in Antarctica. He had to make assumptions about the density. The calculation was a one dimensional convolution with a depth invariant wavelet, which produced an expected gain corrected A scope radio echo profile at the site. This model had a lot in common with the early synthetic seismogram models. Unfortunately there was no radio echo sounding data from the site for comparison, but the modelling did show that conductivity variations could produce internal reflections.

The next modelling was done by a group at Münster University, Germany (Stock, 1993;

Blindow, 1994 a, b). They had information from a 215 m long core from site B13 on the Filchner Ronne ice shelf. The density was measured every metre and the ice conductivity was determined from the electrolytic conductivity of melted samples. The monopulse radio echo system used at the site had a 40 MHz carrier frequency. The forward model was a matrix formulation such as Wuenchel (1960), which considered the behaviour of monochromatic waves travelling through the ice. This model included primary and multiple reflections and by the use of an inverse Fourier transform gave the expected time domain record. The measured and modelled radio echo show similar magnitude internal reflections, in particular the reflection from the boundary between the meteoric and marine ice inside the ice shelf.

In the course of this thesis similar models will be developed and tested on two new ice cores.

1.9 Comparing internal reflections with glacier flow models.

Glacier flow models require a great deal of information about the state of the glacier such as: the accumulation at the surface, the stress and strain at depth, the past history of the glacier flow and accumulation. In most cases not all this information is available and assumptions need to be made. These models then predict the age against depth relation and the velocities for the ice at depth. Such models can predict the depth of isochrones. These calculated isochrones can then be compared with the observed position of the internal reflections on Z scope RES data.

The first paper to suggest that an IRH could be considered as an isochrone was Robin et al. (1969). Their suggestion was based on the following reasoning: an internal reflection needs a permittivity change to produce it. One way that such a permittivity change can occur is by

having a layer of clear ice inside bubbly ice. Layers of clear ice can form at the surface of a glacier on hot sunny days. They calculated an example for a Greenland glacier using a steady state model, and found that the predicted depth of the AD 957 surface deviates at the most by 6% from the depth of the internal reflection, see figure 1.5.

There are two problems with this interpretation; firstly it requires a very thick ice layer to form the reflection (§1.8.a); secondly a single stratigraphic layer does not produce a reflection consistent with many of the properties that characterise an internal reflection (§1.6.b).

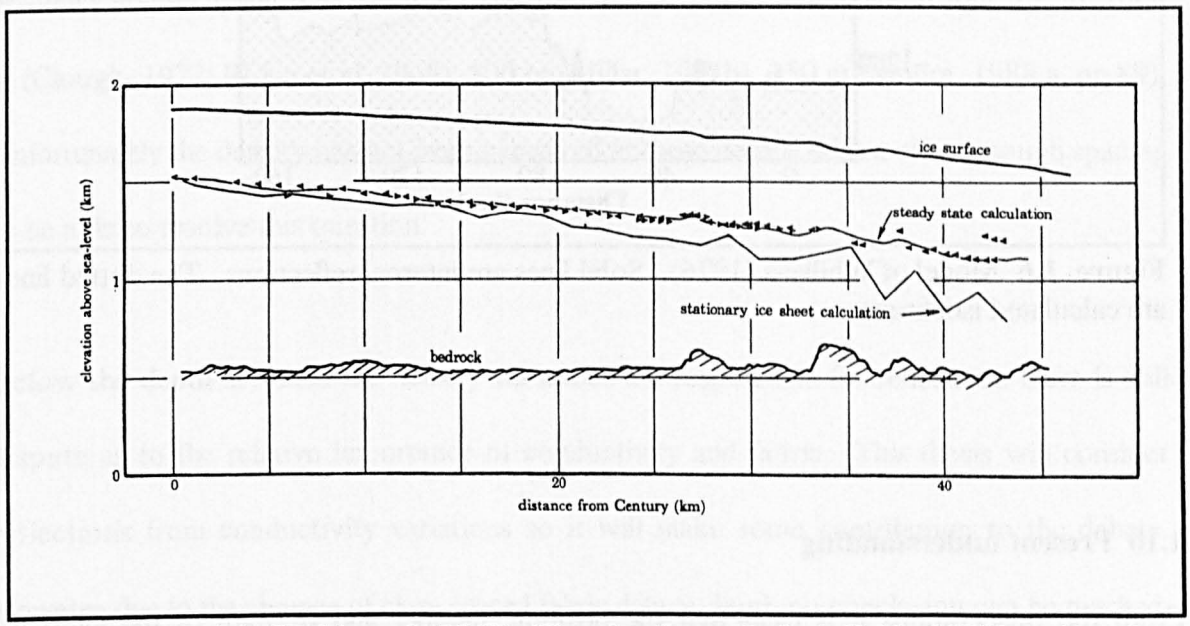

Figure 1.5 Model of Robin et al. (1969). The triangles mark the individual IRH position from each A scope scan. The solid lines are calculated isochrones using two different models.

Whillans (1976) improved on the calculation of Robin et al. (1969) when he analysed IRH near Byrd base in Antarctica. He determined the strain rates at the surface and used these strain rates in a steady state model to see where the isochrones would lie inside the ice sheet. His calculated isochrones and the internal reflections show remarkable agreement. See figure 1.6. This agreement was used by Whillans to support the concept that the internal reflections are

connected with depositional stratigraphy. Any disagreement between the position of the IRH and the isochrones he attributed to a slight separation of the RES and the strain network.

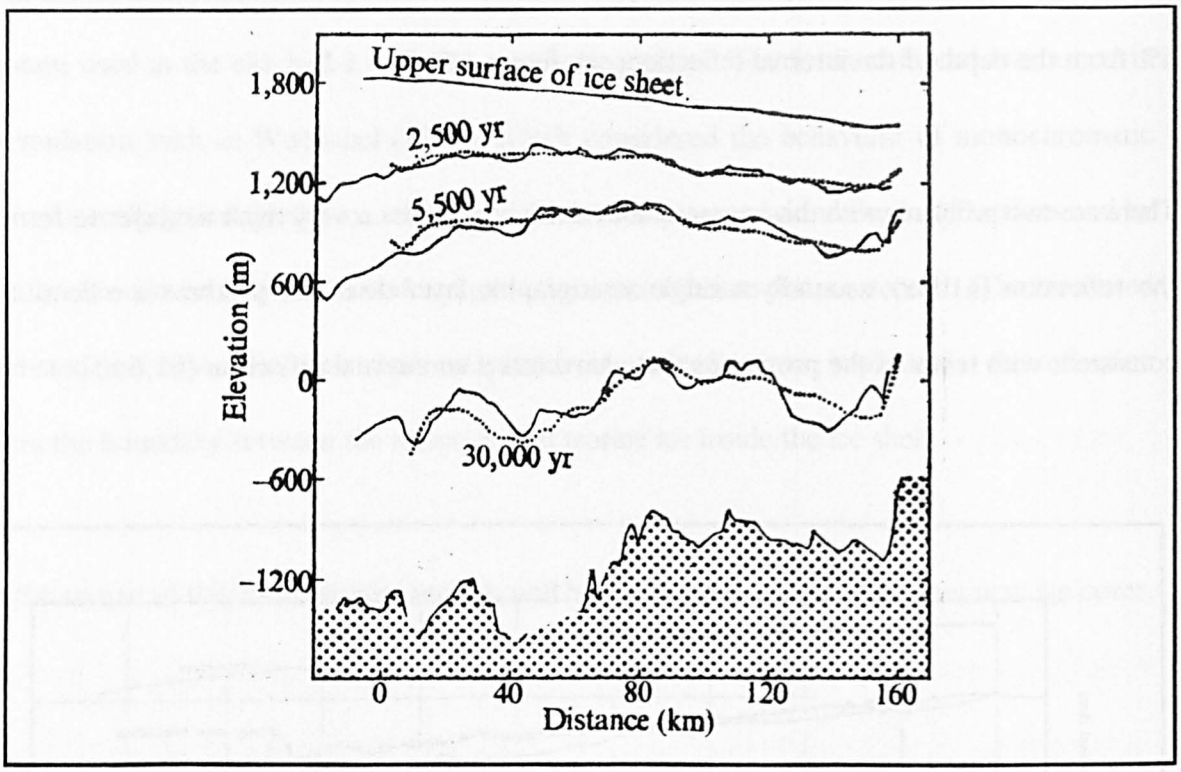

Figure 1.6 Model of Whillans (1976). Solid lines are internal reflections. The dotted lines are calculated isochrones.

1.10 Present understanding

From the observations it is clear that the position, number and strength of the internal reflections depends on the radio echo system. In parts of the echo where there is no single strong reflection then the echo received at the surface consists of the interference between many weak wavelets reflecting from small changes in the complex permittivity (Harrison, 1973; Gudmandsen and Overgaard, 1978; Millar, 1981 a, b).

From laboratory measurements on ice it has been shown that the complex permittivity depends on five variables: temperature, pressure, density, chemical impurity concentration and the

orientation of the crystals in the ice. Of these variables the temperature and pressure change slowly inside an ice sheet, and the rate of change of these two quantities with depth is too slow to cause reflections.

The density (§2.3), chemical impurity concentration (§2.8) and fabric (§2.9) can change significantly over a short depth in the glacier. So it is likely that these will be responsible for any reflections. The present consensus is that in the top few hundred metres of an ice sheet complex permittivity variations are dominated by the changing density. Many differing values are given for the depth at which density is thought to be no longer dominant; its value has been gradually revised upwards as research has progressed: 1500 m (Paren and Robin, 1975), 1000 m (Clough, 1977; Robin et al. 1969), 500 m (Millar, 1981b), 250 m (Moore, 1988 a, pp 89). Unfortunately the density has not been measured at these depths with a close enough spacing to be able to resolve this question.

Below the depth at which the density variations are responsible for reflections there is still dispute as to the relative importance of conductivity and fabric. This thesis will consider reflections from conductivity variations so it will make some contribution to the debate. However due to the absence of close spaced fabric data at depth no conclusion can be reached.

1.11 Contribution of this thesis

This thesis makes further progress towards deciding whether internal reflections can be treated as isochrones. The method will be by the use of forward modelling. I have information from two ice cores and radar surveys. One is a site in the centre of the Greenland ice sheet, which was drilled as part of the Greenland Ice Core Project (GRIP). For this site I have been given

the ice core conductivity profile and the radio echo profile in the vicinity of the drill site. The other site is a coastal ice rise in Antarctica called Berkner Island. For this site I have collected the conductivity data along a 181 m ice core and have been given the ice core density and the radio echo profile in the vicinity of the drill site. Due to recent advances in measurement techniques all of these data are at a higher resolution than many previous measurements.

By combining the ice core data with forward modelling, it is my intention to create a model of how the transmitted electromagnetic pulse interacts with the glacier. During the development of the model many different interactions between the electromagnetic pulse and the ice will be investigated. The final model produces a predicted radio echo that, as closely as possible, matches the observed radio echo profile. Such a model will clarify the connection between changes in the ice core properties and the observed internal reflections.

CHAPTER 2

COLD GLACIERS

This thesis deals with using radio echo sounding to look inside a cold glacier. The observed internal reflections are a result of the internal properties of cold glaciers. In this chapter some background information is given on cold glaciers.

As many properties of glaciers are a result of the properties of ice, this chapter starts with some background on the structure of ice. It then goes on to consider how the ice crystals originally in snow are transformed into glacial ice.

During this chapter attention is paid to three questions: firstly whether snow that accumulated at the surface at the same time will remain together when buried; secondly how the properties that affect the permittivity will alter with depth; thirdly whether the ice brought to the surface in an ice core is an accurate representation of the properties of the ice sheet at depth.

2.1 Crystal Structure

The crystal structure of ice is important in understanding its electrical properties. Ice consists of water molecules (H_2O) which are held together by hydrogen bonds that form between the oxygen atom and a hydrogen atom in an adjacent water molecule. The defect free structure of ice obeys some rules set out by Bernal and Fowler (1933).

1) Each H bond has one H on it.

2) Each O has 2 H near to it.

Obeying these simple rules it is still possible to construct many possible arrangements of the hydrogens around each oxygen atom. Snow that falls on the surface of a glacier has a structure called Ih (Hobbs, 1974). Ice (Ih) refers to the ice phase of lowest density where the oxygen atoms are arranged in a hexagonal close packed structure. This allows the identification of a series of parallel planes called basal planes. The normal to the basal planes is known as the c-axis or optic axis of the crystal. This is shown in the figure below:

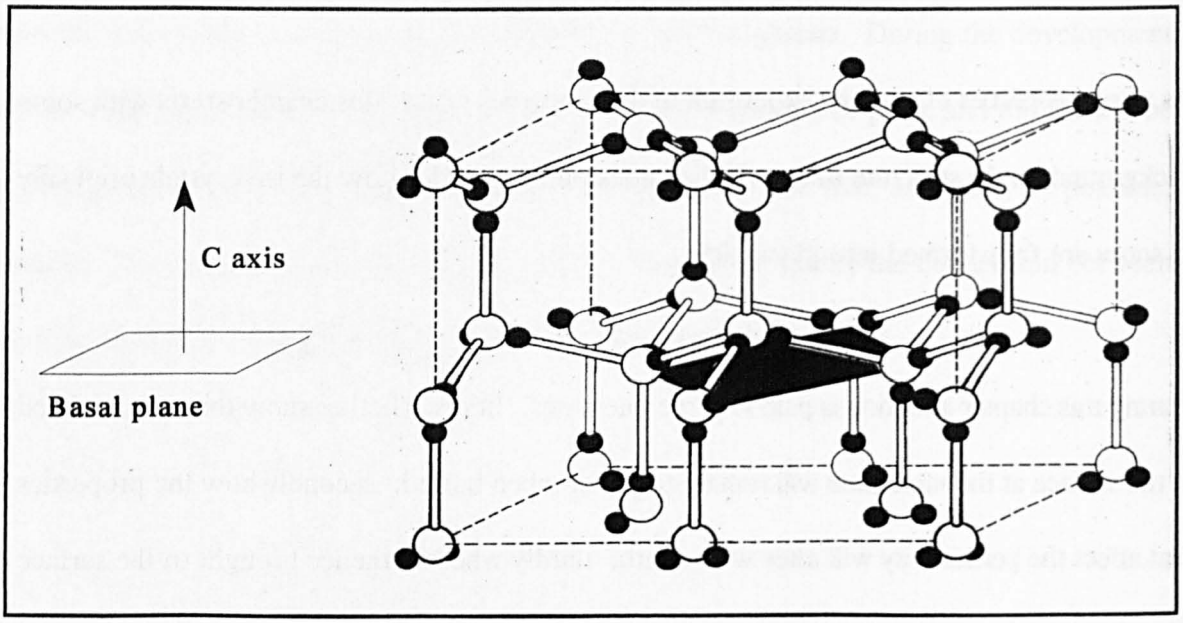

Figure 2.1 The structure of ice Ih. The positions of the oxygen and hydrogen atoms in pure solid ice Ih (from Fletcher, 1970). The base of the unit cell has been marked out.

For ice crystals the lack of complete hydrogen bonding at the surface leads to a surface that has liquid-like properties different to the properties of the bulk. This has often been termed the quasi-liquid layer.

2.2 Snow

The arrival of the snow and its transformation into ice needs to be considered as it affects how the properties in the ice sheet such as density, conductivity and fabric alter with depth. It is

also necessary to consider how plausible it is to assign a date to features in the ice.

2.2.a Precipitation and Accumulation

Precipitation is the discharge of water (as rain, snow, hail or sleet) from the atmosphere onto the Earth's surface. Accumulation covers all the processes that add, or subtract, snow to a glacier including: snowfall, condensation, riming, sublimation, avalanching, transport by the wind etc. At one site the precipitation and the accumulation can be different. Snow falls throughout the year on a high polar ice sheet, although it is generally assumed that more accumulates during the warmer summer periods (Shoji and Langway, 1989). The present annual accumulation at a site is related to the temperature, altitude and distance from the coast.

2.2.b The break up of snow

The wind, temperature and pressure all contribute to the metamorphism of snow into ice. The wind continually stirs the snowflakes on the surface of the glacier. This jostling is one mechanism that causes the initial breaking up of snowflakes. Snow left on the surface can be redistributed along the surface or mixed in with previous deeper snow. The wind also aids the sublimation of the snow.

The temperature influences the rate of transformation of snow to ice. With warmer temperatures the transformation occurs more rapidly and on very warm days sublimation can occur from the surface of the glacier. The surface temperature together with the surface barometric pressure also influences the flow of water vapour inside the loose firn at the top of the glacier.

The pressure is one of the main driving forces for the compaction that occurs. As each

successive snowfall accumulates on top of the glacier, this leads to an increasing overburden that applies a stress to the snow underneath.

The surface snow has a porosity of 90% (Lock, 1990) and a density of about 100 kg m^{-3} (Paterson, 1994). Most of the grains consist of one or two crystals (Gow, 1968).

2.3 Firn

The snow grains settle into a closer packing regime, stacking together to reduce the porosity to 40% (density 550 kg m^{-3}) (Lock, 1990). It is now possible to call the structure firn. Firn can either be defined as porous grain-like ice, transitional between snow and glacier ice (Kotlyakov and Smolyarova, 1990); or snow that is over one year old (Shoji and Langway, 1989).

The touching grains then develop necks to join together in a process called sintering. This is the rearrangement of the water molecules using four processes: viscous or plastic flow, transfer through the vapour phase, volume diffusion through the grains and surface diffusion over the grains (Hobbs, 1974).

The porosity (y) is the primary variable that dictates the density in the firn. Of secondary importance are the pressure (P) and temperature (T) which only become significant when the porosity has decreased to zero. The relationship between the density and the porosity has been studied by many authors (Schwander et al, 1993; Shabtaie and Bentley, 1994). The density of the firn (ρ_{firn}) is related to the porosity (y) by the equation below (Salamatin and Lipenkov, 1993):

$$\rho_{firn} = \rho_{ice}(1 - y) \qquad (2.1)$$

where

ρ_{ice} = density of solid ice at given temperature and pressure.

The seasonal variation in the wind and surface temperature affects the metamorphism of the snow. Snow that accumulated during the summer usually has a coarse grained matrix with low bulk density. Winter accumulation is finer grained and has a higher density. In cases of exceptionally warm or windy weather special features can form inside the firn or on the surface. It is features such as these that may form internal reflections. These features are described in the table below.

Table 2.1 Features found in the firn layer of cold glaciers (based on Shoji and Langway, 1989)

Feature	**Appearance in cold glaciers**	**Density compared to surrounding firn**	**Formation process in cold glaciers**	**Season of snow in which feature typically appears**		
				Summer	**Autumn**	**Winter**
Melt Phenomena, Ice layers	Thin layers (typically <2mm) of clear ice.	higher	Formed on or near the surface by solar radiation.	prominent		
Wind Crusts	Thin layers (<2mm) of harder close packed small grained snow.	higher	Due to a strong wind disintegrating the snow and compacting it.	present		present
Radiation Crusts	Thin layers (<2mm) of harder close packed small grained snow.	higher	Formed on the surface by solar radiation	present		none
Depth Hoar	Layer of thickness of order 10 mm containing large grain crystals of 2-5 mm diameter.	lower, highly porous with a density 100 to 300 kg m^{-3}	When a warm snow surface is covered by a blanket of colder snow. This prevents upwards heat and vapour transport causing vapour to condense at the interface.		present	

2.4 Pore close off

The point at which the permeability of the firn becomes zero is taken as the firn-ice transition (Shoji and Langway, 1989). This point is often called the pore close off. The density at pore close off varies with temperature (Martinerie et al. 1992) but typically is at a density of 800-840 kg m^{-3} (Schwander and Staffer, 1984). The depth at pore close off varies with the accumulation rate and temperature at the site. For cores near the coast this typically occurs at a depth of 60-70 m and between 100 and 300 years after the snow originally fell (Paterson, 1994). The mean distance travelled by a water molecule as vapour during its densification prior to pore close off can be 8-10 cm (Johnsen, 1977).

The pore close off depth is of great interest to glaciologists as it is the point at which the air in the bubbles becomes separated from the atmosphere. This air is then trapped and stored allowing samples from previous atmospheres to be sampled. Gow (1968) showed that at pore close off there are as many bubbles as grains per unit volume with most bubbles lying at the junction of three or more grains.

2.5 Glacier ice

Glacier ice is ice containing bubbles of air. Below the firn-ice transition the density increase is a result of the compression of the air bubbles due to pressure. How pressure, stress and strain are related is explained below.

The stress at any point is represented by a second order tensor. The principal axes for a glacier

are the vertical and the horizontal. The diagonal elements are the normal stress components (σ), and the off diagonal elements are the shear stresses (τ). For incompressible ice in equilibrium the shear stress components balance. The pressure (P) at a point in the glacier is the mean value of the three normal stresses. Subtracting this value from the normal stress components gives the stress deviators (s_x , s_y , s_z) whose sum is zero.

$$STRESS = \begin{pmatrix} P+s_x & \tau_1 & \tau_2 \\ \tau_1 & P+s_y & \tau_3 \\ \tau_2 & \tau_3 & P+s_z \end{pmatrix} \qquad (2.2)$$

The pressure is assumed to increase uniformally in the glacier but the stress deviators alter in both the firn and in the solid ice.

The stress and resultant strain at depth leads to a thinning of the annual layers of accumulation as the incompressible solid ice extends in the horizontal direction and compresses in the vertical direction.

2.6 Clathrates

At a certain depth the bubbles start to decrease in size faster than expected due to the pressure. At these depths new transparent inclusions form with a higher refractive index than the surrounding ice. These inclusions are clathrate hydrate crystals where individual molecules of gas (O_2, N_2, CO_2, and CH_4) are incorporated into cages of water molecules. There are two possible structures (I and II) for the cages, structure II being the larger cage. In deep ice cores there is only structure I with a volume percentage of between 0.02% (Shoji and Langway, 1982) and 0.06% (Millar, 1973).

This process of formation starts to happen when the enthalpy gained in putting the molecule into the cage is greater than the energy penalty in forming the cage. At 0°C in ice this occurs at a pressure of 12.2 MPa for O_2 and at 16.2 MPa for N_2 (Millar, 1973). It is not necessary for all the cages to be occupied. In the GRIP core the depth range where clathrate formation occurs is 700-1300 m (Pauer et al. 1995).

2.7 Grain size and fabric

The grain size of the ice is measured from thin sections and in this thesis the size will be expressed as an average area (Gow, 1969; Jacka, 1984; Thorsteinsson, 1996). The term given to the collective orientation of the crystals is the fabric. When the snow first settles the c-axes of the crystals are randomly oriented. The vertical compressive stress causes rotation of the c-axis towards the vertical (Herron and Langway, 1982).

In deeper firn recrystallisation becomes the dominant mechanism for changing the fabric. This first stage of recrystallisation is called normal grain growth. The grain boundaries migrate as atoms in smaller grains transfer to larger grains. The recrystallisation causes an almost linear increase in grain size with depth, with the new crystals forming at 45° to the vertical (Paterson, 1994). For example at site 2, Greenland, the average grain size at 100 m was 2.7 mm^2 increasing to 4.9 mm^2 at 300 m (Langway, 1967).

The grain growth is primarily controlled by the stress and temperature and secondly controlled by the impurities in the ice. Any impurities already in the ice grains are subjected to the forces exerted by the migrating grain boundaries. If there are small clusters of soluble impurities they are carried through the lattice on the grain boundary, in the process impeding the speed of

travel of the boundary. If there are large clusters of impurities, or large bubbles, the migrating grain boundaries will flow past such large features without moving them. These observations can be explained theoretically (Alley et al. 1986a, 1986b). The crystals of clathrate hydrate act as barriers to the migration of grain boundaries.

Once the strain on crystals reaches a critical value they start to develop internal dislocations. This second type of recrystallisation is called polygonalisation. The dislocations then migrate to rearrange themselves in sub-grain boundaries. These boundaries separate areas of the crystal with c-axis orientations of a few degrees. When the difference in orientation reaches about 15 degrees it is appropriate to speak of separate grains. Such a process means that there is a limit to the size of the crystal grains in the ice sheet.

Near the base of the glacier, heat is supplied from the bedrock. If the ice becomes warmer than -10^0C (Thorsteinsson, 1996) then it is possible to have nucleation and rapid growth of new dislocation-free grains at a different orientation to the surrounding grains. This third type of recrystallisation is called migration recrystallisation. If there is considerable heat energy this can cause the melting of the ice to form a subglacial lake.

2.8 Impurities

In this section a brief outline is given of the types of impurities that can be expected in the cold glaciers found in polar regions. An indication of the sources and the transport mechanisms is given, eventually showing where the impurities may lie inside the polycrystalline water crystals. Many different molecules fall under the heading of impurities, so this is not a comprehensive review. The impurities that are incorporated into the snow on the surface of an ice sheet at a

given instant are one possible means of the formation of isochrones.

2.8.a Sources

Some chemical species measured in ice cores are produced by reactions in the atmosphere. Hydrogen peroxide (H_2O_2) is related to the oxidation capacity of the atmosphere. Nitrate (NO_3^-) is produced by various mechanisms including the action of lightning in the atmosphere. Other chemicals get swept up into the atmosphere from the ground. Dust containing chemicals such as aluminium, calcium and silicon is lifted up by the wind from deserts. When the wind is strong, it can whip spray from the sea surface and this puts an aerosol of sea salt (especially NaCl) into the atmosphere. This effect is highest during stormy, winter periods (Mulvaney and Wolff, 1994). Another proposed source of sea salt in the winter is the existence of freezing sea water close to the coast that causes frost flowers to grow (Hall and Wolff, 1998). The action of the marine creatures, mostly algae, can produce various sulphur species which become oxidised to give sulphate (SO_4^{2-}) and methane sulphonic acid (CH_3SO_3H). These species are produced in the greatest quantities in the summer. This means that there can be a seasonal pattern in the chemicals in an ice core. Some sulphate is also found in sea salt and therefore in ice core records the expected contribution from the sulphate in sea salt is often removed and it is the non sea salt (nss) sulphate concentration that is displayed.

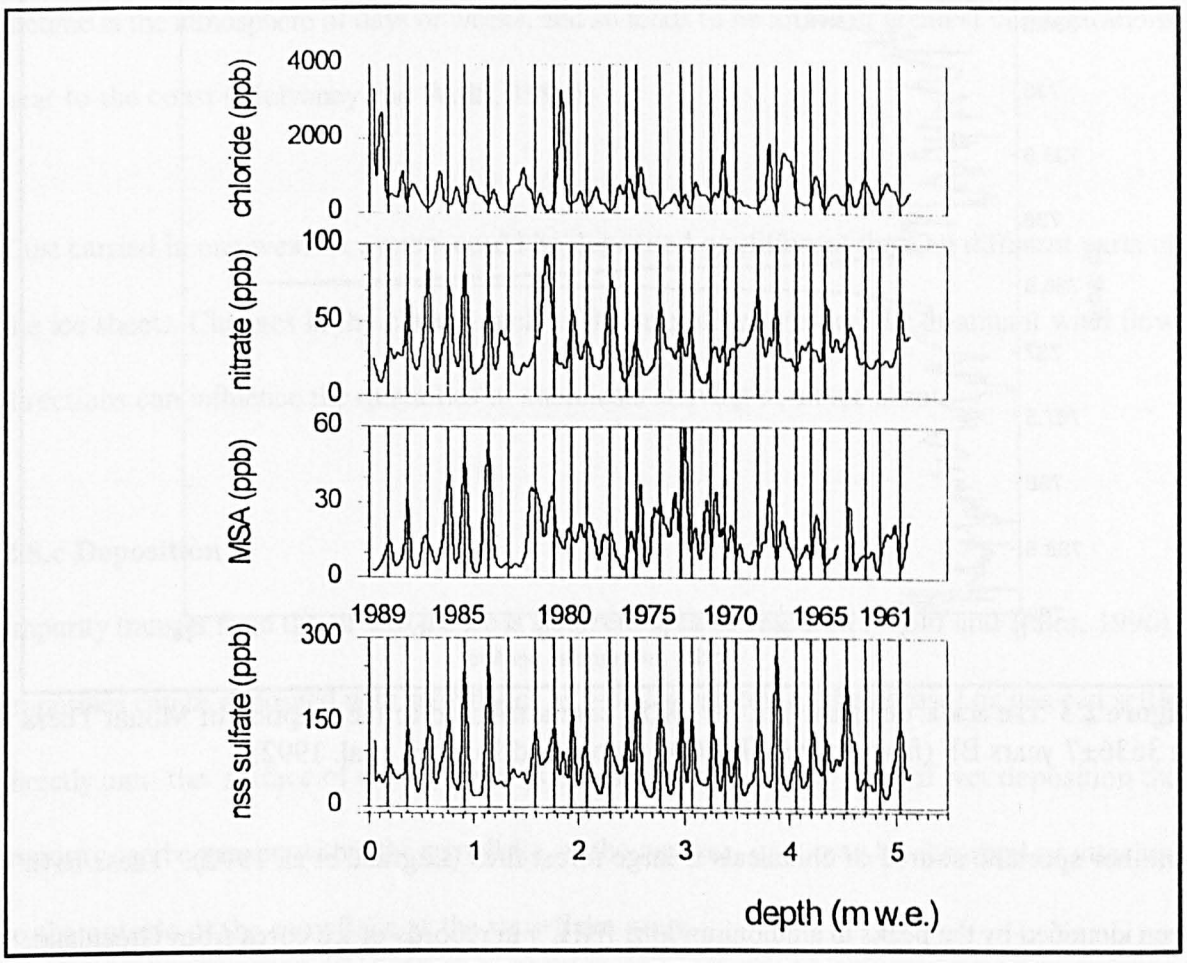

Figure 2.2 Variation in four chemicals in parts per billion (ppb) from the firn of South Dome Berkner Island. Depth is in metres of water equivalent (m.w.e.), the vertical lines are when the summers are thought to occur. MSA = Methane Sulphonic Acid (CH_3SO_3H) (from Wagenbach et al. 1994).

The non sea salt sulphate comes mainly from biological sources and from sporadic volcanic events. Millar (Appendix 1, 1981 a) has a description of the spread of sulphate from the Gunung Agung eruption of March 1963. Volcanic events also put a small amount of hydrochloric acid (HCl) into the atmosphere. The acidic deposition from volcanoes is often clearly seen as spikes in ice core records such as in the figure below. Such a feature is a definite isochrone.

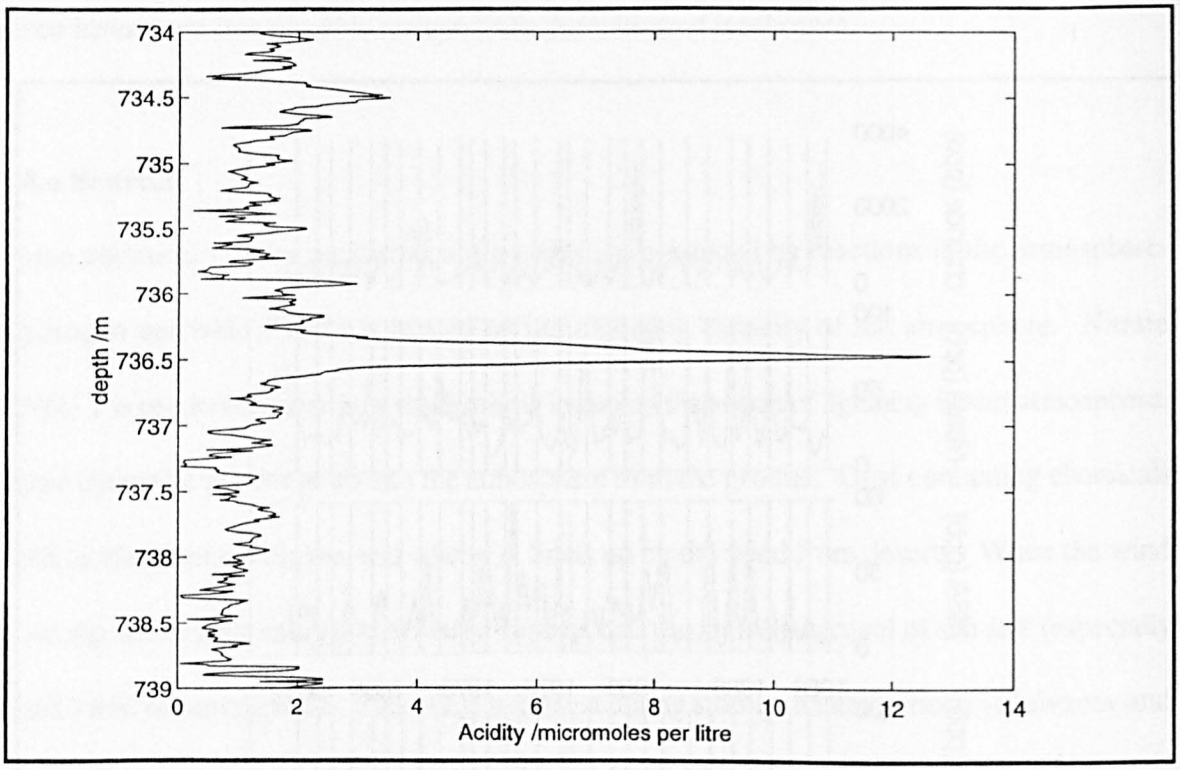

Figure 2.3 The acidic deposition in the GRIP core attributed to the eruption of Mount Thera in 3636±7 years BP (from the GRIP ECM record and Johnsen et al. 1992)

Another sporadic source of chemicals is large forest fires (Legrand et al. 1992). These have been identified by the peaks in ammonium ions (NH_4^+) in records of ice cores from Greenland. Such ammonium peaks are not visible in Antarctic records due to the large distances between the continent and large forests.

These sporadic inputs from volcanoes and forest fires stand out in ice cores from the seasonal variation.

2.8.b Transport

The movement of local air circulation systems and the jet stream can influence the transport of chemicals from their source to the ice sheet. Higher wind speeds will transport the species to the polar regions faster. There is also the need to consider any precipitation that will have removed the species during its passage. Different species have different lifetimes in the

atmosphere and so will be deposited at different rates. Sea salt aerosol, for example, has a lifetime in the atmosphere of days or weeks, and so tends to be found in greatest concentrations near to the coast (Mulvaney and Wolff, 1994).

Dust carried in one weather system could be deposited on different days on different parts of the ice sheet. Changes in the climate such as the size of deserts and the dominant wind flow directions can influence the quantities of chemicals arriving at an ice sheet.

2.8.c Deposition

Impurity transfer from the air into the ice is a current area of research (Wolff and Bales, 1996). Impurities can be deposited with snowflakes as wet deposition, or the aerosol or gas can settle directly onto the surface of the ice sheet as dry deposition. In the case of wet deposition the impurity can be present within the snowflake, as the nucleus, or it may be absorbed or attached to the outside of the snowflake as the snowflake grew.

2.8.d Redistribution in the firn and ice

All chemical species with a finite vapour pressure will be redistributed in the vapour phase through the open pore space or from the surface. As the firn becomes less permeable, then any impurities in the pore space will become trapped on the walls of the pores. Once the firn turns to ice the location of the impurities will be a result of their interaction with the grain growth that is occurring. Two characteristics of the impurities that affect their eventual location in the ice are: firstly the freezing point for the ice, water and impurity mixture. There is a thermodynamic argument showing that any liquid phase prefers to exist as channels at the three grain boundaries (Paren and Walker, 1971); secondly, the solubility of the impurity in water and ice (distribution coefficient), which will determine what proportion of the impurity exists

in the solid or liquid phase.

2.8.e Equilibrium location in deep ice

Mulvaney et al. (1988) used scanning electron microscopy with an X-ray detector to show that there is some sulphur (probably H_2SO_4) at the triple grain boundaries. For sea salt in meteoric ice, it is thought that fractionation occurs and that most of the chloride ions are inside the ice grains, while the sodium ions remain at the grain boundaries (Addison, 1969; Moore et al., 1994).

2.9 Rapid changes in fabric associated with impurities

Rapid changes in the fabric has been proposed as a cause of internal reflections. In this section the evidence for rapid fabric changes is reviewed. In the fabric section (§2.7) it was stated that the presence of impurities can impede the migration of grain boundaries. Having considered fabric and impurities separately in the two previous sections it is now necessary to consider how they can interact.

The association of a change in fabric simultaneously with a change in impurity concentration was observed in the Byrd core (length 2164 m), in which there were as many as 2000 cloudy bands in the core, of thickness 1 mm to 60 mm, occurring mostly between the depths of 1200 and 1800 m. Twenty bands were examined and all contained volcanic debris although this does not tell us that all the other bands contain volcanic debris as well. Examination of unbanded ice revealed very few or no debris. The grain sizes in the bands are much smaller than the surrounding ice (Gow and Williamson, 1976).

The fabric in the bands at 910 m and those below 1800 m is more tightly clustered to the vertical compared to the fabric in the surrounding ice. However the bands at 788 m, 1310 m, 1415 m and 1532 m have a similar fabric in the band and the surrounding ice. Below 1800 m as the bedrock approaches and the ice is warmed, the bulk of the ice has undergone migration recrystallisation into large crystals with diverging axis orientations; however the ice in the cloudy bands has not been affected and retains its vertical fabric.

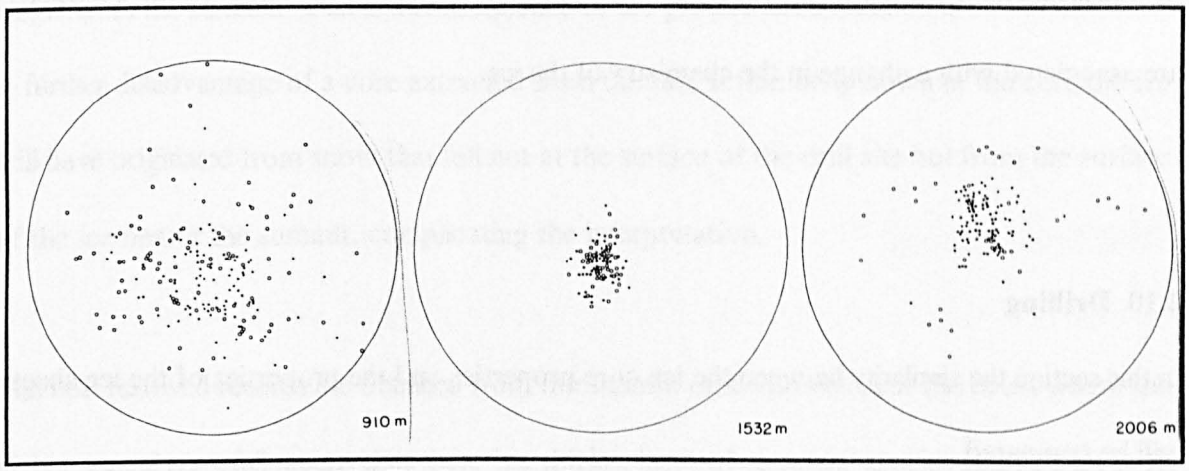

Figure 2.4 The fabric in the Byrd core at three depths, the dots are in the cloudy bands, the circles are in the surrounding ice. At 910 m and 2006 m the fabric inside the band (dots) differs from the fabric in the surrounding ice (circles), but at 1532 m the difference is negligible (from Gow and Williamson, 1976).

In the Camp Century ice core in Greenland there is a reported sudden change in the fabric at the transition from a glacial to interglacial climate. At 1136 m the fabric is clustered to the vertical with several maxima. Then at 1149 m the fabric is very strongly oriented to the vertical (Herron and Langway, 1982). A similar change is reported in the Byrd core when comparing a fabric measurement at 1137 m with one at 1210 m (Gow and Williamson, 1976). In both cores there is also a rapid decrease in the grain size at this point. For the GRIP core Thorsteinsson (1996) noticed that the grain size was inversely related to the calcium concentration which increased during the glacial. However there was no jump to a strongly

oriented single fabric as the depth increased across the transition from interglacial to glacial.

One depth on the GRIP core where an abrupt change in fabric was observed was at Event 1 in the late Eemian at a depth of 2797.08 m. This is thought to have been deposited when the climate briefly switched to a cold state. It is a 100 mm thick band of fine grained ice with a stronger vertical fabric than the ice on either side.

In conclusion there are a few published examples of rapid changes in the fabric of the ice; these are associated with a change in the chemistry of the ice.

2.10 Drilling

In this section the similarity between the ice core properties and the properties of the ice sheet will be compared.

2.10.a The drill site

The sequence of annual snowfalls that now lies trapped in glaciers makes certain sites potentially excellent archives of the past atmosphere. This information can be accessed by using a drill to extract a core. The preferred site for ice core drilling is at the summit of an ice dome; here the ice divide and the flow divide should coincide. The ice divide is an imaginary line through the ice sheet which separates the points where ice flows to the left and the right. The flow divide is an imaginary line which joins points where the horizontal component of the ice velocity is zero. In figure 2.5 below is shown an example.

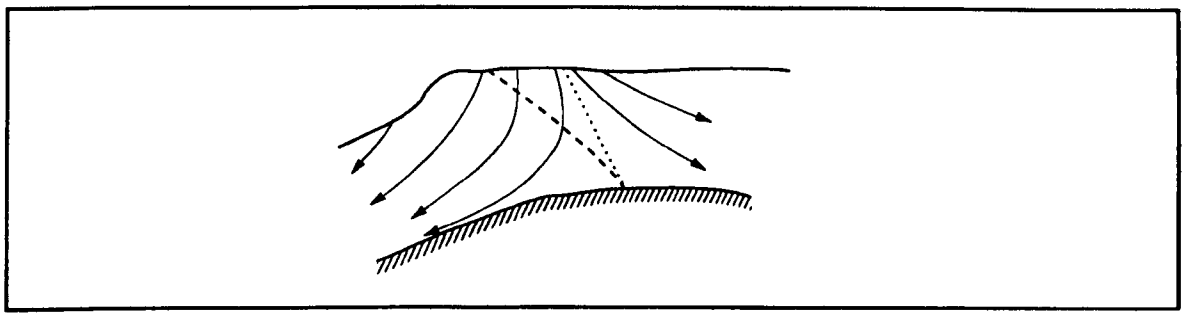

Figure 2.5 The dotted line is the ice divide, the dashed line is the flow divide (from Paterson, 1994)

A core extracted from a position on the side of the dome will span fewer years than the same length from the summit. This is a consequence of the greater accumulation at lower altitudes. A further disadvantage of a core extracted from the side is that deep down in the core the ice will have originated from snow that fell not at the surface of the drill site but from the surface of the ice nearer the summit, complicating the interpretation.

The best resolved records are obtained from the summit of ice domes near the coast where the higher annual snowfall means that there is a thicker layer of chemical species trapped for each year. However, at the coastal sites the thickness of an ice sheet is less, so the high resolution record goes back fewer years. Drilling at the summit of the continental polar ice sheets gives a much longer record. The GRIP core in central Greenland was 3028 m long and has been confidently dated back 100 000 years.

2.10.b How extraction affects the ice

When a core is extracted from a glacier and brought up to the surface various properties will change.

2.10.b.i Temperature change.

When an ice core is extracted from deep inside a glacier and recovered to the surface, it may

be moved into a region of a different temperature. This will change the electrical impedance of the ice from the *in situ* values. It will also cause some annealing as the crystals in the ice change their shape and size; any chemicals inside the ice may also be redistributed. Moore (1988b) calculated that an ice core going into a chamber 10°C warmer then the glacier would warm to within 0.1°C of the temperature in the chamber within 18 minutes. However this calculation did not include the effect of any polyethene bag and insulating cardboard tube. Reynolds (1985) left his samples for 18 hours in order to give them time to stabilise. He recommends that cores should be stored at -20°C or at the annual average temperature of a site if that is lower.

2.10.b.ii Stress change.

The removal of the stress when an ice core is recovered can lead to various effects. The first effect is an increase in the volume due to any remaining elasticity (Nakawo, 1986). The air trapped in bubbles at high pressure will find the constraining pressure is removed (Langway, 1958). This can lead to the formation of cracks radiating out from the bubbles, causing brittleness in ice from certain depths. However the ice will reach equilibrium with the surface pressure within a few months and is then no longer brittle.

2.10.b.iii Chemical change.

The core that comes up will be contaminated on the outside by any drilling fluid used. This is discussed for the Byrd core by Fitzgerald and Paren,(1975). Drilling fluid is typically hydrocarbon based so itself is unlikely to cause electrical problems. It is only if the drilling fluid contains ionic dopants such as Cl^- that the electrical conductivity will be affected (Moore, pers com). A standard procedure is to use a saw to remove the outer layers of the ice core, and thereby removing the contamination in solid cores.

Additional contamination may occur if the core is left exposed for long periods, for it has been shown that an ice core will absorb chemicals from the atmosphere (Schwander et al. 1983). The converse effect is that some chemical species on the outside of the core may evaporate.

2.11 Conclusions

An attempt will now be made to answer the three questions at the start of this chapter.

Question one: will snow that accumulated at the surface at the same time remain together when buried?

Answer: There may be a slight migration of a few centimetres of individual water molecules which will blur the chronological dating of an event. The bulk properties of density and impurity content are emplaced in the ice at the surface and do not alter their chronological order.

Question two: how will the properties that affect the permittivity alter with depth?

Answer: There has been a review of how various physical properties such as the density, grain size and fabric alter with depth.

Question three: is the ice brought to the surface in an ice core an accurate representation of the properties of the ice sheet at depth?

Answer: The ice brought to the surface will differ from the ice at depth. However many of the alterations such as temperature can be corrected for or the effect is insignificant.

CHAPTER 3

PERMITTIVITY OF GLACIER ICE

How electromagnetic waves propagate inside a glacier is determined by the electrical properties of the ice. In this chapter I will first describe the equations for an electric field in ice. Ice is described as a lossy dielectric, as there is a small conductivity that is present at all frequencies. Towards the end of the chapter the possible variation in the electrical properties of the ice inside a glacier is discussed. The notation introduced in this chapter will be used later on to model the internal reflections.

3.1 The electric field inside ice

A quantity such as the electric field ($\boldsymbol{E}$, V m^{-1}) will appear in a variety of forms, all of which are functions of position and time.

$\tilde{\boldsymbol{E}}$ = complex vector, $\tilde{E}$ = complex scalar,
$\boldsymbol{E}$ = real vector, E = real scalar measurable quantity

While a vector notation will be used here the present treatment will consider ice to be isotropic. In ice when an electric field is applied the positive and negative charges can separate, a process called polarisation. The separation of the positive and negative charges gives rise to a polarisation field ($\boldsymbol{P}$, C m^{-2}). The constitutive equations are simplified by the introduction of a displacement field ($\boldsymbol{D}$, C m^{-2}) which is determined from the polarisation and the electric field. Ice is considered to be a linear material, this means that only the first power of the polarisation is used in the equation 3.1 below:

$$\begin{aligned} \boldsymbol{D} &= \varepsilon_0 \boldsymbol{E} + \boldsymbol{P} \\ &= \varepsilon_0 \boldsymbol{E} + \varepsilon_0 \chi_e \boldsymbol{E} \\ &= \varepsilon_0 \varepsilon_r' \boldsymbol{E} \end{aligned} \tag{3.1}$$

where

ε_o = Permittivity of a vacuum, 8.54×10^{-12} F m^{-1}
χ_e = electric susceptibility, dimensionless
ε_r' = real relative permittivity, also called dielectric constant, dimensionless

The permittivity ($\varepsilon' = \varepsilon_0 \varepsilon_r'$) is the ratio of the displacement of electric charge to the strength of the electric field in the ice. Permittivity has units of Farads per metre (F m^{-1}), and it is one of the electrical properties of ice that will be looked at in this chapter.

The other property of interest is the conductivity (σ, with units of Siemens per metre, S m^{-1}) which is the ability to carry charge through the material. It also controls the transfer of energy from the electric field to heat. The conductivity is related to the current density in the ice. The macroscopic current density (J_{free}, A m^{-2}) only has a conductivity component as there are no source terms inside the ice:

$$\begin{aligned} \boldsymbol{J}_{free} &= \boldsymbol{J}_{Cond} + \boldsymbol{J}_{Source} \\ &= \sigma \boldsymbol{E} + 0 \end{aligned} \tag{3.2}$$

This above equation is called Ohm's law. In this thesis the conductivity is the "effective" conductivity. This means that it includes the contributions due to the free carriers which give a small dc (or static) conductivity (σ_{dc}) and also the contribution due to the rotation of bound charges in phase with the applied electric field (σ_{rot}):

$$\begin{aligned} \sigma &= \sigma_{dc} + \sigma_{rot} \\ &= \sigma_{dc} + \varepsilon_0 \varepsilon_r'' \omega \end{aligned} \tag{3.3}$$

where

ω = angular frequency, radians per second = $2\pi f$

ε''_r = relative imaginary permittivity, also known as the dielectric loss factor.

In the above equation an imaginary permittivity was introduced. It is quite common to consider the permittivity as a complex quantity, and this will be represented in this thesis by the use of the ~ symbol. The real (ε'_r) and imaginary (ε''_r) components of the relative permittivity will sometimes be considered separately as shown below:

$$\tilde{\varepsilon}_r = \varepsilon'_r - i\,\varepsilon''_r \tag{3.4}$$

where

$i = \sqrt{-1}$

The other common electrical parameter is the complex refractive index:

$$\tilde{n} = n' - i\,n'' \tag{3.5}$$

where

$\tilde{n}^2 = \tilde{\varepsilon}$ $\qquad n'^2 - n''^2 = \varepsilon'$ $\qquad 2\,n'\,n'' = \varepsilon''$

The final parameter that needs to be described is the loss tangent:

$$\tan\delta = \frac{\varepsilon''}{\varepsilon'} \tag{3.6}$$

In this chapter first the pure solid monocrystalline form of ice will be discussed. Then the bulk properties of impure, polycrystalline, bubbly glacier ice will be considered.

3.2 The permittivity of pure solid monocrystalline ice

The real relative permittivity of pure solid ice has a plateau in the frequency range of interest to this thesis (10^6-10^8 Hz). On either side of this plateau are dispersions where the real relative permittivity increases or decreases. This can be seen in figure 3.1 below. The frequency at which these dispersions occur in pure solid monocrystalline ice is dependent on the temperature and pressure.

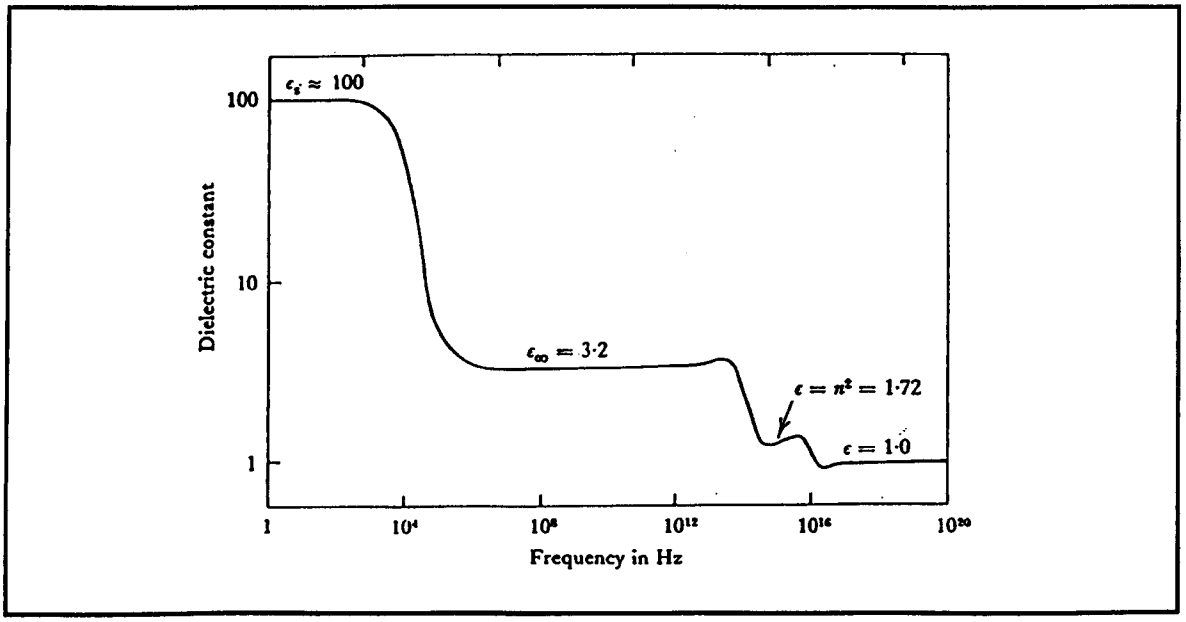

Figure 3.1 Variation in the dielectric constant of pure solid ice (from Fletcher, 1970)

3.2.a Audio-frequency to Low frequency dispersion (AF-LF)

In all of the reported experimental work a strong dispersion is detected, centred at a frequency of a few kHz (Hobbs, 1974). This dispersion is a relaxation type and is attributed to the movement of hydrogen ions around the oxygen ions in the ice lattice. There are different names for this dispersion depending on the author: orientational, principal, Debye or intrinsic. Many experiments have reported anisotropy in the strength of this dispersion (Johari and Jones, 1978).

3.2.b High frequency plateau

For frequencies immediately above the AF-LF dispersion there is a plateau in the real relative permittivity and the conductivity. These values are called the high frequency values and are given the subscript ∞ (ε_∞ and σ_∞). Most of the work in this thesis will be at frequencies whose real relative permittivity and conductivity lie on this plateau.

3.2.c Infra red frequency dispersion

Another strong dispersion is centred in the far infra red region beyond 10^{12} Hz (Warren, 1984). It is a resonance type dispersion due to the vibration of the bond linking the hydrogen and oxygen atoms in the water molecule. There is a slight anisotropy in the strength of this dispersion (Matsuoka et al. 1996).

The most successful and widespread classical model for the low frequency electrical behaviour of ice from dc up through the AF-LF dispersion to the high frequency value is named after Jaccard (1959, 1963, 1964). An outline of this model is given in the next section.

3.3 The Jaccard model for ice

This model can explain many of the observed experimental results. For example, it can explain the low frequency dispersions in samples of a finite size (Petrenko and Ryzshkin, 1984). However, it does have its failings; theoretically (Nagle, 1974) no large anisotropy in the electrical properties is expected parallel and perpendicular to the c-axis, yet such an anisotropy is observed in experiments. Good descriptions of the model can be found in publications by Hobbs (1974) or Petrenko (1993).

3.3.a The defects

Jaccard modelled the observed conductivity and permittivity by considering the mobility and charge carrying capacity of defects in the ice structure. These defects violate the Bernal-Fowler rules (see chapter 2, section 2.1) and were first postulated by Bjerrum (1951). The defects allow the movement of protons through the ice, giving the observed dc conductivity; they also allow the water molecules to change their orientation, giving the observed polarisation in the ice.

Four defects are considered to carry charge, two of which are due to either the addition or removal of a hydrogen ion to a water molecule. These are the positive hydroxonium ion H_3O^+ and the negative hydroxyl ion OH^-. The other two defects are due to imperfect bonding, with either an extra hydrogen between two oxygen atoms (D defect), or no hydrogens between two oxygen atoms (L defect).

The number of defects formed is controlled by the minimum of Gibbs free energy in the structure. In the table below are listed the expected number of defects at -10 °C and 1 bar. These values can be compared with the number of molecules in a cubic metre of pure ice 3×10^{28} (Hobbs, 1974).

Table 3.1 Defects in pure solid Ice Ih (Petrenko, 1993; Hobbs, 1974)

All values in the table are for -10 °C

Defect Type	Energy to create defect (eV)	Number Density (m^{-3})	Charge associated with defect (e)	Mobility ($m^2 V^{-1} s^{-1}$)	Energy to move defect (eV)
H_3O^+	0.74	9×10^{20}	0.62	$(1\text{-}2.7)\times10^{-8}$	0 ‡
OH^-	0.74	9×10^{20}	-0.62	2.4×10^{-8}	0 ‡
D	0.68	5×10^{21}	0.38	$<1.8\times10^{-8}$	0.19 - 0.235
L	0.68	5×10^{21}	-0.38	$(2\text{-}5)\times10^{-8}$	0.19 - 0.235

‡ The activation energy of ionic defects is controlled by the quantum mechanical tunnelling of protons along hydrogen bonds.

3.3.b The high frequency real relative permittivity (ε'_∞)

This can be described mathematically by the equation below (Petrenko, 1993, pp 15):

$$\varepsilon'_r = \frac{J_{displacement} + J_{drift}}{\left(\varepsilon_0 \frac{dE}{dt}\right)} \tag{3.7}$$

where

E = Electric field ($V\ m^{-1}$)

$J_{displacement}$ = The displacement current density ($A\ m^{-2}$)

J_{drift} = The drift current density ($A\ m^{-2}$)

The displacement current density depends on the changing electric field while the drift current density depends on the motion and the history of movement of the charge carriers.

3.3.c The high frequency conductivity (σ_∞)

The application of a high frequency alternating electric field causes the defects to displace only slightly from their initial positions. The defects are considered to be well separated and behave independently, so the conductivity is given as the sum of contributions from all the defects:

$$\sigma_\infty = \sigma_L + \sigma_D + \sigma_{H_3O^+} + \sigma_{OH^-} \tag{3.8}$$

The high frequency conductivity is controlled by the carrier with the greatest partial conductivity. In impure ice this is usually L defects due to their greater number density and mobility (see table 3.1). Therefore any effect that causes an increase in the number of L defects will increase the high frequency conductivity. L defects can be formed by the presence of Cl^- ions. D defects can be formed by the presence of NH_4^+ ions (Moore et al. 1994; Wolff et al. 1997).

The Jaccard theory can predict, as a function of temperature, quantities such as the intrinsic relaxation period, the static conductivity and the high frequency conductivity. It is therefore very successful and provides an insight into the processes at work in ice.

One of the outcomes from the Jaccard model is an equation that expresses the permittivity in a similar manner to that of the simple Debye model. This is explained in the next section.

3.4 The Debye equation

Debye (1929) first proposed an equation for the permittivity of a collection of permanently polarised gas molecules, which are considered as dipoles. In Debye's model the dipoles are only able to respond to the applied electric field by rotating. This leads to an anomalous or relaxation dispersion in which the real part of the complex permittivity decreases with increasing frequency. In this section the Debye model will first be applied to pure solid monocrystalline ice and then applied to glacier ice.

3.4.a Simple model for pure solid monocrystalline ice

The Debye model considers the rotation of dipoles. This is a very similar process to the

movement of defects around the oxygen atoms. Between 0 and 500 MHZ, pure solid ice can be approximated as the combination of a dc conductivity and a single simple Debye dispersion, (Granicher, 1969; Johari, 1981). The complex relative permittivity is given by:

$$\tilde{\varepsilon}_r = \varepsilon'_{\infty r} + \frac{\Delta\varepsilon_{D r}}{1 + i\,\omega\,\tau_D} - \frac{i\,\sigma_{dc}}{\omega\,\varepsilon_0} \qquad (3.9)$$

where

$\varepsilon'_{\infty r}$ = High frequency real relative permittivity
$\Delta\varepsilon_{D r}$ = Relative strength of the Debye dispersion
τ_D = Debye relaxation period = $1/(2\pi f_r)$ (where f_r is the relaxation frequency)
σ_{dc} = dc conductivity

Typical values for the above quantities are: $\varepsilon'_{\infty r} = 3.16$ (Petrenko, 1993), $\Delta\varepsilon_{D r} = 97$ (Petrenko, 1993), $\tau_D = 5\times10^{-5}$ s (at -10 °C, Camplin et al. 1978; Petrenko, 1993), $\sigma_{dc} = 10^{-6}$ to 6×10^{-10} S m^{-1} (at -10°C, Petrenko, 1993) (the value depends on the purity).

This above equation 3.9 gives a permittivity behaviour that is shown in figure 3.2 below. The frequency range displayed extends from kHz to GHz. This range covers the MHz frequencies transmitted by the radio echo sounding equipment and this frequency range will be used in all subsequent figures which consider frequency dependence.

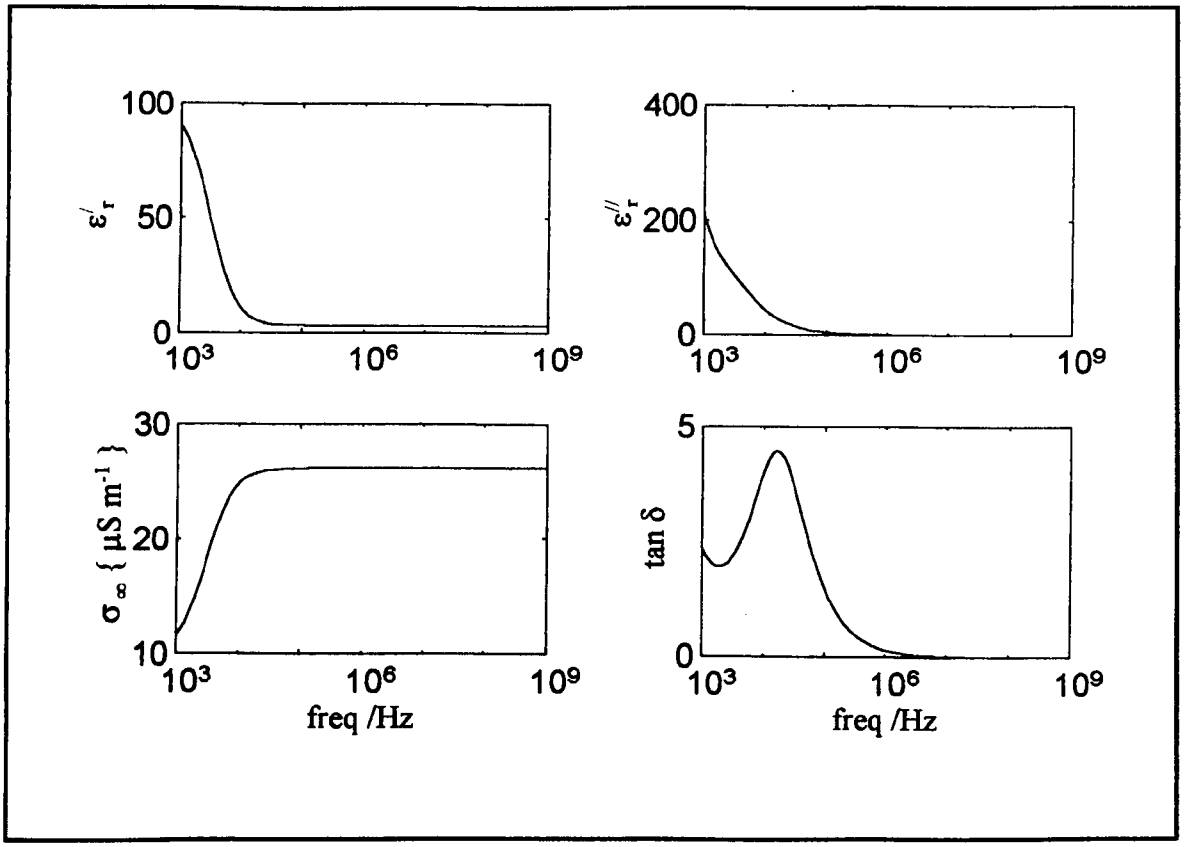

Figure 3.2 A model for pure ice with the parameters:
$\{\varepsilon'_{\infty r} = 3.16 \quad \Delta\varepsilon_{Dr} = 97 \quad \tau_D = 5\times10^{-5}\ \text{s} \quad (f_r = 3\ \text{kHz}) \quad \sigma_{dc} = 10\ \mu\text{S m}^{-1}\}$

3.4.b A summation model for glacier ice

Measurements on glacier ice reveal many dispersion processes, which are mostly due to space charge polarisation (SCP). This polarisation is the result of the build up of local concentrations of mobile charge carriers at boundaries in the ice. These boundaries can be between different crystal lattices inside the polycrystalline ice, or at interfaces with air at fractures, or at the measurement electrodes. The build up of charge at the measurement electrodes is especially significant if the ice has a high dc conductivity and an imperfect contact with the electrodes. It is difficult to distinguish the origin of the SCP effects when looking at experimental results (Johari, 1976).

All of these dispersions due to SCP can be expressed as Debye dispersions. When considering a certain frequency range it is necessary to consider all the dispersions, this is done as a summation. Any dispersions outside the frequency range are represented by a single high frequency real value. Consider an example below with *n* dispersions.

$$\tilde{\varepsilon}_r = \varepsilon'_{\infty r} + \sum_{k=1}^{n} \frac{\Delta\varepsilon_{rk}}{1 + i\omega\tau_k} - \frac{i\sigma_{dc}}{\omega\varepsilon_0} \tag{3.10}$$

where

$\Delta\varepsilon_{rk}$ = Relative strength of the k dispersion.
τ_k = Relaxation period of the k dispersion
= $1/(2\pi f_k)$ (where f_k is the relaxation frequency of the k dispersion)

In this example k = 1 has the longest relaxation period. Its dispersion strength ($\Delta\varepsilon_{r1}$) spans the range from the dc permittivity to the high frequency permittivity of the first dispersion. The high frequency permittivity of the first dispersion is also the same value as the low frequency permittivity of the second dispersion.

If there is a multiplicity of relaxation processes occurring, then there is a continuum of relaxation times, all of which contribute to the response. It is therefore necessary to replace the summation in the equation for the complex permittivity with an integral. Depending on the resolution of the measurement technique the experimenter may see this distribution of relaxation times as a series of discrete peaks.

An example of a spectrum that is seen when measuring ice comes from Moore and Paren (1987). This is shown in the table 3.2 and figure 3.3 below where there are three dispersions. There is no dc conductivity term due to the use of an insulating film between the ice and the electrodes.

Table 3.2 Measurement for firn at -9 °C, with polyethene between the ice and the electrodes, (Moore and Paren, 1987).

Dispersion	Relaxation frequency {Hz}	Dispersion strength ($\Delta\varepsilon / \varepsilon_0$)
1	1×10^2	3
2	2.5×10^3	12
3	15×10^3	25

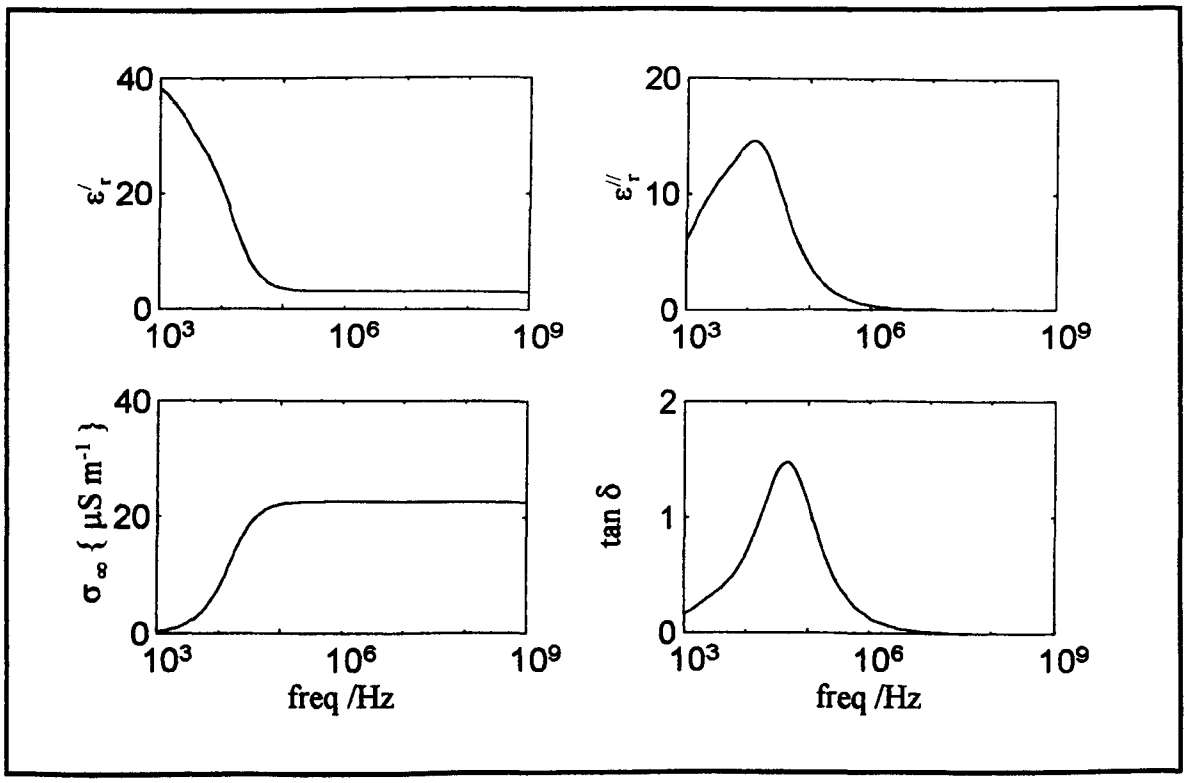

Figure 3.3 A typical measurement for firn at -9 °C with polyethene between the ice and the electrodes. The graphs have been determined using the parameters in table 3.2 and equation 3.10.

3.5 The behaviour in the high frequency region

The frequency range 10^5 to 10^9 Hz lies between the strong AF-LF dispersion and the strong vibrational dispersion in the infra-red. Due to the difficulty in measuring samples in this range it is still undecided if there exists a weak dispersion in the high frequency region of *in situ* glacier ice.

3.5.a Results

In the following two tables are a summary of some published experimental work that have given evidence of dispersions above the AF-LF dispersion. The evidence from these publications are divided into two tables; observed dispersions and inferred dispersions.

Table 3.3 Observed dispersions at frequencies higher than the AF-LF dispersion

Author	**Sample**	**Frequency Range of measurements { Hz }**	**Temperature {°C}**	**Possible strength of dispersion inside the frequency range. $\Delta\varepsilon/\varepsilon_0$**
Von Hippel et al., (1971, 1972)	Pure single crystals	8×10^{-3} to 100×10^{3}	0 to -180	Weak dispersions visible at colder temperatures
Camplin and Glen, (1973)	HF doped single crystals	70 to 20×10^{3}	-3 to -83	When colder than -33 °C a dispersion observed at a frequency 10x that of the AF-LF dispersion with a maximum strength 1/10 that of the AF-LF dispersion.
Paren and Glen, (1978)	Shaved ice	60 to 200×10^{3}	-7 to -45	Dispersion observed at a frequency about 10x that of the AF-LF dispersion with a maximum strength 1/10 that of the AF-LF dispersion.
Bamber (1987)	Glacier ice from Spitsbergen	20 to 100×10^{3}	-2.5 to -44	At lowest temperatures a plot of ε' vs $1/f^2$ is not linear implying a higher dispersion present.

Table 3.4 Inferred results due to measurements either side of the region of interest.

Author	Sample	Measured Frequencies { Hz }		Temperature { °C }	Possible Strength of dispersion inside the frequency range. $\Delta\varepsilon/\varepsilon_0$
		Low	High		
Johari (1976)	Polycrystalline pure ice	0.5×10^{6}	100×10^{6}	-5	0.08
Matsuoka et al. (1996)	Polycrystalline pure ice and previous worker's data.	35×10^{6}	5×10^{9}	-8 to -23	0.030 ± 0.009
Matsuoka et al. (1997 a)	Single ice crystal from Mendenhall glacier, Alaska	1×10^{6}	39×10^{9}	-21	Parallel to the C axis 0.0448 ± 0.007
					Perpendicular to the C axis 0.0432 ± 0.007

3.5.b Discussion

In all of the above cases there was evidence of a weak dispersion in the high frequency region. Sometimes the dispersion has only been observed at the coldest temperatures. However it is not clear if the dispersion is a property of the ice or the measurement process, which itself can cause space charge polarisation (Glen and Paren, 1975; Paren and Glen, 1978). If the weak dispersion is a property of pure single crystal then the dispersion will also exist in polycrystalline glacier ice.

After considering the temperature range of interest to this thesis (-8 to -33 °C, §3.5.a), the experimentally determined strength of the weak dispersion, and the level of accuracy in the modelling of this thesis, I make the assumption that there is no need to consider the weak dispersion in the radio frequency range. Therefore, following previous authors (Evans, 1965; Paren, 1970; Taubenberger et al. 1973; Johari, 1981; Moore, 1988 a, b) the electrical

behaviour in the radio frequency range is dominated by the dispersions to either side.

So in the radio frequency region there is a high frequency relative real permittivity ($\varepsilon'_{\infty r}$) and a conductivity (σ_∞) that have no frequency dependence. The properties of these are explained below.

At frequencies above 10^5 Hz the value of the relative real permittivity reaches a plateau which is maintained up to a frequency of 10^{12} Hz. The plateau value varies as the environment of the ice varies. This variation is looked at in section 3.6.

At frequencies above 10^5 Hz the conductivity of ice reaches a steady value (Evans, 1965; Hobbs, 1974). Because it is independent of the type of electrodes used in the measurement, this high frequency bulk conductivity of pure ice has been well established (Petrenko, 1993). Using the notation of Debye, the value of the conductivity at a frequency can be expressed using the equation below:

$$\sigma_\infty = \sigma_{dc} + \frac{\varepsilon_0 \Delta\varepsilon_D}{\tau_D} \qquad (3.11)$$

The dc conductivity, dispersion strength and dispersion relaxation time all vary as the physical properties of the ice varies. Many researchers have looked at the variation in each of these components (Hobbs, 1974); for the purposes of this thesis it is sufficient to consider only the total effect that is seen in the variation of the value of σ_∞. This variation is looked at in section 3.6.

3.6 Variation of high frequency permittivity and conductivity.

In a glacier the ice is subjected to various forces and its form varies. This means that its high frequency permittivity and conductivity change. The five variables that will be looked at in the rest of this chapter are shown below. At the end of the chapter is a table containing a summary of the expected variability in the ice considered in this thesis. The effect of **Fabric** will not be considered here. For the moment the ice is considered to have a random orientation of the crystals and so is isotropic.

Temperature

The quantity of heat energy affects the generation of charge carriers and their mobility.

Pressure

The pressure will influence the ability of the charge carriers to migrate.

Impurities

The presence of chemicals in the glacier ice inside the grains changes the defect concentrations while chemicals at grain boundaries can provide an alternative conduction path.

Porosity/Density

As glacier ice from shallow depths will contain air bubbles or channels this affects the electrical properties and it is necessary to consider an ice air mixture.

There are four areas which will not be dealt with in detail, the first of these is ageing. **Ageing** refers to time dependent changes in the electrical properties, over periods of months to years. Previous observed alterations in the high frequency relative real permittivity and high frequency conductivity are now thought to have been either artefacts of the measurement (Johari and Jones, 1978) or due to the uptake of atmospheric ammonium (Schwander et al. 1983). It has also been pointed out that there is no observed systematic change in electrical properties with the age/depth of the ice, which suggests no ageing (Moore, 1988 a, pp 114).

Secondly **grain size** has been shown to have no affect on the high frequency permittivity and conductivity (Fitzgerald and Paren, 1975; Moore, 1988a, pp 113). However grain size does affect low frequency properties (Ambach and Denoth, 1980). Thirdly ice which has undergone **strain** for which there are no clear results from measurements (Hobbs, 1974; Noll, 1978; Itagaki, 1987). Lastly the **clathrate hydrate crystals** formed at depth which have a slightly higher refractive index than the ice (Shoji and Langway, 1982). However these crystals are a very small volume percentage in glacier ice (Gough and Davidson, 1973; Gough et al. 1973). This means that there is no observed effect to the conductivity as the transition zone for their formation is crossed in the GRIP core (Wolff et al. 1995).

3.6.a Temperature

The temperature range of concern to this thesis ranges from the coldest temperature in the GRIP borehole of -33 °C to the warmest temperature of -8 °C recorded on the surface while measuring an ice core at GRIP, (core which started with bag G1147).

3.6.a.i High frequency relative real permittivity (ε'_{r})

The real permittivity in both pure solid ice and glacier ice increases as the sample gets warmer. For pure single crystals, the temperature dependence of the high frequency permittivity is isotropic to within ±0.5% (Johari, 1976; Johari and Jones, 1978). The temperature dependence has been measured by a number of authors. Two of the results are listed in the table below.

Table 3.5 Temperature dependence of the high frequency relative real permittivity.

Publication	Sample	Frequency {Hz}	Temperature Range {°C}	Temperature dependence {K^{-1}} $\frac{1}{\varepsilon_\infty}\left(\frac{\partial \varepsilon_\infty}{\partial T}\right)$
Paren (1970)	Eight Greenland glacier ice samples	10^5	-20 to - 80	$[5.3 \pm 1.5] \times 10^{-4}$
Johari (1976)	Pure ice single crystal and pure ice polycrystal	10^6	0	7.2×10^{-4}
			-28	1.9×10^{-4}

There is a wide variation in the values for the temperature dependence given by many authors (Hobbs, 1974).

3.6.a.ii High frequency conductivity (σ_∞)

With warming the high frequency conductivity increases. For pure ice this can be modelled over a wide temperature range -70 to 0 °C, using one activation energy. The relation is given in the equation below:

$$\sigma_\infty = C_t e^{\left(\frac{-E_t}{k_B T}\right)} \qquad (3.12)$$

where

T = Temperature (K)
k_B = Boltzman constant 1.38×10^{-23} J K^{-1}
E_t = activation energy in electron volts, 1 eV = 1.602×10^{-19} J. Using $e^{\left(\frac{-E_t}{k_B L T}\right)}$ as an alternative equation where L is the Avogadro constant (and k_B L = R the gas constant) would require the energies to be given in J mol^{-1} where 1 eV mol^{-1} = 96.5 kJ mol^{-1}.

For single crystal measurements by Ruepp at 0 °C, 300 kHz (Paren, 1970; Hobbs, 1974 pg 96)
Parallel to the c axis $\|C$ σ_∞ = (44 - 46) μS m^{-1}, E_t = (0.57 - 0.59) eV
Perpendicular to the c axis $\perp C$ σ_∞ = (37 - 42) μS m^{-1}, E_t = 0.61 eV

For glacier ice with impurities the activation energy is lower and has been shown to vary with

the permeability of the sample (Reynolds, 1985). For firn, the activation energy is 0.21 ±0.02 eV, while for glacier ice the value is 0.25 eV. The activation energy also varies with the presence of chemical species in the glacial ice. For the Dolleman island core, Moore et al. (1992b) considers three contributions using the equation below:

$$\sigma_{\infty} = \sum_{k=1}^{3} C_{tk}\, e^{\left(\frac{-E_{tk}}{k_B T}\right)} \tag{3.13}$$

where

$E_{t1} = 0.19 \pm 0.02$ eV for the salt contribution
$E_{t2} = 0.26 \pm 0.03$ eV for the acid contribution
$E_{t3} = 0.30 \pm 0.02$ eV a constant term.

In a later paper (Moore et al. 1994) the correction is reduced to two terms: a contribution due to the pure ice of 0.5 eV, the other contribution being the average of the salt and acid values of 0.22 eV.

3.6.b Pressure

3.6.b.i High frequency relative real permittivity ($\varepsilon'_{\infty r}$)

The pressure dependence of many dielectric properties (σ_{∞}, ε'_{dc}, τ_D) has been investigated and published. But there does not appear to be any published result on the pressure dependence of $\varepsilon'_{\infty r}$ (Bogorodsky et al. 1985, pp 37).

3.6.b.ii High frequency conductivity (σ_{∞})

For pure ice monocrystals, as the pressure increases, the high frequency conductivity decreases (Taubenberger et al. 1973). This is expressed by the equation below:

$$\sigma_{\infty} = C_p\, e^{\left(\frac{-\Delta V P}{R T}\right)} \tag{3.14}$$

where

P = Pressure in Pascals (N m^{-1}) (1 atmosphere = 101325 Pa)
C_p = Constant 9×10^{-6} S m^{-1} (value assumes 9 μS m^{-1} conductivity at 1 atmosphere)
ΔV = The activation volume, $(-2.6 \pm 0.2) \times 10^{-6}$ m^3 mol^{-1}
R = Molar Gas Constant, 8.32 J K^{-1} mol^{-1}

The activation volume becomes more positive as the concentration of defects increases. It is positive when the concentration is greater than 5×10^{-6} mole l^{-1} of hydrogen fluoride.

For impure laboratory grown polycrystalline ice (doped with ammonia or hydrogen fluoride) Hubmann (1978) considers the pressure effect on each of the Bjerrum defects in the ice. This leads to a summation with four activation volumes which is shown below:

$$\sigma_\infty = \sum_{k=1}^{4} C_{pk} e^{\left(\frac{-\Delta V_k P}{RT}\right)} \qquad (3.15)$$

where

ΔV_1 = For L defects
ΔV_2 = For D defects
ΔV_3 = For H_3O^+ defects
ΔV_4 = For OH^- defects

ΔV_1 and ΔV_2 are positive, and independent of concentration, while ΔV_3 and ΔV_4 are negative. The constants C_{pk} are functions of the concentrations of chemicals. Often one or two of the terms will be small enough to be neglected.

3.6.c Impurities

The evidence for the effect of impurities on permittivity has been built up mainly from experimental work on laboratory doped artificial ice. Laboratory ice is often constructed from freezing liquid water and this is different from the formation of glacier ice. Due to the different processes of formation the relevance of this laboratory work to meteoric ice is questionable

(Fitzgerald and Paren, 1975; Fitzgerald et al. 1977). It is only recently that ice core researchers have started to compare the measured permittivities of ice cores with the subsequent chemical analysis.

3.6.c.i High frequency relative real permittivity ($\varepsilon'_{\infty r}$)

There is no significant variation in the relative real permittivity due to the effect of impurities (Bogorodsky et al. 1985, pg 40). In Matsuoka et al. (1997b, pp 6220) the variation seen in $\varepsilon'_{\infty r}$, using a frequency of 5 GHz, as impurities were added was within experimental error.

3.6.c.ii High frequency conductivity (σ_∞)

There are vast numbers of publications considering the variation in σ_∞ with impurities. The research has been carried out on doped laboratory grown crystals and on glacier ice (Hobbs, 1974). For polar ice cores the comparison of measured σ_∞ with subsequent chemical measurements on the melted samples has been studied (Moore, 1988 a; Wolff et al. 1997). The technique used to measure σ_∞ has been dielectric profiling (DEP). The DEP high frequency conductivity at -15 ^{0}C, for solid ice, over the ranges of concentrations typical for glacier ice, can be described as:

$$\sigma_\infty = A + B[H^+] + C[NH_4^+] + D[Cl^-] \qquad (3.16)$$

where

σ_∞ = high frequency conductivity in $\mu S\ m^{-1}$
[ ] = concentrations in μM
A = Pure ice conductivity at -15 ^{0}C this is 9 $\mu S\ m^{-1}$ (Camplin et al. 1978)
B = 4 ± 1 $\mu S\ m^{-1}\ \mu M^{-1}$ at -15 ^{0}C (Wolff et al. 1995)
C = 1 ± 0.2 $\mu S\ m^{-1}\ \mu M^{-1}$ at -15 ^{0}C (Moore et al. 1994).
D = 0.55 $\mu S\ m^{-1}\ \mu M^{-1}$ at -15 ^{0}C (Moore et al. 1992b).

Each of these terms (A, B, C, D) varies with temperature, a simplified consideration of which was looked at in section 3.6.a.

3.6.d Density

The equations relating density, $\varepsilon'_{\infty r}$ and σ_{∞} can be divided into those that are theoretical and those that are empirical. There has been very little experimental work published on the effect of density, the main source of experimental data in the GHz range being Cummings (1952) and then Nyfors (1982). Three phase relations that consider ice, air and water are starting to appear in the literature (Nghiem et al. 1996). These are more realistic than the two phase relations, as all firn will contain some liquid. This liquid is on the walls of the pores spaces or at the grain boundaries. Cummings (1952) results are considered to have contained between 0 and 1.6% weight liquid water (Ulaby et al. 1986). However, the level of accuracy provided by these three phase relations exceeds that in the measured data, so only a dry snow-air mixture is considered here.

3.6.d.i High frequency relative real permittivity ($\varepsilon'_{\infty r}$)

Due to the frequency independence of the real permittivity in the radio frequency region, there are many publications examining the relation between the density and the high frequency permittivity. Field based measurements, such as calculating the permittivity from the travel time of a radio echo, can be inaccurate (Jezek and Roeloffs, 1983), so it is better to use laboratory measurements on small samples to examine the relationship.

Cumming (1952) used the Polder-Van Santen equation to model his laboratory measurements. A simpler linear empirical equation was proposed by Robin et al. (1969) relating the specific gravity (density of ice divided by density of water) and $\varepsilon'_{\infty r}$. Subsequent work by Paren (1970), Glen and Paren (1975) which considered the fit over a wider frequency range found the Looyenga relation (which considers firn to be made of spheres of ice in air) to be a good

model. Subsequent work by Stiles and Ulaby (1981), Sihvola et al. (1985) and Sihvola and Lindell (1992) have looked at many different models, concluding that there is little to distinguish between the many possible formulae.

The Looyenga equation for the real part of the permittivity has no cross terms. The derived equation using $\varepsilon'_{\infty r}$ for solid ice of 3.17 is:

$$\varepsilon'_{\infty r\,firn} = \left(1 + 0.469\,v\right)^3 \tag{3.17}$$

where

v = the volume fraction of ice in the firn

Using the relation $\rho_{firn} = v\,\rho_{ice} + (1 - v)\,\rho_{air}$ with a density of solid ice (ρ_{ice}) of 917 kg m^{-3} gives the approximate equation:

$$\varepsilon'_{\infty r\,firn} = \left(1 + 0.51 \times 10^{-3}\,\rho_{firn}\right)^3 \tag{3.18}$$

3.6.d.ii High frequency conductivity (σ_∞)

Many authors have considered the density dependence of the imaginary permittivity (Cummings, 1952; Evans, 1965; Ulaby et al. 1981). Fewer authors have considered the density dependence of the high frequency conductivity. The most recent work being that of Glen and Paren (1975). I will use the relation given by Glen and Paren (1975), as it is sufficiently accurate for the data that will be used. It is shown in the original form below:

$$\sigma_{\infty\,firn} = \sigma_{\infty\,ice}\,v\left(0.68 + 0.32\,v\right)^2 \tag{3.19}$$

where

v = volume fraction of ice in the firn

Rewriting this in terms of the density (kg m^{-3}) gives

$$\sigma_{\infty\, firn} = \sigma_{\infty\, ice}\, \rho_{firn} \left(2.24 \times 10^{-2} + 1.15 \times 10^{-5}\, \rho_{firn}\right)^2 \qquad (3.20)$$

3.7 Summary

The table below is a brief summary of the expected variation in the high frequency permittivity and conductivity for the range of conditions expected inside a typical ice sheet.

Table 3.6 Possible variation of permittivity in glacier ice. All are for random orientated multi-grained pure ice, with porosity of zero, temperature of -15 ^{0}C, pressure of 1 MPa, and frequency of 10 MHz, unless stated otherwise.

Variable	Variation	High frequency relative permittivity		High frequency conductivity /μS
		real	imaginary	
Temperature T {°C}	- 15	3.15	0.016	9.0
	- 33	3.12	0.007	3.9
Pressure P {MPa}	1	3.15	0.016	9.0
	28	3.15	0.015	8.7
Density ρ_{firn} {kg m^{-3}}	350	1.67	0.004	2.2
	917	3.15	0.016	9.0
Impurities [H^+] {μM}	0	3.15	0.016	9.0
	4	3.15	0.045	25.0
Frequency ν {MHz}	10	3.15	0.016	9.0
	40	3.15	0.004	9.0

The real permittivity is controlled, in order of importance for these conditions, by: density then temperature. The imaginary permittivity is controlled, in order of importance, by: impurities, frequency, temperature then density. The pressure appears to be the least important variable. The importance of fabric will be considered in chapter eight.

CHAPTER 4

PLANAR MONOCHROMATIC WAVES

The simplest way to consider the movement of electromagnetic energy through an ice sheet is to consider monochromatic (single frequency) waves. In this chapter plane parallel monochromatic waves propagating normal to a stratified medium will be considered. The first three sections (§4.1, §4.2, §4.3) consider the solution of Maxwell's equations. Then the propagation of electromagnetic waves in a continuous homogeneous medium is considered to determine parameters such as wavelength, velocity and absorption (§4.4). Finally, the reflections from interfaces, single layers and multi layers are considered (§4.5, §4.6, §4.7).

In the previous chapter the high frequency relative real permittivity and high frequency conductivity were discussed. This chapter will investigate how much error is introduced if these high frequency values are used close to the AF-LF dispersion. This will be done in sections 4.5.e and 4.7.c where the reflection coefficients will first be calculated using a Debye model for the electrical properties of the ice sheet, then secondly calculated using the frequency independent high frequency values for the electrical properties. The result of these investigations will be used in chapter 5 to decide whether it is necessary to have dispersive ice properties or whether high frequency values are sufficient when modelling the radar.

4.1 Maxwell's Equations

Maxwell's equations consider how the interaction of the electric and magnetic fields allows the propagation of energy through the ice. The electric field was introduced in chapter three. It

is now necessary to introduce the magnetic field. The observed magnetic field ($\boldsymbol{B}$, T) is a function of the applied magnetic field ($\boldsymbol{H}$, A m^{-1}) and the magnetisation ($\boldsymbol{M}$, A m^{-1}).

$$\begin{aligned} \boldsymbol{B} &= \mu_0(\boldsymbol{H} + \boldsymbol{M}) \\ &= \mu_0(\boldsymbol{H} + \chi_m \boldsymbol{H}) \\ &= \mu_0 \mu_r \boldsymbol{H} \end{aligned} \tag{4.1}$$

where

χ_m = magnetic susceptibility, which is negligible in ice.
μ_r = relative permeability. In ice the relative permeability is set equal to 1.

In the table below the four general forms of Maxwell's equations are shown in column two. In the case of ice various conditions can be imposed, as shown above. These conditions produce the equations shown in column three.

Table 4.1 Maxwell's equations for macroscopic fields

Original Law	Maxwell's equation in general form	Maxwell's equations for ice
Ampere	$\nabla \times \boldsymbol{H} = \boldsymbol{J}_{free} + \frac{\partial \boldsymbol{D}}{\partial t}$	$\nabla \times \boldsymbol{H} = \sigma \boldsymbol{E} + \varepsilon_o \varepsilon_r' \frac{\partial \boldsymbol{E}}{\partial t}$
Faraday's Law of induction	$\nabla \times \boldsymbol{E} = -\frac{\partial \boldsymbol{B}}{\partial t}$	$\nabla \times \boldsymbol{E} = -\frac{\partial \boldsymbol{B}}{\partial t}$
Coulomb	$\nabla \cdot \boldsymbol{D} = \rho_{free}$	let $\rho_{free} = 0$ $\nabla \cdot \boldsymbol{E} = 0$
Gauss	$\nabla \cdot \boldsymbol{B} = 0$	$\nabla \cdot \boldsymbol{B} = 0$

In order to proceed the equations are combined. This is done in most textbooks (take the curl of Faraday's Law then substitute in a vector identity and Ampere's Law) to give a general relation called the equation of telegraphy, the telegrapher's equation or the source free wave equation:

$$\nabla^2 \boldsymbol{E} = \mu_0 \sigma \frac{\partial \boldsymbol{E}}{\partial t} + \mu_0 \varepsilon_0 \varepsilon_r' \frac{\partial^2 \boldsymbol{E}}{\partial t^2} \qquad (4.2)$$

It is this equation that will be solved for a number of geometries in the course of this study.

There is one common approximation made to this equation: if the conductivity is small (less than 10 mS m^{-1}), then the medium can be treated as a dielectric (Davis and Annan, 1989). This involves neglecting the displacement term ($\partial \boldsymbol{E} / \partial t$), and produces a diffusion equation which is easier to solve. Such an approach was used by Harrison (1973). The solutions that result from considering the wave equation in a loss free medium are also known as the Wentzel Kramers Brillouin (WKB) solutions (Budden, 1985) and these are widely used in the propagation of electromagnetic waves in the atmosphere. As the influence of conductivity variations is one of the hypotheses that is to be tested this term cannot be neglected.

4.2 Model Geometry and Scalar fields

The model will use a right handed Cartesian coordinate system with z axis pointing downwards. A linear polarised monochromatic (single frequency) wave of radian frequency ($\omega = 2\pi f$), with $\boldsymbol{E}$ in the x direction and $\boldsymbol{B}$ in the y direction is applied. The direction of propagation is given by the wave vector k. The wave propagates normal to the layers in the z direction (the transverse electric and magnetic fields, TEM case) where both the electric and magnetic fields are transverse to the direction of travel.

$$\tilde{E} = \left(\tilde{E}_x(z,t), 0, 0\right) \qquad \tilde{B} = \left(0, \tilde{B}_y(z,t), 0\right) \tag{4.3}$$

Such a system is shown in the figure below.

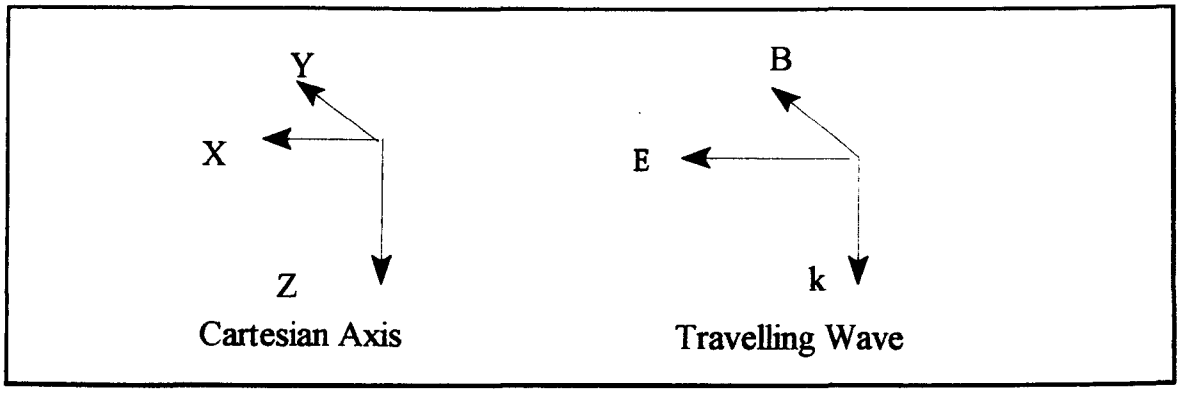

Figure 4.1 Travelling wave.

When this geometry is substituted into the telegrapher's equation the result is:

$$\frac{\partial^2 \tilde{E}_x}{\partial z^2} = \mu_0 \sigma \frac{\partial \tilde{E}_x}{\partial t} + \mu_0 \varepsilon_0 \varepsilon_r' \frac{\partial^2 \tilde{E}_x}{\partial t^2} \tag{4.4}$$

This equation is solved by separation into two complex variables.

$$\tilde{E}_x(z,t) = \tilde{E}_{xz}(z)\tilde{E}_{xt}(t) \tag{4.5}$$

Then solved using a method involving a separation constant.

Position

$$separation\ constant = \frac{1}{\tilde{E}_{xz}} \frac{\partial^2 \tilde{E}_{xz}}{\partial z^2} \tag{4.6}$$

Time

$$separation\ constant = \frac{\mu_0 \sigma}{\tilde{E}_{xt}} \frac{\partial \tilde{E}_{xt}}{\partial t} + \frac{\mu_0 \varepsilon_0 \varepsilon_r}{\tilde{E}_{xt}} \frac{\partial^2 \tilde{E}_{xt}}{\partial t^2} \qquad (4.7)$$

The separation constant can be either positive or negative. I will choose to assign these to be as shown in table 4.2 below:

Table 4.2 Separation constants

Name	Symbol	Separation constant
Propagation constant	$\tilde{\gamma}$	$\tilde{\gamma}^2$
Wave number	$\tilde{k}$	$-\tilde{k}^2$

It can be seen that $\tilde{k} = i\tilde{\gamma}$. The time dependence can take either of two forms with either a positive or negative exponent. The differing possible solutions are shown in the table below.

Table 4.3 Solutions to the telegraph equation, unique U (up going wave) and D (down going wave) which can be complex, with examples of authors who have used each form.

	Separation constant	
Time	$\tilde{\gamma}$	$-\tilde{k}^2$
$e^{i\omega t}$	$\tilde{E}_x = e^{i\omega t}\left(U e^{\gamma z} + D e^{-\gamma z}\right)$ $\gamma^2 = -\mu_0 \varepsilon_0 \varepsilon_r' \omega^2 + i\mu_0 \sigma \omega$ (Wait, 1962, 1996), (Kraus, 1988)	$\tilde{E}_x = U e^{i(\tilde{k}z + \omega t)} + D e^{i(-\tilde{k}z + \omega t)}$ $\tilde{k}^2 = \mu_0 \varepsilon_0 \varepsilon_r' \omega^2 - i\mu_0 \sigma \omega$ (Scaife, 1989), (Feynmann et al. 1963), (Staelin et al. 1994), (Budden, 1985)
$e^{-i\omega t}$	$\tilde{E}_x = e^{-i\omega t}\left(D e^{\gamma z} + U e^{-\gamma z}\right)$ $\gamma^2 = -\mu_0 \varepsilon_0 \varepsilon_r' \omega^2 - i\mu_0 \sigma \omega$	$\tilde{E}_x = D e^{i(\tilde{k}z - \omega t)} + U e^{i(-\tilde{k}z - \omega t)}$ $\tilde{k}^2 = \mu_0 \varepsilon_0 \varepsilon_r' \omega^2 + i\mu_0 \sigma \omega$ (Stratton, 1941), (Born and Wolff, 1975)#, (Hecht, 1987), (Chew, 1990)

Born and Wolff use cgs (Gaussian) units, a good explanation of which can be found in an appendix in Jackson (1975).

I will use the k notation with the positive time exponent, this is the top right box in table 4.3. The measurable field is the real part of the expression.

$$E(z,t) = \mathbb{R}\left[\tilde{E}_x(z,t)\right] \tag{4.8}$$

4.3 The wave number (k)

The complex wave number $\tilde{k}$ can be split into its real and imaginary components. For conductive materials, using the convention chosen here, the imaginary component is negative.

$$\tilde{k} = k' - ik'' \tag{4.9}$$

The real part has a magnitude $k' = (2\pi / \lambda)$ which is the change in phase per unit length. It is also common to find k' given the symbol β (propagation factor, propagation constant or phase constant) and k'' given the symbol α (attenuation factor or constant). The size of these components can be determined by taking the square root of k^2 in table 4.3, or determined separately using the equations below:

$$\begin{aligned} k' &= \omega\sqrt{\frac{\mu_0 \varepsilon_0 \varepsilon_r'}{2}\left(1 + \sqrt{1 + \tan^2\delta}\right)} \\ k'' &= \omega\sqrt{\frac{\mu_0 \varepsilon_0 \varepsilon_r'}{2}\left(-1 + \sqrt{1 + \tan^2\delta}\right)} \end{aligned} \tag{4.10}$$

If either the relative real permittivity or the conductivity are altered then both the real and imaginary components of the wave number alter. The variation in the wavenumber for a typical piece of ice, whose permittivity follows a Debye relaxation, is shown in figure 4.2.

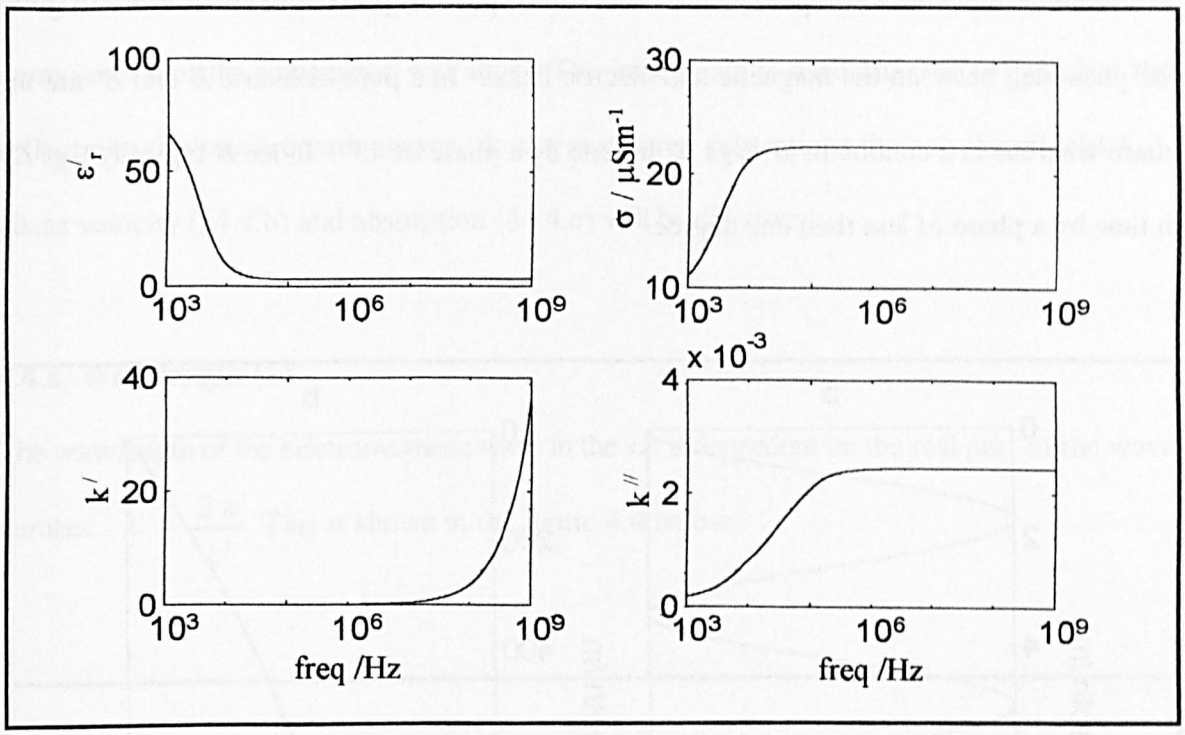

Figure 4.2 Plot of k vs frequency for a sample of ice with Debye type behaviour: $\{\sigma_{dc} = 10\ \mu S\ m^{-1}\ ,\ \Delta\varepsilon_{Dr} = 70,\ \tau_D = 5\times10^{-5}\ s,\ \varepsilon'_{r\infty} = 3$ used in equation 3.9$\}$

4.4 Propagation of monochromatic waves

The equation for a linear polarised wave, of initial amplitude 1, propagating in the direction of increasing z is:

$$\tilde{E}_x(z,t) = e^{i(\omega t - \tilde{k}z)} \tag{4.11}$$

The magnetic field can be determined by combining the above equation for $\tilde{E}_x$ with Maxwell's form of Faraday's law of induction:

$$\begin{aligned} \tilde{B}_y &= -\int \frac{\partial \tilde{E}_x}{\partial z}\,\partial t \\ &= \int \left(i\tilde{k}\,e^{i(\omega t - \tilde{k}z)}\right)\partial t \\ &= \frac{\tilde{k}}{\omega}\,e^{i(\omega t - \tilde{k}z)} \end{aligned} \tag{4.12}$$

The product $\tilde{k}/\omega$ is a complex number that can be put into polar notation in order to give the phase lag between the magnetic and electric fields. In a pure dielectric $\boldsymbol{B}$ and $\boldsymbol{E}$ are in phase whereas in a conductor $\boldsymbol{B}$ lags $\boldsymbol{E}$ in time by a phase of 45^0. In ice $\boldsymbol{B}$ typically lags $\boldsymbol{E}$ in time by a phase of less than one degree.

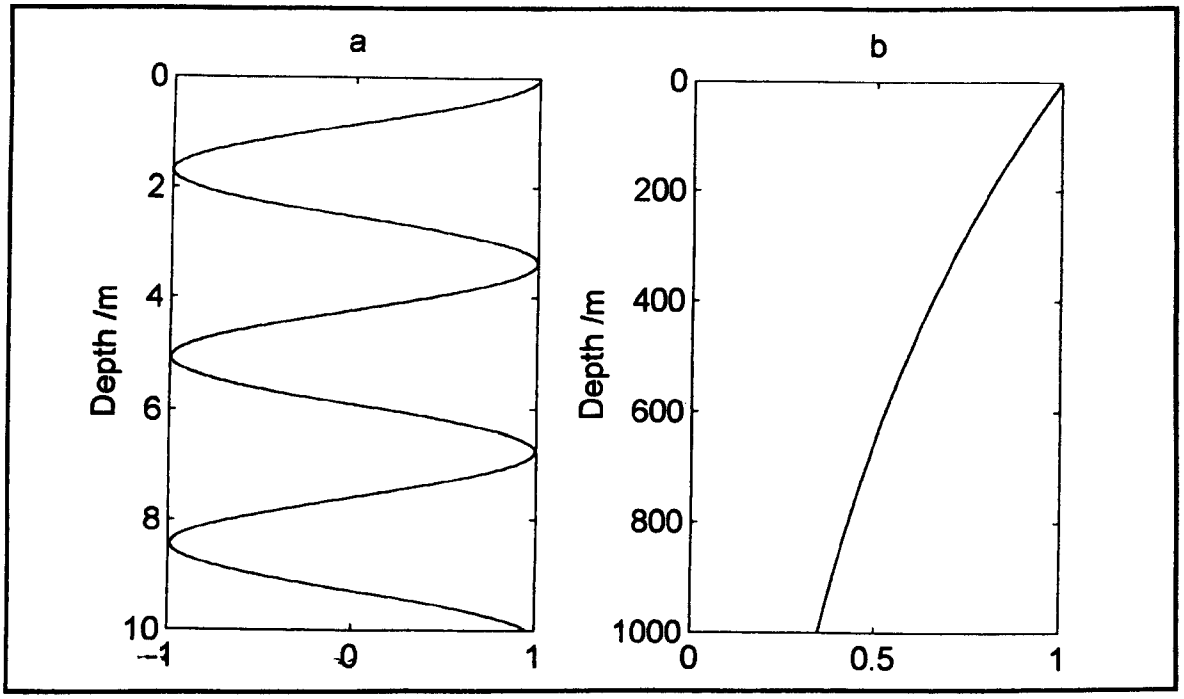

Figure 4.3 a) *E* field for a 50 MHz plane polarised wave in ice. b) Magnitude of the wave with depth.

Having determined $\tilde{B}$, the intrinsic (or bulk) impedance of a medium which is a complex quantity can be defined:

$$\tilde{Z} = \frac{\tilde{E}}{\tilde{H}} = \frac{\omega \mu_0}{\tilde{k}} = \sqrt{\frac{\mu_0}{\varepsilon_0 \varepsilon_r' - i\frac{\sigma}{\omega}}} \qquad (4.13)$$

In a non-conductive material the *E* and *H* fields are in phase and the impedance is a real quantity. In ice with a small conductivity the impedance is complex, with the real and imaginary parts both positive (in the chosen convention). If there is a change in the value of

either the relative real permittivity or the conductivity, then both the real and the imaginary components of the impedance will alter. The impedance is used later on to calculate the reflection of monochromatic waves. In the next three subsections the wavelength (§4.4.a), phase velocity (§4.4.b) and absorption (§4.4.c) will be discussed.

4.4.a Wavelength (λ)

The wavelength of the electromagnetic wave in the ice is dependent on the real part of the wave number. $\lambda = \frac{2\pi}{k'}$ This is shown in the figure 4.4 below.

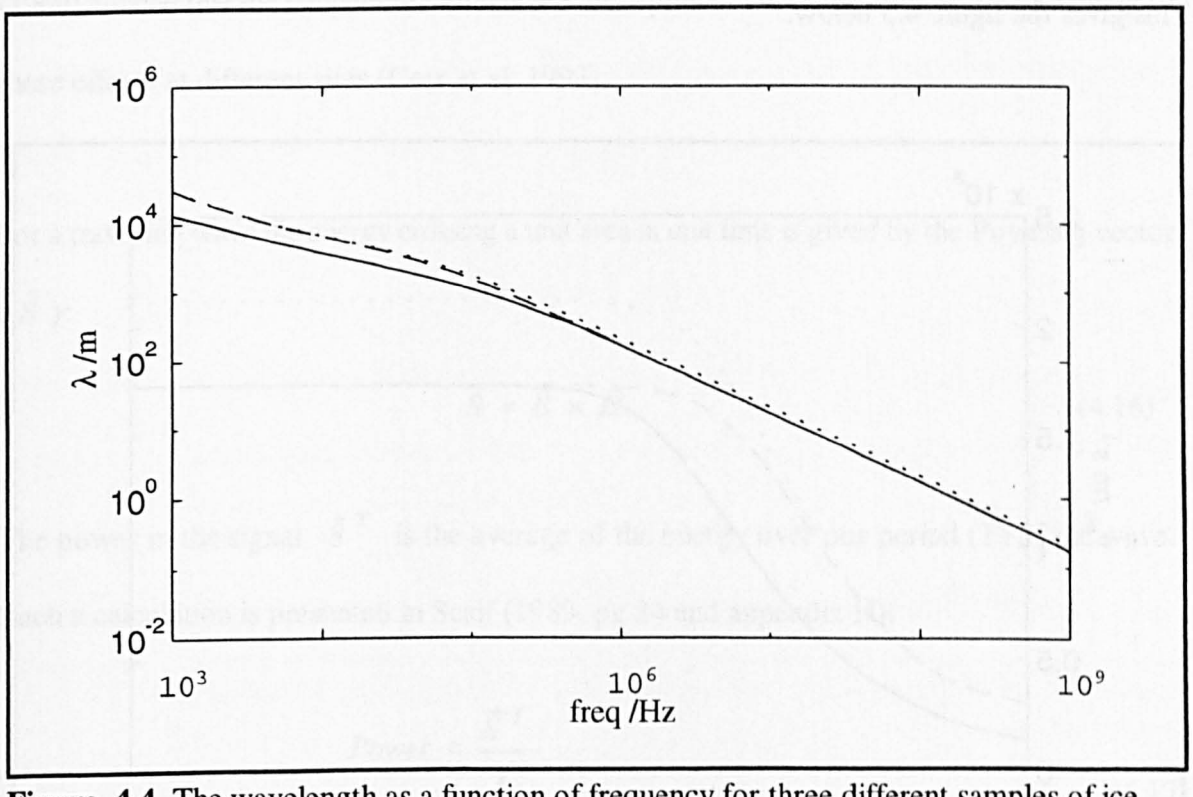

Figure 4.4 The wavelength as a function of frequency for three different samples of ice.
1) dashed line, $\{\sigma_{dc} = 5\ \mu S\ m^{-1}, \Delta\varepsilon_{Dr} = 70, \tau_D = 5\times10^{-5}\ s, \varepsilon'_{r\infty} = 3\}$
2) dotted line, low $\varepsilon_{r\infty}$ $\{\sigma_{dc} = 5\ \mu S\ m^{-1}, \Delta\varepsilon_{Dr} = 70, \tau_D = 5\times10^{-5}\ s, \varepsilon'_{r\infty} = 2\}$
3) solid line, high σ_{dc} $\{\sigma_{dc} = 50\ \mu S\ m^{-1}, \Delta\varepsilon_{Dr} = 70, \tau_D = 5\times10^{-5}\ s, \varepsilon'_{r\infty} = 3\}$

4.4.b Phase Velocity (v_{ph})

The electric field, (amplitude 1 at z = 0) with each peak in the wave travelling in the direction

of increasing depth (z), is given by:

$$\begin{aligned} \tilde{E} &= e^{i(\omega t - \tilde{k} z + \phi)} \\ &= e^{i\theta} \end{aligned} \tag{4.14}$$

where the phase is θ and the phase velocity (v_{ph}) is given by the reciprocity relation:

$$v_{ph} = \left(\frac{\partial z}{\partial t}\right)_{\theta} = -\frac{\left(\frac{\partial \theta}{\partial t}\right)_{z}}{\left(\frac{\partial \theta}{\partial z}\right)_{t}} = \frac{\omega}{k'} \tag{4.15}$$

This gives the figure 4.5 below:

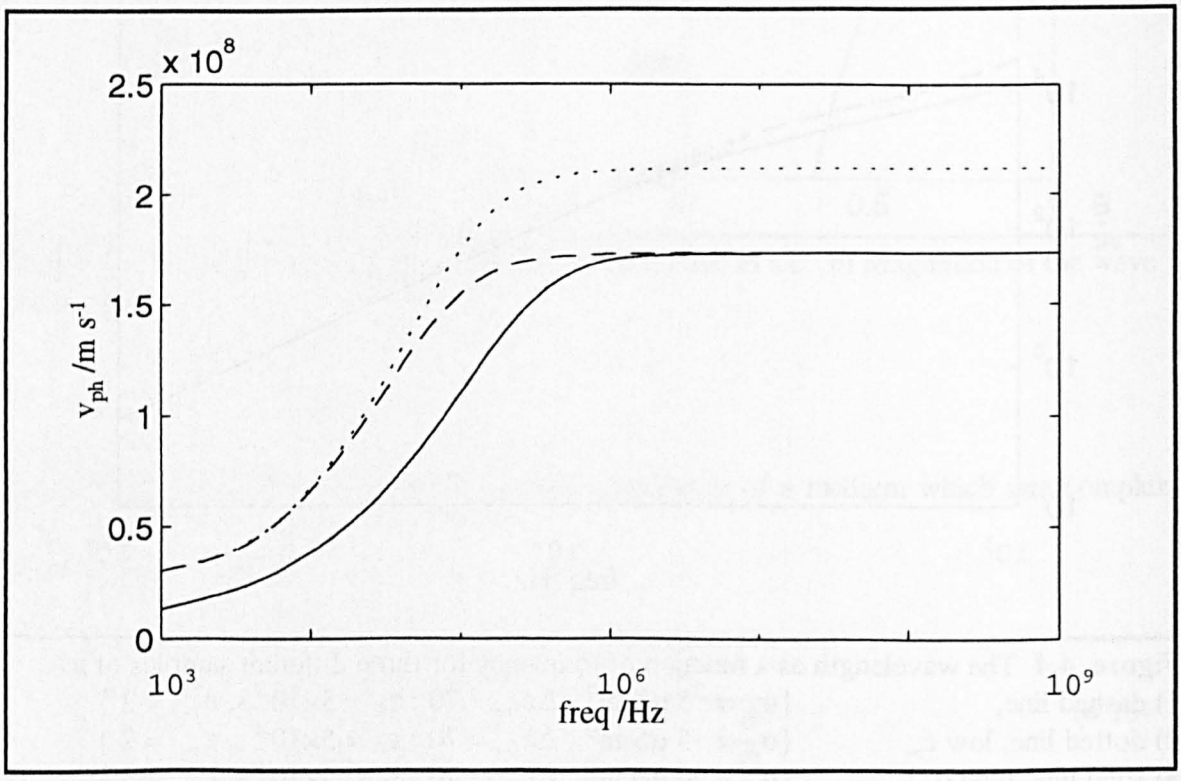

Figure 4.5 The phase velocity as a function of frequency for the same three samples of ice.

From the figure it can be seen that the phase velocity is a function of the frequency, and it has a positive gradient; this means that ice is classified as anomalously dispersive. But the gradient

is slight over the frequency range of interest to this thesis (>10^6 Hz, for radio echo sounding), so that sometimes it is possible to approximate that the ice is non-dispersive. This approximation will be further investigated later.

4.4.c Absorption

The intensity of an electromagnetic wave decays exponentially as it passes through a dissipative medium. This is a result of the conductivity and it has been noticed by previous authors how factors that affect the conductivity also affect the absorption: Walford (1968) noticed that losses in the band 3 to 300 MHz are proportional to the ionic impurity in the ice; Robin et al. (1969) noticed that the temperature affects the absorption. There has been some modelling of these effects at different sites (Corr et al. 1993).

For a travelling wave the energy crossing a unit area in unit time is given by the Poynting vector ($\tilde{S}$):

$$\tilde{S} = \tilde{E} \times \tilde{H} \tag{4.16}$$

The power in the signal $\tilde{S}^T$ is the average of the energy over one period (T) of the wave. Such a calculation is presented in Scaif (1989, pg 24 and appendix H):

$$\begin{aligned} Power &= \frac{\overline{S}^T}{T} \\ &= \frac{1}{2T} k' \, | \, \tilde{E} \cdot \tilde{E}^* \, | \, e^{(-2k''z)} \end{aligned} \tag{4.17}$$

The factor 2 k'' is often called K the absorption coefficient. The decay in power can be represented as:

$$P_z = P_0 e^{(-2k''z)} \tag{4.18}$$

Inserting values of: $\sigma = 10\ \mu S\ m^{-1}$, $\varepsilon'_r = 3.2$ and $f = 50$ kHz; gives a value of -0.9 decibels per hundred metres. Similar values are returned if the formulas in Robin et al. (1969) and Smith and Evans (1972) are used. Though their formulas require a temperature term, from which the conductivity effect is calculated (see effect of temperature on conductivity (§3.6.a)).

The effect of absorption on the amplitude as a function of frequency is shown in figure 4.6 below:

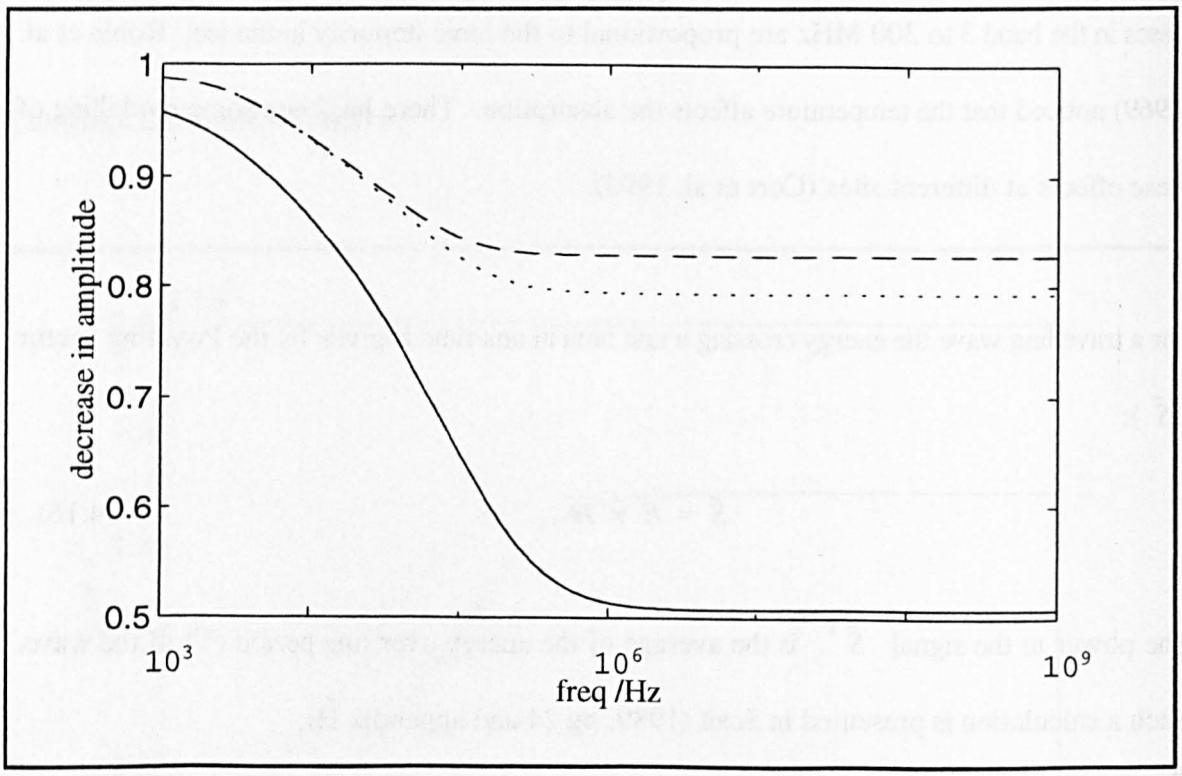

Figure 4.6 Absorption, effect on amplitude, after traveling 100 m, for the same three samples of ice.

4.5 Monochromatic reflections from an interface

This section will consider the full derivation of the result for two reasons. First it gives an opportunity to introduce the application of the continuity equations and the question of the presence of sheet current at the boundary. Secondly, it removes the need to include the derivation for the propagation-matrices model later in this chapter (§ 4.7.b).

4.5.a Orientation of TEM fields

I will follow the orientation convention described in Clarke and Grainger (1971) to specify the coordinates and the direction of travel of the waves. In the diagram below the boundary between the two media lies along the xy plane and the plane of incidence is the yz plane. The electric fields $\boldsymbol{E}$ always point in the same direction in the three waves (incident, reflected and transmitted). The $\boldsymbol{B}$ (and $\boldsymbol{H}$) field is given in a direction so that the Poynting theorem applies (equation 4.16).

A continuous linear polarised monochromatic wave, initially of unit amplitude at $z = z_1$ is propagating in a semi infinite half space with boundary at $z = z_1$. The medium is isotropic with properties σ_1 and $\varepsilon'_{r\,1}$; the reflected wave has amplitude α at $z = z_1$. The orientation of the incident and reflected fields is given using the right hand rule as shown in figure 4.7:

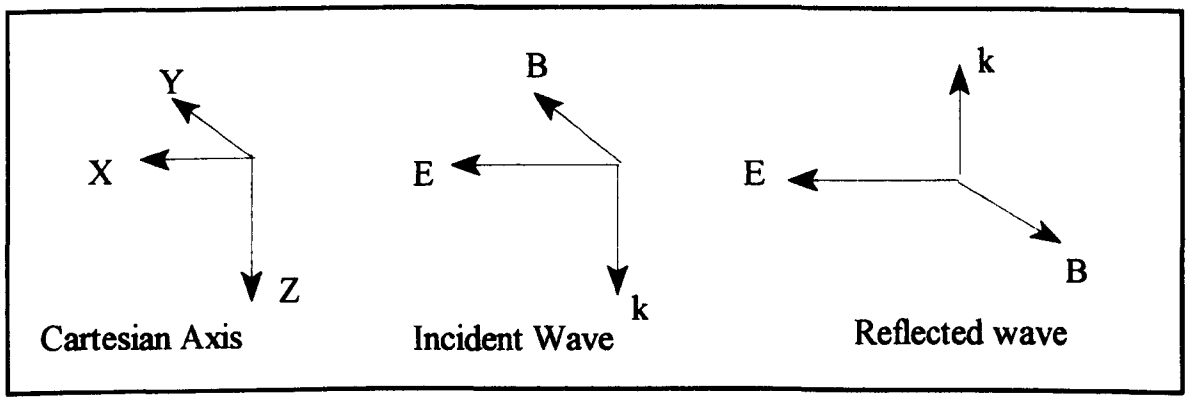

Figure 4.7 Orientation of field vectors

The equations for the fields in medium 1 are:

$$\begin{aligned}
\tilde{E}_1 &= e^{i\left(\omega t - \tilde{k}_1 (z - z_1)\right)} + \alpha\, e^{i\left(\omega t + \tilde{k}_1 (z - z_1)\right)} \\
\tilde{H}_1 &= \frac{\tilde{k}_1}{\mu_0 \omega} e^{i\left(\omega t - \tilde{k}_1 (z - z_1)\right)} - \frac{\tilde{k}_1}{\mu_0 \omega} \alpha\, e^{i\left(\omega t + \tilde{k}_1 (z - z_1)\right)} \\
\tilde{k}_1^2 &= \mu_0 \varepsilon_0 \varepsilon'_{r1} \omega^2 - i \mu_0 \sigma_1 \omega
\end{aligned} \tag{4.19}$$

The boundary between the two media occurs at $z = z_1$. In medium 2, which has σ_2 and $\varepsilon'_{r\,2}$, there is only a down going wave and the field is given by:

$$\begin{aligned}
\tilde{E}_2 &= \beta\, e^{i\left(\omega t - \tilde{k}_2 (z - z_1)\right)} \\
\tilde{H}_2 &= \frac{\tilde{k}_2}{\mu_0 \omega} \beta\, e^{i\left(\omega t - \tilde{k}_2 (z - z_1)\right)} \\
\tilde{k}_2^2 &= \mu_0 \varepsilon_0 \varepsilon'_{r2} \omega^2 - i \mu_0 \sigma_2 \omega
\end{aligned} \tag{4.20}$$

4.5.b The solution for the interface

In order to solve the two unknowns (α, β) in terms of the known parameters, two boundary conditions are used. The first, from Faraday's law, is continuity of the tangential components of E:

$$\begin{aligned}
\tilde{E}_1(z = z_1) &= \tilde{E}_2(z = z_2) \\
1 + \alpha &= \beta
\end{aligned} \tag{4.21}$$

The second condition at the boundary, from Ampere's law, is the change in the tangential component of $\boldsymbol{H}$ across a boundary, which is equal in magnitude to the sheet current J_{SURFACE} at the boundary. If the materials on both sides of the boundary are loss free then the sheet current density is zero on either side and the tangential components of $\boldsymbol{H}$ are treated as constant across the boundary.

$$\tilde{H}_1(z = z_1) = \tilde{H}_2(z = z_1)$$
$$\tilde{k}_1 - \tilde{k}_1 \alpha = \tilde{k}_2 \beta \tag{4.22}$$

The same assumption of continuity of $\boldsymbol{H}$ is made when both the permittivity and the conductivity change on either side (Stratton, 1941; Wait, 1958; Wait, 1996). This assumption cannot be made when the interface separates a conductor from an insulating material. In such a case it is necessary to consider the current sheet at the boundary. The other two conditions at an interface are that the normal components of $\boldsymbol{D}$ and $\boldsymbol{B}$ are continuous, although these are not applicable in the TEM wave case.

Combining the above two equations from each condition gives the amplitude reflection coefficient (r_{AF}) and the amplitude transmission coefficient (t_{AF}). These coefficients are described by the Fresnel equations (hence I have chosen to use the F subscript). These equations are applicable to the boundary between two semi-infinite, linear, isotropic, homogeneous media. This reflection coefficient gives the ratio for up-going and down-going electric fields just above the interface:

$$r_{AF12} = \frac{\alpha}{1} = \frac{\tilde{k}_1 - \tilde{k}_2}{\tilde{k}_1 + \tilde{k}_2} \qquad t_{AF12} = \frac{\beta}{1} = \frac{2\tilde{k}_1}{\tilde{k}_1 + \tilde{k}_2} \tag{4.23}$$

where $|r_{AF}|+|t_{AF}| = 1$. The reflection equation can also be expressed in either terms of impedance (Z), refractive index (n) or admittance (Υ). These have a different order for the terms in the numerator:

$$r_{AF12} = \frac{Z_2 - Z_1}{Z_2 + Z_1} = \frac{n_1 - n_2}{n_1 + n_2} = \frac{\Upsilon_1 - \Upsilon_2}{\Upsilon_1 + \Upsilon_2} \tag{4.24}$$

Following Bennet and Bennet (1978), and Clarke and Grainger, (1971) any phase change given by the calculation is relative to the situation as drawn in figure 4.7.

4.5.c For loss free materials

For loss free media (insulators), where $\tilde{k}$ is real, the reflection coefficient is a real number and there is agreement in the literature that at a boundary to a higher impedance material (higher refractive index) the phase change is 180^0. (This reflection coefficient is independent of the convention used to solve the Maxwell equations.)

Table 4.4 Reflection coefficients for loss free materials (50 MHz)

		ϵ'_r	n	Z	k	$\lvert r_{AF12} \rvert$	δ_{AF12}
Density increase	**material 1**	2.9	5.067×10^{-6}	221.226	0.284016	8.47×10^{-3}	180°
	material 2	3.0	5.154×10^{-6}	218.507	0.288872		
Density decrease	**material 1**	3.0	5.154×10^{-6}	218.507	0.288872	8.47×10^{-3}	0^0
	material 2	2.9	5.067×10^{-6}	221.226	0.284016		

The transmitted wave does not undergo a phase change.

4.5.d For lossy materials

The phase change on reflection at conductive boundaries is more involved and the value assigned depends on the convention used for the solution of Maxwell's equations. The reflection coefficient is a complex number $r = r' + i\,r''$ and can be presented using Euler's equation as a real magnification and a phase change:

$$\begin{aligned} &\textit{magnitude} \qquad |r_i| = \sqrt{r'^2 + r''^2} \\ &\textit{phase} \qquad \delta_i = \tan^{-1}\left(\frac{r'}{r''}\right) \pm n\,180^0 \quad \textit{where } n = 0, 1, 2, 3, \ldots\ldots \end{aligned} \tag{4.25}$$

4.5.e An example: the reflection coefficient for a single interface

In this section the reflection of a monochromatic wave from the interface between two semi-infinite pieces of lossy ice is considered.

4.5.e.i Calculated using dispersive material properties

In figure 4.8 below are shown the phase change and the amplitude change when the ice either side of the interface has an AF-LF dispersion modelled using the Debye equation (eqn 3.9).

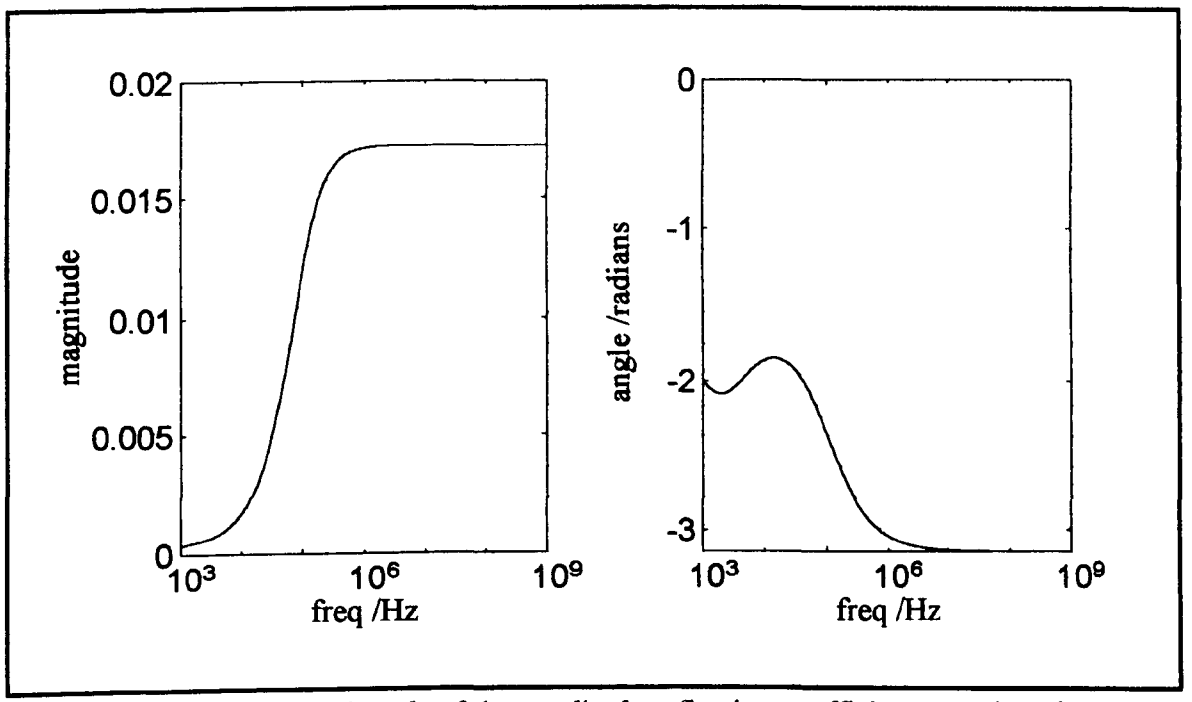

Figure 4.8 Magnitude and angle of the amplitude reflection coefficient at an interface between two dispersive media.
upper material: $\sigma_{dc} = 6\ \mu S\ m^{-1}$, $\Delta\varepsilon_{Dr} = 60$, $\tau_D = 5\times10^{-5}$ s, $\varepsilon'_{r\infty} = 2.8$, $\sigma_\infty = 16.6\ \mu S\ m^{-1}$
lower material: $\sigma_{dc} = 6\ \mu S\ m^{-1}$, $\Delta\varepsilon_{Dr} = 60$, $\tau_D = 5\times10^{-5}$ s, $\varepsilon'_{r\infty} = 3.0$, $\sigma_\infty = 16.6\ \mu S\ m^{-1}$

Figure 4.8 shows the expected trend of an increasing amplitude reflection coefficient as the frequency increases. This is a result of the difference in the admittances divided by the sum of the admittances becoming larger(see eqn 4.24 and eqn 4.28).

4.5.e.ii Calculated using high frequency values

In this section the reflection coefficient is calculated again. However, this time the materials

on either side of the interface are approximated by using the high frequency values ($\varepsilon'_{r\infty}$ and σ_∞) over the entire frequency range. This means that the reflection coefficient has a frequency independent value of -0.01725.

The reflection coefficients calculated using the Debye model (§4.5.e.i) and the high frequency model merge as the frequency increases. At a frequency of 5.4 kHz they differ by 10%, at a frequency of 94.7 kHz they differ by 1% (the relaxation frequency of the AF-LF dispersion is 3.2 kHz in both materials).

4.5.f Approximation of Paren

Paren and Robin (1975) and Paren (1981) considered the power reflection coefficient at a boundary from ice with admittance $\Upsilon_1 = \Upsilon$ to ice with admittance $\Upsilon_2 = \Upsilon + \Delta\Upsilon$. For such a situation a Taylor expansion can be made:

$$\begin{aligned} |r_p| &= \left| \frac{\Upsilon_1 - \Upsilon_2}{\Upsilon_1 + \Upsilon_2} \right|^2 \\ &= \left| \frac{\Delta\Upsilon}{2\Upsilon + \Delta\Upsilon} \right|^2 \\ &= \left| \left(\frac{\Delta\Upsilon}{2\Upsilon} \right) \left(1 - \left(\frac{\Delta\Upsilon}{2\Upsilon} \right) + \ldots. \right) \right|^2 \end{aligned} \tag{4.26}$$

The authors considered only the first term in the expansion. Then use equation 4.27 below to express the change in the admittance as a change in the natural logarithm of the admittance.

$$\frac{1}{2}\frac{1}{y}\frac{dy}{dx} = \frac{1}{2}\frac{d\,ln\,y}{dx} \tag{4.27}$$

The derivation then proceeds as in Paren (1981). When considering only permittivity changes

(from material with ε'_r to material with $\varepsilon'_r + \Delta\varepsilon'_r$) the approximation becomes:

$$r_p = \left(\frac{1}{4} \frac{\Delta\varepsilon'_r}{\varepsilon'_r} \right)^2 \tag{4.28}$$

When considering this equation for changes in the loss tangent then:

$$r_p = \left(\frac{1}{4} \Delta (\tan\delta) \right)^2 \tag{4.29}$$

It was by using this equation that Paren and Robin (1975) postulated that changes in loss tangent could be responsible for the internal reflections observed deep inside ice sheets. Sivaprasad and Lessow (1976) discuss the validity of the approximation.

4.6 Monochromatic reflections from a single layer

If there is a single layer of material 2 lying inside material 1 then a monochromatic wave will be reflected from the top and bottom interface of the layer. An observer will see one wave returning from the layer with a different amplitude and phase to the wave that was incident on the layer. The amplitude reflection coefficient (r_{A12}) (no longer the Fresnel subscript) just above the layer depends on the thickness (l) of the layer and the properties of materials 1 and 2. As r_{A12} depends on the amplitudes of the waves and the medium may be absorbent it is important to say that the value is being determined for just above the single layer. The reflection coefficient oscillates with the frequency of the incident wave and the thickness of the layer. In the literature this phenomenon is called tuning. In particular a layer thickness of one half wavelength will result in a considerable increase in reflection amplitude. The reflection coefficient from a single layer of material 2 in material 1 can be greater than the Fresnel reflection coefficient at an interface between two semi infinite half spaces of materials 1 and 2.

In this section, four equations for the reflection coefficient of a layer will be presented. The first three equations are exact, all derived in slightly different ways. All three are presented as all have been used by different researchers in radio-glaciology. The fourth equation is the form that is presently common in glaciology. It is an approximation and differs from the three exact results at the singularities.

4.6.a Stratton's equation

Consider medium 1 with wavenumber $\tilde{k}_1$ which contains an incident wave (unit amplitude just above the layer) and a reflected wave (amplitude α just above the layer). Medium 2 is the layer which starts at depth z = 0 and has thickness l with wave number $\tilde{k}_2$. In it there are up going and down going solutions (which I choose to define just above the bottom interface). Medium 3 is the same material as medium 1 (it has wave number $\tilde{k}_1$) and contains the final transmitted wave (which I choose to define just below the interface). The derivation proceeds using continuity of the boundary conditions at the two boundaries, in a similar manner to §4.5.a.

$$r_{A12} = \frac{r_{AF12} + r_{AF23} e^{-2i\tilde{k}_2 l}}{1 + r_{AF23} r_{AF12} e^{-2i\tilde{k}_2 l}} \tag{4.30}$$

where

r_{AI2} = amplitude reflection coefficient in medium 1 at the boundary from 1 to 2.
l = layer thickness {m}
$\tilde{k}_2$ = wave number inside layer 2.
r_{AF12} = Fresnel amplitude reflection coefficient between media 1 and 2
r_{AF23} = Fresnel amplitude reflection coefficient between media 2 and 3

An example of the derivation can be found in Stratton (1941, pg 512). Stratton uses a negative exponential for time when solving Maxwell's equations and his result has positive exponential terms. This exact equation (eqn 4.30) produces a complex amplitude reflection coefficient,

which implies a phase change as well as an amplitude change on reflection.

From the amplitude reflection coefficient the power reflection coefficient is obtained by $r_p = |r_A|^2$ (Stratton, 1941). Previous authors considering radio echo sounding have given equations for the power reflection coefficient of a single layer (Robin et al. 1969; Harrison, 1973). The equations they presented can be derived from Stratton's equation (Clough, 1974).

In figure 4.9 below equation 4.30 is used to examine the frequency variation in the reflection coefficient.

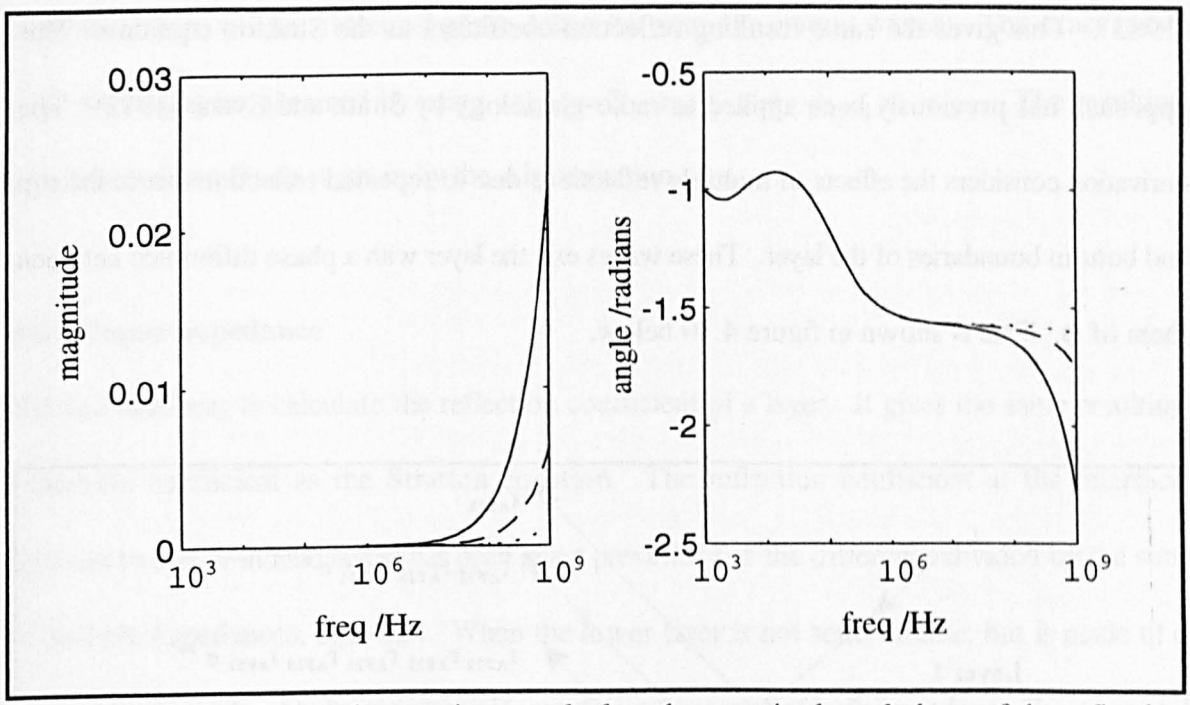

Figure 4.9 Using Stratton's equation to calculate the magnitude and phase of the reflection coefficient for a higher real relative permittivity layer, typical of an ice layer in firn, as a function of frequency:
surrounding material $\sigma_{dc} = 6\ \mu S\ m^{-1}$, $\Delta\varepsilon_{Dr} = 60$, $\tau_D = 5\times10^{-5}$ s, $\varepsilon'_{r\infty} = 2.8$, $\sigma_\infty = 16.6\ \mu S\ m^{-1}$
layer material $\sigma_{dc} = 6\ \mu S\ m^{-1}$, $\Delta\varepsilon_{Dr} = 60$, $\tau_D = 5\times10^{-5}$ s, $\varepsilon'_{r\infty} = 3.0$, $\sigma_\infty = 16.6\ \mu S\ m^{-1}$
three layer thicknesses: dotted line: 1 mm, dashed line 5 mm, solid line 20 mm.

Figure 4.9 displays the effect mentioned at the beginning of section 4.6: *a layer thickness of one half wavelength will result in a considerable increase in reflection amplitude*. So that the

three layers will each have a maximum reflected amplitude at 4 GHz for 20 mm, 16 GHz for 5 mm and 80 GHz for 1 mm. Lower frequencies (longer wavelengths) are not reflected by thin layers. In the previous section (§4.5) where the reflection from an interface was considered there was little variation in the reflection coefficient at high frequency. In this figure it is shown that for layers with thicknesses typically found in ice cores (see table 2.1) the reflection coefficient is sensitive to the thickness of the layers.

4.6.b Interferometry

A different derivation to that of Stratton can be found in interferometry books such as Steel, (1983). This gives the same resulting reflection coefficient as the Stratton equation. This approach has previously been applied to radio-glaciology by Smith and Evans (1972). The derivation considers the effects of multiple reflections due to repeated reflections from the top and bottom boundaries of the layer. These waves exit the layer with a phase difference between them of ϕ. This is shown in figure 4.10 below.

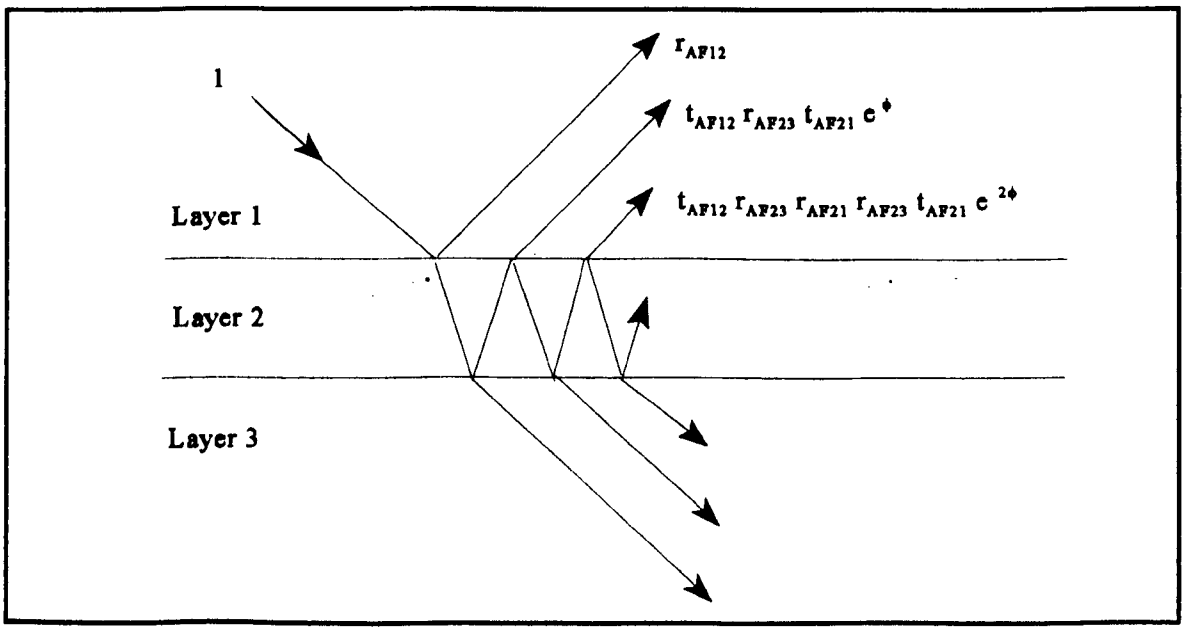

Figure 4.10 The reflection of multiples (Shown with oblique incidence for clarity.)

The reflected amplitude r_{A12} in medium 1 at the boundary is given as a summation of reflections from all the multiples in terms of the Fresnel amplitude reflection coefficients by:

$$r_{A12} = r_{AF12} + t_{AF12} r_{AF23} t_{AF21} e^{i\phi} + t_{AF12} r_{AF21} r_{AF23}^2 t_{AF21} e^{i2\phi} + \ldots\ldots$$
$$= r_{AF12} + \frac{t_{AF12} t_{AF21} r_{AF23} e^{i\phi}}{1 - r_{AF21} r_{AF23} e^{i\phi}} \qquad (4.31)$$

where

ϕ = increment in phase between exiting waves.

When the wave is incident vertically then $\phi = -2\tilde{k}_2 l$. (If the wave enters the layer at an angle then there will be additional phase delays between the exiting waves). The exact result (eqn 4.30) can be obtained by using $t_{AFij} = 1 + r_{AFij}$ and $r_{AFij} = -r_{AFji}$ The resulting transmission amplitude is given by the Airy equation.

4.6.c Input impedance

This is a third way to calculate the reflection coefficient of a layer. It gives the same resulting reflection coefficient as the Stratton equation. The reflection coefficient at the interface between two semi-infinite layers has been given previously as the difference divided by the sum of the bulk impedances, eqn 4.24. When the lower layer is not semi-infinite, but is made of a layer of thickness l and bulk impedance Z_2 overlying a material of bulk impedance Z_3 , then the reflection coefficient at the top interface between material 1 and 2 is given by the equation below:

$$r_{A12} = \frac{\hat{Z}_2 - Z_1}{\hat{Z}_2 + Z_1} \qquad (4.32)$$

where

$\hat{Z}_2$ = Surface (or input) impedance of layer, material 2

Z_1 = Characteristic (or bulk) (or surge) impedance of first material

The input impedance of the layer is given by:

$$\hat{Z}_2 = Z_2 \frac{Z_3 + Z_2 i \tan(\tilde{k}_2 l)}{Z_2 + Z_3 i \tan(\tilde{k}_2 l)} \tag{4.33}$$

This equation for the input impedance can be derived by taking the exact result of Stratton (eqn 4.30) and substituting the eqn 4.24 for the Fresnel reflection coefficient. The same result has been obtained by Staelin et al. (1994, pp 222). Wait (1958, 1996) also obtains a similar result but uses different constants for his solution of Maxwell's equations. This input impedance type of equation is further developed in §4.7.a.

4.6.d Paren's equation

This is the most common form of the reflection coefficient for a layer in glaciology. It considers layers of material 2 inside material 1 and comes from Paren and Robin (1975), with further detail in Paren (1981). The equation for the power reflection coefficient (r_p) considers ice of admittance Υ containing a layer of admittance $\Upsilon + \Delta\Upsilon$. It is valid for small values of $\Delta\Upsilon$ and thin layers ($l \ll \lambda_m$).

$$r_{P12} = 4 \sin^2\left(\frac{2\pi l}{\lambda_m}\right) \left|\frac{1}{2}\frac{\Delta\Upsilon}{\Upsilon}\right|^2 \tag{4.34}$$

where

λ_m = the wavelength of the wave in the ice layer

It has previously been shown (§4.5.f) how the admittance term on the right was approximated by Paren (1981) when considering small changes in either the permittivity (eqn 4.28) or the loss tangent (eqn 4.29). The use of these equations is compared with the Stratton equation in figure

4.11 below.

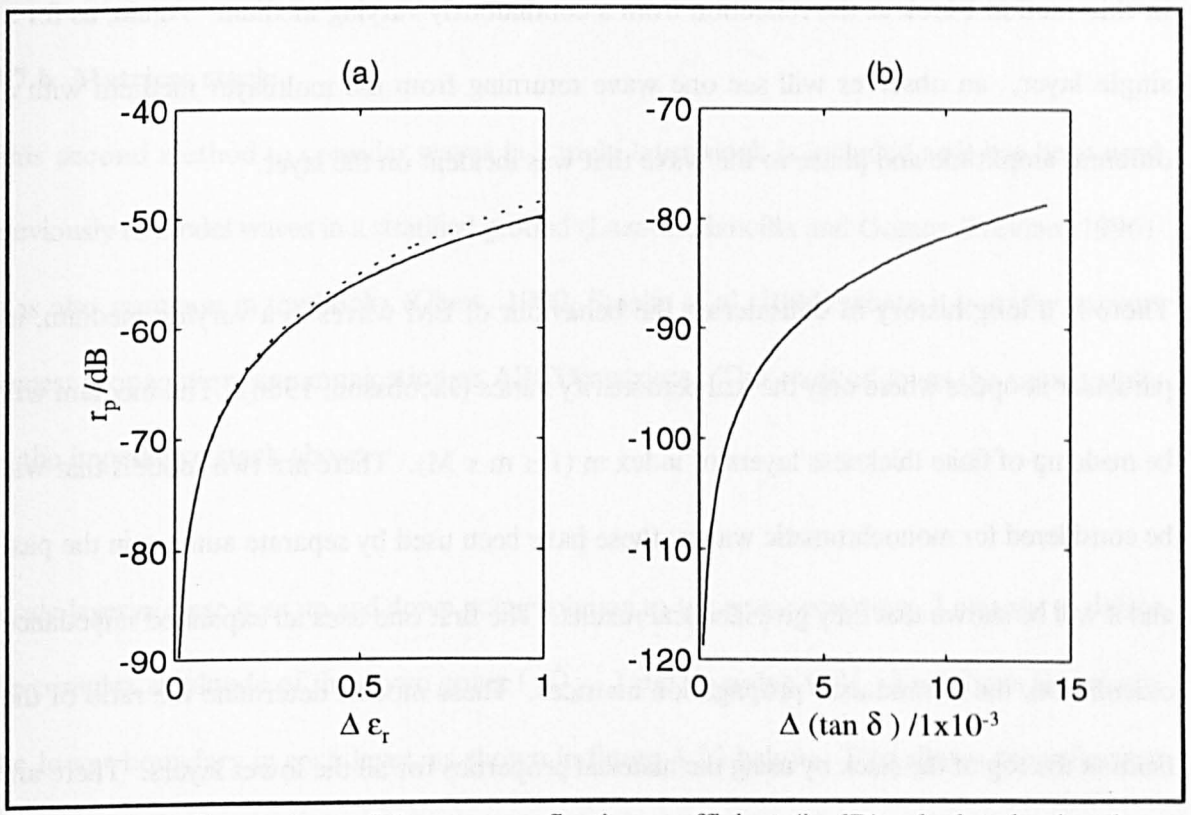

Figure 4.11 Comparison of the power reflection coefficient (in dB) calculated using the exact equation of Stratton (solid line) and Paren's approximation (dotted line). For a layer thickness l of 10 mm, and a frequency of 50 MHz ($\lambda \approx 3.6$ m).
a) Where only the real permittivity changes ($\Delta\varepsilon_r$) from a surrounding medium of $\varepsilon_r = 2.56$.
b) Where only the loss tangent changes ($\Delta \tan\delta$) due to an increase in the conductivity. The surrounding medium has $\sigma_\infty = 10\mu$S m^{-1}, the layer has a conductivity of 10μS m^{-1} $< \sigma_\infty <$ 100μS m^{-1} . For this range the difference in the decibel value of the power reflection coefficient between Stratton's equation and Paren's approximation only alters in the third decimal place so the dotted line is coincident with the solid line on this scale.

It can be seen in figure 4.11 that Paren's approximation is very good for the range it is intended; ie when there is only a small difference between the properties of the layer and the surrounding medium and when the layer is thin in relation to the wavelength of the radiation.

A recent adaption of Paren's equation in Fujita and Mae (1994) uses the bulk impedance instead of the admittance.

4.7 Monochromatic reflections from a multi layer medium

In the previous sections I have considered a single boundary (§4.5) and a single layer (§4.6). In this section I look at the reflection from a continuously varying medium. Again, as for a single layer, an observer will see one wave returning from the multilayer medium with a different amplitude and phase to the wave that was incident on the layer.

There is a long history of considering the behaviour of EM waves in a varying medium, in particular in optics where only the real permittivity varies (Jacobsson, 1966). The medium will be made up of finite thickness layers of index m ($1 \le m \le M$). There are two models that will be considered for monochromatic waves; these have been used by separate authors in the past and it will be shown that they give identical results. The first one uses an expanded impedance calculation, the second uses propagation matrices. These models determine the ratio of the fields at the top of the stack by using the material properties for all the lower layers. There are other models such as the Ricatti equation outlined in Chew (1990). After describing the two models an example will be considered.

4.7.a Impedance stack

In §4.6.c the input impedance of a layer was considered. By continuing this process the reflection coefficient at a given depth as a function of all the material below that depth can be calculated. This is done by taking the input impedance calculation and substituting $\hat{Z}_3$ for Z_3. The input impedance of the layer *m* is given by:

$$\hat{Z}_m = Z_m \frac{\hat{Z}_{m+1} + Z_m i \tan(\tilde{k}_m l_m)}{Z_m + \hat{Z}_{m+1} i \tan(\tilde{k}_m l_m)} \qquad (4.35)$$

This method has been used to consider the reflection coefficient of monochromatic waves by

Ackley and Keliher (1979) and Moore et al. (1988 a, b). It is described further in Wait (1958, 1996).

4.7.b Matrices stack

This second method to consider waves in a multi layer stack is included as it has been used previously to model waves in a stratified ground (Lazaro-Mancilla and Gomez-Trevino, 1996). It is also common in textbooks (Chew, 1990; Staelin et al. 1994) where it goes by various names: propagation, communication or ABCD matrices. This method gives the same results as the impedance stack above.

Inside layer m there is an up and down going solution to the wave equation. I choose to define the complex amplitude of the down going ($\tilde{D}_m$) and up going ($\tilde{U}_m$) solutions just above the lower boundary in each layer, as shown in figure 4.12 below. This allows the reflection coefficient to be easily calculated just above each boundary, so that the coefficient given by the matrix method can be compared with that given by the impedance stack method. Other authors define the amplitudes at the top of the layer and therefore obtain a different expression. In the majority of seismic models the amplitudes are defined at the top of the layers (Robinson, 1968).

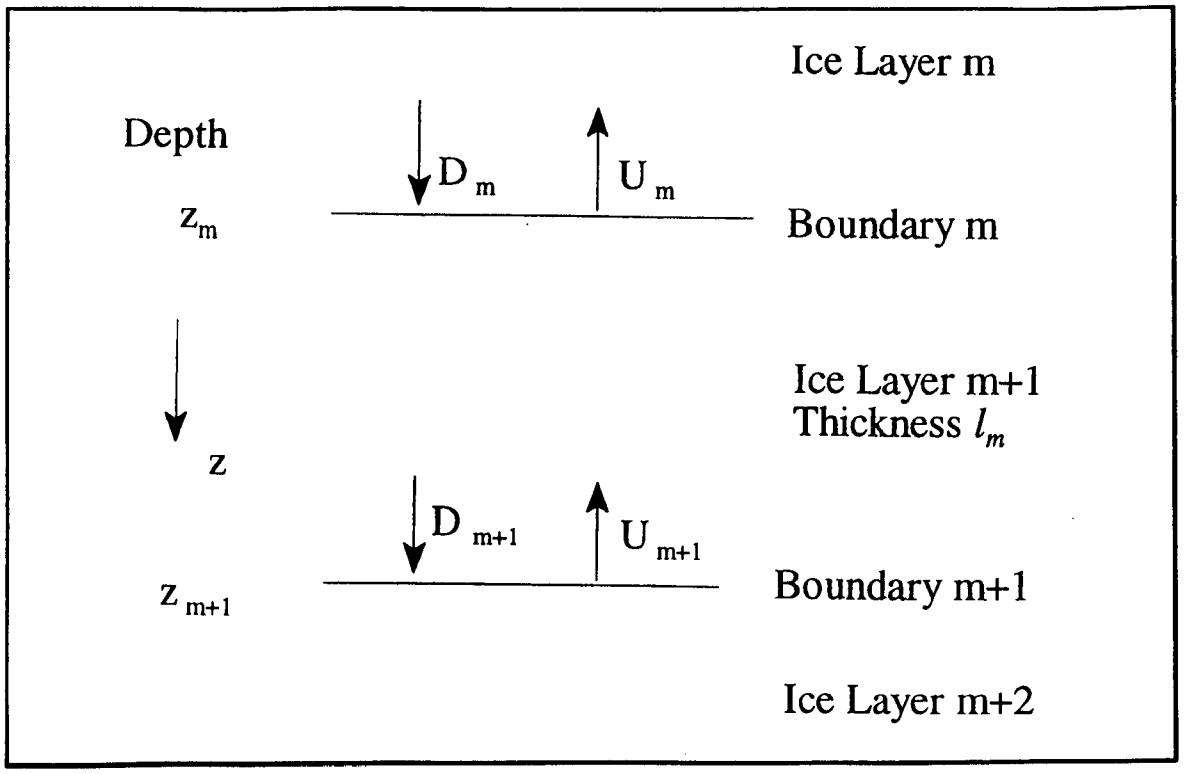

Figure 4.12 Waves inside one layer of the matrix model.

The wave in layer m can be described using the same equations as in §4.2 :

$$\tilde{E}_m = \tilde{D}_m e^{i(\omega t - \tilde{k}_m (z - z_m))} + \tilde{U}_m e^{i(\omega t + \tilde{k}_m (z - z_m))}$$

$$\tilde{H}_m = \tilde{D}_m \frac{\tilde{k}_m}{\mu_0 \omega} e^{i(\omega t - \tilde{k}_m (z - z_m))} - \tilde{U}_m \frac{\tilde{k}_m}{\mu_0 \omega} e^{i(\omega t + \tilde{k}_m (z - z_m))} \qquad (4.36)$$

$$\tilde{k}_m^2 = \mu_0 \varepsilon_0 \varepsilon'_{r2} \omega - i \mu_0 \sigma_2 \omega$$

where:

$\tilde{U}_m$ *and* $\tilde{D}_m$ = Magnitudes of the $\boldsymbol{E}$ field at $z = z_m$ in layer m .
z = The depth below the surface for which the field is being determined.
z_m = The depth below the surface of boundary m.

At the boundary continuity conditions are considered, in a similar manner to the previous section, to give relations between the waves in the layers m and m+1. These equations can be expressed in matrix form:

$$\begin{bmatrix} \tilde{U}_{m+1} \\ \tilde{D}_{m+1} \end{bmatrix} = \begin{bmatrix} \left(1+\frac{\tilde{k}_m}{\tilde{k}_{m+1}}\right)\frac{e^{i\tilde{k}_{m+1}l_{m+1}}}{2} & \left(1-\frac{\tilde{k}_m}{\tilde{k}_{m+1}}\right)\frac{e^{i\tilde{k}_{m+1}l_{m+1}}}{2} \\ \left(1-\frac{\tilde{k}_m}{\tilde{k}_{m+1}}\right)\frac{e^{-i\tilde{k}_{m+1}l_{m+1}}}{2} & \left(1+\frac{\tilde{k}_m}{\tilde{k}_{m+1}}\right)\frac{e^{-i\tilde{k}_{m+1}l_{m+1}}}{2} \end{bmatrix} \begin{bmatrix} \tilde{U}_m \\ \tilde{D}_m \end{bmatrix} \tag{4.37}$$

This matrix is given the symbol $\underline{\underline{C}}_m$. The amplitude of the monochromatic wave at the top of a stack of M layers is determined by multiplying as many communication matrices as there are layers. This gives:

$$\begin{aligned} \begin{bmatrix} \tilde{U}_M \\ \tilde{D}_M \end{bmatrix} &= \underline{\underline{C}}_{M-1}\underline{\underline{C}}_{M-2}\underline{\underline{C}}_{M-3} \cdots\cdots \underline{\underline{C}}_1 \begin{bmatrix} \tilde{U}_1 \\ \tilde{D}_1 \end{bmatrix} \\ &= \underline{\underline{C}}_{\Pi} \begin{bmatrix} \tilde{U}_1 \\ \tilde{D}_1 \end{bmatrix} \end{aligned} \tag{4.38}$$

where

$\underline{\underline{C}}_{\Pi}$ = the characteristic (or profile) matrix.

To determine the reflection from the stack consider a unit amplitude oscillation at the bottom of the first layer $\tilde{D}_1 = 1$ and consider layer M as the base which is a continuous medium extending downwards to infinity, and so has a down going wave in it but no up going wave $\tilde{U}_M = 0$

$$\begin{bmatrix} 0 \\ \tilde{D}_M \end{bmatrix} = \begin{bmatrix} C_{11} & C_{12} \\ C_{21} & C_{22} \end{bmatrix} \begin{bmatrix} \tilde{U}_1 \\ 1 \end{bmatrix} \tag{4.39}$$

Multiplying this out gives $\tilde{U}_1 = -C_{12}/C_{11}$, which is the reflection coefficient for the stack of layers under consideration.

4.7.c An example: the reflection coefficient for a stack of ice layers

The reflection coefficient from a stack of layers is calculated. Initially the calculation will use dispersive properties for the material in each layer. This is then compared with the result using only the high frequency values.

The ice core data comes from a 2 metre long piece of the GRIP core, which when cut up had its top section in bag G1292 at a depth of 711 metres. The data available at 2 cm resolution are σ_∞ , $\varepsilon'_{r\infty}$ and the relaxation time of the AF-LF dispersion. There is a large error in the values of $\varepsilon'_{r\infty}$.

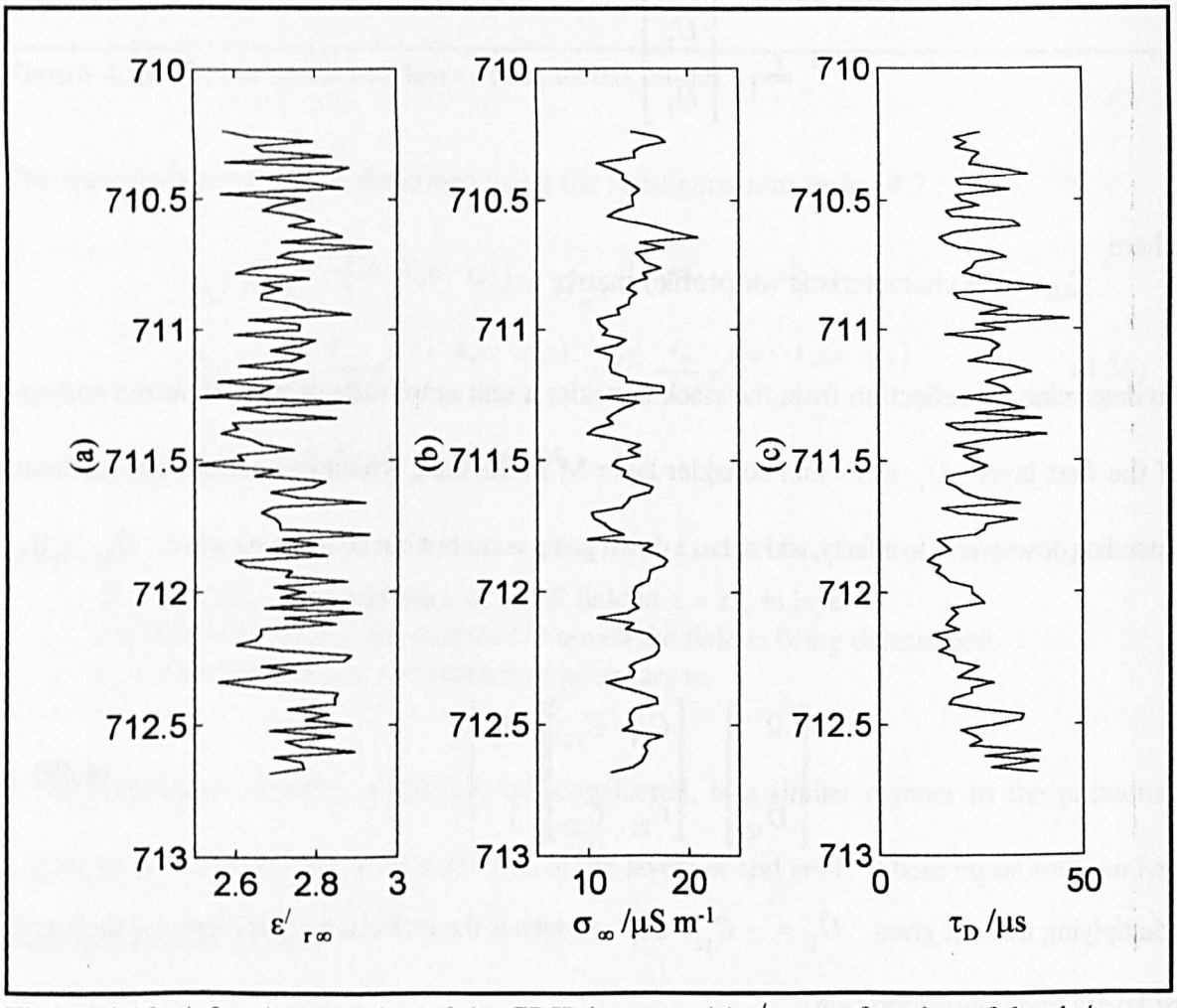

Figure 4.13 A 2 m long section of the GRIP ice core (a) $\varepsilon'_{r\infty}$ as a function of depth /m. (b) σ_∞ as a function of depth /m. (c) the Debye relaxation period τ_D as a function of depth /m.

4.7.c.i Calculated using dispersive material properties

In order to express the complex relative permittivity as a function of frequency, using equation 3.9 (the Debye model), the dc conductivity and the dispersion strength are both required. Unfortunately the GRIP analysis program does not predict either of these. Therefore a small routine was written to try a variety of values for the dispersion strength while the dc conductivity was held at 6 $\mu S\ m^{-1}$ until a good fit to the known high frequency conductivity was obtained. This then allows a simple dispersive model of the ice properties at each depth. These dispersive ice properties are used to calculate the frequency dependence of the amplitude reflection coefficient at the top of the stack.

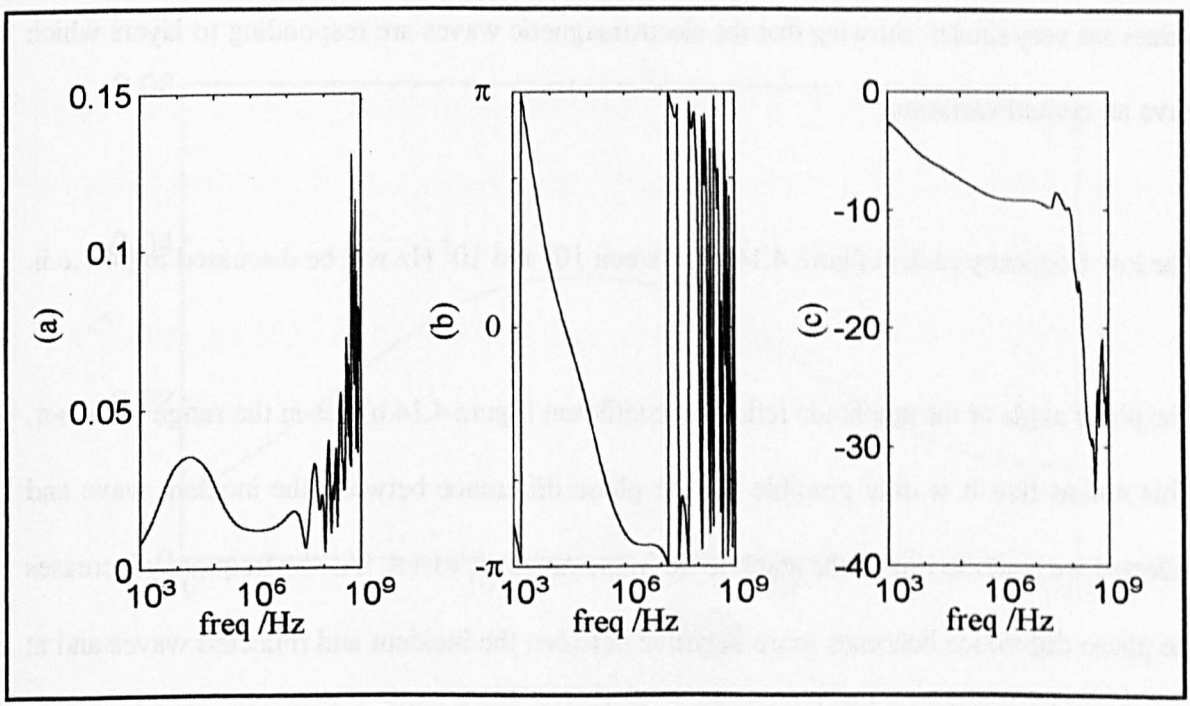

Figure 4.14 Reflection coefficient as a function of frequency for a short section of the GRIP core, where the ice properties are dispersive. (a) the magnitude of the amplitude reflection coefficient, (b) the phase angle in radians of the amplitude reflection coefficient, (c) the unwrapped phase angle in radians of the amplitude reflection coefficient. The plots are discussed below.

The magnitude of the amplitude reflection coefficient (figure 4.14.a) appears to be noisy on the right hand side of the plot. This is the tuning effect where layer thickness equals half the wavelength. The effect starts for the 2 metre section under consideration at a frequency given by the equation: $v/\lambda = f$ i.e: $\left(c \div \sqrt{\varepsilon'_{r\infty}}\right) \div \lambda = \left(3\times10^8 \div \sqrt{2.8}\right) \div (2 \times 2\,m) = 45\,MHz$. Then as the frequency increases (wavelength gets shorter) the effect of the smaller layers inside the section becomes more important and the magnitude of the amplitude reflection coefficient increases. The peak in the magnitude of the amplitude reflection coefficient is 0.1308 at 0.55 GHz. This frequency 0.55 GHz corresponds to a layer thickness of 0.165±0.005 m, with the variation in thickness being due to the choice of relative real permittivity used in the equation above. From fitting a glacier flow model to measurements on the GRIP ice core the thickness of the annual cycles at this depth is 0.17±0.01 m (Wolff, pers com using model SS08). These values are very similar, showing that the electromagnetic waves are responding to layers which have an annual variation.

The low frequency peak in figure 4.14.a between 10^4 and 10^5 Hz will be discussed in §4.7.c.ii.

The phase angle of the amplitude reflection coefficient (figure 4.14.b) lies in the range $-\pi$ to $+\pi$. This means that it is only possible for the phase difference between the incident wave and reflected wave at the top of the stack to be in the range $-\pi$ to $+\pi$. As the frequency increases the phase difference becomes more negative between the incident and reflected waves and at certain frequencies the phase difference changes from $-\pi$ to $+\pi$. Though the difference between the incident and reflected waves is only slight the change looks dramatic when plotted on this limited range. In figure 4.14.c the unwrapped phase is shown. This means that the axis is not limited to the range $-\pi$ to $+\pi$ and the phase continues to become more negative as $-\pi$ is crossed. This makes it easier to see the trend in the results without the dramatic jumps from

$-\pi$ to $+\pi$ as the frequency increases.

4.7.c.ii Calculated using high frequency values

In this section the amplitude reflection coefficient is calculated again. However, this time the material in each layer is approximated by using the high frequency values ($\varepsilon'_{r\infty}$ and σ_{∞}) over the frequency range. The amplitude reflection coefficient at high frequencies is similar to that calculated using the dispersive properties. However, the low frequency magnitude of the amplitude reflection coefficient is a constant 0.0401 which becomes similar to the value calculated using dispersive properties as the frequency increases. The low frequency behaviour of the dispersive and high frequency results are compared in figure 4.15 below:

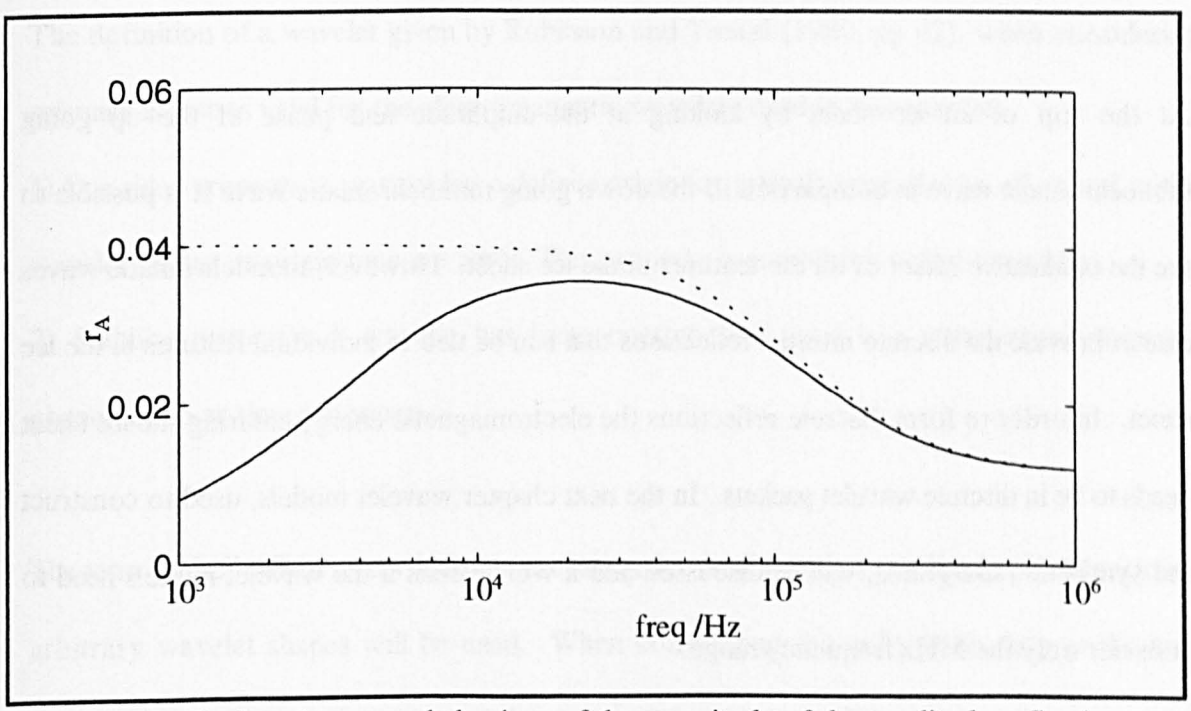

Figure 4.15 The low frequency behaviour of the magnitude of the amplitude reflection coefficient calculated using two different methods. The solid line has been calculated using dispersive material values (§ 4.7.c.i). The dotted line has been calculated using the high frequency values (§4.7.c.ii).

In figure 4.15 the values at 22 kHz differ by 10% and at 536 kHz differ by 1%. In the stack

of layers under consideration the AF-LF relaxation frequencies vary between 3.5 kHz and 13.4 kHz. In the dispersive material the relative real permittivity increases on the low frequency side of the AF-LF dispersion. This causes the magnitude of the amplitude reflection coefficient to decrease in a similar manner to that seen in section 4.5 figure 4.8.

4.8 Conclusion

In sections 4.5.e and 4.7.c the difference in the reflection coefficient calculated using dispersive or non-dispersive ice properties was shown to be less than 1% in the MHz range. In this thesis the radio echo sounding systems operate at MHz frequencies, so it would seem reasonable to use the high frequency values for the ice (σ_∞ and $\varepsilon'_{r\infty}$) in the modelling.

At the top of an ice sheet by looking at the amplitude and phase of the up going monochromatic wave in comparison to the down going monochromatic wave it is possible to see the cumulative effect of all the features in the ice sheet. However, monochromatic waves cannot provide the discrete internal reflections that can be tied to individual features in the ice sheet. In order to form discrete reflections the electromagnetic energy entering the ice sheet needs to be in discrete wavelet packets. In the next chapter wavelet models, used to construct the synthetic radargrams, will be discussed and it will be seen if the wavelet models need to consider only the MHz frequency range.

CHAPTER 5

PLANAR REFLECTION OF WAVELETS

In chapter four monochromatic waves were considered. In this chapter the plane parallel, electromagnetic waves are grouped into finite duration packets, which will be called wavelets. These wavelets are normally incident on a planarly layered medium.

5.1 Representation of the wavelet

5.1.a Time domain

The definition of a wavelet given by Robinson and Treitel (1980, pp 62), when considering seismics is just as valid for the electromagnetic wavelets used in this chapter.

1) One sided property: A wavelet has a definite origin (or arrival) time; that is, all values of the wavelet before its origin time are zero. This property is sometimes called causality.

2) Stability property: A wavelet has finite energy; that is, it is a transient or decaying phenomenon as time progresses.

The term "pulse" will be reserved for an excitation that is all positive amplitude. In this section arbitrary wavelet shapes will be used. When considering the radio echo data in the next chapter there will be a discussion on the shape of the transmitted wavelet.

I will not, during the course of this thesis, be using the mathematical theory of wavelet transforms or wavelet analysis which is a theory for describing wavelets that change in time and space, see for example Georgiou and Kumar (1994).

The wavelet is discretely sampled at intervals (Δt) and has a limited length. The number of samples on the time axis is N. The index for the samples is n where $1 \leq n \leq N$ so that the time (t) is given by: $t = (n - 1)\,\Delta t$. In this thesis when modelling time series of finite duration the number of samples (N) used will always be two raised to an integer power {*i.e*: $N = 32, 64, 128$ etc}. If necessary, zeros can be added to the sequence to ensure that this number of samples is reached. This is to allow the use of fast Fourier transforms (FFT), see appendix 2.

5.1.b The Nyquist sampling theorem

Consider a signal with a finite bandwidth where the frequency content beyond f_{Nyq} is zero. Then the signal can be uniquely determined by discrete samples if the sample spacing (Δt) used to sample the series is given by the equation:

$$\Delta t < \frac{1}{2 f_{Nyq}} \tag{5.1}$$

where

f_{Nyq} = The Nyquist frequency

If the sample spacing is greater than the value given above then the frequency content of the signal will be misrepresented, called aliasing. The Nyquist frequency is the highest frequency that can be represented in the data.

5.1.c Discrete Fourier transform (DFT)

The Fourier transform produces a frequency domain representation of the signal. As the time domain is discrete the frequency domain is also discrete. In this thesis the Fourier transform from time to frequency has a negative power in the exponential term. This is the form used by the MatLAB computer software. The discrete Fourier transform or analysis equation gives

a complex number $\tilde{F}(p)$ where p is the index for the frequency and ($1 \leq p \leq N$). There is no normalisation in the analysis equation:

$$\textit{Analysis equation} \qquad \tilde{F}(p) = \sum_{n=1}^{N} E(n) W_n^{(n-1)(p-1)} \tag{5.2}$$

where $W_n = e^{-\left(\frac{2\pi i}{N}\right)}$

In this thesis where the number of samples used (N) will always be two raised to an integer power. Therefore the Nyquist frequency is at index p = N/2+1 and the dc value (zero hertz) at p = 1. The other frequencies are related to p as shown in below:

$$\begin{array}{lccccc} p = & 2 & 3 & 4 & \ldots\ldots & \frac{N}{2}+1 \\ f = & \frac{2f_{Nyq}}{N} & 2\times\frac{2f_{Nyq}}{N} & 3\times\frac{2f_{Nyq}}{N} & \ldots\ldots & f_{Nyq} \end{array} \tag{5.3}$$

The DFT of a real series, where N is 2 raised to an integer power, has a symmetry property so that the values in the region from p = N/2+2 to N are the conjugate of the region p = N/2 to 2. The conjugate is represented by the symbol *. The values of the analytic function beyond p = N/2+1 are shown in equation 5.4 below:

$$\begin{array}{lccccc} p = & \frac{N}{2}+2 & \frac{N}{2}+3 & \frac{N}{2}+4 & \ldots\ldots & N \\ \tilde{F} = & \left(\tilde{F}_{p=\frac{N}{2}}\right)^* & \left(\tilde{F}_{p=\frac{N}{2}-1}\right)^* & \left(\tilde{F}_{p=\frac{N}{2}-2}\right)^* & \ldots\ldots & \left(\tilde{F}_{p=2}\right)^* \end{array} \tag{5.4}$$

The inverse discrete Fourier transform or synthesis equation transforms from the frequency domain back to the time domain.

$$\textit{Synthesis equation} \quad E(n) = \mathbb{R}\left(\frac{1}{N} \sum_{p=1}^{N} \tilde{F}(p) W_n^{-(n-1)(p-1)} \right) \tag{5.5}$$

An example of a single 30 MHz monocycle is shown in figure 5.1.

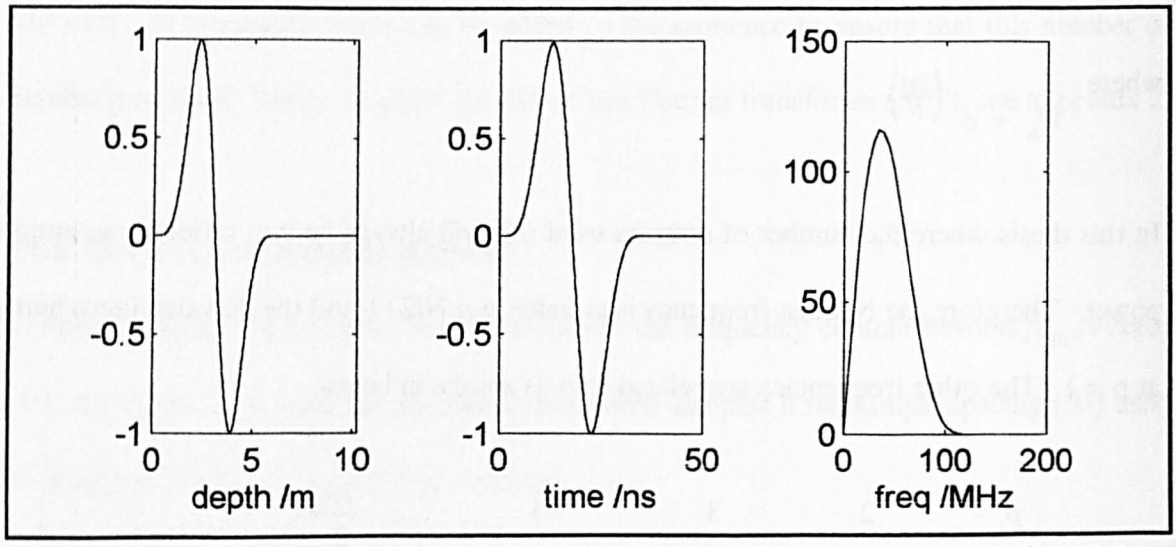

Figure 5.1 A 30 MHz monocycle in the space, time and frequency domains. Δt = 0.1 ns, 2048 samples, f_{Nyquist} = 5000 MHz.

If the wavelet has been described symmetrically in the time domain, with equivalent positive and negative amplitudes, then the dc (p = 1) frequency component (non-travelling component) in the wavelet has a value of zero. This will be the type of wavelet used in this thesis as it removes the difficulty of considering the reflection of the dc component.

5.2 The type of model

5.2.a A plane wave geometry

There are four reasons for choosing a plane wave geometry: Firstly, the exact radial distribution of radiation from the RES system is unknown. This prevents the development of the three dimensional model. However it is known that the bulk of the energy travels directly

downwards because the antenna has its major lobe pointing down. Secondly, the increasing density with depth (Rees and Donovan, 1992) causes the refraction of the waves to the vertical. Thirdly, any energy travelling out at large angles to the normal will be totally internally reflected at any strong permittivity contrasts it meets. These internal reflections will not direct the returning energy back to the antenna. Finally, if the permittivity is altering as a function of depth and the strength of the reflections is proportional to the gradient, then a wave travelling at an angle to the vertical will pass through gentler gradients in permittivity than a wave travelling vertically. This results in weaker off-vertical reflections. Other authors have used similar arguments to discount large angle reflections (Berry, 1975, pp 69).

There is also a close connection between how appropriate the plane wave model is and whether the internal reflections are isochrones. If it is necessary to consider a spherical model this implies the importance of reflections from non-normal angles. These reflections are off layers that are younger than the layer that would be contributing to the normal incident reflection. This is shown in figure 5.2 below.

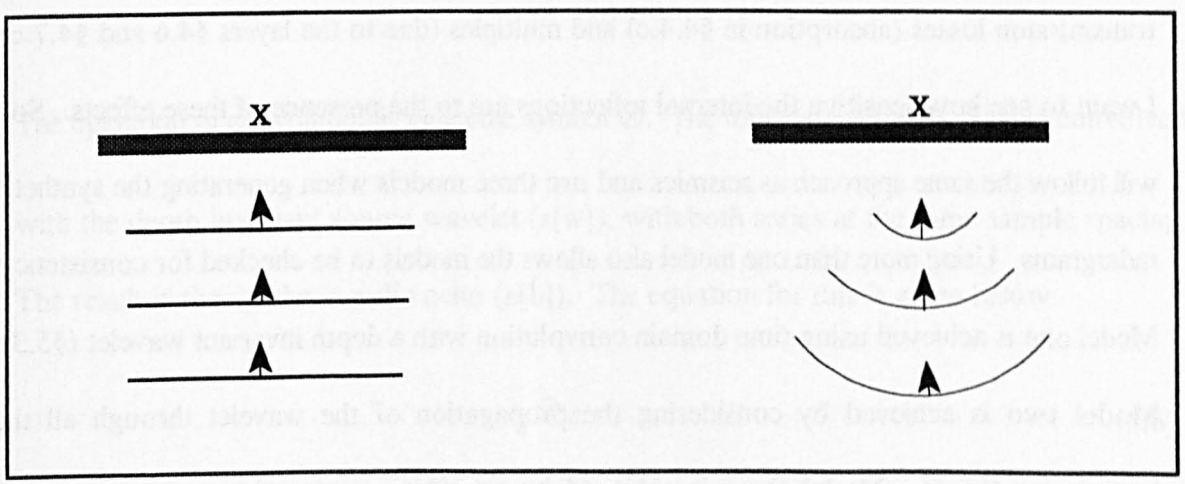

Figure 5.2 A comparison of the reflecting surfaces returning energy to an antenna at X in a plane wave model and a spherical model.

In order for the internal reflections to be isochrones the reflection at a given two-way travel time must be linked to a definite depth. This is not possible if the reflected energy arriving at

any instant has been reflected from a curved surface.

5.2.b The different models

In seismics it is traditional (O'Doherty and Anstey, 1971, pp 443) to produce three synthetic seismograms for a site. The first model considers only primary reflections without transmission losses. Transmission losses include the two effects of absorption and the decrease in amplitude on crossing each interface. The second model considers only primary reflections and includes transmission losses. The third model considers primary and multiple reflections and includes transmission losses. These three models give different results. The result of the first model is a series of clear reflections from each of the interfaces in the ground. The result from the second model has an appreciable decay in the received reflections as the two way travel time increases. In the third model the presence of the multiples counteracts some of the decay (this effect is described later on in §5.7.d).

The work done in chapter 4 with monochromatic waves has shown that in ice sheets there are transmission losses (absorption in §4.4.c) and multiples (due to the layers §4.6 and §4.7.c). I want to see how sensitive the internal reflections are to the presence of these effects. So I will follow the same approach as seismics and use three models when generating the synthetic radargrams. Using more than one model also allows the models to be checked for consistency. Model one is achieved using time domain convolution with a depth invariant wavelet (§5.3). Model two is achieved by considering the propagation of the wavelet through all the boundaries (§5.4). Model three is achieved by considering monochromatic waves in a frequency domain convolution (§5.5).

I will also be using a fourth model: depth dependent primaries and multiples with transmission

losses. This model will be calculated using the finite difference time domain technique (§5.6). This is the most common technique used for modelling ground penetrating radar (§1.8.f.ii). In this chapter the four models will be described, and at the end of the chapter the results given by each model on some small sections of core will be compared (§5.7).

5.3 Model one, primary reflections without losses

This model only calculates the primary reflections, energy returning straight to the surface from each interface in the ice. This is done by convolution. It is a useful model due to its simplicity and the speed with which it can be computed. However it is only an approximation to the processes that are going on inside the ice.

5.3.a Background

This section has some background information on convolution. The actual method followed in model one is explained in the subsequent sections.

The operation of convolution is given the symbol $\otimes$. The reflection series (r_A [a]) is convolved with the depth invariant source wavelet (s[w]), with both series at the same sample spacing. The result is the synthetic radio echo (e[b]). The equation for this is given below:

$$e = r_A \otimes s. \tag{5.6}$$

where

r_A = the reflection series, index $1 \le a \le A$
s = the source wavelet, index $1 \le w \le W$
e = the synthetic radio echo, index $1 \le b \le B$, where $B = A+W$

In the time domain the source wavelet can either be placed centred so that the middle of the

wavelet lies on each reflection coefficient; or placed offset, so that the start of the wavelet lies on each reflection coefficient. In the convolution done in this thesis the source is placed offset. This is explained in equation 5.7 below:

$$e[b] = \begin{cases} \sum_{i=1}^{b} r_A[b-i+1]\,s[i] & \text{if } b \le W \\ \sum_{i=1}^{W} r_A[b-i+1]\,s[i] & \text{if } (b>W)\wedge(b \le A) \\ \sum_{i=1}^{B-b+1} r_A[b+i-W]\,s[W-i+1] & \text{if } b>A \end{cases} \tag{5.7}$$

In convolution the wavelet does not change shape or attenuate as it propagates down to the interface. But it is allowed to undergo a phase change as it reflects at the interface. In a convolution algorithm such as described in equation 5.7 the phase change can be 0° or 180°.

In an ice sheet modelled as a stack of layers where the permittivity and conductivity are different in each layer it is necessary to model a wider range of possible phase changes. This was pointed out by Blindow when he considered the reflection at the meteoric-marine ice boundary in an ice shelf (Blindow, 1994). The algorithm that will be used to do this is described in section 5.3.c. However first it is necessary to ensure that the source wavelet and reflection series for the ground are at the same resolution. This is done by calculating the Goupillaud layered medium for the ice sheet.

5.3.b Goupillaud layered medium

This is a horizontally layered model for the ground that is common in seismic modelling (Goupillaud, 1961). It is necessary for the eventual convolution of the ground with a time

domain wavelet. The equally spaced measurements with depth ($1 \le m \le M$) are converted to a set of layers ($1 \le g \le G$) where the electromagnetic wave takes the same amount of time to cross each layer, i.e. the layers have a thickness inversely related to the velocity in the layer. These equally spaced measurements in time are necessary for the eventual convolution with a wavelet sampled at the same resolution. In this thesis the Goupillaud layers are calculated by the following method:

1) Calculate a non-dispersive interval velocity in each depth layer m:

$$v_{int} = \frac{c}{\sqrt{\varepsilon'_{r\infty}}} \tag{5.8}$$

where

c = speed of light, 3×10^8 m s^{-1}

2) Use the interval velocity in each layer to calculate the time to travel from the surface to the depth of each measurement and then back to the surface. This is the two-way travel time (t_{twtt}):

$$\begin{aligned} &for\ m = 1 \qquad t_{twtt}[m] = \frac{\Delta z}{v_{int\,m}} \\ &for\ m > 1 \qquad t_{twtt}[m] = \frac{\Delta z}{v_{int\,m}} + \sum_{r=1}^{m-1} \frac{2\Delta z}{v_{int\,r}} \end{aligned} \tag{5.9}$$

where

Δz = thickness of the layers

3) Resample the series $t_{twtt}[m]\ \varepsilon'_{r\infty}[m]$ using interpolation at the desired resolution $t_{twtt}[g]$. This time interval of the new series is chosen to be small enough so that each real data point is sampled at least once, typically < 0.1 ns for 10 mm measurements. This new series $t_{twtt}[g]\ \varepsilon'_{r\infty}[g]$ is the Goupillaud model of the ground. A similar interpolation is used on the series $t_{twtt}[m]\ \sigma_{\infty}[m]$. The final step is to sample the wavelet series at the same time step as the

Goupillaud series.

5.3.c Convolution

The wavelet entering the ground is modelled as a finite length series, of a length which is a power of two, with the same sample interval as the Goupillaud medium. This wavelet is converted into its analytic function (DFT) $\tilde{F}_w(p)$, and then only the frequencies in the range p = 2 to N/2+1 ($0 < f \leq f_{\text{Nyquist}}$) are retained.

Each interface in the Goupillaud medium is considered in turn. The Fresnel amplitude reflection coefficient r_{AF} is calculated at each frequency in the range p = 2 to N/2+1. As shown in chapter 4 (and discussed later in 5.3.d) the high frequency values ($\varepsilon'_{r\infty}$, σ_∞) can be used as approximations for the dispersive values (ε'_r , σ) in the calculation of the complex wavenumber in layer m at frequency p ($\tilde{k}_{mp}$). The formula for r_{AF} is equation 4.23.

The multiplication of the frequency spectrum of the wavelet $\tilde{F}_w(p)$ for $2 \leq p \leq N/2+1$ with the frequency spectrum of r_{AF} for $2 \leq p \leq N/2+1$ produces the frequency spectrum of the reflected wavelet for $2 \leq p \leq N/2+1$. The next step is to specify the rest of the p range. The dc value (p=1) is set to 0 and the frequency range beyond the Nyquist ($N/2+2 \leq p \leq N$) is set to the conjugate of the first half due to the symmetric properties of real functions (the measured *E* field is real) (see §5.1.c). This series is then inverse Fourier transformed and the resulting reflected wavelet is added to the record starting at the t_{twtt} of the interface. The same procedure is repeated for all the boundaries in the Goupillaud medium.

This model does not include absorption; absorption could be introduced by either multiplying the reflection profile by a decay function before convolution, or multiplying the result by a

decay function after the convolution. Neither of these options will be used as one of the aims is to compare a result from a model with no absorption with results from models that have absorption. Such a comparison will be done in section 5.7.

5.3.d The frequencies used in model one

The dc value (p = 1) is not required in model one, so that the lowest frequency used is p = 2 and depends on the sample interval and the duration of the incident wavelet. For the Berkner modelling in chapter 6 (§6.7.b) the sample interval used is the same sample interval as required for the FDTD model (§5.6.c.ii) 50 ps (f_{Nyq} = 10 GHz) and N of 2048 means that the frequency of p = 2 is 9.8 MHz (see eqn 5.3). For the GRIP modelling in chapter 7 (§7.7.c) the sample interval comes from the shortest two way travel time between the layers in the Goupillaud model of the ground 0.1695 ns (f_{Nyq} = 2.95 GHz) and N of 2048 means that the frequency of p = 2 is 2.9 MHz (see eqn 5.3). As the lowest frequency used by the model at both sites is in the MHz range then the use of $\varepsilon'_{r\infty}$ and σ_{∞} is justified following the arguments in section 4.8.

5.4 Model two, primary reflections with losses

This model calculates the primary reflections including absorption and transmission losses. This gives the wavelet the opportunity to change shape and be attenuated as it travels down to the interface. The reflection is treated as dispersive, with a unique reflection coefficient for each frequency. Then the wavelet can alter shape as it travels back to the surface. This model does not need the use of the Goupillaud medium.

5.4.a The propagation of the wavelet

The wavelet can be initially described as a function of time or depth. If time is used then the

temporal frequency components (f or ω) are considered; if depth is used then the spatial frequency components (k) are used. The dispersion relation transforms between the two relations: $k = k(\omega)$. In this thesis time will be considered. This will describe the wavelet at a later depth if given original shape in the time domain at an original position.

Many text books dealing with electromagnetic waves consider electric fields that are described in a continuous time domain (Ginzburg, 1960; Budden, 1985; Mickleson, 1992). These authors model the propagation of wavelets by using the slowly varying envelope approximation. In the approximation the analytic function (DFT) of the wavelet is considered to be sharply peaked and so it is only necessary to carry out the integration over a limited frequency range; this allows a Taylor expansion of the wavenumber function about the central frequency of the wavelet.

In this thesis the time domain is discrete so the method used is different. The wavelet is described in the time domain at the top of the ice with a sufficient number of zeros after the wavelet to allow the recording off all the expected reflections. As in model one it is only necessary to consider the frequencies $2 \le p \le N/2+1$.

Each depth layer in the stack of layers in the model is considered in turn. The analytic function at the base of depth layer s for the wavelet ($\tilde{F}_{wsp}$) can be expressed in terms of the analytic function of the wavelet at the surface ($\tilde{F}_{w0p}$):

$$\begin{aligned} \tilde{F}_{wsp} &= \tilde{F}_{w0p}\left(\prod_{m=1}^{s} e^{-i\Delta z \tilde{k}_{mp}} \right)\left(\prod_{m=1}^{s-1} \frac{2\tilde{k}_{mp}}{\tilde{k}_{mp} + \tilde{k}_{m+1p}} \right) \\ &= \tilde{F}_{w0p}\left(e^{-i\Delta z \sum_{m=1}^{s} \tilde{k}_{mp}} \right)\left(\prod_{m=1}^{s-1} \frac{2\tilde{k}_{mp}}{\tilde{k}_{mp} + \tilde{k}_{m+1p}} \right) \end{aligned} \qquad (5.10)$$

where

M = the depth index of the layer before the reflection

$\tilde{k}_{mp}$ = the complex wave number in layer m at frequency p

5.4.b The reflection of the wavelet

The reflection coefficient at the boundary between layer s and s+1 is calculated using a similar process to section 5.3.c. This is the Fresnel amplitude reflection coefficient, described previously in chapter 4 (eqn 4.23).

Finally equation 5.10 is used to propagate the frequency components back to the surface. At the surface the synthesis equation (eqn 5.5, or the inverse fast Fourier transform) is used to produce the time domain image of the reflected wavelet. The reflected wavelet is added in the time domain along with the other reflections.

Due to the operations in this model being commutative it is possible to apply the absorption in both directions and the transmission loss in both directions to the analytic function of the wavelet as the calculation proceeds down the ice core. Then it is only necessary to multiply by the reflection coefficient at each boundary prior to doing an inverse Fourier transform to obtain the reflected wavelet at the surface. This final time series has the reflection occurring at the correct time along the series. All the time series for each boundary are added together to give the final time series for the ice sheet.

5.4.c The frequencies used in model two

As in model one, the dc value (p = 1) is not required in model two, so that the lowest frequency used is p = 2. For the Berkner modelling in chapter 6 (§6.7.b) using a sample interval of 50 ps (f_{Nyq} = 10 GHz) and N of 32768 in order to cover all the reflections means that the frequency of p = 2 is 610 kHz and p = 3 is 1.2 MHz (see eqn 5.3). The p = 2

frequency is low enough that there will be an appreciable error in the reflection coefficient if it is calculated using $\varepsilon'_{r\infty}$ and σ_∞ (i.e. §4.7.c.ii). However, there are 160 frequencies considered between 1 MHz and 100 MHz, where the bulk of the energy in the monopulse lies (see figure 5.1). It is thought that the error introduced, in the position and strength of the Berkner wavelet reflections, by using $\varepsilon'_{r\infty}$ and σ_∞, will not be significant. Model two is not used on the GRIP core.

5.5 Model three, primaries and multiples with losses

In this algorithm the amplitude and phase changes to monochromatic waves are considered as the waves travel down and up through the ice sheet. This gives the amplitude reflection coefficient for the ice sheet at the surface. This is called the analytic function of the impulse response of the ice sheet. This analytic function is then multiplied in the frequency domain with the analytic function of the wavelet entering the ground. This gives the analytic response of the ice sheet, and then by using an inverse Fourier transform the time domain solution is obtained.

5.5.a Primaries and multiples in synthetic seismograms

In chapter one the background to synthetic seismograms was given using as an example the publication by Wuenschel (1960). He considered a unit impulse at the surface of the multi-layered half space, which was expressed in the frequency domain as a Laplace transform. For this impulse input he used matrices to determine all the reflections including multiples. Then the inverse transform brought the solution back into the time domain. For a wavelet source, the time response can be obtained by convolution and requires the assumption of a depth invariant wavelet.

A number of authors followed up this work: Robinson and Treitel (1977) introduced the z transform notation and the same notation was used by Choate (1982) to speed up the algorithm. Later the Laplace transform notation (s) was reintroduced in order to avoid confusion with the depth variable (z) (Robinson, 1985).

Trorey (1962) discussed how the frequency domain solution contains all the multiples that last for infinite time. Transforming this (using an inverse Fourier transform) into a finite time domain would cause problems and could introduce aliasing errors. A way round this was described by Nielsen (1978): assuming a periodic pulse going into the layer it was possible to use a discrete Fourier transform as long as the period of the transmission was much longer than the multiples that are of interest.

5.5.b Method

5.5.b.i Selection of frequencies

The radio echo trace that is going to be modelled is Fourier transformed. This gives an indication of the frequency content in the radio echo. The Nyquist frequency for the model is chosen so that it is greater than the highest frequency in the radio echo. This gives the range of frequencies to be considered: $0 < f \leq f_{\text{Nyquist}}$. The next selection is the number of frequencies that need to be considered. In order to calculate this the time step is calculated from the Nyquist frequency: $\Delta t = 1/(2 \times f_{Nyq})$. The number of time steps required to cover the duration of the incident wavelet and all of the recording and multiples is N. Usually N is chosen to be a power of two in order to allow the use of FFT. The number of frequencies that needs to be considered is $N/2$:

$$f = \frac{2f_{Nyq}}{N}, \frac{4f_{Nyq}}{N}, \frac{6f_{Nyq}}{N}, \ldots\ldots, f_{Nyq} \qquad (5.11)$$

5.5.b.ii Calculation

This algorithm will use the true thickness of the layers. This gives the option, as shown in chapter 4, of describing the amplitude of each frequency at the surface in terms of the propagation matrices (§4.7.b) or the impedance stack (§4.7.a). In this case the impedance stack will be used as it is quicker. The frequency domain solutions for the ice sheet are calculated at the surface, using the impedance stack model. This includes the absorption and all of the reflection and transmission effects at the interfaces. This produces the analytic function for the ice sheet for the frequencies $2f_{Nyq} / N$ to f_{Nyq} .

The wavelet entering is described in the time domain using the same sample interval (Δt) and number of samples N. The Fourier transform of the wavelet is calculated and the frequency components in the analytic function of the wavelet and the analytic function of the ground are multiplied together. This produces the analytic function of the ground response.

It is then necessary to define the other frequencies. The dc value is set to zero. The frequencies beyond the Nyquist are obtained using the symmetry properties of real series (the conjugate of the frequencies below the Nyquist as shown in eqn 5.3). The final stage is an inverse Fourier transform to the time domain. The final time domain record is that which would be seen at the top of the chosen stack of layers.

Some examples of the results from this model are shown in section 5.7.

5.5.c The frequencies used in model three

For Berkner the frequency range under consideration is similar to that used in model two

(§5.4.c). For the GRIP modelling in chapter 7 (§7.7.c) using a sample interval of 50 ps (f_{Nyq} = 10 GHz) and N of 1048576 (2^{20}) in order to cover all the reflections means that the frequency of p = 2 is 19 kHz and p = 3 is 38 kHz (see eqn 5.3). It is not until p = 54 that the MHz frequencies are reached. For all these low frequencies there will be an appreciable error in the reflection coefficient if it is calculated using $\varepsilon'_{r\infty}$ and σ_∞ (i.e. §4.7.c.ii). This will mean that there is an error in the low frequency values in the analytic impulse response of the ground. However, the long duration of the GRIP wavelet means that its analytic function is sharply peaked in the frequency domain (see figure 7.20.c) with no energy at these low frequencies. Therefore, after frequency domain multiplication of the analytic function of the wavelet and the analytic impulse response these low frequencies are excluded from the result. There will be no error introduced if $\varepsilon'_{r\infty}$ and σ_∞ are used to determine the analytic impulse response of the ground.

5.6 Model four, finite difference time domain

The finite difference time domain (FDTD) method is able to model the propagation equations by their conversion from continuum equations into discrete difference equations. The use of FDTD techniques for resolving electromagnetic problems was introduced by Yee (1966), and then later applied to the production of synthetic seismograms by Kelly et al. (1976). This method is now the most common way to model ground penetration radar, but is typically only used when considering the reflections from one subsurface boundary (Plumb, 1998). This is due to a lack of knowledge about the spatial variation in the properties of the ground. Typically a small target such as a landmine is considered in a homogeneous medium.

The advantage of the FDTD method is that it is not necessary to consider many frequencies.

However in the formulation given here it is only possible to specify a single, non-dispersive conductivity, permittivity and permeability at each point. This is in agreement with the earlier decision in chapter four that it was only necessary to consider the high frequency values. However, both the electric field ($\boldsymbol{E}$) and magnetic field ($\boldsymbol{H}$) are needed. In most FDTD applications the fields are defined in the space domain and the gradient is used to determine the change in the fields with time (Kunz and Luebbers, 1993).

5.6.a The equations

In this thesis the one dimensional formulation is used (Luebbers et al. 1990; Bergmann et al. 1996). Consider the case of a one dimensional plane wave propagating in the z direction $\boldsymbol{E} = E_x$ and $\boldsymbol{H} = H_y$. The two equations are considered in a discrete time domain $\{t = (n-1)\,\Delta t\}$ and a discrete space domain $\{ z = (m-1)\,\Delta z \}$.

The second order time and space approximation [O(2,2)].

Using the Maxwell equation derived from Faraday's Law of induction:

$$\frac{\partial \boldsymbol{B}}{\partial t} = -\nabla \times \boldsymbol{E}$$

$$\therefore \quad \frac{\partial H_y}{\partial t} = -\frac{1}{\mu}\frac{\partial E_x}{\partial z}$$

$$\therefore \quad \frac{H_{m+1/2}^{n+1/2} - H_{m+1/2}^{n-1/2}}{\Delta t} = -\frac{1}{\mu_{m+1/2}}\frac{E_{m+1}^{n} - E_{m}^{n}}{\Delta z} \tag{5.12}$$

$$\therefore \quad H_{m+1/2}^{n+1/2} = H_{m+1/2}^{n-1/2} - \frac{\Delta t}{\mu_{m+1/2}}\frac{E_{m+1}^{n} - E_{m}^{n}}{\Delta z}$$

where

$H_{m+1/2}^{n+1/2}$ = the magnetic field at time n+1/2 at position m+1/2
$\mu_{m+1/2}$ = the permeability at position m+1/2 (for ice equals μ_0)

Using the Maxwell equation derived from Ampere's law:

$$\frac{\partial \boldsymbol{D}}{\partial t} = (\nabla \times \boldsymbol{H}) - \boldsymbol{J}$$

$$\therefore \quad \frac{\partial E_x}{\partial t} = -\frac{1}{\varepsilon}\left(\frac{\partial H_y}{\partial z} + \sigma E_x\right)$$

$$\therefore \quad \frac{E_m^{n+1} - E_m^n}{\Delta t} = -\frac{1}{\varepsilon_m}\left(\frac{H_{m+1/2}^{n+1/2} - H_{m-1/2}^{n+1/2}}{\Delta z} + \sigma_m E_m^n\right) \tag{5.13}$$

$$\therefore \quad E_m^{n+1} = E_m^n - \frac{\Delta t}{\varepsilon_m}\left(\frac{H_{m+1/2}^{n+1/2} - H_{m-1/2}^{n+1/2}}{\Delta z} + \sigma_m E_m^n\right)$$

where

ε_m = real permittivity (non dispersive)
σ_m = conductivity (non dispersive)

The grid used for the time and space steps of the electric and magnetic fields is shown in figure 5.3. The m and n notation of the mathematics and the natural numbers p and q are used in the computer program.

	TIME n q			
D E P T H m p		E (m-2, n) E (p-2, q)		E (m-2 , n+1) E (p-2, q+1)
	H (m-3/2, n-1/2) H (p-2, q)		H (m-3/2, n+1/2) H (p-2 , q+1)	
		E (m-1, n) E (p-1 , q)		E (m-1, n+1) E (p-1 , q+1)
	H (m-1/2, n-1/2) H (p-1 , q)		H (m-1/2, n+1/2) H (p-1, q+1)	
		E (m, n) E (p. q)		E (m, n+1) E (p , q+1)
	H (m+1/2, n-1/2) H (p, q)		H (m+1/2, n+1/2) H (p, q+1)	
		E (m+1, n) E (p+1 , q)		E (m+1 , n+1) E (p+1 , q +1)
	H (m+3/2 , n-1/2) H (p+1, q)		H (m+3/2, n+1/2) H (p+1, q+1)	
		E (m+2, n) E (p+2, q)		E (m+2, n+1) E (p+2, q+1)

Figure 5.3 The FDTD grid used in the calculations

5.6.b Absorbing boundary conditions

If at the surface waves are only allowed to travel upwards, then this condition is given by the equation:

$$\left[\frac{\partial}{\partial z} - \frac{1}{v}\frac{\partial}{\partial t}\right]E(z,t) = 0 \qquad (5.14)$$

where

v = velocity, ideally a non-dispersive velocity, but as the ice is slightly dispersive the boundary conditions are not ideal.

This differential equation can be developed into a discrete equation to determine the electric field at the left hand boundary (Mur, 1981):

$$E_1^{n+1} = E_2^n + \left(\frac{v\Delta t - \Delta z}{v\Delta t + \Delta z}\right)\left(E_2^{n+1} - E_1^n\right) \qquad (5.15)$$

where

E_1^{n+1} = the first position value at the new time step.
E_1^n = the position zero value at the old time step.
E_2^n = the adjacent value at the old time step.
E_2^{n+1} = and the adjacent values at the new time step.

In a similar manner the condition for the bottom of the core can be obtained where only downwards propagation is allowed:

$$E_M^{n+1} = E_{M-1}^n + \left(\frac{-v\Delta t - \Delta z}{-v\Delta t + \Delta z}\right)\left(E_{M-1}^{n+1} - E_M^n\right) \qquad (5.16)$$

5.6.c Grid size

5.6.c.i Depth increment.

The depth increment is the sample spacing for the measurements on the ice core. The recommended sampling of EM waves is at least 5 gridpoints per minimum wavelength and preferably 20 gridpoints per wavelength (Bergmann et al. 1996). This gives an upper limit on the wavelengths that can be considered in the data, as shown in table 5.1. So for a 20 mm sample spacing (using the 20 grid point criterion) frequencies up to 550 MHz can be modelled. In section 5.7.c when modelling the reflection from a typical volcanic deposit in an ice sheet (a 200 mm high conductivity layer), it was found that using a 20 mm sampling interval caused problems with the FDTD algorithm. It was necessary to use a 5 mm sampling interval to get stable results. Therefore it appears that there is also a condition relating the number of gridpoints to the minimum wavelength in the ground data.

5.6.c.ii Time increment

The time increment is chosen using the Courant condition. The Courant condition ensures that the FDTD remains accurate, as each bit of information registers at each position and cannot skip a position:

$$C_R = \frac{v_{max}\Delta t}{\Delta z} \leq \frac{6}{7} \qquad \textit{which implies} \qquad \Delta t \leq \frac{6}{7}\frac{\Delta z}{v_{max}} \tag{5.17}$$

where

C_R = the Courant number

v_{max} = maximum possible speed in the ice = 2.2×10^8 m s^{-1}

Possible combinations are shown in table 5.1 below.

Table 5.1 Possible parameters for a finite difference model

Sampling Δz {mm}	Dispersion analysis (if using 20 grid point condition)		Stability analysis
	Minimum wavelength which can be accurately modelled {m}	Maximum frequency which can be accurately modelled {MHz}	Maximum possible time step {ps}
10	0.2	1100	38
15	0.3	733	58
20	0.4	550	78

To be safe smaller time steps are usually used in the modelling.

5.6.d Initial wavelet

For the FDTD method it is necessary to define the electric field ***E*** at a position in time and space. It is also necessary to define the magnetic field ***H*** at an offset of half a position in time and space. Once the ***E*** field is specified at a given position $E(z=z_0, n\Delta t)$ it is possible to calculate the ***H*** field, $H(z = z_0, n\Delta t)$ using $H = E/Z$ where Z is the impedance. This was done by Yee (1966), but the paper does not specify how to then obtain the necessary half index offsets for the H field.

In this thesis the wavelet will be defined in the space domain E_1 $(m\Delta z, t_0)$. It is then propagated a single time step forward using a constant velocity to give E_2 $(m\Delta z, t_0+\Delta t)$. The H field at the intermediate point H $(z = z_0 + \Delta z/2, (n+1/2)\Delta t)$ can then be defined by interpolating the intermediate electric field and then using the impedance (Z).

It is necessary to define the wavelet in the space above the ice sheet. For this thesis the top layer of the ice sheet will be extended out, with the same properties. The wavelet is defined

in this space. The recording point for the time signal is at the top of the ice sheet. Such a recording point will record the down going wavelet, then only start to record reflections once the down going wavelet has passed. The decay in the strength of the down going wavelet will be an important factor in how soon it is possible to identify the returning reflections. None of the other three models records the down going wavelet.

5.6.e Calculation time

The time taken to do the calculation is investigated using a 300 MHz monocycle wavelet (wavelength ~ 0.6 m). The models are run on a 200 MHz Pentium with $\Delta z = 0.02$ m and $\Delta t = 10$ps.

Table 5.2 Time taken for the FDTD algorithm

Distance in model /m	5.66	9.66	13.66	17.66	21.66
Time taken to do calculation	2 min 10 sec (130 sec)	7 min 3 sec (423 sec)	16 min 15 sec (975)	30 min 14 sec (1814 sec)	50 min 9 sec (3009 sec)

As the calculation times were becoming long, as the distance in the model increased, the program was altered from running in MatLAB on a 200 MHz Windows Pentium PC to using IDL on a 513 MHz UNIX Dec Alpha.

5.7 Comparison

In this section the four different models are compared mainly to test whether they all give the same result. The models are: Model 1 primary reflections only, no losses; Model 2 primary reflections only, with losses; Model 3 primary and multiple reflections, with losses (frequency domain); Model 4 primary and multiple reflections, with losses (FDTD).

In models one, two and three the result consists only of the reflections. There is no allowance for the transmission and recording of the down going wavelet. This needs to be remembered when using models one, two and three to look at the reflections from shallow features. For shallow features the decay in the strength of the transmitted wavelet becomes an important consideration.

In section 5.7.a.i the method will be explained while considering the reflection from a permittivity step. The ice sections to be considered are: firstly interfaces (5.7.a), secondly layers (5.7.b) and thirdly a twenty metre length of ice core (5.7.c). The wavelet used in these comparisons will be a 30 MHz monocycle with a wavelength of about 6 m (see figure 5.1).

5.7.a Reflection from steps

5.7.a.i Reflection from a permittivity step

In this section an ice core section is considered where the relative real permittivity steps from 2.5 to 3 while the conductivity is constant at 9 μS m^{-1}. The results from the different models are looked at in detail to explain the differences. First the FDTD model is used. The depth step (Δz) chosen is less than one twentieth of the smallest feature in the model, whether this is the wavelength of the incident wavelet or a layer in the ice. In this case $\Delta z = 0.1$ m. The Courant condition is then used to calculate that Δt needs to be 0.25 ns. For the initial

conditions the 30 MHz monocycle wavelet is described in the space domain, with the positive lobe deepest with maximum amplitude of 1. The wavelet then propagates down past a recording point A. It then propagates a further 10 m before striking the step. This 10 m ensures that the down going wavelet no longer registers at A when the reflected up going wavelet returns to A. In the figure 5.4 below is the time domain recording at A.

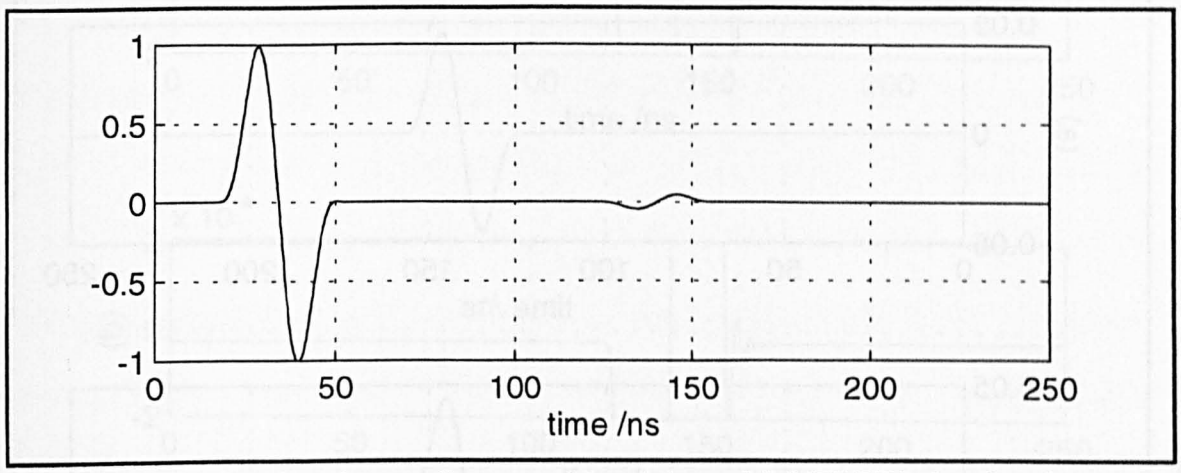

Figure 5.4 The time domain recording at position A in model 4 (FDTD) showing the passing of the down going wavelet and the return of the reflected wavelet.

From this time recording at A the down going wavelet is extracted to be used for models one, two and three. The extraction is done by putting a tapering window across the wavelet. This is shown in figure 5.5 below.

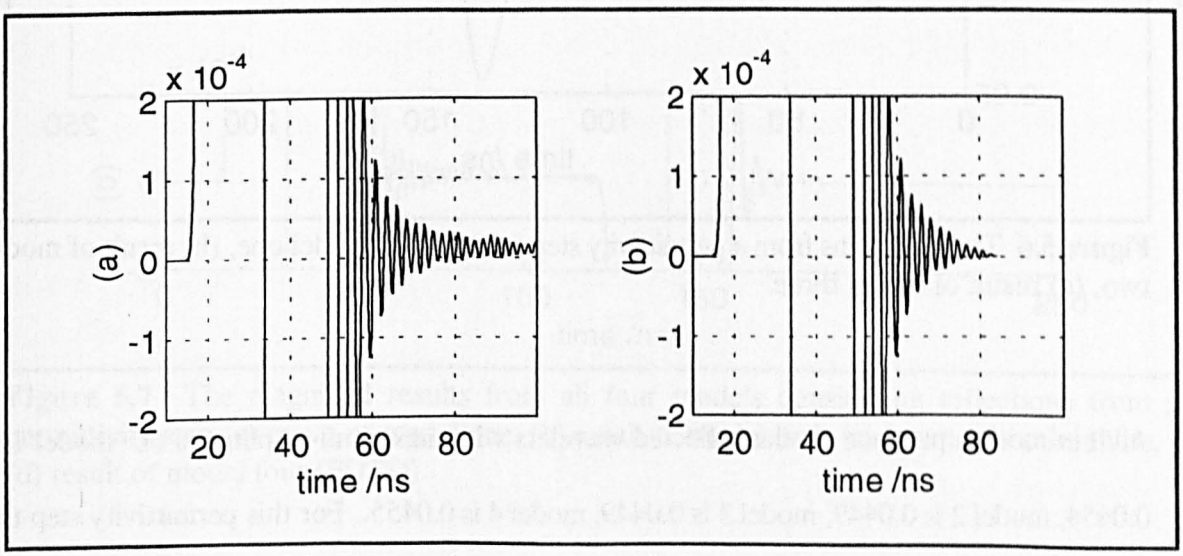

Figure 5.5 The end of the down going wavelet (a) before extraction, (b) after extraction and tapering.

For model one, convolution, the medium is converted into a Goupillaud medium using the same time step as the FDTD. For model three, frequency domain, the Nyquist frequency is determined from the time step in the FDTD. The results of models one, two and three are shown in figure 5.6 below.

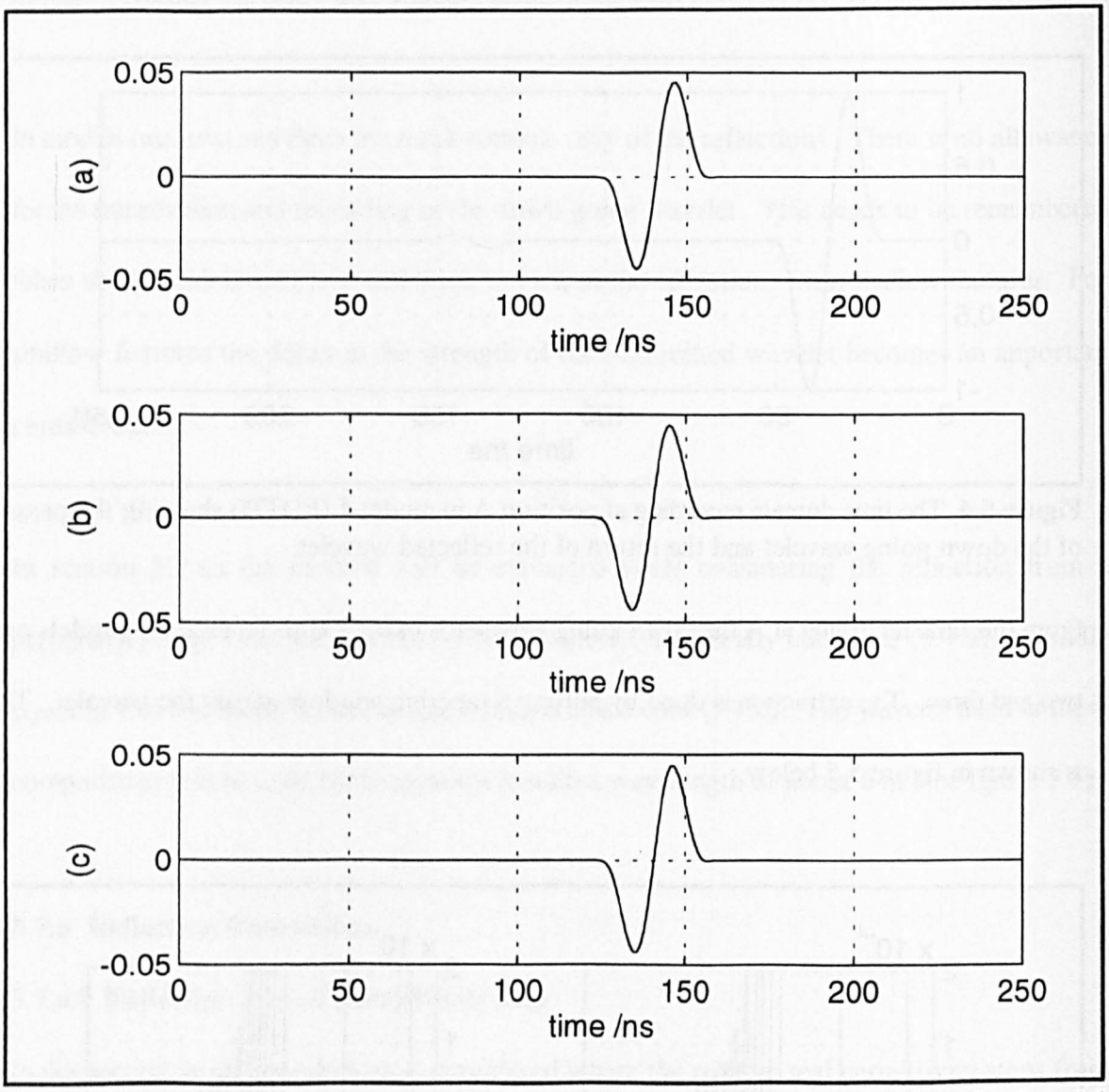

Figure 5.6 The reflections from a permittivity step (a) result of model one, (b) result of model two, (c) result of model three.

All four models produce similar reflected wavelets with maximum amplitudes of: model 1 is 0.0454, model 2 is 0.0449, model 3 is 0.0449, model 4 is 0.0455. For this permittivity step the amplitude reflection coefficient calculated for a 30 MHz monochromatic waves is 0.0455.

The differences between the model results are easier to see when the results are magnified. This is done in figure 5.7 below.

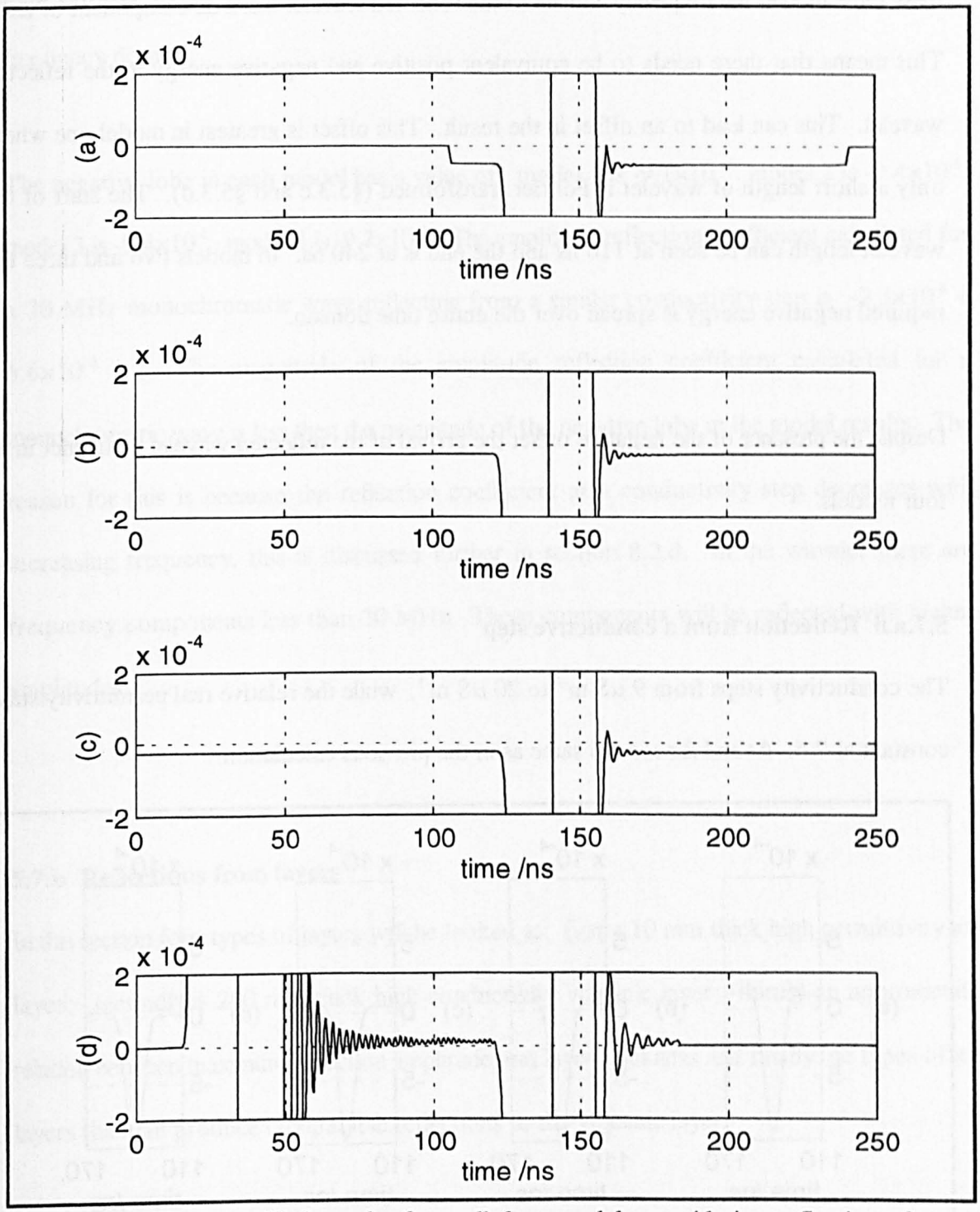

Figure 5.7 The magnified results from all four models considering reflections from a permittivity step (a) result of model one, (b) result of model two, (c) result of model three, (d) result of model four (FDTD).

In the above figure 5.7 the results from models one (a), two (b) and three (c) have slight offsets. The electric field before the arrival of the reflection is not zero. The reason is that in these three models the frequency domain of the reflected wavelet has a dc component of zero. This means that there needs to be equivalent positive and negative energy in the reflected wavelet. This can lead to an offset in the result. This offset is greatest in model one where only a short length of wavelet is Fourier transformed (§5.3.c and §5.3.d). The start of the wavelet length can be seen at 110 ns and the end is at 240 ns. In models two and three the required negative energy is spread over the entire time domain.

Despite the presence of the negative offset the arrival of the reflected wavelet is distinct in all four models.

5.7.a.ii Reflection from a conductive step

The conductivity steps from 9 μS m^{-1} to 20 μS m^{-1}, while the relative real permittivity stays constant at 2.5. Δt and Δz are the same as in the previous calculation.

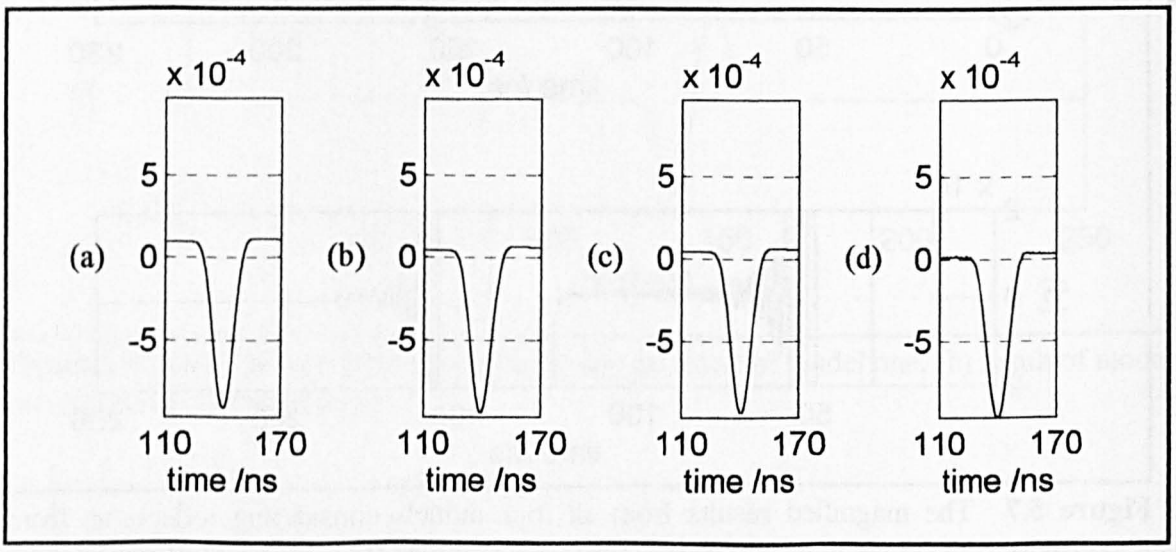

Figure 5.8 The amplitude recording at the top of the model, the model contains a single step in the conductivity, the down going monocycle wavelet had a maximum amplitude of 1. a) Model 1, b) Model 2, c) Model 3, d) Model 4.

In figure 5.8 the results of models one, two and three have a positive electric field recorded before the arrival of the negative lobe and then once the negative lobe has passed the electric field remains positive. This artifact is the result of having a dc component of zero in the frequency domain.

The negative lobe in each model has a value of: model 1 is -9.1×10^{-4}, model 2 is -9.4×10^{-4}, model 3 is -9.4×10^{-4}, model 4 is -9.7×10^{-4}. The amplitude reflection coefficient calculated for a 30 MHz monochromatic wave reflecting from a similar conductivity step is $-2.3\times10^{-6} + 6.6\times10^{-4}\ i$. The magnitude of the amplitude reflection coefficient calculated for a monochromatic wave is less then the magnitude of the negative lobe in the model results. The reason for this is because the reflection coefficient at a conductivity step decreases with increasing frequency, this is discussed further in section 8.2.d. In the wavelet there are frequency components less than 30 MHz. These components will be reflected with higher amplitudes.

5.7.b Reflections from layers

In this section four types of layers will be looked at: first a 10 mm thick high permittivity ice layer; secondly a 200 mm thick high conductivity volcanic layer; thirdly an approximate relation between maximum reflection amplitude and layer thickness and finally the types of ice layers that can produce comparable reflections to the volcanic layer.

5.7.b.i Primary reflection from a higher permittivity ice layer

The permittivity increases from 2.5 to 3 for a centimetre thick layer while the conductivity stays constant at 9 μS m^{-1}. The depth step is 1 mm, the time step is 2.5 ps.

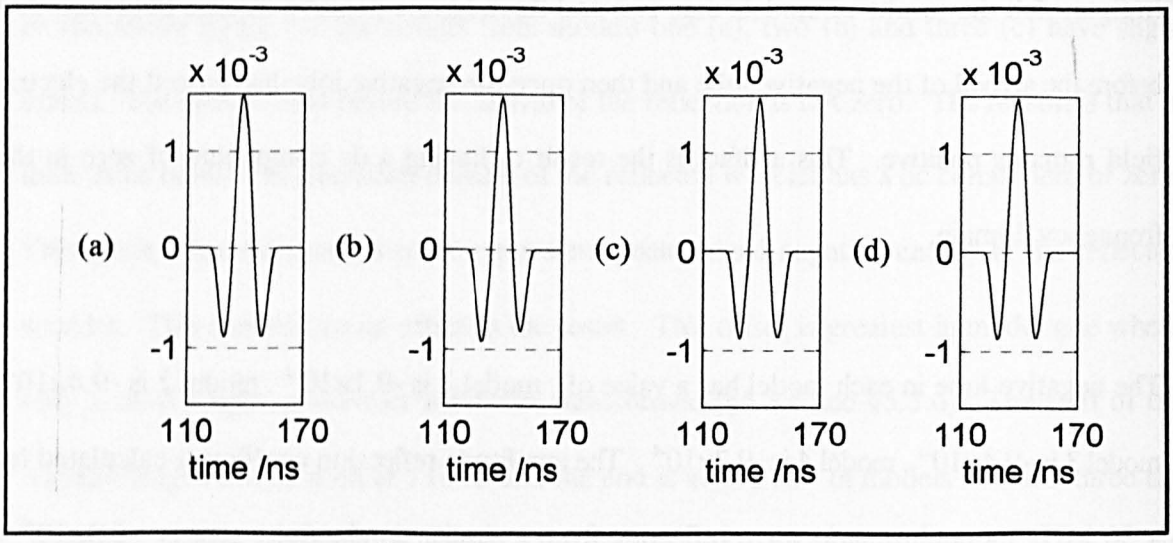

Figure 5.9 Amplitude recording at the top of the model, the model contains a single higher permittivity layer, the down going monocycle wavelet had a maximum amplitude of 1.
a) Model 1, b) Model 2, c) Model 3, d) Model 4.

5.7.b.ii Primary reflection from a higher conductivity volcanic layer

Volcanic layers are of great interest as they are easily identifiable depth surfaces inside an ice sheet that are isochrones. Consider a volcanic deposit, a layer in which the conductivity rises from 9 μS m^{-1} to 20 μS m^{-1} following a Gaussian shape with maximum width 200 mm. The high frequency real relative permittivity remains at 2.5, using a depth step of 5 mm and a time step of 12.5 ps.

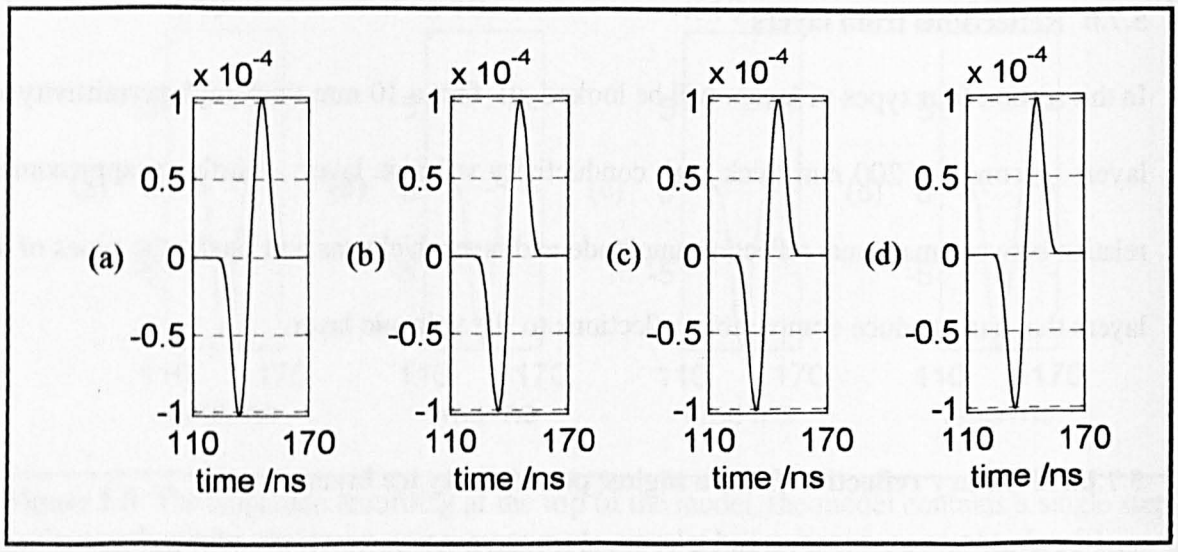

Figure 5.10 Amplitude recording at the top of the model, the model contains a single higher conductivity layer, the down going monocycle wavelet had a maximum amplitude of 1.
a) Model 1, b) Model 2, c) Model 3, d) Model 4.

5.7.b.iii Discussion, Widess's equation for thin layer reflections

Widess (1973) considered the reflection of seismic wavelets incident on thin layers in the ground. It is interesting to compare his result with the results obtained for electromagnetic wavelets incident on thin layers. Widess classified thin layers as those whose thickness was less than an eighth of a wavelength. So for a 30MHz wavelet with a wavelength of 6 m, this is 0.75m. In these cases a first order approximation for the maximum amplitude in the reflected wavelet is:

$$\frac{A_b}{A} \approx \frac{4\pi b}{\lambda_b} \tag{5.18}$$

where

A_b = maximum amplitude of wavelet reflected from thin layer/bed.
A = maximum amplitude of wavelet reflected from a single interface.
b = thin layer/bed thickness.
λ_b = wavelength in the thin layer/bed.

Consider the reflection from the 1 cm ice layer at $\varepsilon'_{r\infty} = 3$. From the equation 5.18 the prediction is $A_b/A = 4\pi 0.01/6 = 0.02$. From the results of the model runs above, $A = 0.045$ (from 5.7.a.i), and $A_b = 0.0015$ (from 5.7.b.i) so the models give $A_b/A = 0.033$.

Consider the reflection from the 0.2 m layer at $\sigma_\infty = 20\ \mu S\ m^{-1}$. From the equation the prediction is $A_b/A = 4\pi 0.2/6 = 0.4$. From the results of the model runs above, $A = 9.4\times10^{-4}$ (from 5.7.a.ii) and $A_b = 1\times10^{-4}$ (from 5.7.b.ii), so the models give $A_b/A = 0.1$. If a smaller thickness is used, which may be more suitable considering the Gaussian profile of the conductivity in the ice, then the equation prediction will be smaller and closer to the model results.

Therefore Widess's first order approximation appears to be applicable in these cases. A similar equation in radio glaciology to consider the effect of thin layers is Paren's equation (§4.6.d). Though Paren's equation was introduced when considering monochromatic waves it converts to a similar form as Widess's equation. The conversion is accomplished by converting Paren's equation into amplitude instead of power and then using the small angle approximation: $\sin\theta \approx \theta$ for small θ.

5.7.b.iv Thin ice layers

Thin ice layers can generate reflections of comparable maximum amplitude to the previously considered volcanic layers (§5.7.b.ii). In this section the maximum amplitude of the primary reflection from a range of thin ice layers is calculated. This is done using model one which allows a reflection from the top and bottom surfaces of the layer.

The ice has a $\varepsilon'_{r\infty}$ of 2.5 and the higher permittivity layer has a permittivity of $\varepsilon'_{r\infty} + \Delta\varepsilon'_{r\infty}$, where $\Delta\varepsilon'_{r\infty}$ varies between 0.0025 and 0.0175. In terms of the density this would correspond to the density in the surrounding ice being 700 kg m^{-3} and then increasing in the range 701 kg m^{-3} to 707 kg m^{-3}. The thickness of the layer varies between 2 mm and 52 mm.

In figure 5.11 below is a mesh surface of the maximum amplitude of the reflected wavelet as a function of the thickness of the layer and the step size. This can be compared with the reflected wavelet from the volcanic layer (200 mm at 20 μS m^{-1}) which had a maximum amplitude of 1×10^{-4}.

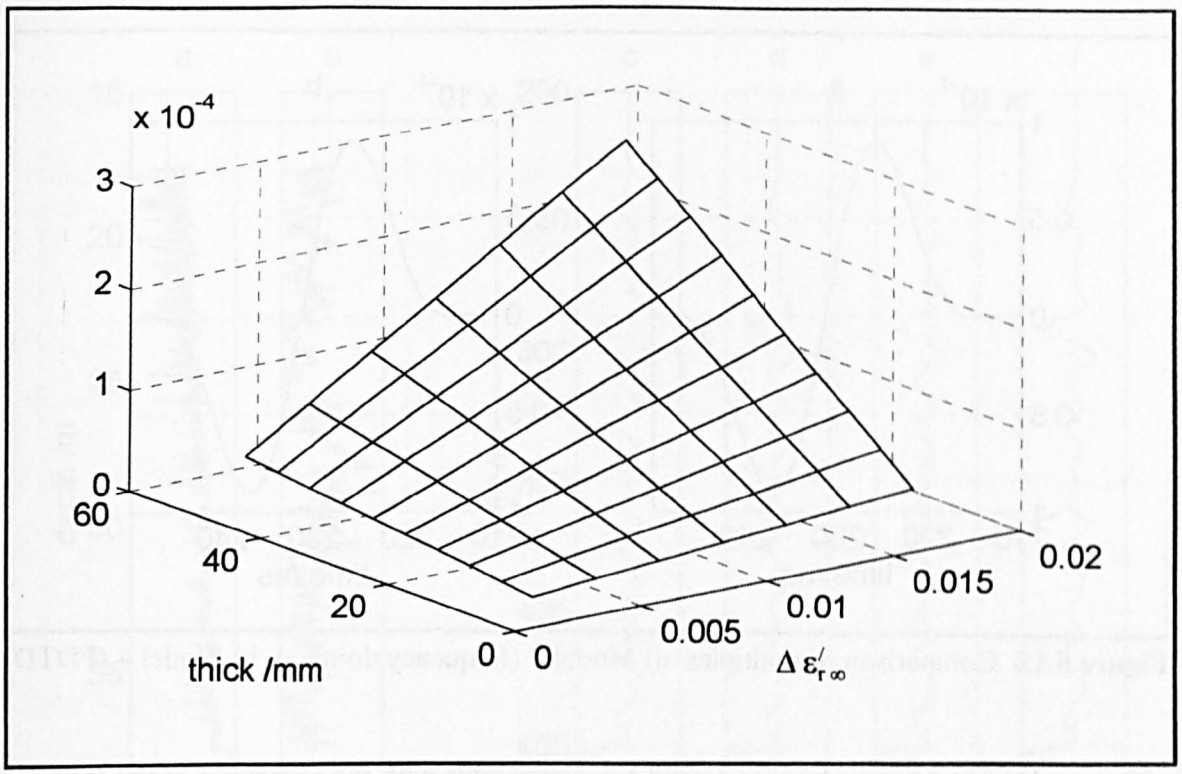

Figure 5.11 Maximum amplitude of a wavelet reflected from a range of small ice layers

It can be seen that it is only necessary for a variation in the density of the order 5 kg m^{-3} in 40 mm thick layers before the reflections generated are stronger than the reflections from a typical volcanic layer.

5.7.b.v Multiples from thick layers

Models 3 (frequency domain) and 4 (FDTD) are capable of modelling multiples caused by a wavelet striking a thick layer. In this section the multiples generated are compared. The layer has a thickness of 4 m, which is slightly longer than half the wavelength in order to separate the multiple from the primary reflection. The relative real permittivity rises from 2.5 to 3 in the layer. Δz =0.1 m, Δt = 12.5 ps.

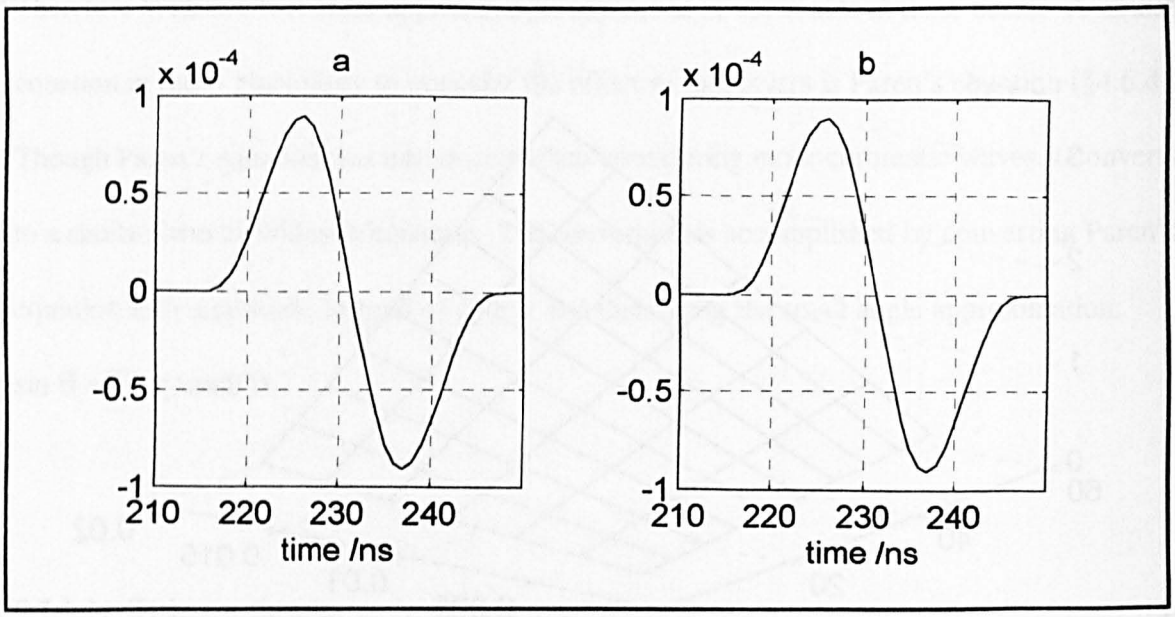

Figure 5.12 Comparison of multiples a) Model 3 (frequency domain), b) Model 4 (FDTD)

The amplitude of this multiple ($\sim 1\times10^{-4}$) is comparable with the amplitude of the reflection from the volcanic layer ($\sim 1\times10^{-4}$) studied earlier (§5.7.b.ii). However, layers that are this thick are unlikely to occur in an ice sheet.

Wuenschel (1960) argued that multiples may be even weaker than the value calculated here. Due to rough boundaries less energy is reflected normal to the boundary than shown in the above calculation. As multiples strike at least three boundaries, the effect is multiplied.

5.7.c Reflection from a varying medium

In this section the wavelet is put into a twenty metre section of the Berkner core, where $\varepsilon'_{r\infty}$ and σ_∞ change every 0.02 m. This piece of core is used to test the models on a larger data set than previously and also to show the existence of an unexpected effect: the O'Doherty-Anstey effect. An artificial boundary is put at the bottom of the section with the real permittivity increasing by 25% to 3.6. This section of ice core is shown in figure 5.13 below along with the model results.

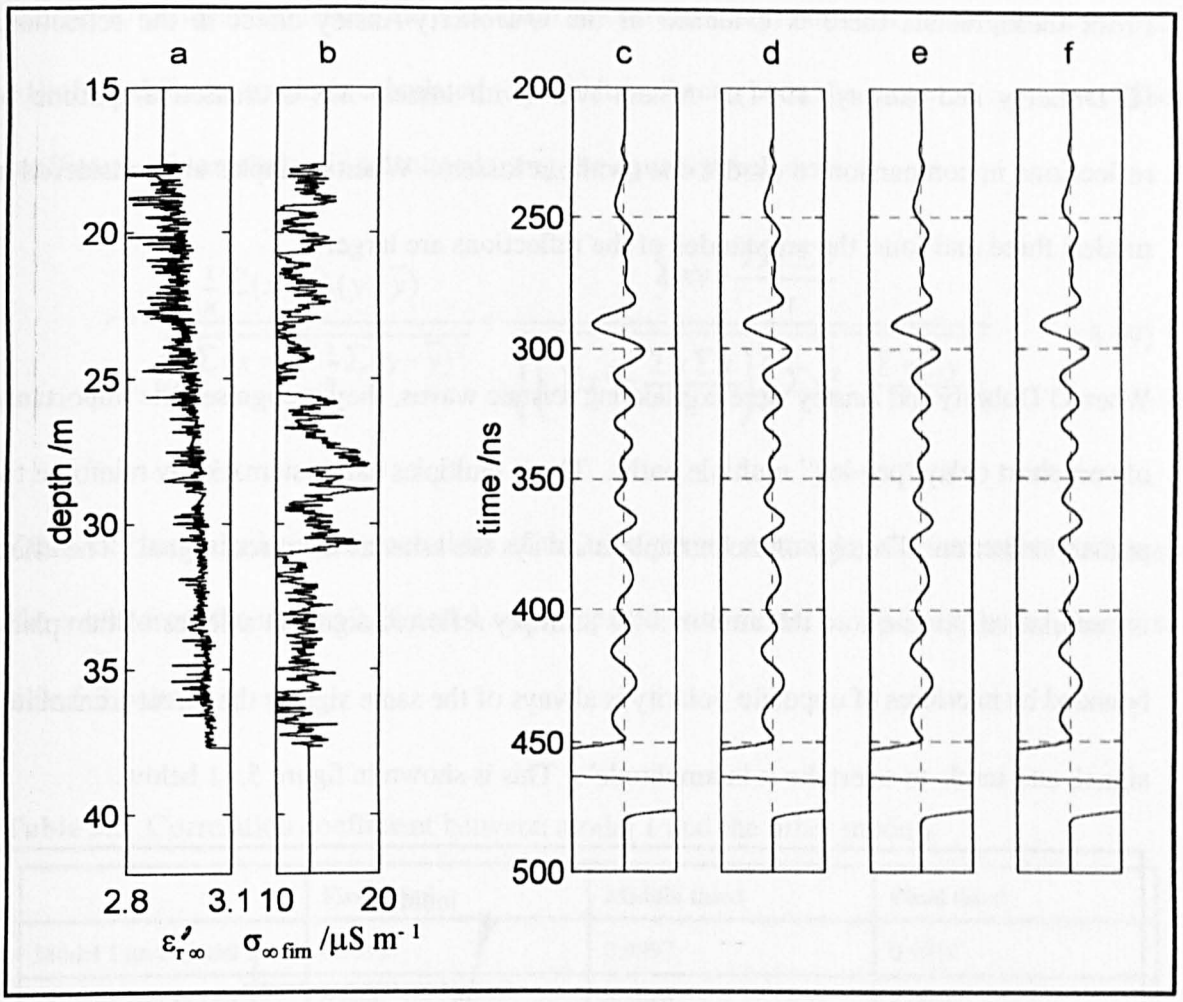

Figure 5.13 A short section of the Berkner core and the relative amplitude of the calculated reflections plotted in the range -0.01 to +0.01. a) relative real permittivity, b) conductivity, c) Model 1, d) Model 2, e) Model 3, f) Model 4.

The largest internal reflections generated all occur at the same time in the four models at a t_{twtt} of 291 ns. The amplitudes of the internal reflections are: Model 1: 0.00590, Model 2: 0.00547, Model 3: 0.00552, Model 4: 0.00550.

The reflections from the base of the section all arrive at the same time: 470 ns. The amplitudes of the base reflections are: Model 1: 0.04503, , Model 2: 0.04014, Model 3: 0.04052, Model 4: 0.04056. The absence of absorption in model 1, convolution, means that it produces the strongest reflections.

From these results there is evidence of the O'Doherty-Anstey effect in the reflections (O'Doherty and Anstey, 1971). Model two (with losses) has decreased amplitude of reflections in comparison to model one (without losses). When multiples are considered in models three and four, the amplitudes of the reflections are larger.

When O'Doherty and Anstey were considering seismic waves, they recognised the importance of very short delay "peg-leg" multiple paths. These multiples can systematically reinforce the primary reflection. The sign of the multiple is always the same as the direct signal. The effect is cumulative, so to quote the authors: "A multiply reflected signal in a series of thin plates bounded by interfaces of opposite polarity is always of the same sign as the direct transmitted signal, and tends to overtake it in amplitude". This is shown in figure 5.11 below.

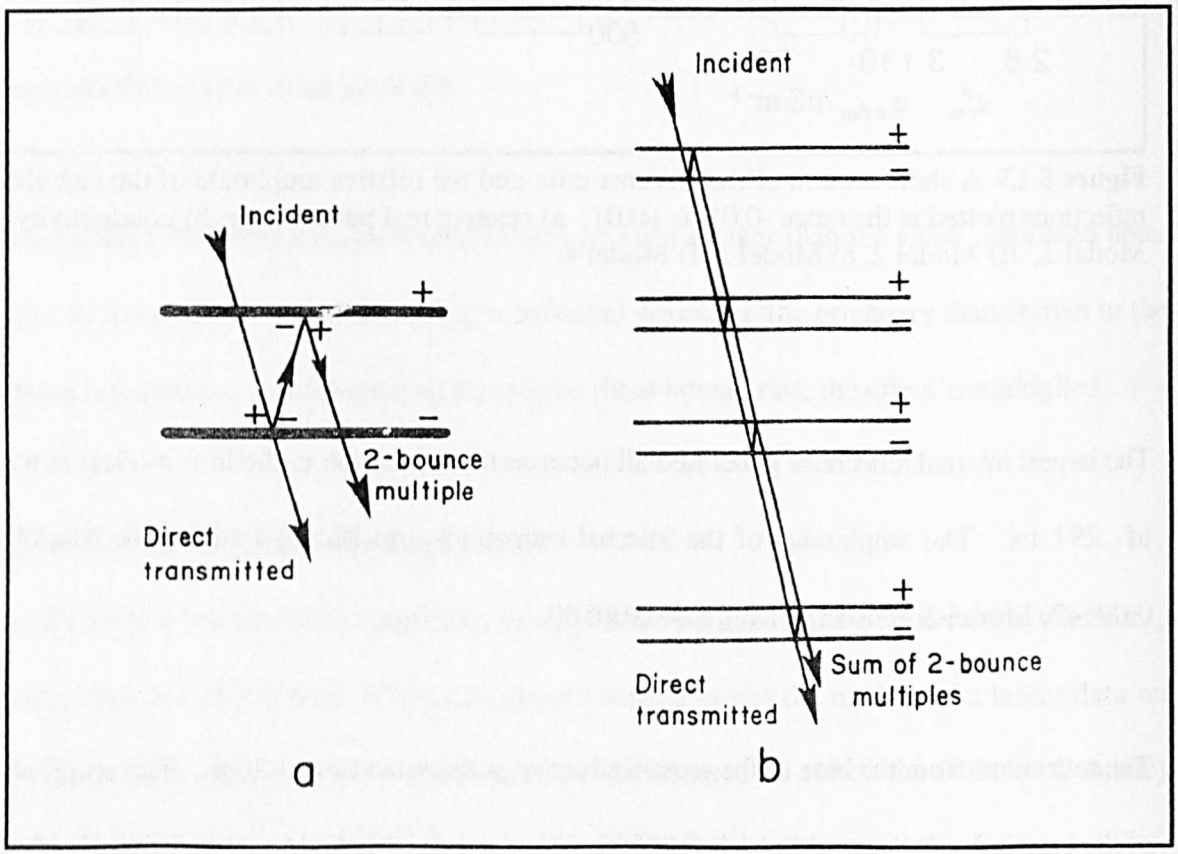

Figure 5.14 The O'Doherty Anstey effect (from O'Doherty and Anstey, 1971).

In order to compare the results the coefficient of correlation (r) between the amplitudes (-1 to +1) of the different results is calculated. The value of r can be in the range: $-1 \geq r \leq +1$. The coefficient of correlation is calculated using the equation below:

$$r = \frac{\frac{1}{n}\Sigma(x-\bar{x})(y-\bar{y})}{\sqrt{\frac{1}{n}\Sigma(x-\bar{x})^2 \frac{1}{n}\Sigma(y-\bar{y})^2}} = \frac{\Sigma xy - \frac{\Sigma x \Sigma y}{n}}{\sqrt{\left(\Sigma x^2 - \frac{\Sigma x \Sigma x}{n}\right)\left(\Sigma y^2 - \frac{\Sigma y \Sigma y}{n}\right)}} \qquad (5.19)$$

Values of r are calculated for each third of the time period containing the internal reflections. The results from the models 2, 3, and 4 are compared with model 1. The results are shown in table 5.3 below.

Table 5.3 Correlation coefficient between model 1 and the other models

	First third	**Middle third**	**Final third**
Model 1 and Model 2	0.9998	0.9997	0.9989
Model 1 and Model 3	0.998	0.9959	0.9935
Model 1 and Model 4	0.9991	0.9982	0.9967

The correlation between the results decreases slightly with increasing t_{twtt} but overall remains very high. This shows that the effects of transmission losses and multiples are small for a 20 m section of core. However, in the next two chapters, which consider the Berkner core and the 3000 m long GRIP core, the difference in the model results will become appreciable.

5.8 Conclusions

Four models have been described and tested on small sections of core. While transmission losses and multiples do cause some difference in the results, with evidence of a slight O'Doherty-Anstey effect when multiples are introduced, the difference in the results is small. At the moment a primaries-only model appears to be adequate for the modelling. In the next two chapters all four models will be tested on the Berkner and GRIP ice core data. This will allow a test of the importance of transmission losses and multiples on longer ice cores.

Using the models on the longer ice cores and comparing the results with the radio echo sounding will also test the suitability of the plane wave geometry being used in the models. As discussed at the start of the chapter (§5.2.a), showing that plane waves are adequate is additional evidence that internal reflections can be treated as isochrones.

CHAPTER 6

MODELLING THE BERKNER ISLAND RECORD

In this chapter the data acquired at Berkner Island will be described, followed by a description of the modelling done. The Berkner Island record is looked at before the GRIP record because it is shorter. The modelling has been done to see if the synthetic radargram matches the RES data. If they match well, then the present model (plane parallel wavelets and a stratified ice sheet) is sufficient to describe internal reflections seen when radio echo sounding.

6.1 Location

Berkner Island is an ice rise that lies between the Ronne and Filchner ice shelves. The outward flowing ice shelf has been parted by a submarine mountain. Onto this, snow has accumulated to form a long raised ridge. There are two peaks on the ridge, the northern one, called Reinwarthhöhe and the southern one Thyssenhöhe.

Table 6.1 Details for Berkner (from Mulvaney and Wolff, 1994)

Site	Location	Altitude* (metres)	Distance to nearest coast (km)	Accumulation (mm of water equivalent per year)
Reinwarthhöhe north dome	78°18' S 46°17' W	730	50	226
Thyssenhöhe. south dome	79°37' S 45°43' W	900	150	174

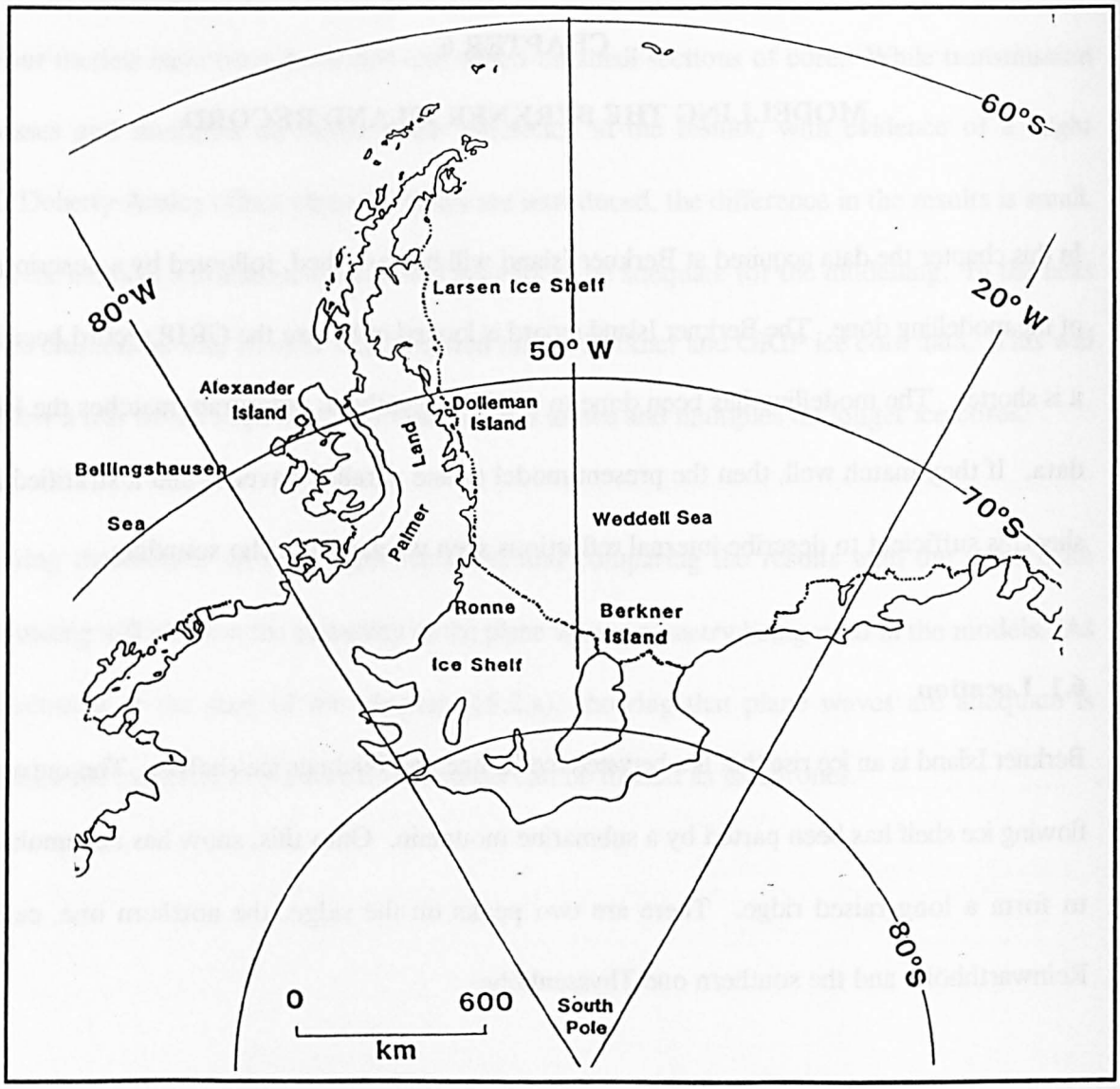

Figure 6.1 Location of Berkner Island (from Moore, 1988 a, pg 9).

During the 1994/1995 field season the British Antarctic Survey (BAS), Alfred Wegener Institute (AWI), Bremerhaven, Germany and Forschungsstelle Fur Physikalische Glaziologie (FPG), University of Munster, Germany cooperated on a project on Berkner Island. Many ice cores were drilled on Berkner (Mulvaney, 1995; Oerter, 1997). This thesis uses data from core B25, which was drilled at S 79°36.85' W 45° 43.46', 5 km to the south of the southern dome, during the period 30th January 1995 to 8th February 1995. The core was not drilled on the summit to leave the summit uncontaminated for a possible future deep drilling project.

6.2 The Radio Echo

The radio echo system used on Berkner belonged to the FPG and was operated by Daniel Steinhage (Steinhage and Blindow, 1995). The same apparatus had been used by Ludwig Hempel at GRIP a few years earlier (Hempel and Thyssen, 1992).

6.2.a The Radio Echo Equipment

The apparatus was mounted on three sledges which were towed behind a snowmobile. The first sledge carried the operator and the electronics, the second sledge the transmitting butterfly

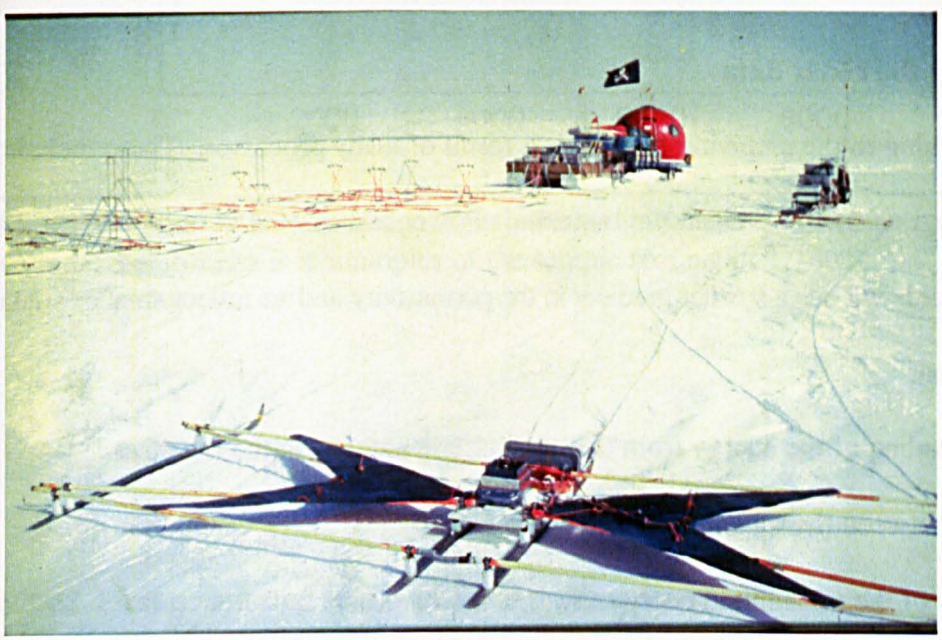

Figure 6.2 The antenna for the FPG mono pulse system in the foreground (photo K.Makinson).

antenna, and the third sledge the receiving butterfly antenna. When operated in a constant offset mode, the sledge could be towed along the ground at a speed of about 1 m s^{-1}. The system excites the antenna with a monocycle of the carrier wave, which was set at 30 MHz. The peak transmitted power is unknown.

6.2.b The raw data at the south dome

At the B25 drill site a series of radar traces were collected with the transmitting and receiving antenna either side of a common midpoint. The first trace was collected with the transmitter five metres to one side of the midpoint and the receiver five metres away from the midpoint on the other side. Then the next trace was collected with each antenna ten metres from the midpoint etc. The common midpoint was about 100 m from the borehole. The trace below is the raw record with an offset of 10 m between the transmitting and receiving antennas. The returning signal is recorded at a sample spacing of 1.7 ns (Nyquist frequency of 294 MHz) for 8192 samples. This gives the trace shown in figure 6.3 below.

6.2.c Processing the radar data

The energy returning to the receiving antenna is a result of many processes. These include:

1) The polar diagram of the transmitting antenna. Power transmitted at angles other than vertically downwards will see a smaller gradient in the permittivity and so reflect smaller signals back to the antenna.

2) Spherical spreading of the energy from the transmitting antenna in the ice sheet.

3) The distance between the transmitter and receiver

4) The refraction of the transmitted energy towards the vertical.

5) The variation in permittivity over small distances. A large variation in real permittivity near the surface will mean larger reflection coefficients and smaller transmission coefficients. At deeper depths the variation in permittivity is less.

6) Absorption, due to conductivity, causes loss of energy during the downgoing and upgoing propagation.

The models used in this thesis have a plane parallel wavelet propagating normally to a stratified

ice sheet. These models only consider the last two processes. A three dimensional model would be required along with the polar diagram of the antenna to model the other processes. Therefore the processing of the radar record is designed to transform the record into the form that would have been visible if the transmitter and receiver had been coincident, with the transmitter emitting a wavelet that was propagating normally to the medium.

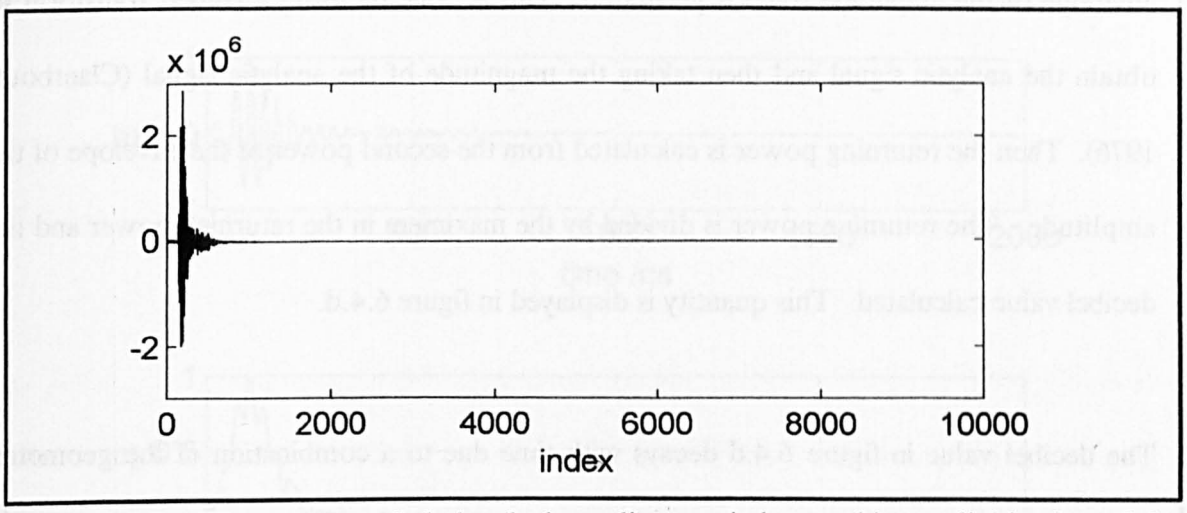

Figure 6.3 The raw recorded signal, the ordinate axis is an arbitrary digitisation of the voltage, the abscissa is in multiples of the sample spacing of 1.7 ns.

The first processing step is assigning a time scale.

6.2.c.i First processing step: Assigning a time scale

The first step in the processing is assigning a time scale to the returning signal. The recording before the arrival of the signal is used to determine the background noise level and variability in the receiver. The offset caused by the background noise is subtracted from the record. The first break (arrival of the signal) is assigned to the first sample where the gradient is three times steeper than any that have occurred in the first 100 samples. The sample immediately before this first break is given a time of 10 m divided by 3×10^8 m s^{-1}. Subsequent samples are given a time which is a multiple of 1.7 ns.

In the figure 6.4 below some of the steps in the processing are displayed. Firstly, figure 6.4.a shows the first part of the raw trace. Secondly, in figure 6.4.b the amplitude has been normalised using the maximum value recorded (the air wave) at the receiving antenna and the time scale has been put on excluding the initial zeros. The initial 300 ns of the signal recorded are thought to be the direct air wave from transmitter to receiver. Thirdly, in figure 6.4.c the envelope of the amplitude trace is generated. This is done by using a Hilbert transform to obtain the analytic signal and then taking the magnitude of the analytic signal (Claerbout, 1976). Then the returning power is calculated from the second power of the envelope of the amplitude. The returning power is divided by the maximum in the returning power and the decibel value calculated. This quantity is displayed in figure 6.4.d.

The decibel value in figure 6.4.d decays with time due to a combination of the geometric spreading, absorption and refraction. It will eventually level off as it approaches the noise floor of the system. This is the noise caused by thermal excitation of electrons in the antenna and receiver circuit. Such noise will drown out any weak reflections, so only strong reflections or the bedrock reflection are then visible. It is uncertain if this phenomena is visible in this portion of the trace starting at around 1500 ns.

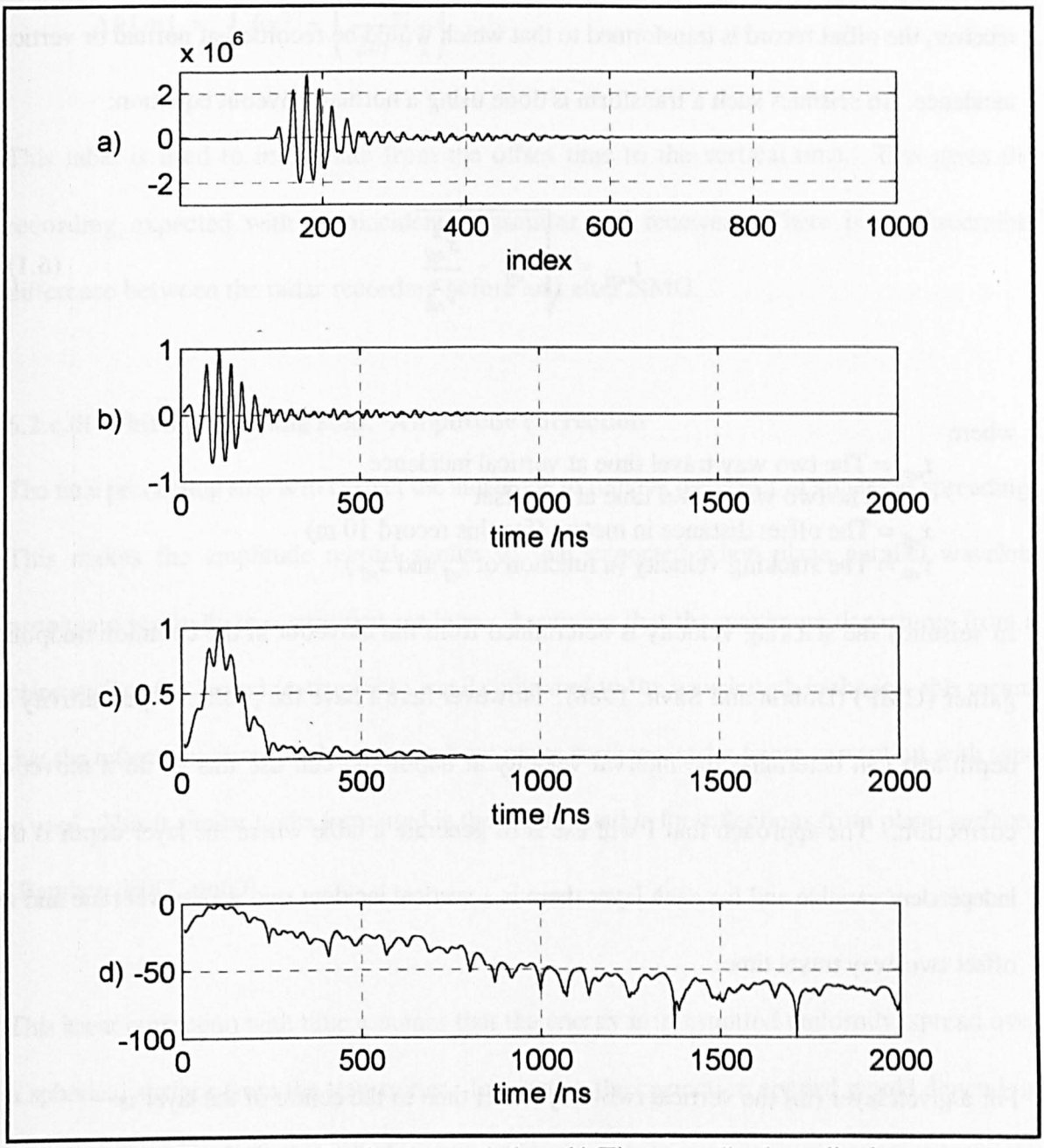

Figure 6.4 a) The raw amplitude trace vs index, b) The normalised amplitude trace vs t_{twtt}, c) The envelope of the amplitude trace vs t_{twtt}, d) The returning power divided by the maximum in the returned power, value given in decibels (dB) vs t_{twtt}.

6.2.c.ii Second processing step: Normal Moveout Correction (NMO)

The second stage in the processing of the radio echo record is transforming the time scale to that which would have occurred for normally incident waves (coincident transmitter and receiver). This is called normal moveout correction.

As the modelling assumes a vertically incident plane wave and coincident transmitter and receiver, the offset record is transformed to that which would be recorded at normal or vertical incidence. In seismics such a transform is done using a normal moveout equation:

$$t_{vert} = \sqrt{t_{off}^2 - \frac{x_{off}^2}{v_{stk}^2}} \tag{6.1}$$

where

t_{vert} = The two way travel time at vertical incidence
t_{off} = The two way travel time at an offset
x_{off} = The offset distance in metres (for this record 10 m)
v_{stk} = The stacking velocity (a function of t_{off} and x_{off})

In seismics the stacking velocity is determined from the moveout in the common midpoint gather (CMP) (Dobrin and Savit, 1988). However here I have the profile of permittivity at depth and can determine the interval velocity at depth and can use this to do a moveout correction. The approach that I will use is to generate a table where the layer depth is the independent variable and for each layer there is a vertical incident two way travel time and an offset two-way travel time.

For a given layer (m) the vertical two-way travel time to the centre of the layer is:

$$t_{vert}[m] = \left(2\sum_{r=1}^{m-1} \frac{\Delta z}{v_{int}[r]} \right) + \frac{\Delta z}{v_{int}[m]} \tag{6.2}$$

For a given layer (m) the offset two-way travel time is:

$$t_{off}[m] = \left(2\sum_{r=1}^{m-1} \frac{\Delta h[m]}{v_{int}[r]} \right) + \frac{\Delta h[m]}{v_{int}[m]} \tag{6.3}$$

where

$$\Delta h[m] = \sqrt{\Delta z^2 + \left(\frac{x_{off}}{2m-1}\right)^2}$$

This table is used to interpolate from the offset time to the vertical time. This gives the recording expected with a coincident transmitter and receiver. There is no discernible difference between the radar recording before and after NMO.

6.2.c.iii Third processing step: Amplitude correction

The final processing step is to correct the amplitude to remove the effect of spherical spreading. This makes the amplitude record similar to that expected when plane parallel wavelets propagate normally to a stratified medium. Assuming that the maximum departures from a plane surface (ie: buried sastrugi) are small compared to the wavelength in the ice, this means that the reflections are treated as coming from plane surfaces, and a linear correction with time is used. This is similar to the form used in the radar equation for reflections from plane surfaces (Bamber, 1987, pp60).

This linear correction with time assumes that the energy is transmitted uniformly, spread over a spherical surface from the transmitter. In practice the correction applied would depend on many things including: the radiation pattern for the antenna, the refraction that occurs with depth, the alteration in reflection coefficient with the angle of incidence, whether the electric field was perpendicular or parallel to the boundary.

6.2.d Examining the processed record

6.2.d.i The frequency content of the recording

The frequency content of the waves is affected by the transmission through the ice. Reflection off thin layers corresponds to a differentiation of the wavelet (Widess, 1973) and shown in §5.7.b.i. This differentiation corresponds to a multiplication by the frequency in the frequency domain, so that the power spectrum $|\tilde{F}(p)|$ in the frequency domain is increased at the higher frequencies. In figure 6.5 below, the power spectrum of the first 300 ns of received signal (the direct wave) is compared with the power spectrum at later times.

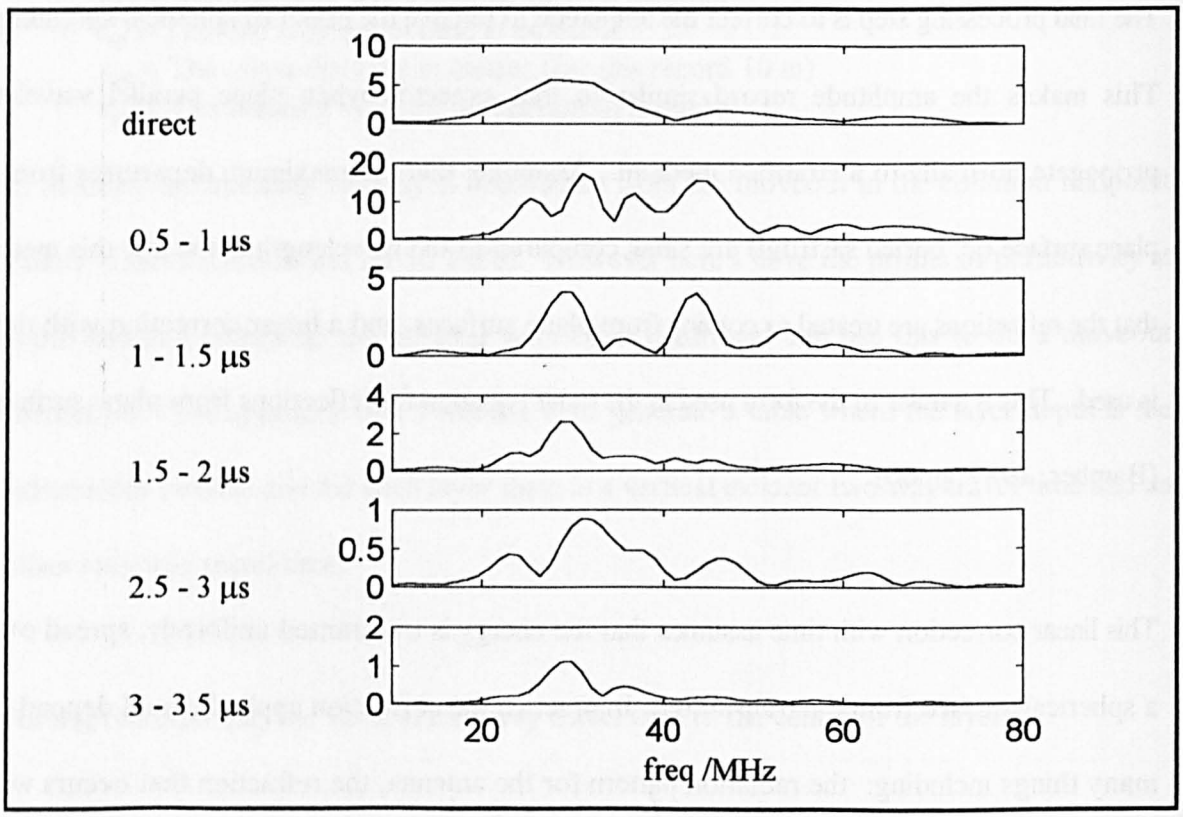

Figure 6.5 The changing power spectrum for different time windows in the radar recording

For the energy being reflected before 1500 ns there is a noticeable peak in the energy spectrum at 45 MHz. This peak may be due to reflection from thin layers. This peak is not visible after 1500 ns. Before using this observation to reach conclusions about the absence of signal below 1500 ns it would be necessary to look at the frequency spectra from other traces.

6.2.d.ii Results along traverse

A large quantity of data was collected along a traverse between the Northern dome Reinwarthhöhe and the southern one Thyssenhöhe. The traces were collected with a fixed offset between the transmitting antenna and the receiving antenna. One hundred soundings were collected per kilometre. In figure 6.6 below a portion of the processed data close to B25 are displayed. The processing has been a frequency filter, tenfold stacking and then automatic gain correction (AGC). This figure does not show the bedrock reflection.

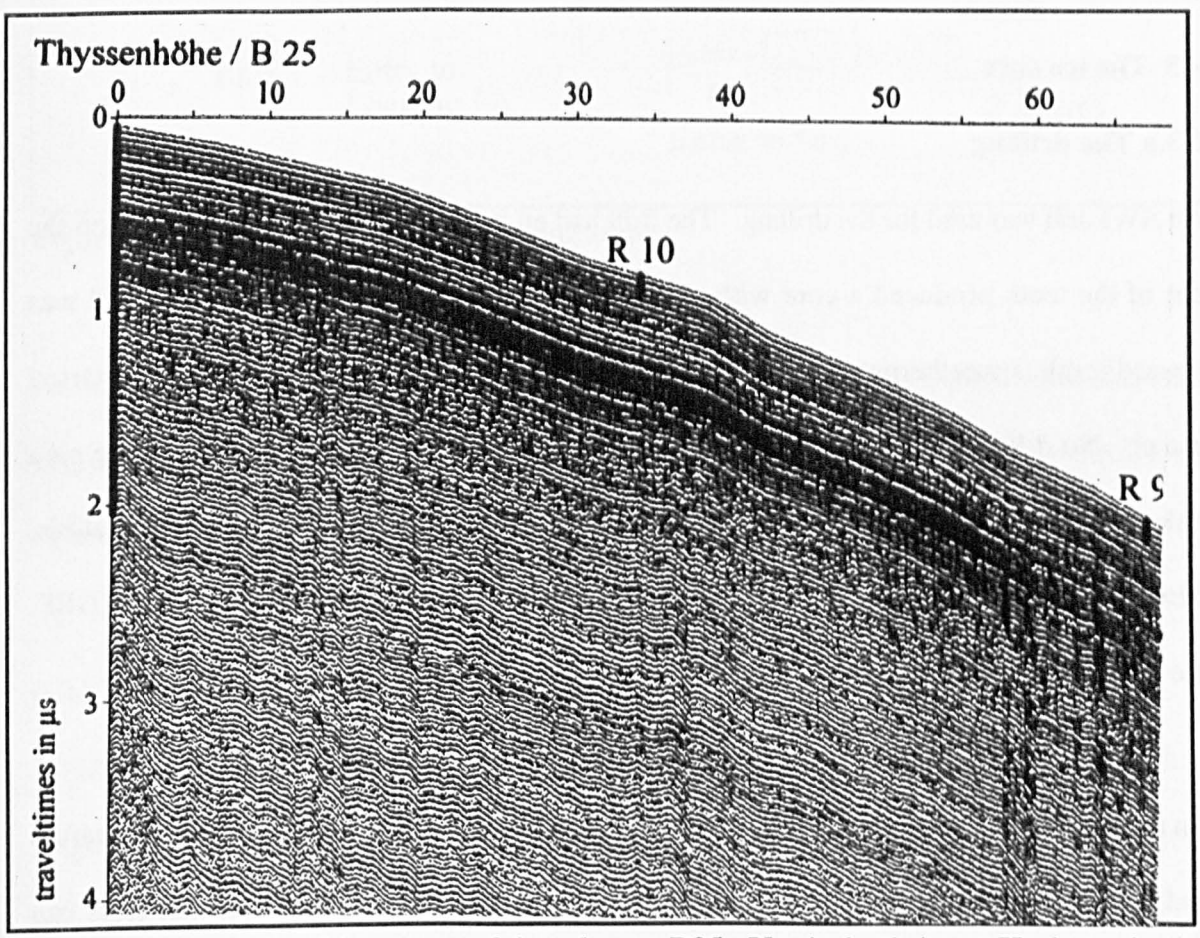

Figure 6.6 A portion of the processed data close to B25. Vertical axis in µs, Horizontal axis in km. (From Steinhage and Blindow, 1995)

In earlier discussion (§6.2.c.i and §6.2.d.i) there was evidence for a change in the quality of signal below 1500 ns. In this figure it is still possible to see continuous internal reflections to a t_{twtt} of 4000 ns. This may be a consequence of the stacking which can increase the signal to

noise ratio. However, stacking will not increase the signal to noise ratio when there is a logarithmic amplifier in the receiver circuit or when the phase of the reflections has not been recorded. This is discussed in the GRIP chapter.

From the radio echo the depth at the south dome is thought to be 950 m (Steinhage and Blindow, 1995).

6.3 The ice core

6.3.a The drilling

An AWI drill was used for the drilling. The drill had an internal diameter of 100 mm, then the cut of the teeth produced a core with an outside diameter of about 98 mm. This drill was housed inside a weatherproof shelter where the floor was dug out so that the drilling started in a pit. No drilling fluid or borehole casing was used during drilling. At the side of the pit a hole was cut through into an adjacent underground chamber where the electrical analysis, Electrical Conductivity Measurement (ECM, see appendix 3) and Dielectric Profiling (DEP, see appendix 4) of the ice core was done.

An underground chamber was used for the electrical analysis to protect the ice core, operators and equipment from the wind and sun. On the surface, with no clouds or wind, tents can become quite warm. Such temperatures would affect the cores, as explained in previous chapters.

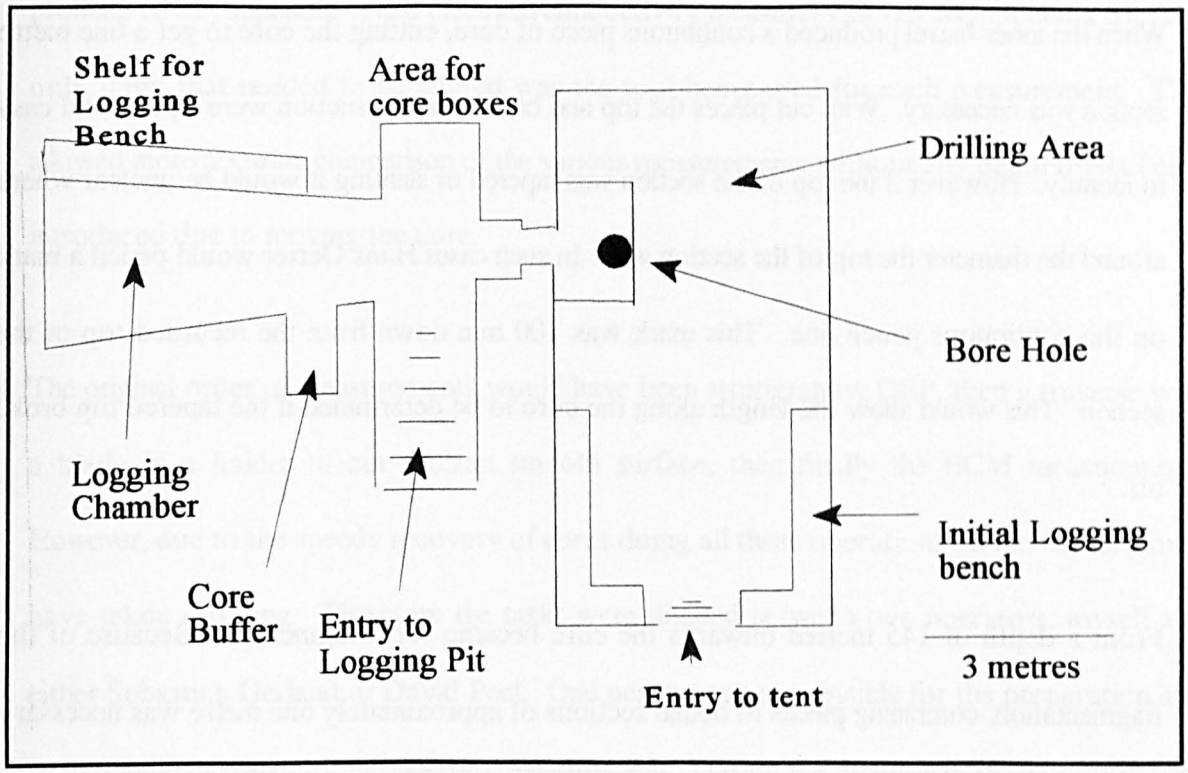

Figure 6.7 Plan of the drilling and logging area.

As there were two inner barrels for the AWI drill, one barrel could be emptied while the other was used for the next core. This meant that the operation was very fast, with 55 metres being drilled in the first day. The drilling was done by Michael Nolting and Christian Lukeit.

6.3.b Logging and bagging

Logging is the initial visual inspection of the ice core and the recording of variables such as length and weight. As the ice core was emptied from the inner barrel of the drill Hans Oerter added the contents to that already lying in a large metal cradle, rotating the top of the new core so that it tessellated with the bottom of the old core. He then marked a pencil line down one side of the core; this line was continuous from the top of the hole. At each metre along this line he put a pencil mark.

The core was then separated into roughly metre long sections. Each section went into one bag.

When the inner barrel produced a continuous piece of core, cutting the core to get a one metre section was necessary. With cut pieces the top and bottom of the section were square and easy to identify. However if the top of the section was tapered or slanting it would be unclear where around the diameter the top of the section was. In such cases Hans Oerter would pencil a mark on the continuous pencil line. This mark was 100 mm down from the recorded top of the section. This would allow the length along the core to be determined if the tapered top broke off.

From a depth of 145 metres onwards the core became very fragmented. Because of this fragmentation, combining pieces to obtain sections of approximately one metre was necessary.

Hans Oerter then weighed the metre long section, took a photo of it and put it into a bag. For the initial firn cores this bag was made of Mylar in order to better protect the more delicate cores. For the deeper sections the bag was made from a polyethene sleeve that was heat sealed at one end. Each bag was then passed through a hole in the wall between drill tent and analysis chamber and put in the core buffer which was a set of shelves cut in the wall of the analysis chamber. The cores spent at least twelve hours on these shelves before being analysed so that they were at the same temperature as the analysis chamber.

6.3.c Analysis

Inside the analysis chamber the core was measured on a bench that I built specially for the field season (Miners and Mulvaney, 1995; and appendix 6). The new bench had a motorised carriage to move the tools for each run across the top of the ice core. The intention of the new bench was to allow the measurement of the core to be done without moving the core between the three measurements: stratigraphy (identifying breaks, ice or hoar in the core), dielectric

profiling (DEP, appendix 4) and electrical conductivity measurement (ECM, appendix 3). The only thing that needed to be altered was the tool being used for each measurement. This allowed more accurate comparison of the various measurements without any depth offset being introduced due to moving the core.

The original order of measurements would have been stratigraphy, DEP, then a traverse with a blade in a holder to cut a clean smooth surface, then finally the ECM measurement. However, due to the speedy recovery of cores doing all these operations on the bench would have taken too long. Therefore the tasks were divided between two operators: myself and either Sebastian Gerland or David Peel. One person was responsible for the preparation and stratigraphy, the other for the electrical measurement. During the analysis both operators wore clean disposable polythene gloves when handling the cores but no other precautions were taken.

Table 6.2 Measurement progress

Date/ February	Bags measured during the day	Number of bags done in day	Comments
1	2 to 17	16	
2	18 to 35	18	
3	36 to 55	21	
4	56 to 74	19	
5	75 to 90	16	
6	91 to 104	14	
7		none	
8	105 to 125	21	
9	126 to 133	8	Change ECM tips and motor.
10	134 to 153	20	
11	154 to 176	29	Seven measurements done on 154, then for some of the other bags only ECM.
12	177 to 197	17	Not all bags logged.

At Berkner it took about 20 to 30 minutes to do all the measurements on each core. The need for speed in the analysis was not appreciated when designing the bench. In previous seasons where electrical measurements occurred there was no need for speed. Most of the Dolleman Island core was measured in the UK, without any time pressure, after an attempt to do the measurements in the field was abandoned. (For the location of Dolleman Island see figure 6.1). At GRIP the core was coming up from a much deeper depth so the core pieces arrived less frequently and there was more storage space.

In figure 6.8 below is a diagram of the components of the electrical bench (see appendix 6).

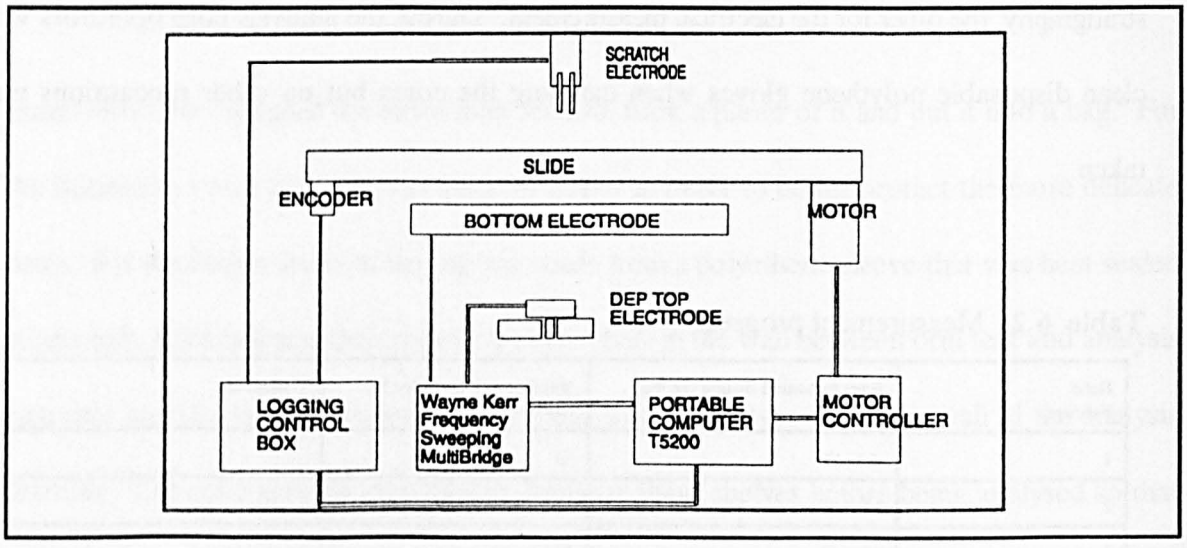

Figure 6.8 The components of the electrical bench

6.3.c.i Stratigraphy

First the core was collected from the core buffer and the name and top and bottom depth of the core were recorded in the stratigraphy book. The core was then removed from its bag and placed in a perspex cradle. A smooth side of the core was selected trying to avoid any core dog marks. The core dogs are three clamps, spaced around the diameter of the drill, that dig into the core to lift it out of the borehole. They cause a small hollow in the ice. The smooth

side was then shaved using the hand microtome knife to give a flat surface about 30 mm wide. Any loose snow was then brushed off. By doing the scraping before the core was put on the bench, time was saved and this also prevented the ice scraped off by the microtome from accumulating in the moving parts of the bench. The distance from the top of the ECM track to the pencil mark, 100 mm down from the official top of the bag, was measured. This was then used to calculate the depth at the top of the ECM track since this depth would be different to the official top of the bag when the end of the core was tapered or slanting. If necessary a small pencil mark was put at the point where the ECM run should start. The length of the ECM track was measured. Then the operator measured and recorded the depth of any hoar layers, crusts or breaks along the ECM track, and any places where there were significant hollows in the reverse side of the core, as the missing ice would affect the DEP value. The core was then transferred to lie on the bottom electrode of the electrical bench.

It should be noted that identification of features was difficult due to the dim light in the chamber. Some sunlight managed to penetrate through the roof and there were two light bulbs. As the logging proceeded along the core, examining deeper ice, the stratigraphic features became less distinct.

6.3.c.ii Electrical measurement

The bench operator then took over. The electrical bench was controlled by a portable computer, a Toshiba T5200/100 that had a 20 MHz Intel 80386 microprocessor and was running a Turbo Pascal program. This computer had a plasma orange screen; such a screen has previously been robust and legible at low temperatures. In figure 6.9 below is a photo of the bench in use.

ECM (see appendix 3).

The first operation was to use the ECM while the cut surface was still fresh. In this instrument the motor dragged the ECM tips along the surface at 40 mm s^{-1} towards the bottom of the core. It was often necessary for both operators to help hold the pieces of ice on the bottom electrode as the tips ran along the core. Usually two ECM runs were done for the first few runs in the morning or afternoon to check repeatability. Two ECM runs were also done if the

Figure 6.9 The electrical bench in use (photo by H.Oerter)

electrode tips lifted off the ice during the first run. Despite initial worries, the large metal electrode below the core did not affect the ECM measurement. The precision of the ECM current measurement was about ±1 μA.

After the ECM the ice core was rotated through 90° about its long axis so that the flat surface was to the side.

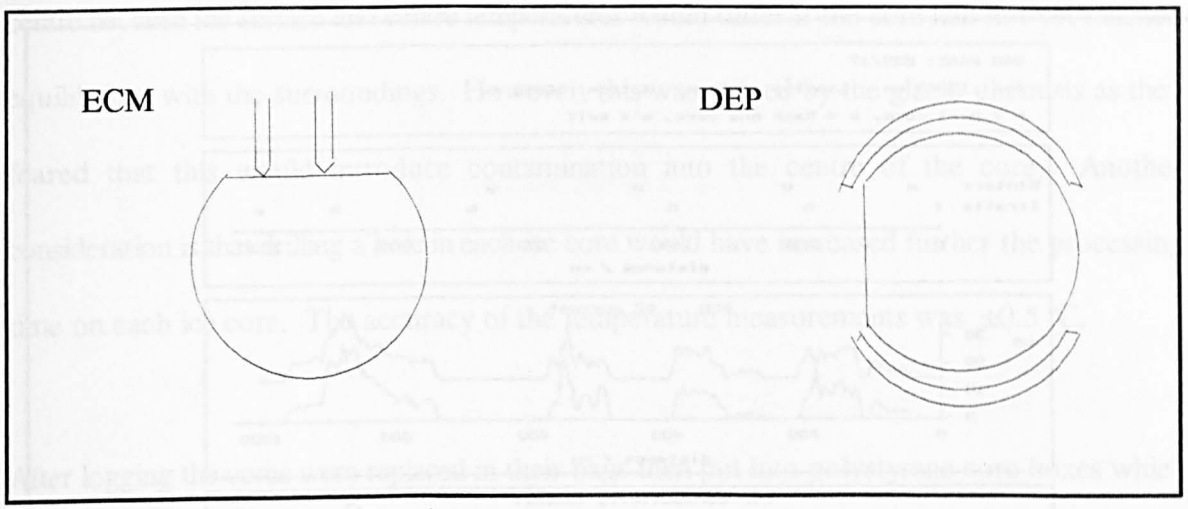

Figure 6.10 The rotation of the ice core

DEP (see appendix 4)

The DEP was used on this core with a 15 mm wide top electrode, sampling every 10 mm. The depth recorded with each measurement was that of the mid point of the electrode. The first measurement was made with the centre of the electrode on the edge of the top of the core, so that for the first and last measurements the entire width of the electrode was not overlying the ice core. The logging was done at only one frequency: 50 kHz. In a previous publication (Moore, 1993) it was concluded that the 50 kHz conductivity was a good approximation to the high frequency conductivity. Therefore, one frequency was used to speed up the profiling. The percentage precision of the conductivity measurement was 1% (see appendix 5).

However, the accuracy of the calculated 50 kHz conductivity of the ice is much less, probably ±15%, because the volume of ice removed to produce the flat surface for the ECM results in the introduction of a large quantity of air. With hindsight, the planing of the surface before the DEP was wrong. The order of operations should have been: stratigraphy, DEP, planing, then

ECM. In figure 6.11 below is an example record for one bag.

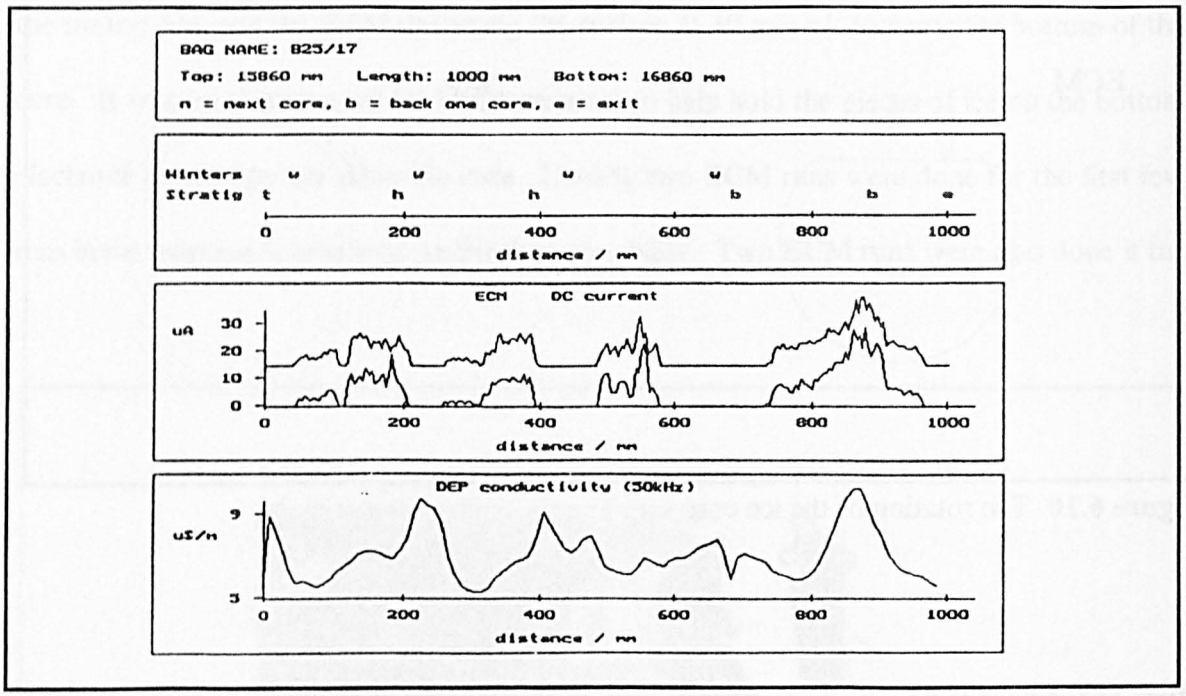

Figure 6.11 A logging record for one bag. Two ECM runs are displayed on the same axis with the second run displaced up the axis by 15 μA. For the stratigraphic record the features are: h = hoar, b = break, This record has been interpreted with the "w" showing where I thought that the winters occurred.

In the above bag the ECM is responding to the higher acidity ice in the summers. The DEP is mainly peaking in the winters in response to the higher concentrations of sea salt. The higher winter sea salt is discussed in section 2.8.a.

At the ends of the ice core the conductivity falls to zero. This is due to the presence of air between the electrodes. A similar effect occurs at any breaks in the bag.

As the conductivity of ice is sensitive to temperature, two temperatures were measured and recorded on the computer with the DEP measurements. The first was the air temperature in the chamber and was measured in the air 50 cm above the bench. During the season the temperature in the chamber varied between -11.9 and -18.0 °C. The second temperature was

measured using a pad sensor pressed up against the end of the ice. The original intention had been to drill a hole in the body of the core and insert a probe to measure the temperature in the centre because the surface and centre temperatures would differ if the core had not yet reached equilibrium with the surroundings. However, this was vetoed by the glacio-chemists as they feared that this would introduce contamination into the centre of the core. Another consideration is that drilling a hole in each ice core would have increased further the processing time on each ice core. The accuracy of the temperature measurements was ±0.5 °C.

After logging the cores were replaced in their bags then put into polystyrene core boxes which were stored underground before being loaded onto planes for the start of the journey back to AWI at Bremerhaven, Germany.

6.3.d Temperature

At the end of the season the temperature inside the borehole was measured by Mulvaney (1995). The method was to lower a cable to the bottom of the borehole. Attached to the cable at 5 m intervals were 10 thermistors which were left in place for two hours during which time the resistances were logged every 10 minutes. The accuracy for the final calculated temperatures is 0.2 °C (Mulvaney, pers com). The temperature profile can be seen in figure 6.13 in section 6.5.

6.3.e Density

At AWI the density of the cores was logged in the cold laboratory by Sebastian Gerland. The density was derived from measurements of the attenuation of a 2 mm diameter beam of gamma rays; the technique comes from Kimura (1983). The instrument used in this measurement was initially developed for the logging of soft sediment cores from shallow marine environments

(Gerland, 1993). The core was moved through the gamma ray beam by a stepping motor in increments of 3 mm. The density was determined from the attenuation using the equation below:

$$\rho = \frac{-1}{\mu d} \log_e \left(\frac{Intensity\ with\ ice}{Intensity\ without\ ice} \right) \qquad (6.4)$$

where

d = diameter of the core
μ = absorption coefficient of water.

The precision of the values used in this thesis is ±2% (Gerland et al. 1996) which is mainly controlled by the precision in the measurement of the diameter. Some ageing may have occurred to the core during transport but this should not have altered the density. It is unnecessary to consider any alterations to the density while the core was recovered from the borehole. The isobaric, isothermal and adiabatic coefficients of cubical expansivity of pure ice due to the removal of the pressure (Hobbs, 1974) are all small enough for the accuracy to be of a similar magnitude to the quoted precision.

There are minima in the density record that occur at any breaks in the ice core. These can be seen in the density record in figure 6.12 below.

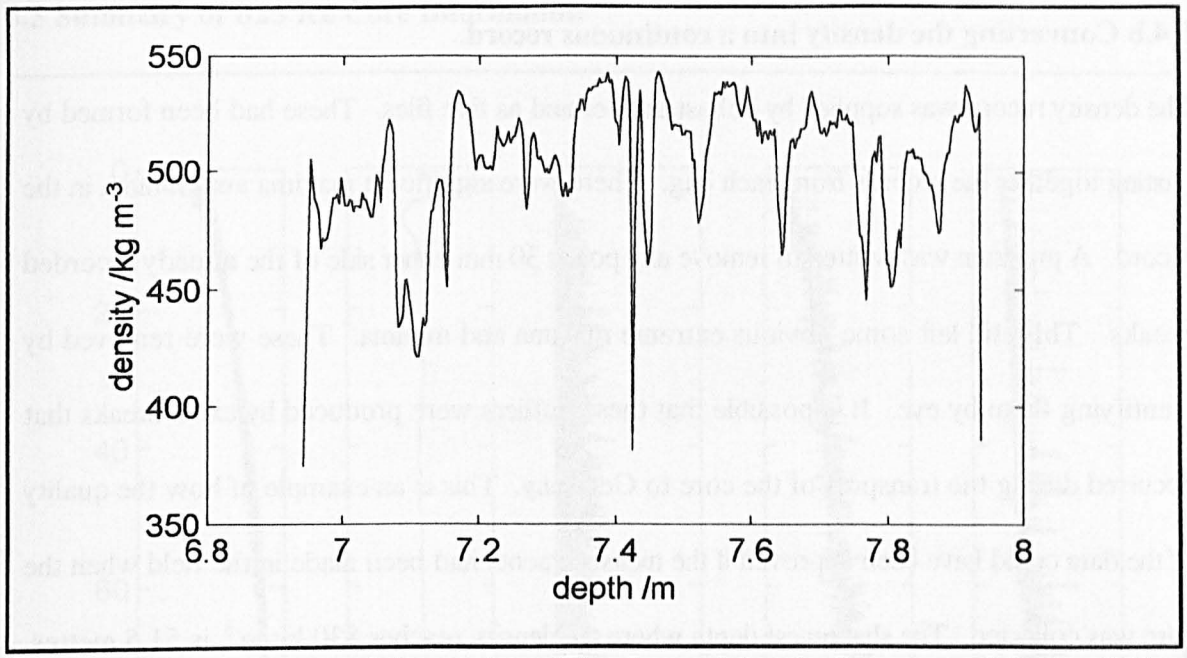

Figure 6.12 Density record for one bag. The sharp minima in the centre of the bag falling below a value of 400 kg m^{-3} is a break. The other smaller minima are due to hoar.

6.4 Forming continuous records

6.4.a Converting the DEP into a continuous record.

When the records from each bag were pasted together, it was necessary to resolve any conflicts that arose due to the slanting at either end of the cores. What occasionally occurred was that the logging from the top bag was long enough to overlap the start of the bottom bag. This occurred due to the introduction of air gaps at breaks. In such cases the values from the top bag are stopped and measurements from the bottom bag take priority. Another problem occurred at breaks in the record. By examining the conductivity values close to breaks the air in the break can be seen to affect the measurements about 30 mm to either side. I therefore removed these values from the record by using the recorded breaks observed during the stratigraphic logging in the field. The continuous record of the conductivity recorded in the field is shown in figure 6.13 below. The many steps observed in the conductivity record are due to alterations in the temperature in the logging chamber.

6.4.b Converting the density into a continuous record.

The density record was supplied by Sebastian Gerland as five files. These had been formed by pasting together the records from each bag. There were significant maxima and minima in the record. A program was written to remove any points 30 mm either side of the already recorded breaks. This still left some obvious extreme maxima and minima. These were removed by identifying them by eye. It is possible that these outliers were produced by extra breaks that occurred during the transport of the core to Germany. This is an example of how the quality of the data could have been improved if the measurements had been made in the field when the core was collected. The shallowest depth where the density reaches 830 kg m^{-3} is 51.5 metres. This can be considered as one indication of the depth of the firn to ice transition.

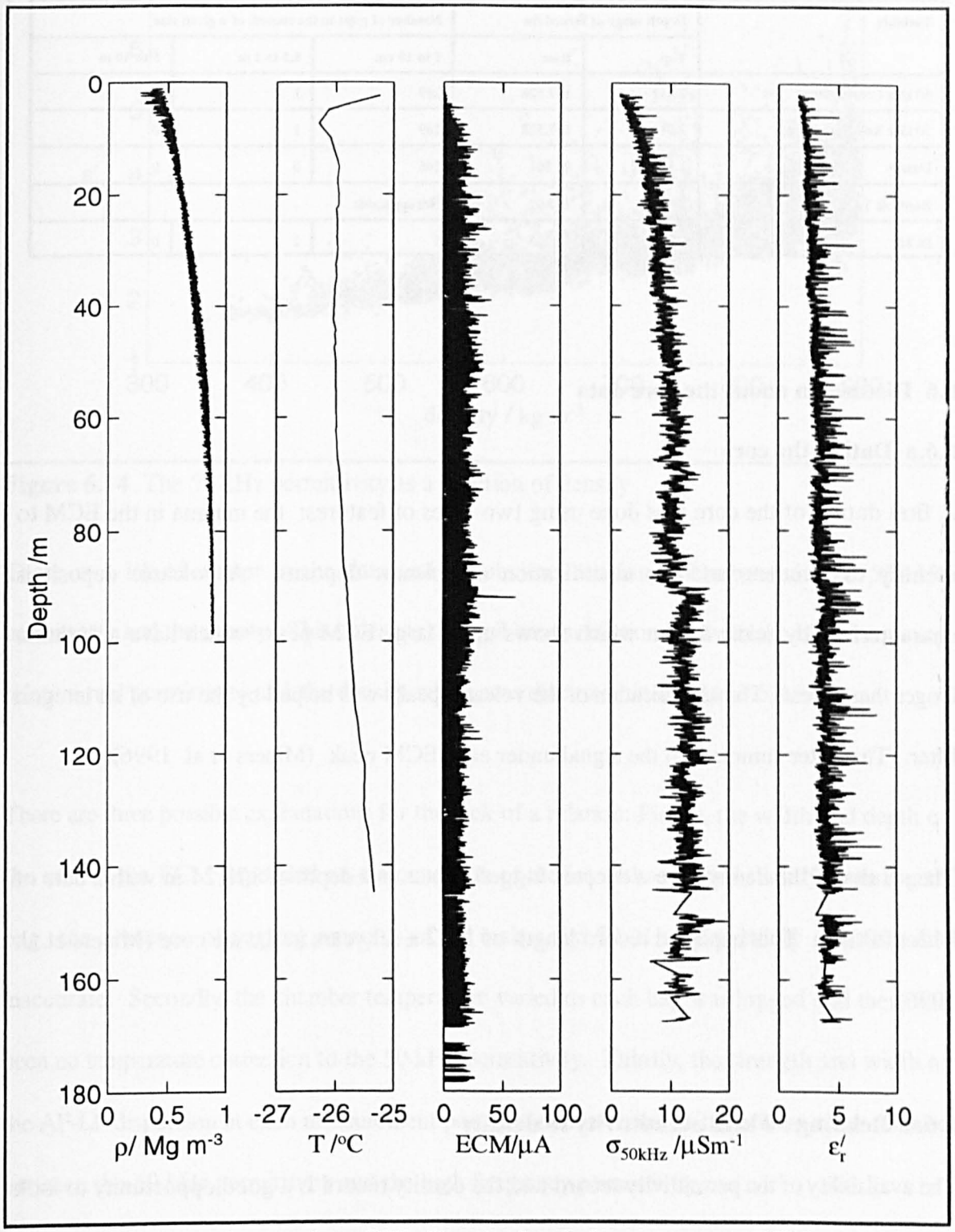

Figure 6.13 Measured properties at B25. Density, borehole temperature, ECM, conductivity and permittivity. The conductivity has not been temperature corrected.

Table 6.3 Information available

Variable	Depth range of record /m		Number of gaps in the record, of a given size		
	Top	Base	5 to 10 cm	0.5 to 1 m	5 to 10 m
50 kHz Conductivity	2.011	167.528	269	1	0
50 kHz Real Permittivity	2.011	167.528	269	1	0
Density	1.157	98.501	146	0	0
Borehole Temperature	2.48	177.02	Not applicable		
ECM	1.975	178.23	5	2	0

6.6 Discussion about the core data

6.6.a Dating the core

A first dating of the core was done using two types of features: the minima in the ECM to identify the winters, and the identification of volcanic deposits. A volcanic deposit is characterised by acidic fallout which shows up as large ECM peaks which have a duration longer than a year. The identification of the volcanic peaks was helped by the use of an integral filter. This filter summed up the signal under each ECM peak (Miners et al. 1996).

The results of the dating give a deepest logged winter at a depth of 178.24 m with a date of 812 ± 20 AD. This implies a record length of 1182 ± 20 years in the ice core (Miners et al. 1996).

6.6.b Relating 50 kHz permittivity to density

The availability of the permittivity record and the density record is a good opportunity to look at the relation between density and the 50 kHz permittivity. This is shown in figure 6.14 below.

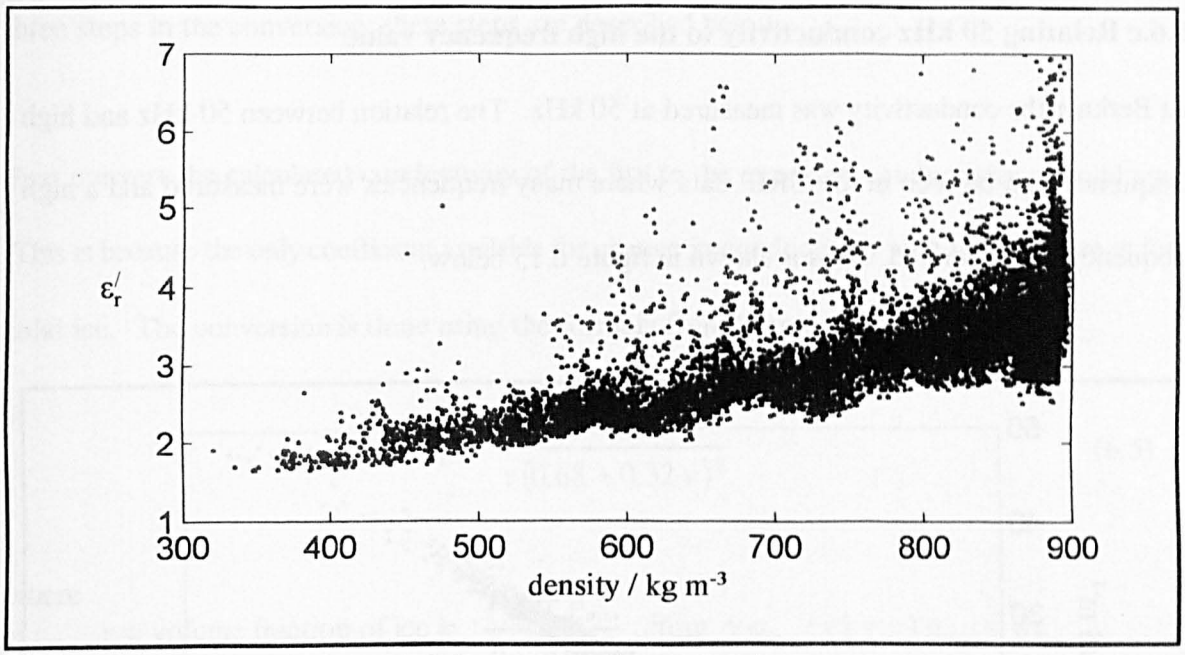

Figure 6.14 The 50 kHz permittivity as a function of density

There is a lot of scatter in the data and no obvious relation exists between the 50 kHz permittivity and the density. This is despite the well known relation between the high frequency relative real permittivity and the density which was discussed in section 3.6.d.i.

There are three possible explanations for the lack of a relation: Firstly, the width and depth of the cut for the ECM depended on the condition of the ice and so varied slightly from bag to bag, the presence of varying amounts of air makes the 50 kHz permittivity measurement inaccurate. Secondly, the chamber temperature varied as each bag was logged and there has been no temperature correction to the 50 kHz permittivity. Thirdly, the strength and width of the AF-LF dispersion at each measurement point is unknown and so there is no clear relation between the 50 kHz permittivity and the high frequency permittivity.

A similar comparison of the conductivity and density also produces an unsatisfactory fit. This is due to the influence of chemical impurities being greater than the influence of density, (see §3.7).

6.6.c Relating 50 kHz conductivity to the high frequency value

At Berkner the conductivity was measured at 50 kHz. The relation between 50 kHz and high frequency can be seen in the GRIP data where many frequencies were measured and a high frequency value derived. This is shown in figure 6.15 below.

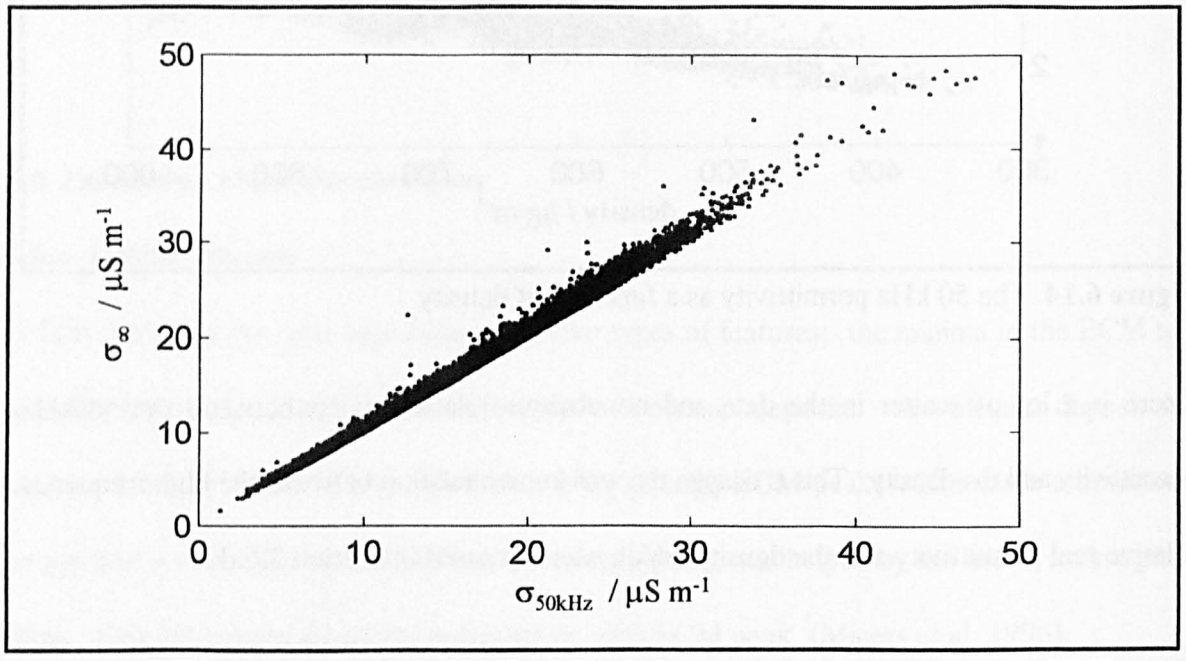

Figure 6.15 The relation between 50 kHz and high frequency conductivity for the GRIP core

On average the high frequency conductivity is only 5% higher than the 50 kHz conductivity. This close agreement between the 50 kHz and high frequency value has been previously observed by Moore (1993) and used to justify the use of a single frequency for a high resolution DEP instrument.

6.6.d Relating surface conductivity measurements to underground conductivity

For input to the model, high frequency conductivity as a function of depth is required. The calculated conductivity of the core at the surface was converted into the expected conductivity at depth by a calculation using the density and the temperatures in the two locations. There are

three steps in the conversion; these steps are described below:

First convert the calculated conductivity of the firn to the expected conductivity of solid ice. This is because the only coefficient available for change in conductivity with temperature is for solid ice. The conversion is done using the formula from Glen and Paren (1975):

$$\sigma_{\infty ICE} = \frac{\sigma_{\infty FIRN}}{v(0.68 + 0.32\,v)^2} \tag{6.5}$$

where

v = volume fraction of ice = $\frac{\rho_{firn} - \rho_{air}}{\rho_{ice} - \rho_{air}}$ from $v\,\rho_{ice} + (1 - v)\,\rho_{air} = \rho_{firn}$

Secondly apply the temperature conversion. The conductivity of solid ice is altered from the temperature it was measured at on the surface (T_S) to the expected conductivity at the temperature at depth (T_Z). The equation for the dependence is of the form:

$$\sigma_\infty(T) = P\,e^{\left(\frac{-E_P}{k_B T}\right)} + C\,e^{\left(\frac{-E_C}{k_B T}\right)} \tag{6.6}$$

where

σ_∞ is in units of μS m^{-1}
E_p = 0.5 eV
E_c = 0.22 eV (Average of salt and acid from previous studies)

Using two known conditions it is possible to determine the values of P and C:

1) The first condition is that the pure ice component at -15^{0}C (258K) is 9 μS m^{-1} :

$$P = 9\,e^{\left(\frac{E_P}{k_B 258}\right)} \tag{6.7}$$

2) The second condition is the conductivity measured at the temperature in the chamber ($\sigma_{\infty T_S}$).

Substituting this gives an equation for C:

$$C = \left(\sigma_{\infty T_S} - P e^{\left(\frac{-E_P}{k_B T_S} \right)} \right) e^{\left(\frac{E_C}{k_B T_S} \right)} \tag{6.8}$$

So overall the conductivity at depth z ($\sigma_{\infty Tz}$) is given by:

$$\begin{aligned}
\sigma_{\infty T_Z} &= P e^{\left(\frac{-E_P}{k_B T_Z} \right)} + C e^{\left(\frac{-E_C}{k_B T_Z} \right)} \\
&= P e^{\left(\frac{-E_P}{k_B T_Z} \right)} + \left[\left(\sigma_{\infty T_S} - P e^{\left(\frac{-E_P}{k_B T_S} \right)} \right) e^{\left(\frac{E_C}{k_B T_S} \right)} \right] e^{\left(\frac{-E_C}{k_B T_Z} \right)} \\
&= \left[9 e^{\left(\frac{E_P}{k_B 258} \right)} \right] e^{\left(\frac{-E_P}{k_B T_Z} \right)} + \left(\sigma_{\infty T_S} - \left[9 e^{\left(\frac{E_P}{k_B 258} \right)} \right] e^{\left(\frac{-E_P}{k_B T_S} \right)} \right) e^{\left(\frac{E_C}{k_B} \left(\frac{1}{T_S} - \frac{1}{T_Z} \right) \right)} \\
&= 9 e^{\left(\frac{E_P}{k_B} \left(\frac{1}{258} - \frac{1}{T_Z} \right) \right)} + \left(\sigma_{\infty T_S} - 9 e^{\left(\frac{E_P}{k_B} \left(\frac{1}{258} - \frac{1}{T_S} \right) \right)} \right) e^{\left(\frac{E_C}{k_B} \left(\frac{1}{T_S} - \frac{1}{T_Z} \right) \right)}
\end{aligned} \tag{6.9}$$

Thirdly convert back from solid ice to the firn density using the formula:

$$\sigma_{\infty FIRN} = \sigma_{\infty ICE} \nu (0.68 + 0.32 \nu)^2 \tag{6.10}$$

6.7 Modelling the radio echo

To model the radar record a wavelet is required and a continuous ice core record is required. The ice core data used is the 50 kHz conductivity (previously shown to be $\approx \sigma_{\infty}$). The permittivity is calculated from the density, using equation 3.17. The DEP measured 50 kHz permittivity is not used due to its poor accuracy.

It is also necessary to supply values of $\varepsilon'_{r\infty}$ and σ_{∞} for the shallowest parts of the ice sheet which were not measured. This is done by using the values from the top of the core. The eventual stack of 5000 layers has a sample spacing of 20 mm extending from a first measurement at 0.01 m to a final measurement at 99.99 m.

6.7.a The transmitted wavelet

The transmitted wavelet needs to be known to model the radio echo. There are two ways to obtain the wavelet, either by recording the transmission and reception of a single wavelet in air, or by extracting the wavelet from the recorded radio echo trace. Both these methods are discussed below.

6.7.a.i The signature wavelet of the FPG system

This signature wavelet (figure 6.16.a) was recorded during a common midpoint profiling experiment at site T43 (Crête) on the Greenland ice cap. It is the direct wave from transmitter to receiver at a distance of "several tens of metres" (Hempel pers com) and has been recorded at a sample spacing of 0.1 ns (Nyquist frequency 5 GHz). At this time the FPG monocycle RES was operating with a carrier frequency of about 35 MHz. In figure 6.16.b the peak in the amplitude spectrum is at 34.2 MHz. In figure 6.16.c is the unwrapped phase spectrum of the

wavelet, unwrapping is explained in §4.7.c.i.

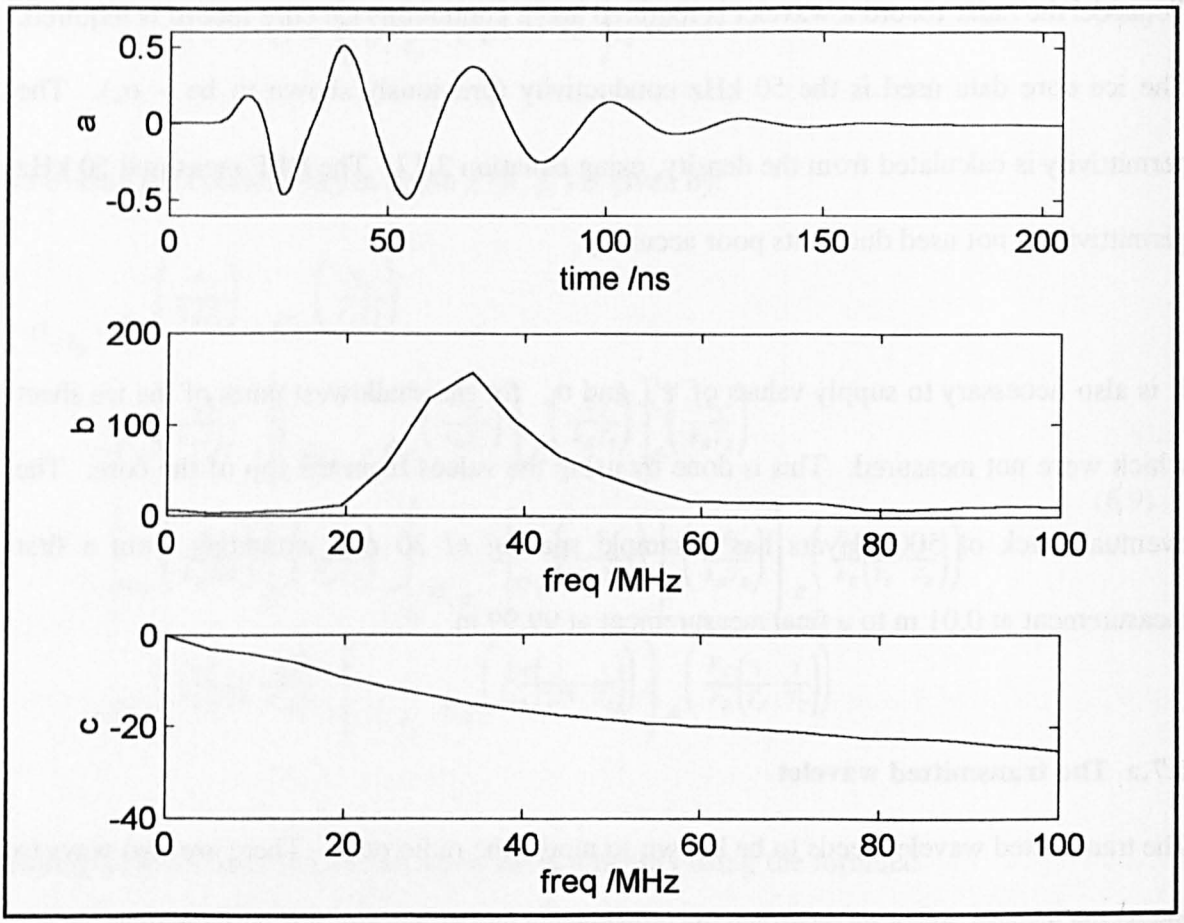

Figure 6.16 The signature wavelet for the FPG monopulse, (a) normalised amplitude in the time domain, (b) the power spectrum derived from the normalised time domain wavelet, (c) the unwrapped phase of the frequency spectrum in radians.

After the GRIP season the antenna was damaged and replaced with a new antenna. The slightly different lengths and angles in the new antenna mean that the centre frequency was closer 30 MHz for Berkner (Norbert Blindow, pers com). However the GRIP result is included here to give an indication of the waveform.

6.7.a.ii Extracting wavelets from the received radio echo

In cases where there is a clear, isolated reflection visible in the radar recording then it is possible to extract the wavelet from the time recording. There have been many attempts to

extract a wavelet by looking at the time recording in the Berkner radar (Arne Hildebrand, pers com). Unfortunately this method does not produce any satisfactory wavelets.

However it is possible to use the frequency content of the returning data to construct a signature wavelet. The amplitude spectrum of the returning data is taken (Fig 6.17.a) and smoothed (Fig. 6.17.b). The maximum in the frequency spectrum is at 29.06 MHz. The smoothed amplitude spectrum is then combined with an artificial phase spectrum. For the artificial phase spectrum it is usual to use either a zero phase (phase is zero for all frequencies) or minimum phase spectrum (Hatton et al. 1986, pp72). The combined amplitude and phase spectrums are inverse Fourier transformed to give a time domain wavelet. The wavelet shown here (Figure 6.17.c) is the result of using a zero phase amplitude spectrum, so is called the zero phase wavelet.

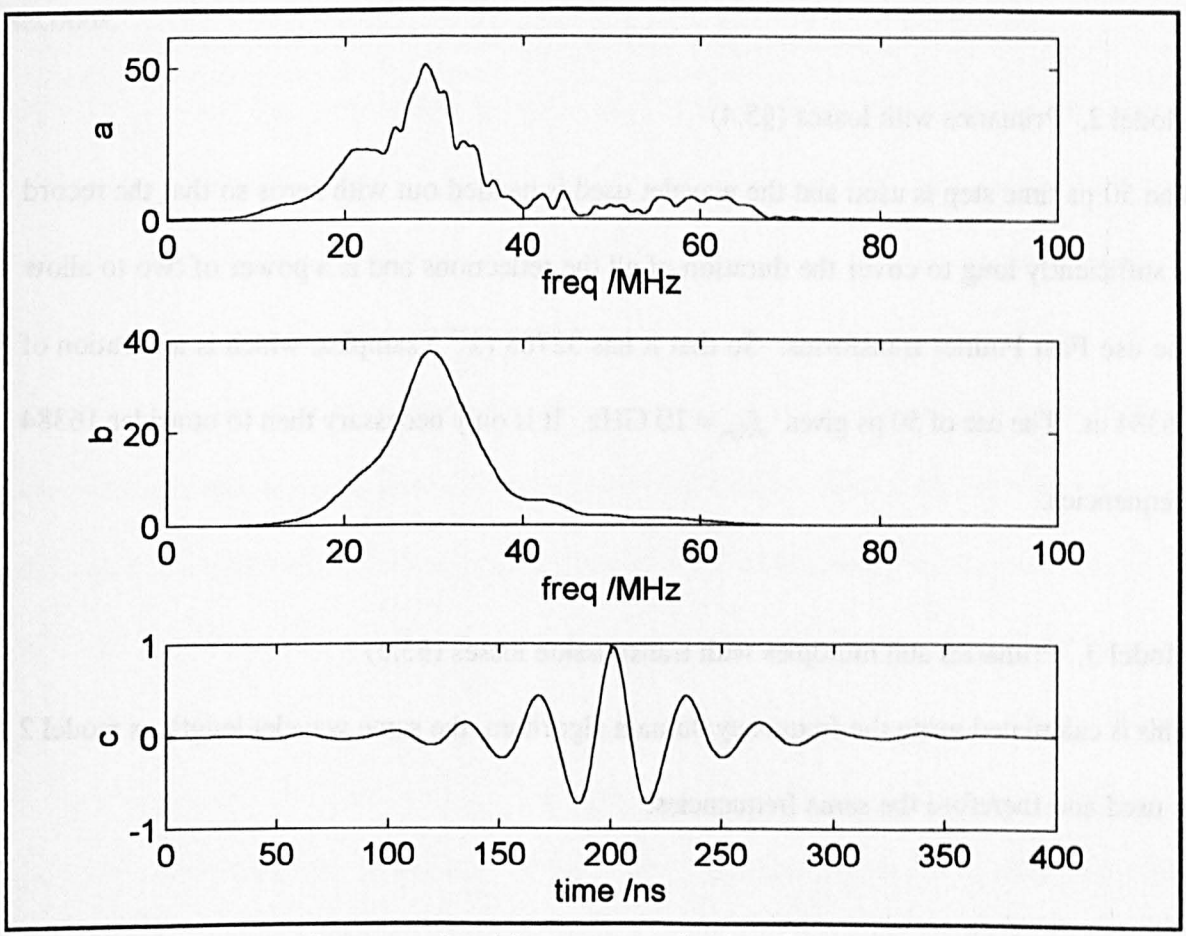

Figure 6.17 The zero phase wavelet. (a) spectrum of radar, (b) smoothed spectrum of radar (c) zero phase wavelet.

In the later modelling these wavelets and a variety of other wavelets will be used.

6.7.b The modelling method

The same four models as were described in chapter five are used. These are briefly described below. The results are shown in a figure in the next section.

Model 1, Primaries without losses (§5.3).

The ground is converted into a Goupillaud medium. The smallest two way travel time between the existing layers is 0.168 ns, so this is chosen as the sample interval for the convolution However in order to allow comparison between the different model results the sample interval of the model 4 (FDTD) of 50 ps is used which gives a stack of 21783 layers. The number of samples in the wavelet used in the convolution is 2048 (2^{11}) with a duration of 102 ns.

Model 2, Primaries with losses (§5.4)

The 50 ps time step is used and the wavelet used is padded out with zeros so that the record is sufficiently long to cover the duration of all the reflections and is a power of two to allow the use Fast Fourier transforms. So that it has 32768 (2^{15}) samples, which is a duration of 16384 ns. The use of 50 ps gives $f_{Nyq} = 10$ GHz. It is only necessary then to consider 16384 frequencies.

Model 3, Primaries and multiples with transmission losses (§5.5)

This is calculated using the frequency domain algorithm, the same wavelet length as model 2 is used and therefore the same frequencies.

Model 4, Depth dependent primaries and multiples with transmission losses (§5.6)

The finite difference time domain method (FDTD) is used. The model has a time step of 50 ps to fulfil the Courant condition. The initial wavelet is described in the space domain above the surface of the ice. The model is then run, with the time domain record at the surface of the ice being used to record the reflections.

As in the comparison in chapter 5, the FDTD model is run first to obtain a time domain record of the downwards propagating wavelet which is used in the other models.

6.7.c Results

Due to the need to model longer ice cores in the future, comparing the run times for these models is interesting. The times taken to run the four models in IDL on a 513 MHz Dec Alpha are: Model 1: 212 seconds, Model 2: 1358 seconds, Model 3: 760 seconds, Model 4: 247 seconds,

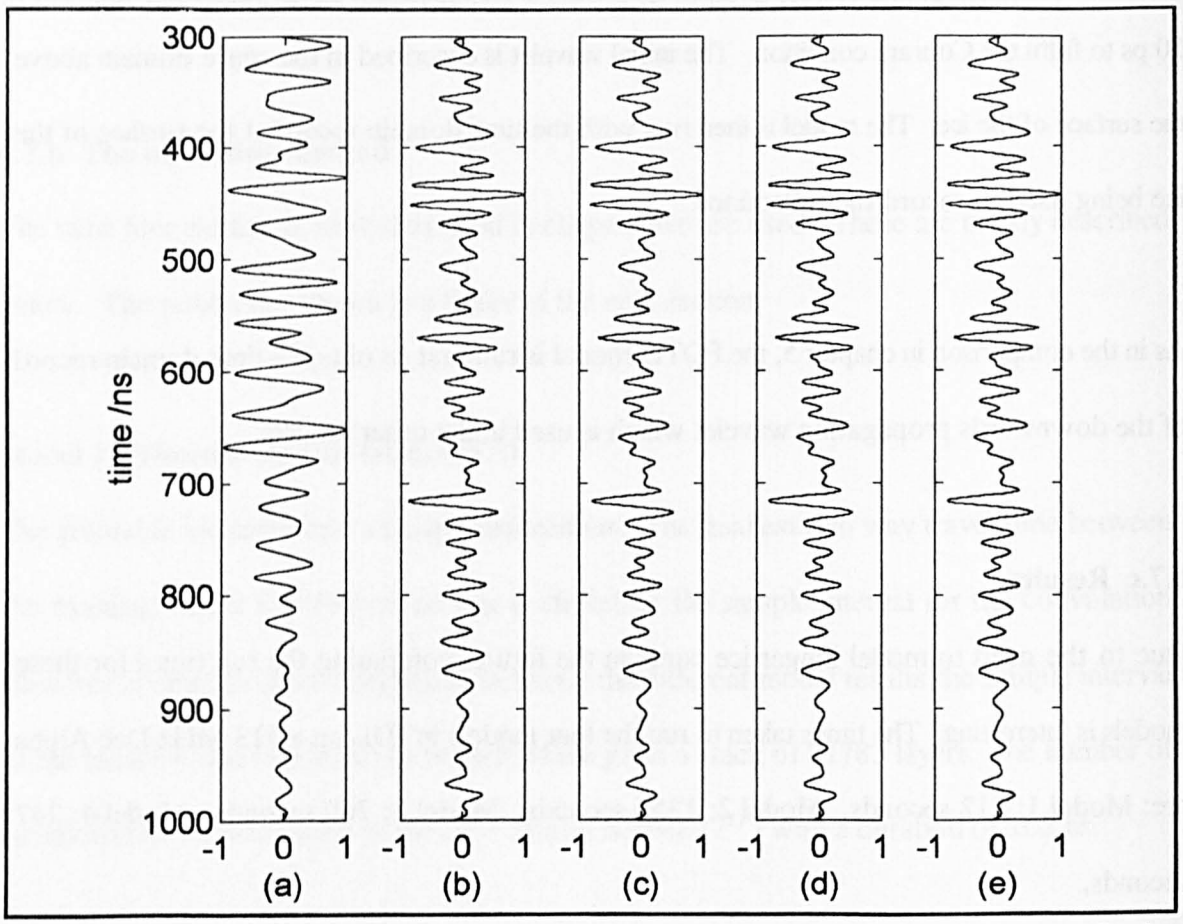

Figure 6.18 The relative amplitude of the radar data (a) compared with the relative amplitudes of the different model results b) Model 1 c) Model 2 d) Model 3 e) Model 4.

6.7.d Discussion

The radar data has strong reflections for its first half and weaker reflections after a time of 700 ns. The four models all give very similar results. The presence of transmission losses, absorption and multiples makes little difference to the model results. In the model results there are strong reflections at 440 ns, 560 ns and 720 ns. The first of these appears to match up with a reflection in the GPR record. However the overall match between the models and the GPR record is poor.

The times and amplitudes of the largest reflection in each model are: model one, 442.9 ns 0.00686; model two, 442.9 ns 0.00608; model three, 443 ns 0.00641; model four, 443 ns

0.00677. The amplitude of the reflection from model one is the largest and the amplitude of the reflection from model two is the smallest. Models three and four have larger amplitude reflections compared to model two. This is another example of the possible influence of the O'Doherty-Anstey effect (O'Doherty and Anstey, 1971), which was observed in section 5.7.c. where peg-leg multiples cause some delay and reinforcing of the amplitude of the primary reflections.

In the sections below the poor comparison between the model results and the radar data are quantified by using three methods: coefficient of correlation (r), the autocorrelation and the frequency spectrum.

6.7.d.i Correlation coefficient

Whether the model produces large amplitudes when the radar has large amplitudes can be shown as a plot of the amplitude of the radar (-1 to +1) vs the amplitude of the model result (-1 to +1). The amplitudes of the data and the amplitudes of the model one result are compared in the left subplot of figure 6.19 below.

It is also possible to compare the magnitudes of the traces (0 to +1). The magnitude is calculated from the absolute value of the Hilbert transform of the real series. The magnitudes of the radar and the model one result are compared in the right subplot of figure 6.19 below:

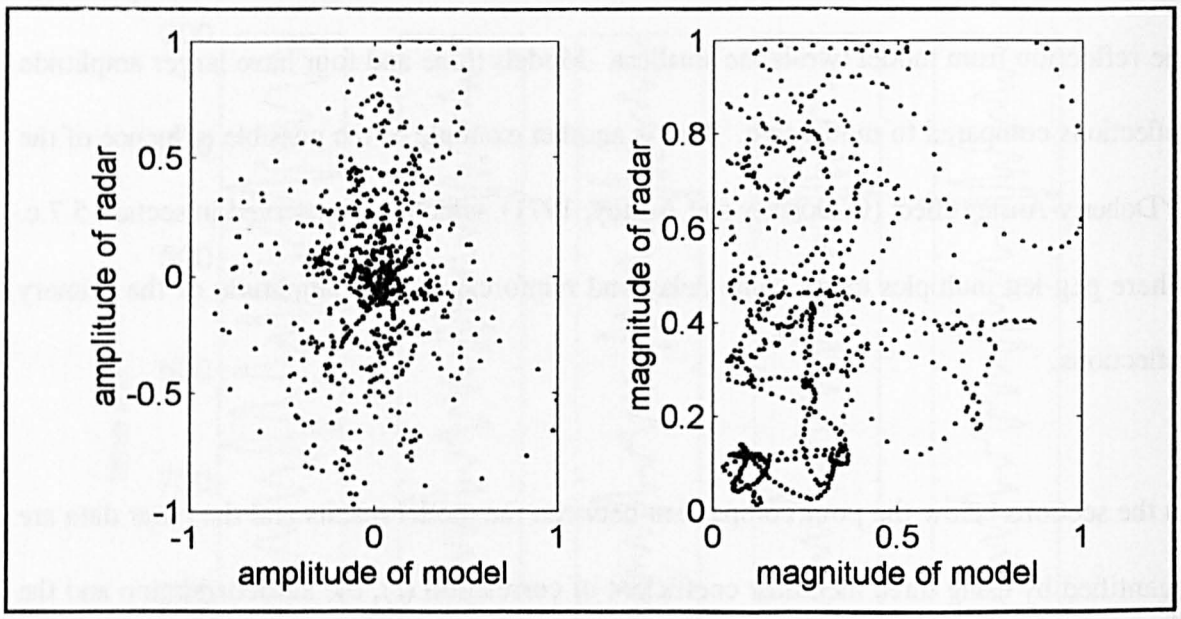

Figure 6.19 (a) Comparing the amplitudes of the radar and frequency domain model result and in (b) comparing the magnitudes of the radar and frequency domain model result.

For the figure above the coefficient of correlation between the amplitude of the model result and the radar is 0.081, the coefficient of correlation between the magnitude of the model result the radar is 0.247. If r is calculated for the comparisons of the other models the values are:

model two (propagating wavelet), amplitudes 0.100, magnitudes 0.271.

model three (frequency domain), amplitudes 0.116, magnitudes 0.264.

model four (FDTD), amplitudes 0.111, magnitudes 0.257.

6.7.d.ii Autocorrelation

Another measure of similarity between the model result and the radar is to compare the autocorrelation functions of both. This will give an indication if the positions of the reflections are spread out in a similar manner on both traces. If x is the echo under consideration with index $1 \le n \le N$, then the output sequence has length 2N-1 with the zero lag occurring at index N with a value of one. The autocorrelation estimate for the lag m where $-(N-1) \le m \le (N-1)$ where c(m) = c(-m)

$$c(m) = \sum_{n=1}^{N-|m|} x(n)\, x(n + |m|)$$

This is a biased auto correlation, no allowance made for the decreasing number of samples at larger lags. The sections compared are the results for the period 300 ns to 1000 ns.

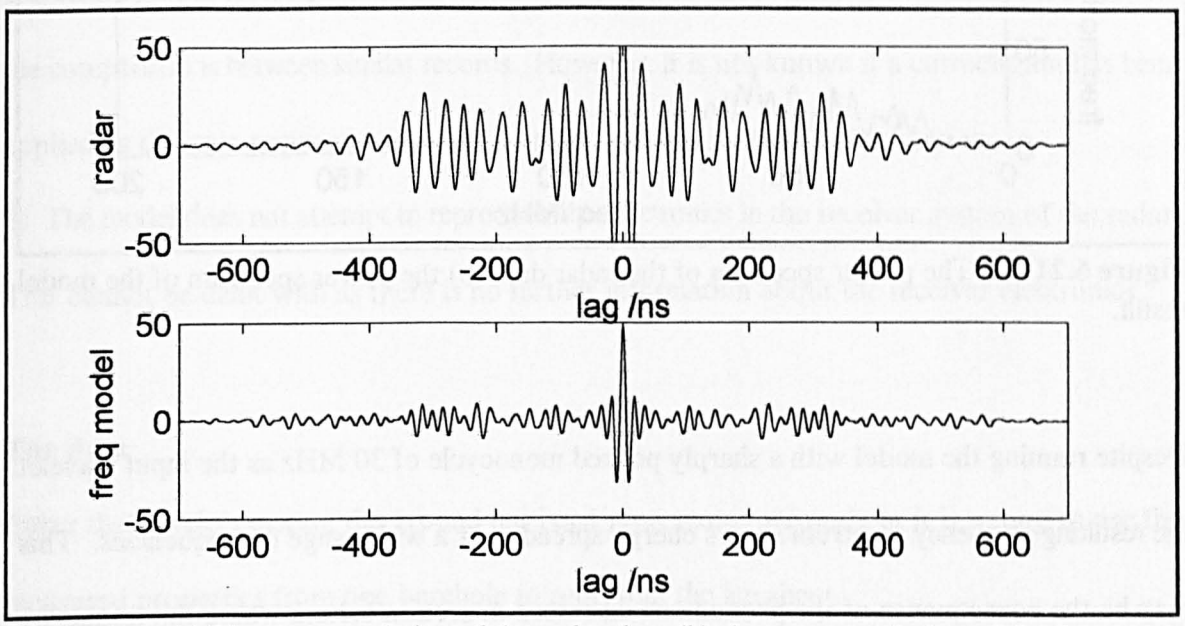

Figure 6.20 (a) The autocorrelation of the radar data (b) the autocorrelation of the frequency domain model result.

From the figure it can be seen that both the radar and the model have higher correlation for lags less than 400 ns. The similarity in the model trace drops very quickly while the radar has a very similar character for the first 400 ns. This is an indication that the model should be run with longer duration wavelets which would average out the properties in the model result.

6.7.d.iii Power Spectrums

Another measure of the similarity between the model result and the radar is to compare the power spectrums. This is done in the figure 6.21 below.

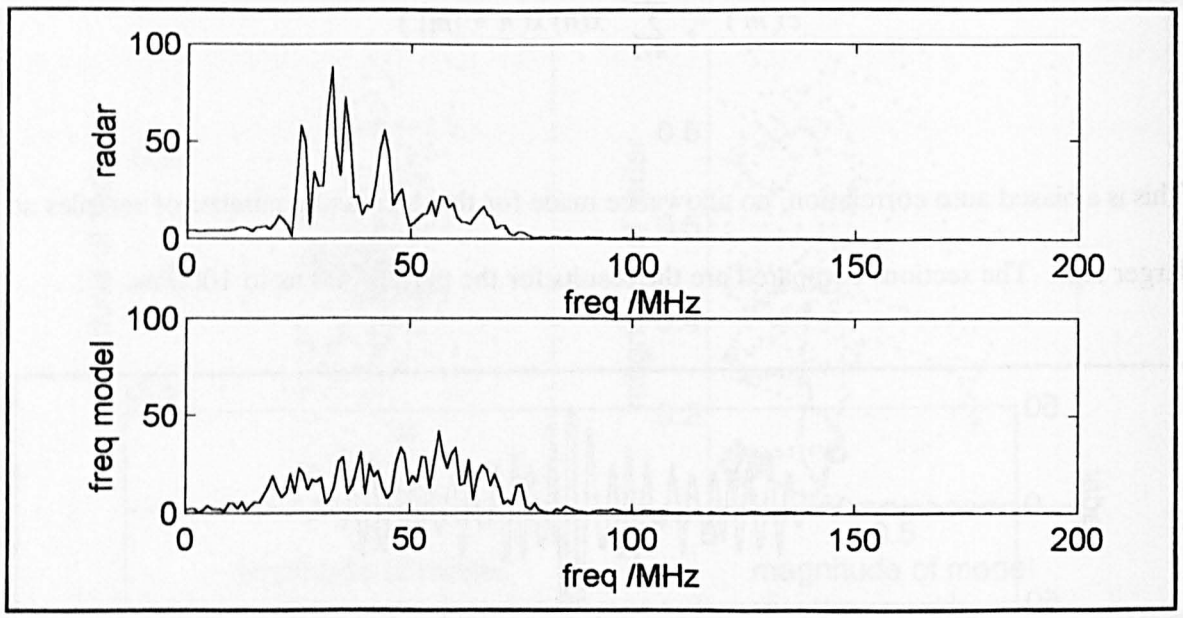

Figure 6.21 (a) The power spectrum of the radar data (b) the power spectrum of the model result.

Despite running the model with a sharply peaked monocycle of 30 MHz as the input wavelet the resulting frequency spectrum shows energy spread over a wide range of frequencies. This may be the consequence of the phenomena discussed in section 6.1.c.ii where the frequency response of the thin layers has caused the frequencies to spread up the spectrum; or there is a 30 MHz resonance in the antenna which remains after the transmission, which would not be produced in the model.

6.7.d.iv Summary

In all three of the comparison methods: coefficient of correlation, autocorrelation and frequency spectrum, the agreement between model and radar is poor. There are two possible explanations for the lack of agreement: that the model is wrong or that the data used in the model are wrong.

The model

The model considers plane parallel waves and may fail for the following reasons:

1) The recorded radio echo includes a decay due to spherical spreading, one of the model steps is to apply a gain to the radio echo to compensate for this decay (§6.2.c.iii). After such decay compensation it is hoped that the RES represents the reflection from normally incident waves. It is then possible to compare the model result and the decay compensated RES in the hope that the comparison is between similar records. However, it is not known if a correct gain has been applied as the gain required will depend on the antenna pattern and refraction.

2) The model does not attempt to reproduce the electronics in the receiver system of the radar. This cannot be dealt with as there is no further information about the receiver electronics.

The data

Either the wavelet entering the ground has been represented wrongly or it is wrong to use the measured properties from one borehole to represent the ice sheet.

The possible improvements are to the model or the data. The present model could be improved to a three dimensional model. However, lacking any knowledge about the spherical distribution function of the antenna (antenna pattern) I would be unable to supply such a model with any data for the wavelet. It would also be possible to improve the model to allow the permittivity and conductivity in the ice sheet to be represented as tensors, but as such information is not available there is no point in such a model improvement. However, some progress can be made on the data entering the present model. The wavelet entering the ground can be altered, and this is considered in the next section (§6.8). It is also possible to alter the ice sheet properties, this will be considered in a subsequent section (§6.9).

6.8 Obtaining a better match between model result and radar by varying wavelet parameters

The wavelet that enters the ice sheet can have a variety of shapes. Four parameters for the wavelet can be changed: Carrier frequency, Duration, Decay and Phase. (Altering the phase produces a whole range of wavelets of different "rotation"). In this section altering two of the four parameters will be considered. First the duration will be changed (§6.8.a), then the carrier frequency (§6.8.b). In the last section (§6.8.c) the correlation obtainable when both parameters are changed will be looked at.

To carry out this investigation it is easiest to use model three, the frequency domain model. The analytic function of the ground can be constructed once and multiplied with the analytic function of many varieties of wavelet. For all the results shown in this section the ice sheet properties come from the B25 core.

6.8.a Changing the duration of the wavelet

First there will be an attempt to reproduce the effects observed by Millar (1981 a). Then the effect on the Berkner Island results will be looked at.

6.8.a.i Trying to reproduce the effect observed by Millar

Millar (1981 a) used an A scope analogue instrument. He observed that a shorter duration wavelet gave more internal reflections; and that a shorter duration wavelet changed the two-way travel time of the internal reflections. In this section it will be seen if the present one dimensional model can replicate this behaviour. In the figure 6.22 below the duration of the wavelet (using a carrier frequency 60 MHz) increases to the right. The wavelet lengths are the

same as those used by Millar. In the next section (§6.8.a.ii) shorter duration wavelets will be used. The B25 ice core data are used for the ground.

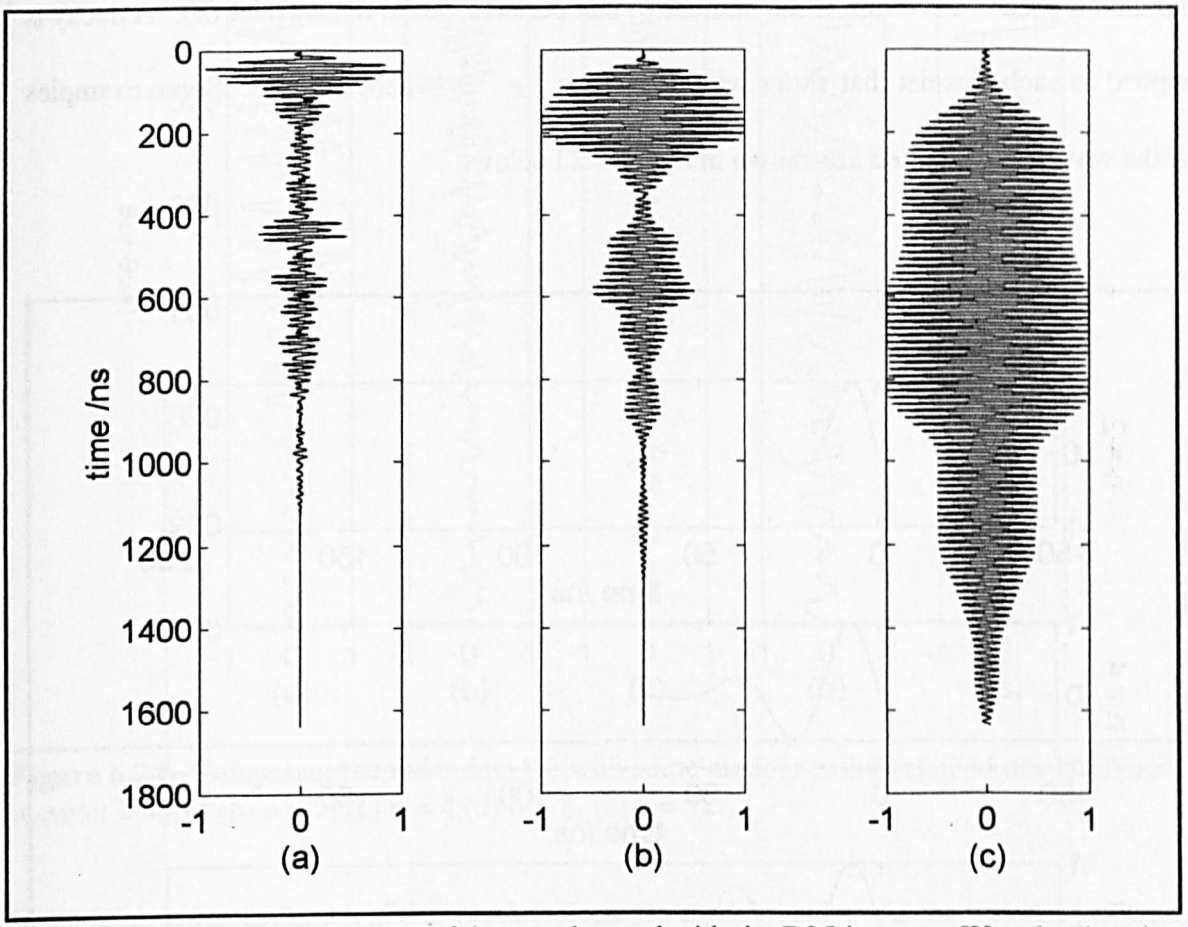

Figure 6.22 Altering the duration of the wavelet used with the B25 ice core. Wavelet duration of: (a) 60 ns, (b) 250 ns (c) 1000 ns.

The analogue system used by Millar was only able to record the envelope of the returning signal. From the figure above the number of reflection envelope peaks does decrease as the duration increases. However, it is not possible to identify a displacement for any individual internal reflection. This is due to the change in the number of reflections, so it is difficult to know which reflection to use for the comparison.

6.8.a.ii Altering the wavelet duration for the FPG radar

In the previous section long duration wavelets were used. In this section shorter duration

wavelets are used. These are the type of wavelets that are transmitted by the FPG radar. Each of the wavelets has the same carrier frequency of 30 MHz, but a different duration. The duration is specified in terms of the number of half period lobes in the wavelet (n). A decay is applied to each wavelet that varies with time (t) as $e^{-\frac{2}{\tau}t}$ where τ is 1 ns. Some examples of the wavelets generated are shown in figure 6.23 below.

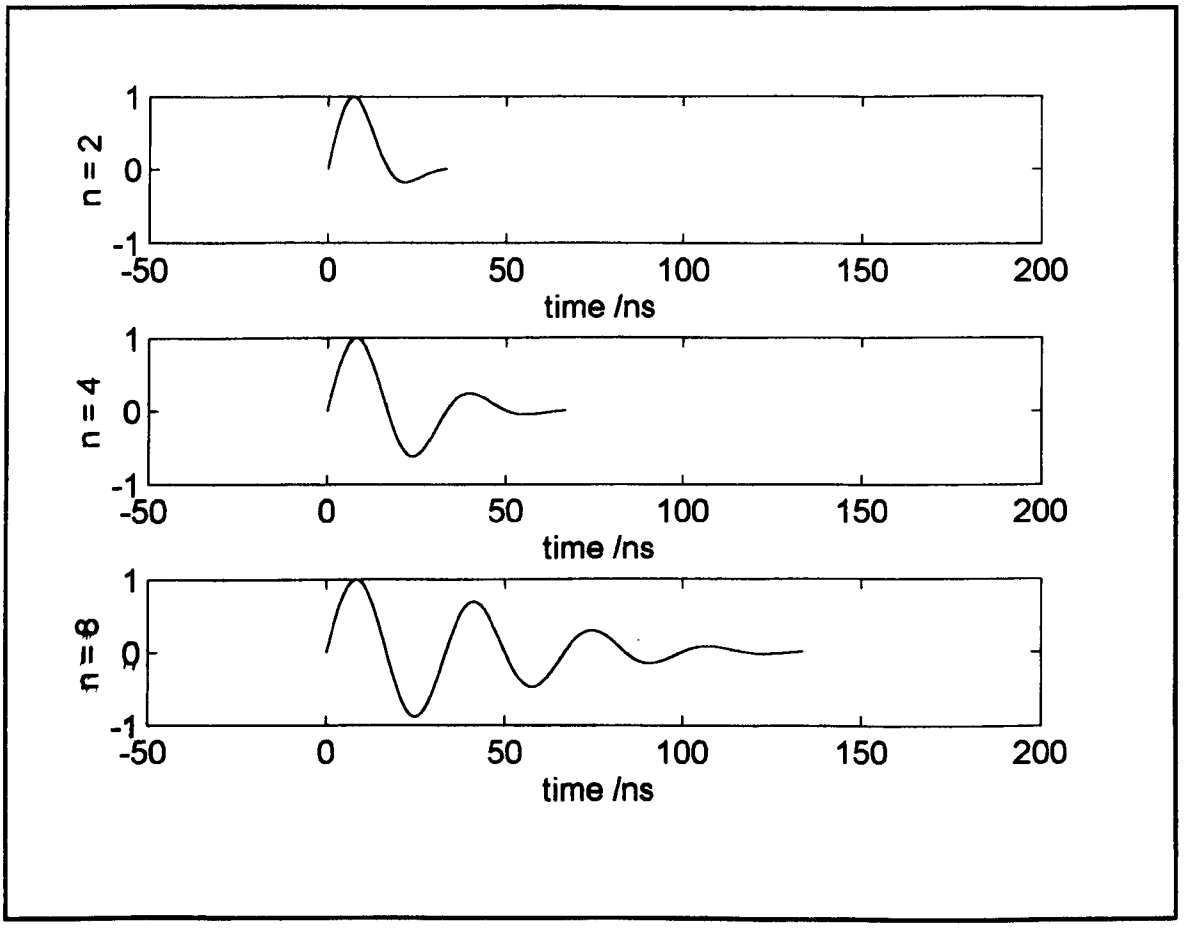

Figure 6.23 Examples of different wavelets (a) n = 2, (b) n = 4 (c) n = 8

The above wavelets and the B25 ice core are combined in model three. The results are shown in figure 6.24 below.

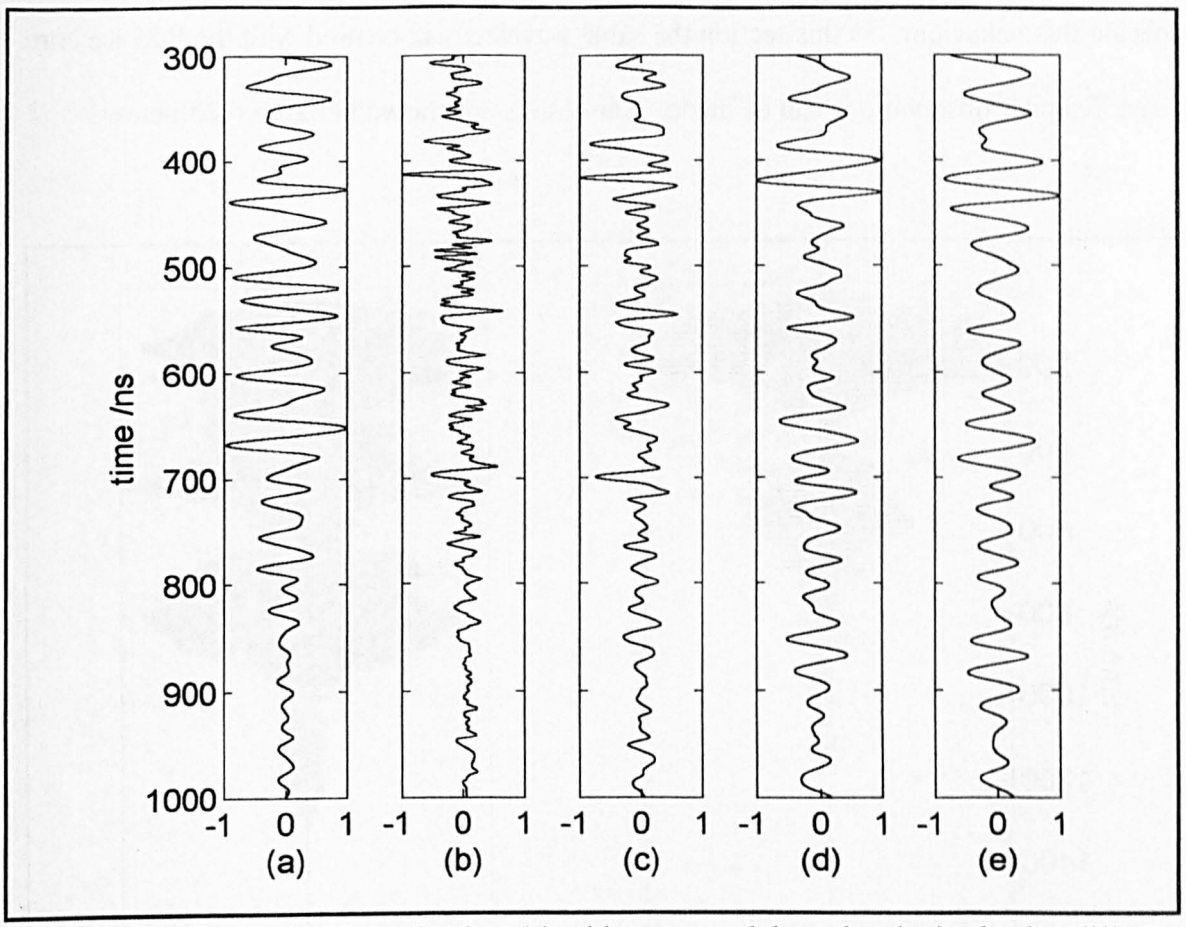

Figure 6.24 Comparing the radar data (a) with some model results obtained using different wavelet lengths (b) n = 2, (c) n = 4 (d) n = 8, (e) n = 12

It can be seen that the length of the wavelet affects the model results. As the wavelet increases in duration the result becomes smoother. In section 6.8.c a quantitative method is used to try to obtain the best fit between the duration of the wavelet used in the model and the correlation between model result and radar data.

6.8.b Changing the carrier frequency of the wavelet

6.8.b.i Trying to reproduce the effect observed by Millar

Millar's (1981 a) observation was that changing the carrier frequency of the wavelet while maintaining the same duration alters the positions of the internal reflections. Millar made this observation when using a wavelet of duration 250 ns, with the carrier frequency changing from 60 MHz to 300 MHz. In this section it will be seen if the present one dimensional model can

replicate this behaviour. In this section the same wavelets will be used with the B25 ice core to see if similar observations can be made. The results are shown in figure 6.25 below.

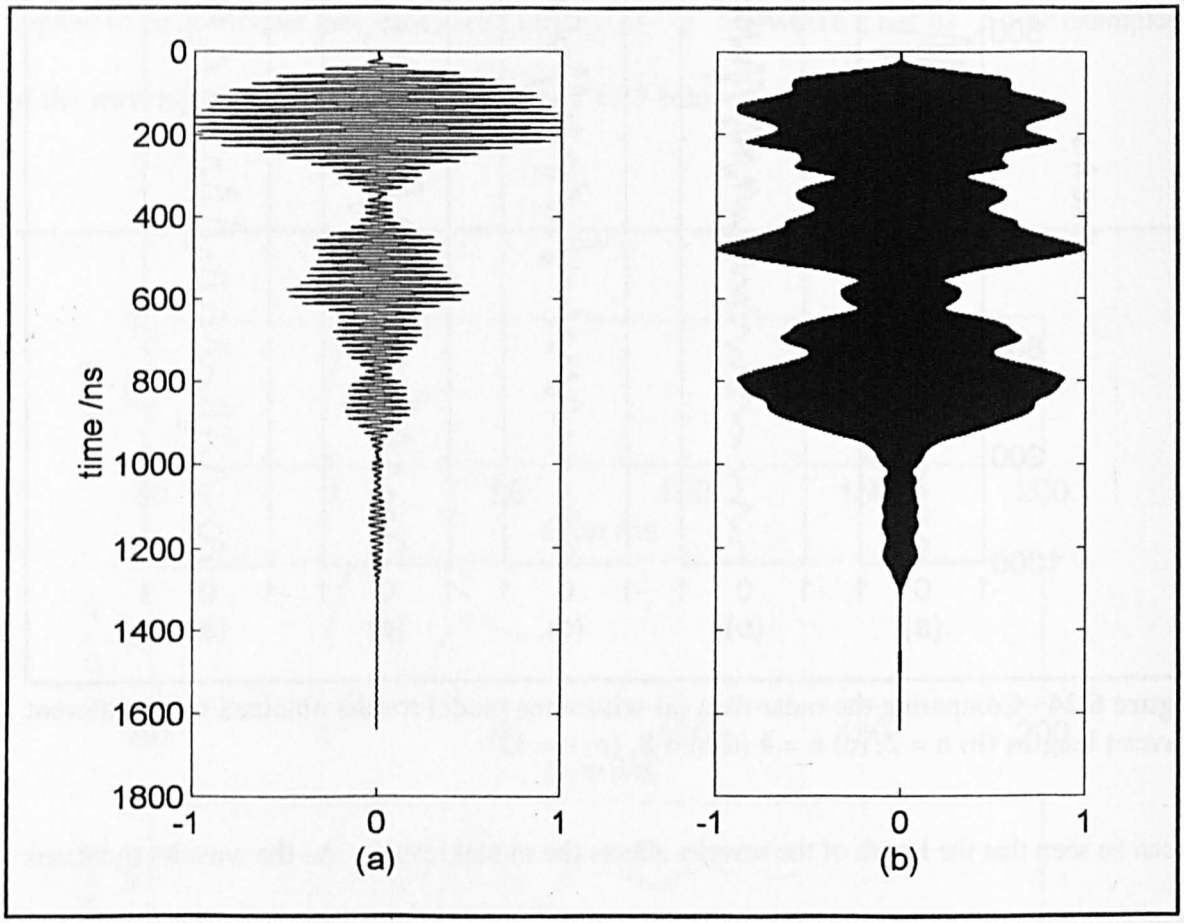

Figure 6.25 Altering the carrier frequency of the wavelet used with the Berkner core, the wavelet has a 250 ns duration and the frequency is: (a) 60 MHz, (b) 300 MHz.

For the 60 MHz wavelet there are peaks in the envelope at 180 ns and 600 ns. For the 300 MHz wavelet there are large peaks in the envelope at 120 ns, 480 ns and 800 ns. The 300 MHz model result has many secondary peaks which are not present on the 60 MHz result. If this result was viewed on an A scope it would appear that the positions of the internal reflections had altered. But when the results are seen with the greater clarity available in the above figure 6.25 it is not possible to identify similar internal reflections in both results.

6.8.b.ii Altering the carrier frequency for the FPG radar

The carrier frequency of an n=6 wavelet is altered to see how sensitive the model result is. The range of variation is from 20 to 40 MHz. The results are shown in figure 6.26 below.

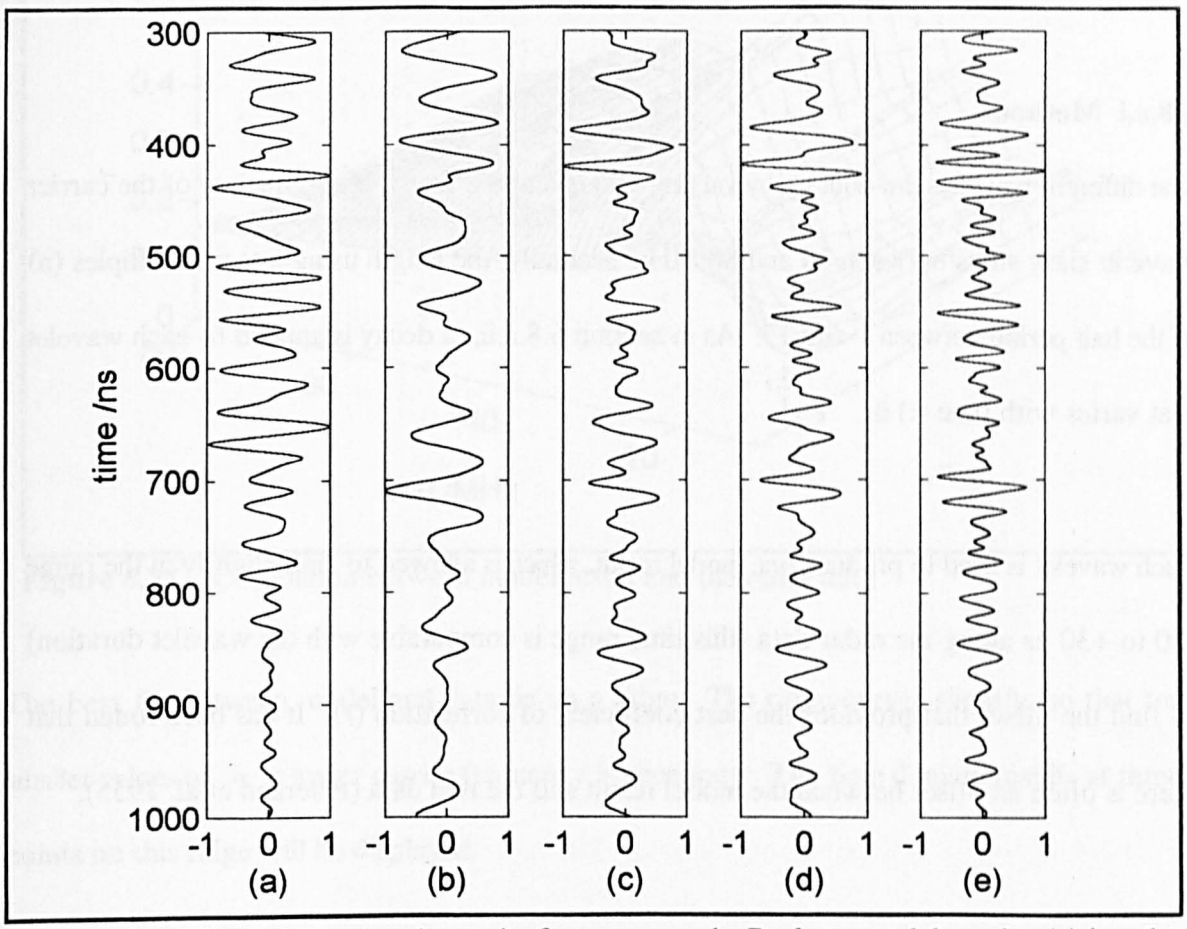

Figure 6.26 Effect of changing the carrier frequency on the Berkner model result. (a) is radar data, the wavelets are n = 6 with a frequency of (b) 20 MHz, (c) 28 MHz, (d) 32 MHz, (e) 40 MHz

There is little difference between the results obtained using 28 MHz and 32 MHz, though results (b) and (e) are noticeably different. However in all four results it is still possible to identify three strong reflections at 400 ns, 550 ns and 700 ns.

This suggests that the model result is more sensitive to variation in the duration of the wavelet than the variation in the carrier frequency.

6.8.c Varying carrier frequency and duration

The investigation presented in this section has been presented as a paper to the Seventh International Conference on Ground Penetrating Radar (Miners et al. 1998).

6.8.c.i Method

The different wavelets are built up by varying two quantities: firstly, the frequency of the carrier wave in sixty steps between 10 and 80 MHz; secondly, the length using integer multiples (n) of the half period between 1 and 15. As in section 6.8.a.ii, a decay is applied to each wavelet that varies with time (t) as $e^{-\frac{2}{\tau}t}$.

Each wavelet is used to produce one model result, which is allowed to shift slightly in the range -30 to +30 ns along the radar data (this time range is comparable with the wavelet duration) to find the offset that provides the best coefficient of correlation (r). It has been found that there is often an offset between the model result and the real data (Peterson et al. 1955).

6.8.c.ii Results

The surface obtained is shown in the figure 6.27 below:

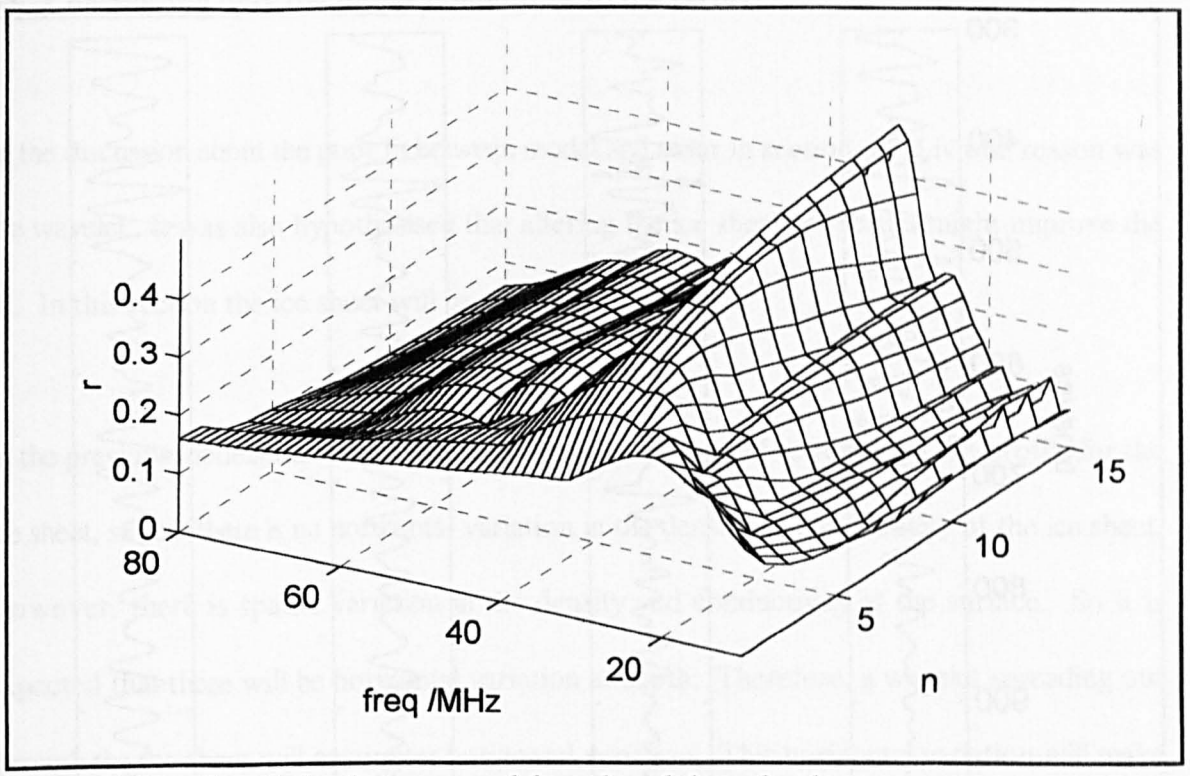

Figure 6.27 Correlation between model result and the radar data

The best fits between model and data lie on a ridge. The ridge curves slightly, so that for smaller values of n a lower carrier frequency is necessary. The time domain results at three points on this ridge will be displayed.

Point 1: $r = 0.328$ with wavelet using 28.98 MHz with 2 half periods at an offset of -24 ns.

Point 2: $r = 0.4398$ with wavelet using 31.36 MHz with 8 half periods at an offset of -24 ns.

Point 3: $r = 0.4881$ with wavelet using 31.36 MHz with 15 half periods at an offset of -24 ns.

The model results when using these three wavelets are displayed alongside the radar data in figure 6.28 below.

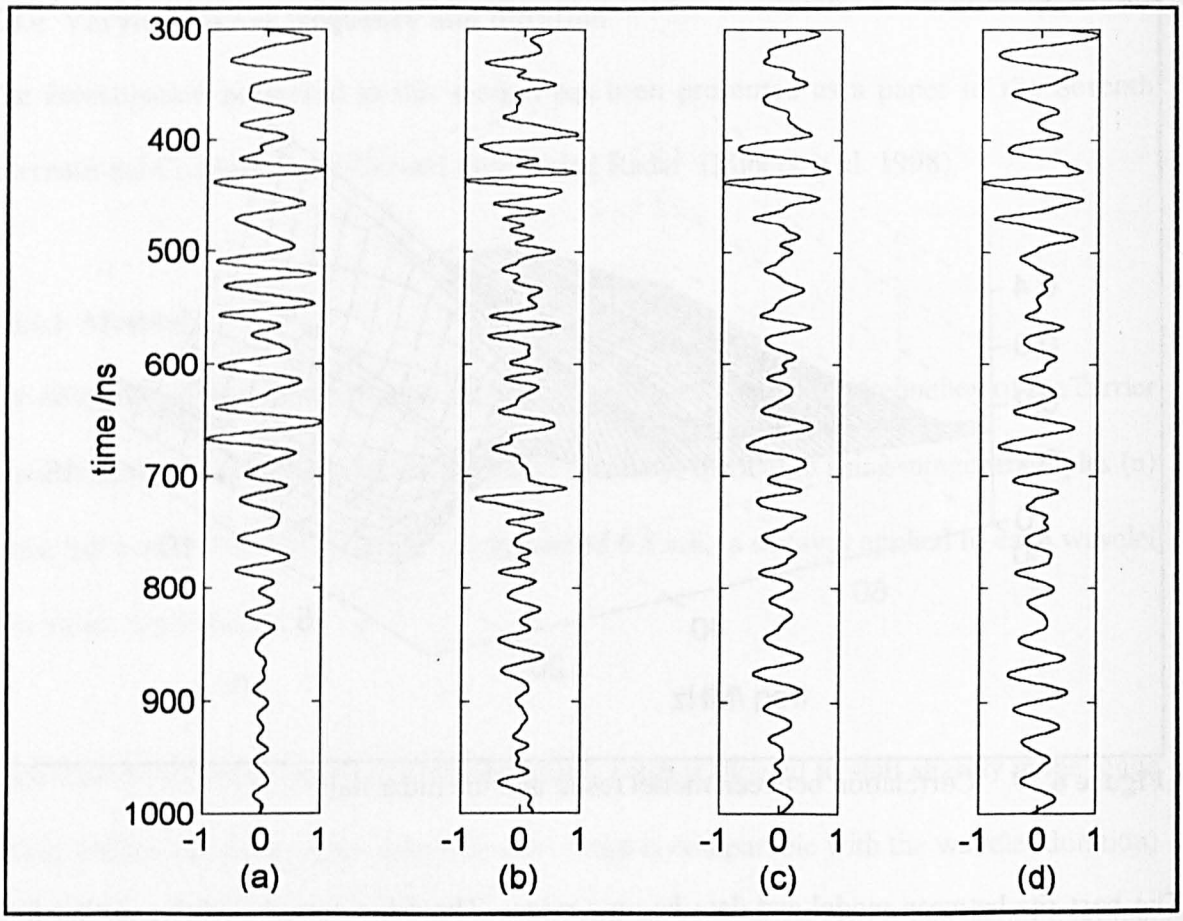

Figure 6.28 The relative amplitude of the processed radar data (a) is compared with the relative amplitude of the three model results (b) point 1, (c) point 2, (d) point 3.

6.8.c.iii Discussion

It has been shown that altering the wavelet can alter the model result. Despite trying a variety of wavelets there remains a poor fit between the model results and the radar data. There is still plenty more scope for trying other types of wavelets: with differing rotations of the incident wavelet and with differing envelopes. However before devoting more time to trying to obtain a perfect fit between model result and radar data it is worth trying other avenues of investigation.

In the next section the influence of the ice sheet data on the model is investigated.

6.9 Considering only the larger boundaries in the record.

In the discussion about the poor fit between model and radar in section 6.7.d.iv one reason was the wavelet. It was also hypothesised that altering the ice sheet properties might improve the fit. In this section the ice sheet will be considered.

In the previous models the values from one ice core were used to represent the profile for the ice sheet, so that there is no horizontal variation in the density or conductivity of the ice sheet. However, there is spatial variation in the density and conductivity at the surface. So it is expected that there will be horizontal variation at depth. Therefore, a wavelet spreading out through the ice sheet will encounter horizontal variation. This horizontal variation will make the boundaries rough.

The mathematics for dealing with scattering from rough surfaces has been looked at by many authors (Berry, 1973). It has been found that a surface can be treated as a plane surface if it has a topography $<\lambda/16$. The radio echo system used at Berkner had a λ~6 m which requires the surface undulations to be less than 40 cm. At Berkner the variation of the surface at the drill site due to snow barchans was less than 20 cm. This implies that the features seen in the ice core can be treated as plane boundaries in the ice sheet.

But treating even the small variations in density and conductivity as plane reflectors may be giving them too much importance. It is hypothesised that small features in the density or conductivity may not form a continuous surface when considered in three dimensions. It may be that only the larger features stand out above the spatial variation and are recognisable as features over a large area. If this is true then it is only necessary to consider the larger features

in the ice core record as forming reflecting surfaces. Such a consideration was made by Moore (1988) who had some 2500 measurements along an ice core; by only considering layers in which the difference between adjacent measurements exceeded $4\ \mu S\ m^{-1}$ he obtained a 695 layer model.

However, this is only a hypothesis. To properly test it would require three dimensional models with an idea of the radiation pattern of the antenna. For this work the antenna pattern is not available and there is not the time to construct a three dimensional model.

In this section the effect of considering only the larger steps will be considered. Two ways to smooth the ice sheet will be considered: firstly, in §6.9.a a similar method to Moore (1988 a, b) will be used. Successive measurements within a certain percentage variation, (in both $\varepsilon'_{r\infty}$ σ_∞) will be considered as a single layer. Secondly in §6.9.b the ice core data will be smoothed by the use of a filter. By making these alterations it is hoped that a better agreement between model and radar may be obtained.

6.9.a Considering only larger changes in the ice sheet properties

The ice sheet data passes through a routine that compares adjacent measurements. If the deeper measurement is within a certain percentage of the measurement above it then the deeper value is set to the shallower value. Otherwise a new layer is started and the same checking routine restarts with successively deeper measurements. The same procedure is carried out on both $\varepsilon'_{r\infty}$ and σ_∞ using the same percentage variation on both. In figure 6.29 below is an example of how this process alters the real relative permittivity.

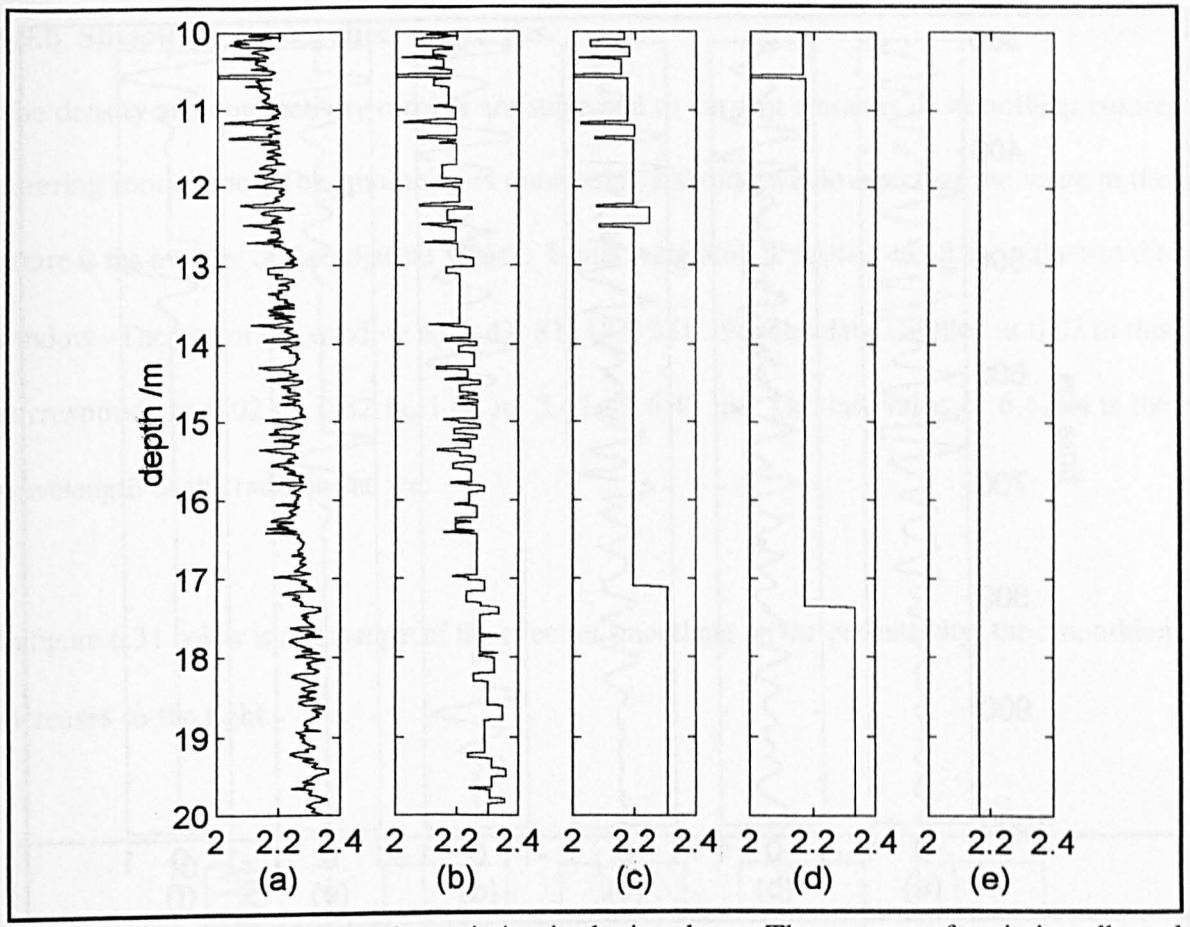

Figure 6.29 Smoothing out the variation in the ice sheet. The amount of variation allowed in the real permittivity in each layer (a) 0% (b) 2% (c) 5% (d) 7% (e) 10%

As the variability in each layer increases the number of layers decreases. Most of the layers are near the surface.

The above layered ice sheets, with $\varepsilon'_{r\infty}$ and σ_{∞} both processed with the same percentage, are used in model one with a wavelet. The wavelet used has n=6 and a carrier frequency of 30 MHz. The results of the models are shown in figure 6.30 below.

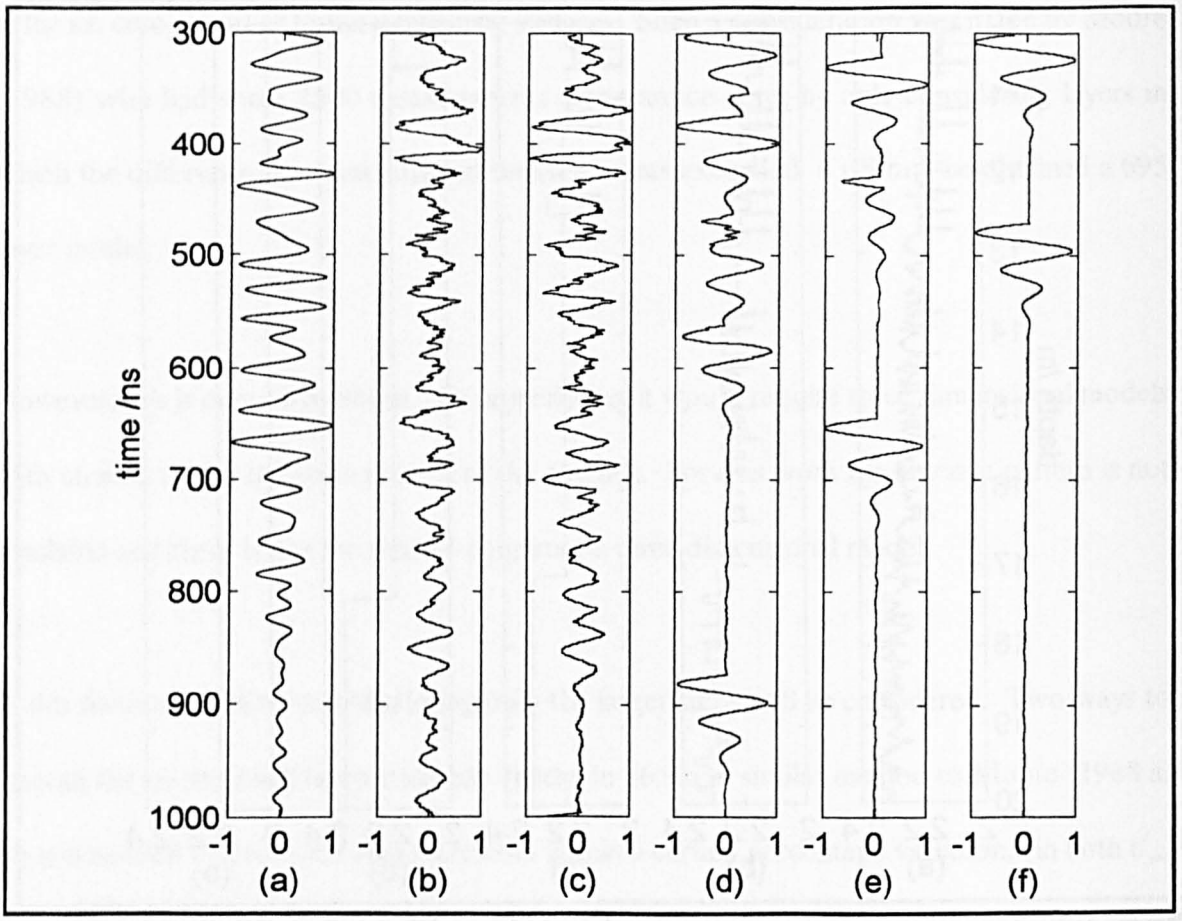

Figure 6.30 (a) is the radar data, (b) to (f) are model results. The subplots on the right have increasingly larger percentage variation amalgamated into each layer b) 0% c) 2% d) 5% (e)7% (f)10%

As the number of layers decreases the steps in the permittivity occur closer to the surface and this is where the reflections occur. The greatest change in the model result occurs between 2%(c) and 5%(d). The reflections in the model at 400 ns and 500 ns are both still recognisable in (c) and (d). However a new reflection is generated in (d) at a t_{twtt} of 580 ns which is not in the radar data.

This does not appear to be a useful way to adjust the model result. The amount of change is insignificant for small percentages and then it becomes excessive very quickly. But it shows that a feature only needs to be 5% greater than the surrounding values to alter the character of the reflection.

6.9.b Smoothing the ice sheet properties.

The density and conductivity records are subjected to varying amounts of smoothing before entering model one. The smoothing is done using a sliding window so that the value in the centre is the average of the adjacent values. Equal weighting is applied to all the values in the window. The size of the window is: 1, 41, 81, 181, 321. For the data sampled at 0.02 m this corresponds to 0.02 m, 0.82 m, 1.62 m, 3.62 m, 6.42 m. The last value of 6.42 m is the wavelength of the radar in the ice.

In figure 6.31 below is an example of the effect of smoothing on the permittivity, the smoothing increases to the right.

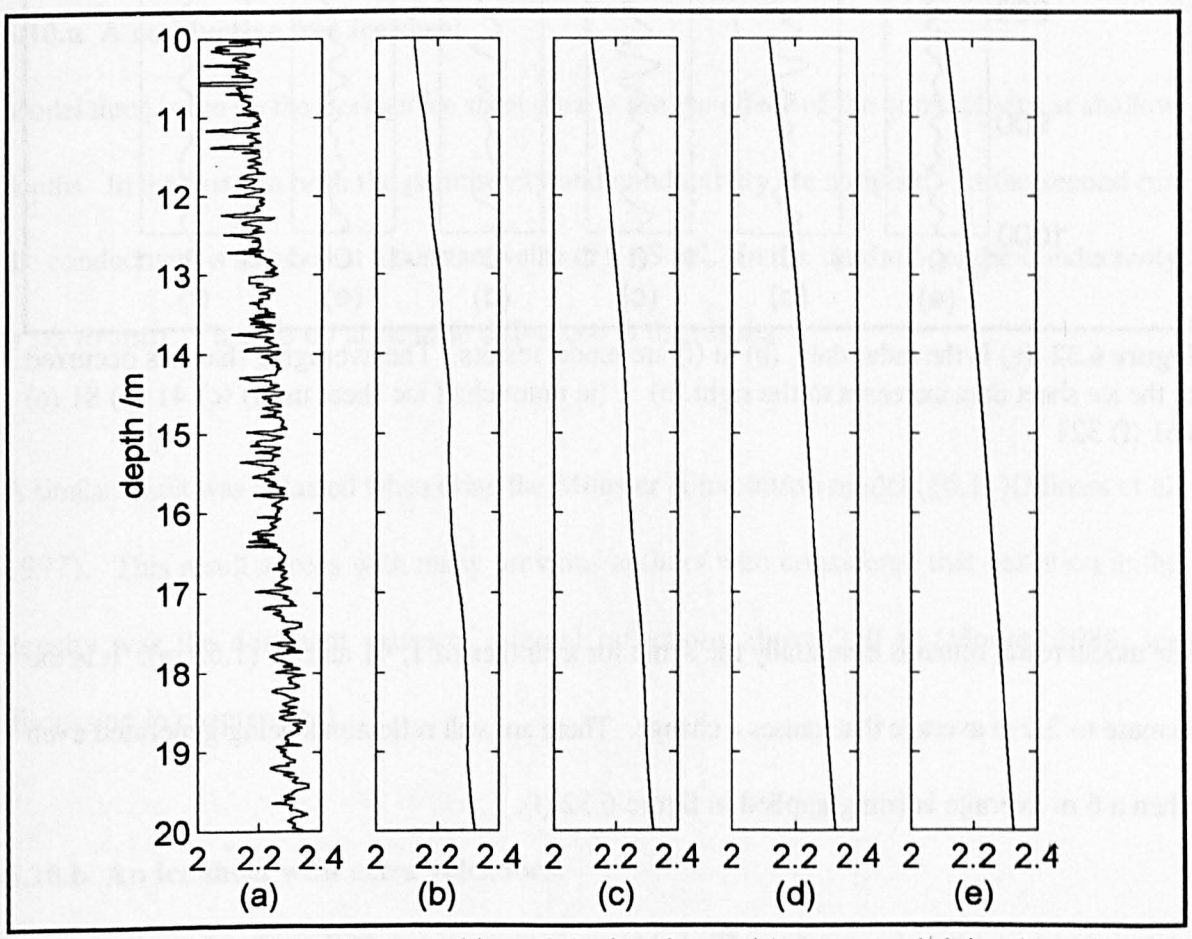

Figure 6.31 Increasing the smoothing of the ice sheet. (a) raw permittivity data, then the permittivity after using increasingly wide windows for averaging: (b) 41, (c) 81 (d) 161 (e) 321.

The generated ice sheets are then used in model one with a 30 MHz, n= 6 wavelet. The results generated are shown in figure 6.32 below.

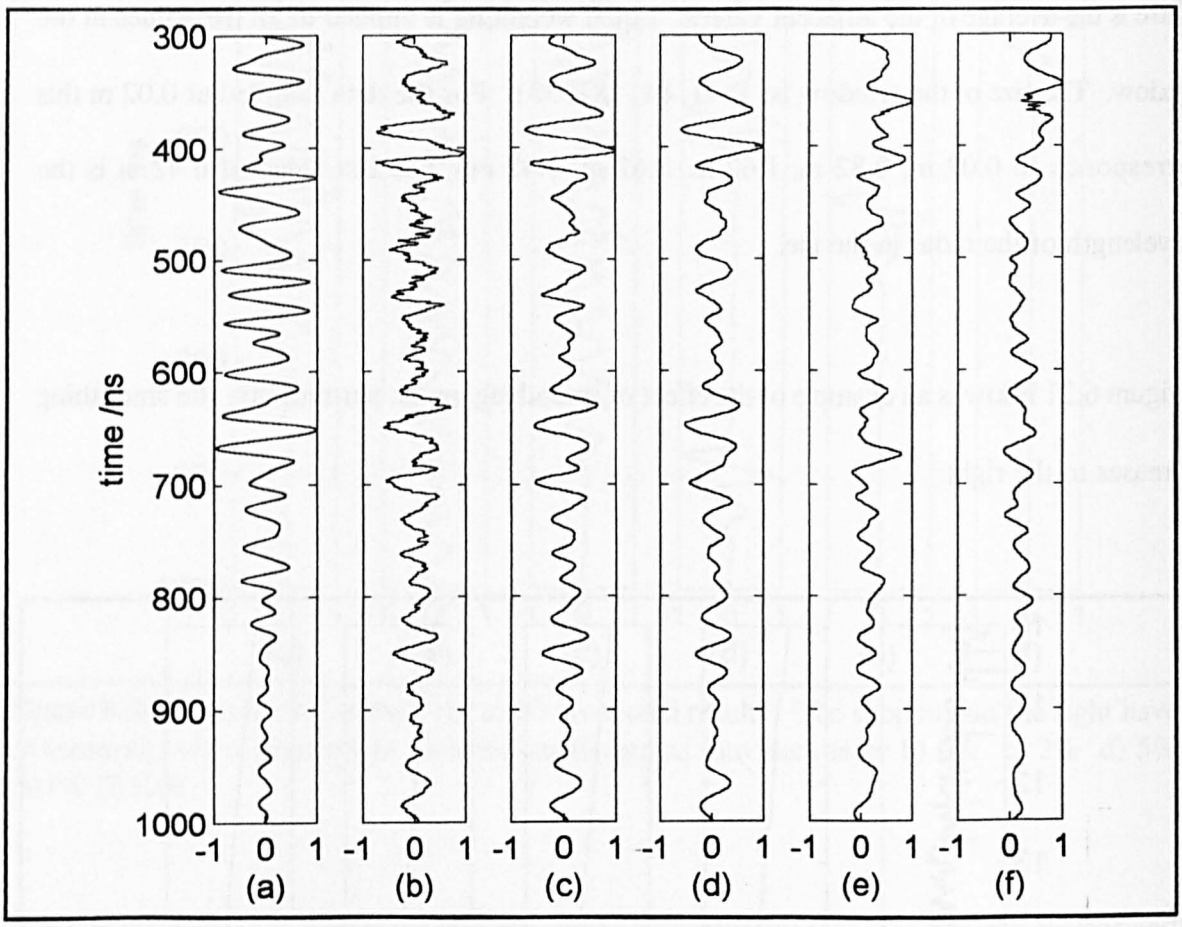

Figure 6.32 (a) Is the radar data, (b) to (f) are model results. The averaging that has occurred to the ice sheet data increases to the right. b) 1 (ie untouched ice sheet used) (c) 41 (d) 81 (e) 161 (f) 321

The model result remains essentially the same for averages of 1, 41 and 81 (1.62 m). It is the increase to 3.2 m average that causes a change. There are still reflections being generated even when a 6 m average is being applied in figure 6.32.(f).

The amount of variation in the model results is insignificant for small amounts of smoothing (ie less than 1.62 m) but then if more smoothing is applied the results change rapidly.

The experiments in sections 6.9.a and 6.9.b have given an indication of how sensitive the model is to changes in the properties of the ice sheet. However, small alterations to the relative real permittivity and conductivity of the ice sheet do not appear to alter the t_{twtt} of the internal reflections in a manner that would enable the fit between model result and radar data to be improved.

In the next section (§6.10) only the conductivity record of the ice sheet is adjusted.

6.10 Adjusting the conductivity of the ice sheet

6.10.a A conductive free ice sheet

Model three is run on the Berkner ice sheet data to test the effect of the conductivity at shallow depths. In the first run both the permittivity and conductivity are supplied. In the second run the conductivity is supplied at a constant value of 9 $\mu S\ m^{-1}$. In the third model the conductivity is set to zero. There is no noticeable difference in the results.

A similar result was obtained when using the Münster convolution model (§6.11)(Miners et al. 1997). This result agrees with many previous authors who considered that variation in the density was the dominant cause of internal reflections above 250 m (Moore, 1988, see discussion in chapter one).

6.10.b An ice sheet with extra volcanoes.

To the ice core data from B25 an extra volcano is added. The volcano takes the form of a peak in the conductivity. A Hanning window function is used of width 50 cm. The maximum

conductivity of the volcanic peak is allowed to increase until it is visible in the model result.

For this modelling the fourth model is used. This model is the most suitable for considering large conductivity variations. A wavelet reflected from a conductivity variation is 90° out of phase with the incident wavelet. If the incident wavelet is a monocycle then the 90° wavelet is a pulse. In models one, two and three the models attempt to maintain the dc term in the frequency spectrum as zero. Therefore these models smear out the small positive or negative contribution over a long time period.

The peak is first inserted into the ice core data at a depth of 10 m (expected t_{twtt} = 111 ns). The model results are shown in figure 6.33 below.

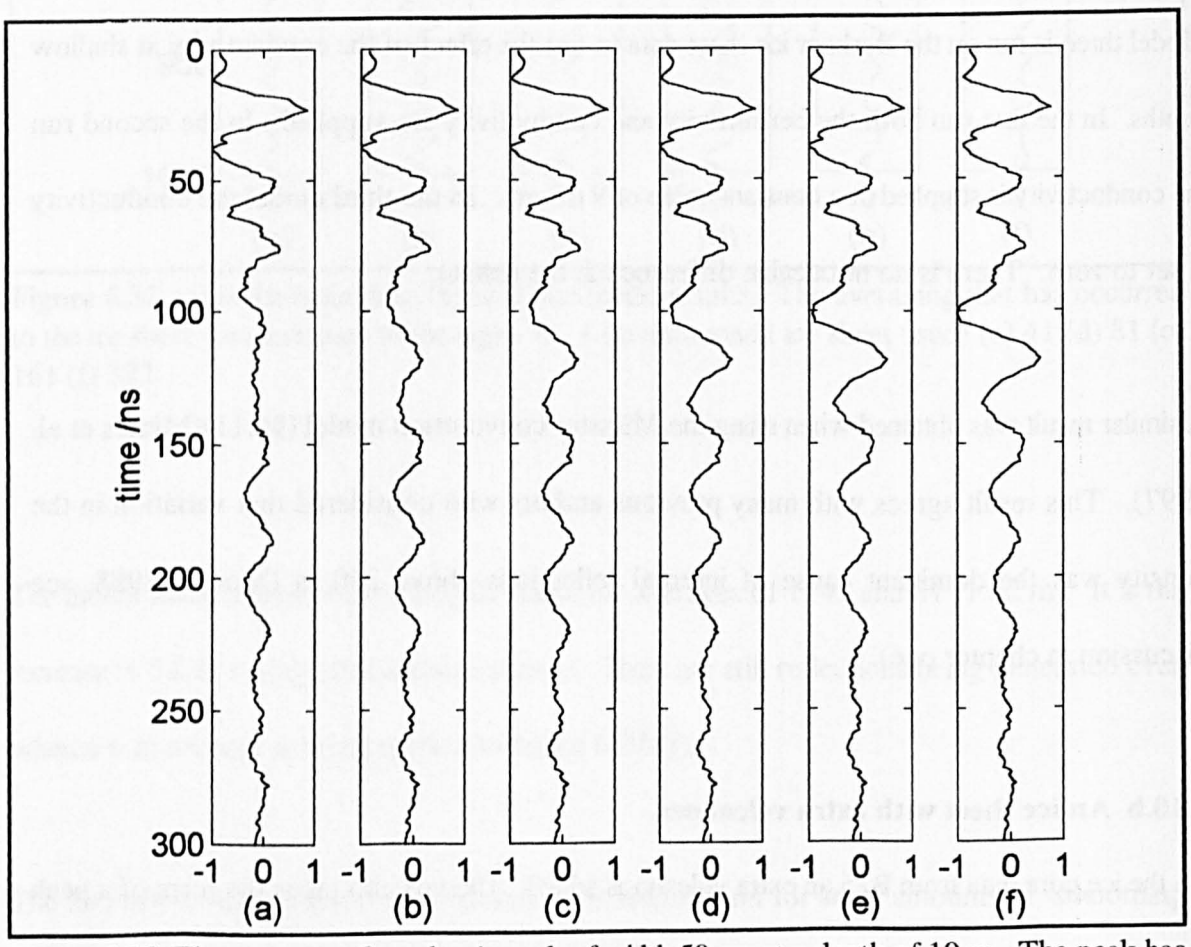

Figure 6.33 The presence of a volcanic peak of width 50 cm at a depth of 10 m. The peak has a maximum conductivity of (a) 0 μS m^{-1}, (b) 200 μS m^{-1}, (c) 300 μS m^{-1}, (d) 400 μS m^{-1}, (e) 500 μS m^{-1}, (f) 600 μS m^{-1}.

The model generates a noticeable reflection when the peak conductivity is about 400 μS m^{-1}. Next the volcanic peak is placed at a depth of 90 m (expected t_{twtt} = 1000 ns). The model results are shown in figure 6.34 below.

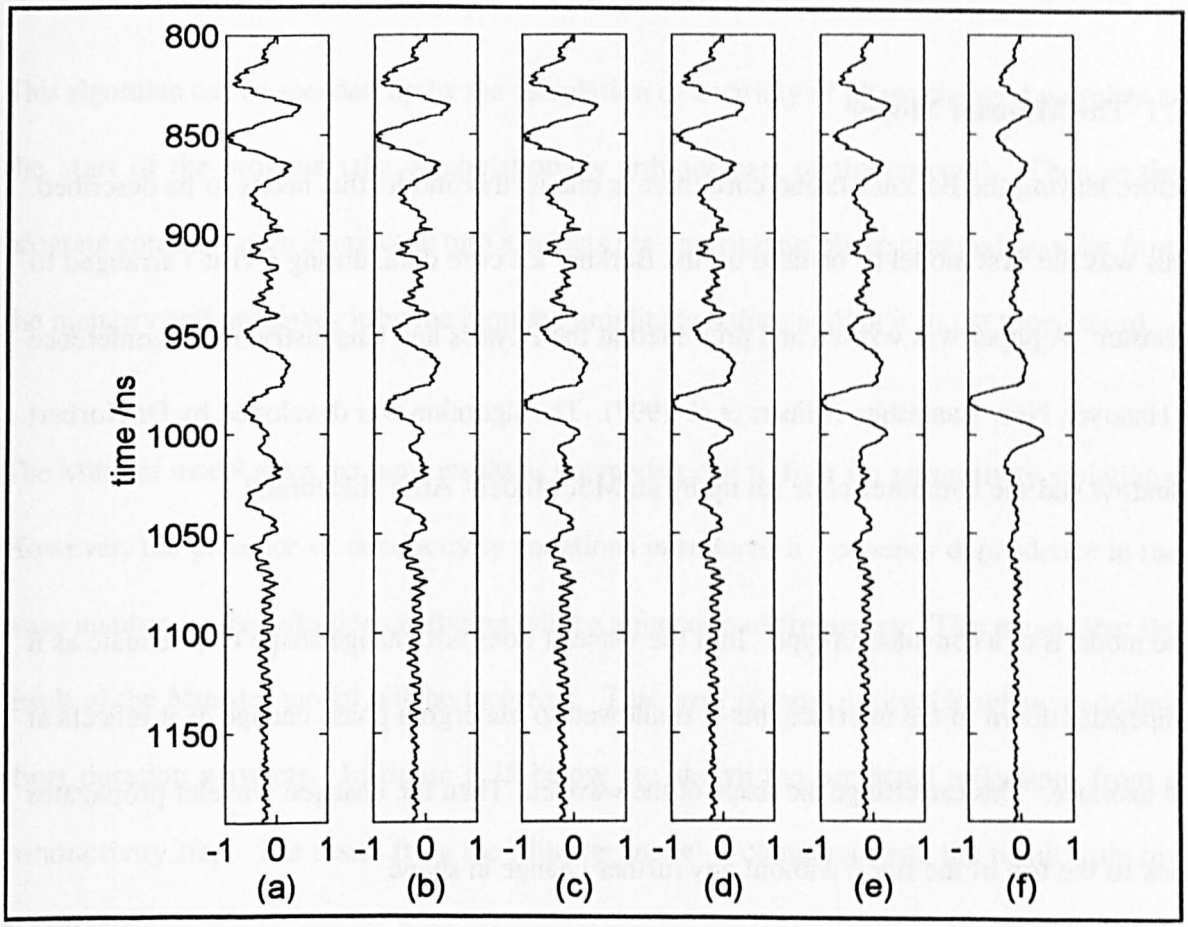

Figure 6.34 The presence of a volcanic peak of width 50 cm at a depth of 90 m. The peak has a maximum conductivity of (a) 0 μS m^{-1}, (b) 20 μS m^{-1}, (c) 50 μS m^{-1}, (d) 70 μS m^{-1}, (e) 100 μS m^{-1}, (f) 200 μS m^{-1},

The reflection starts to become visible at a peak in the conductivity of 100 μS m^{-1}. Both at 10 m and 90 m the maximum conductivity of the peak required to generate a visible reflection, which stands out against the varying permittivity, is still in excess of the peaks seen in typical ice cores. For comparison the eruption of Tambora in the B25 core at a depth of 39 m has a

peak in conductivity of 13 $\mu S\ m^{-1}$. In core G15 from Dronning Maud land the largest volcano is that of 1259 and it has a conductivity of 24.5 $\mu S\ m^{-1}$ at a depth of 95 m; while most of the volcanoes in G15 are below 20 $\mu S\ m^{-1}$ (Moore et al. 1991). This suggests that no volcanic eruption is going to cause a volcanic peak large enough to cause a reflection in the top 100 m of the ice sheet.

6.11 The Münster Model

Before leaving the Berkner Island core there is one further model that needs to be described. This was the first model to be used on the Berkner ice core data, during a visit I arranged to Münster. A paper was written and presented at the Physics and Chemistry of Ice conference in Hanover, New Hampshire (Miners et al. 1997). The algorithm was developed by Dr Norbert Blindow and the computer code set up by an MSc student Arne Hildebrand.

The model is of a convolution type. In it the wavelet does not change shape or attenuate as it propagates down to the interface, but it is allowed to undergo a phase change as it reflects at the interface. This can change the shape of the wavelet. Then the changed wavelet propagates back to the top of the stack without any further change in shape.

The wavelet entering the ground is modelled as a finite length series, of a length which is a power of two, with the same sample interval as the Goupillaud medium. This wavelet is converted into its analytic function and only the frequencies in the range $0 < f \leq f_{Nyquist}$ are retained.

Next the ground is converted into a Goupillaud type medium. Each interface is then considered in turn. At each interface the reflection coefficient is calculated for the carrier frequency (30

MHz) using the high frequency values. The calculation then switches to the frequency domain where the same reflection coefficient is assigned to all the frequencies in the range $0 < f \leq f_{Nyquist}$. These reflection coefficients are multiplied with the analytic function of the wavelet. Then an inverse Fourier transform produces the shape of the reflected wavelet at the interface. This wavelet is added to the reflection time series at a time starting at the t_{twtt} of the interface.

This algorithm can be speeded up by the calculation of a variety of phase changed wavelets at the start of the program (the computationally arduous part of the process). Then as the program considers each interface in turn it selects the appropriate phase changed wavelet from the memory and multiplies it by the required amplitude before adding it to the time record.

The Münster model gives the same results as my models one to four for permittivity variations. However, the presence of conductivity variations introduces a frequency dependence in the wave number, so the reflection coefficient will be a function of frequency. This means that the result of the Munster model will be incorrect. This error is most noticeable when modelling short duration wavelets. In figure 6.35 below are shown the predicted reflections from a conductivity step. The result from the Münster model is compared with the result from my model one.

For the Berkner modelling this caused a negligible effect as the conductivity variations are negligible in comparison to the permittivity variations.

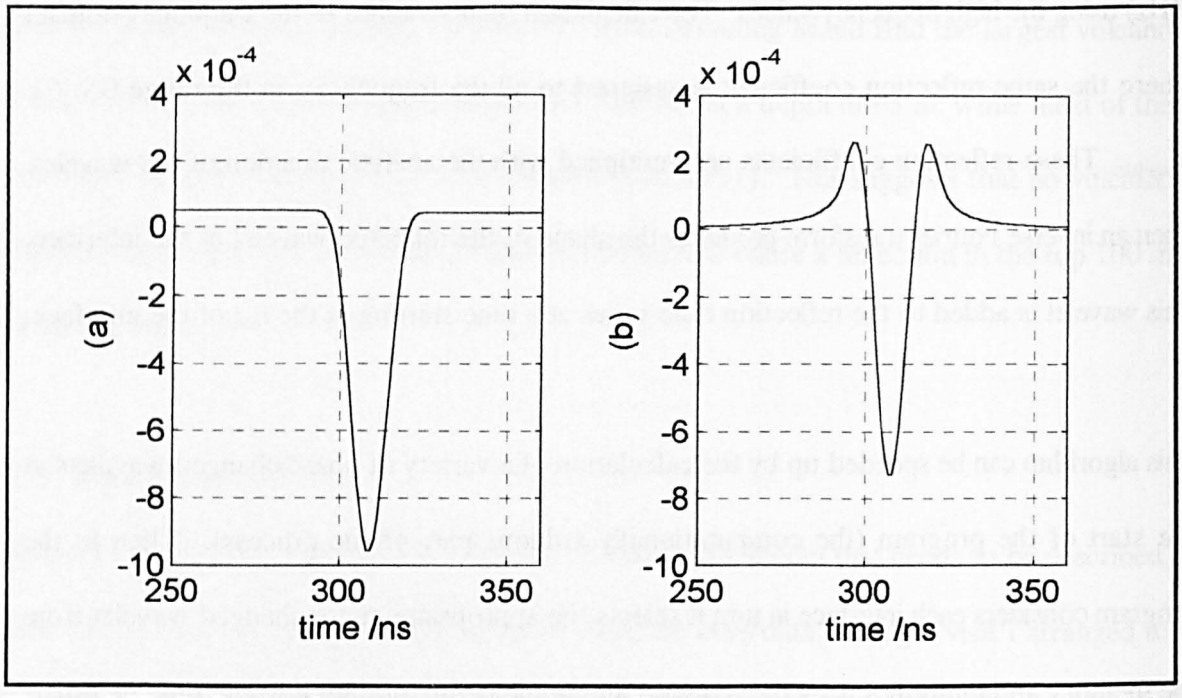

Figure 6.35 Reflection from a conductive step. Comparison of model one result (a) and the Münster model result (b).

6.12 Conclusion from the Berkner modelling

In this chapter all four wavelet models were used on the Berkner data, the difference in the results was negligible. However, in the next chapter dealing with a longer core the differences in the results become significant.

In this chapter a match has not been obtained between the radar results and the results of the models. This may be a result of using the wrong data in the model. Either the ground properties are incorrect, though in section 6.9 the model result is fairly robust to changes in the ground properties; or the wavelet was incorrect. There is certainly more scope for trying other wavelets.

If the failure to obtain a good match is not a result of the data then it is possible that a plane

parallel wavelet model is not adequate for the modelling of internal reflections in this core.

In the next chapter a new ice core will be considered, GRIP. This will allow the opportunity to use new ice core data and new wavelets. However the model used will be the same. If again there is failure to obtain a match between model result and radar data, then it will suggest that the model is at fault.

CHAPTER 7

MODELLING THE GRIP RECORD

In this chapter the present models will be applied to the ice sheet at GRIP.

7.1 The site

The GRIP project, which involved eight European nations, drilled at the highest point in the Greenland Ice sheet. The core is called the Summit core in early publications.

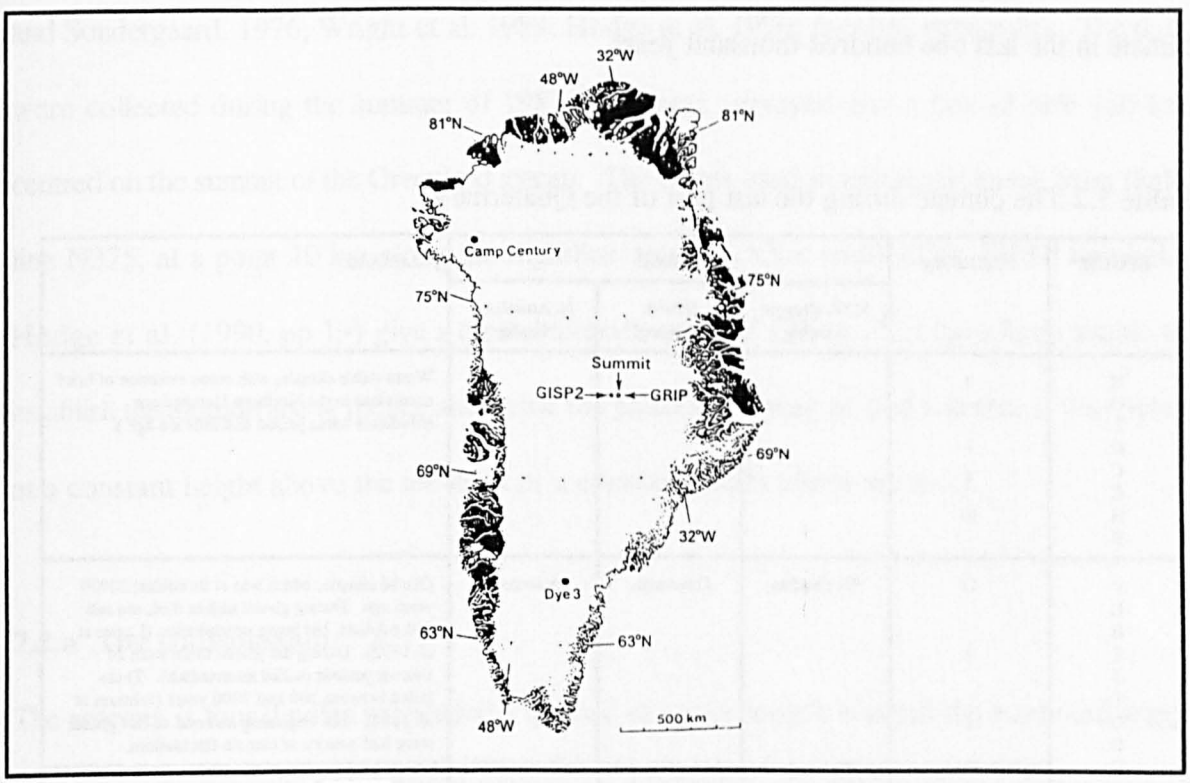

Figure 7.1 Location of GRIP

Various parameters for the site are given by Schwander et al. (1993): accumulation rate: 0.209 m water per year, mean temperature: -31 °C, mean barometric pressure 665 hPa, firn density close to surface 340 kg m^{-3}, pore close off was at 78 ± 2 m. Other parameters are given in table 7.1.

Table 7.1 GRIP core (Dansgaard et al. 1993)

Location	Altitude (metres)	Distance to nearest coast (km). (Times Atlas, Harper Collins, 9 th Edition, 1992)
72°58' N, 37°64'W	3238	250

The GRIP core was drilled to get as long a record as possible of the climate in the Northern Hemisphere. Before the core was drilled it was hoped that the ice in the core would span the entire history of the last interglacial, the Eemian. However at the moment there is some debate about the accuracy of the Eemian record in the GRIP core. Table 7.2 gives details of the climate in the last one hundred thousand years.

Table 7.2 The climate during the last part of the Quaternary

EPOCH	YEARS /ky	STAGE			CLIMATE
		N.W. Europe Naming	British Naming	N. American Naming	
HOLOCENE	0 ⇓ 10				Warm stable climate, with some evidence of brief excursions in the Northern Hemisphere (Medieval warm period and little ice age).
PLEISTOCENE	11 ⇓ 113	Weichselian	Devensian	Wisconsin	Glacial climate, which was at its coldest 20000 years ago. During glacial higher dust, sea salt and sulphate, but lower precipitation (Lorius et al. 1992). During the glacial there were 24 warmer periods (called interstadials). These lasted between 500 and 2000 years (Johnsen et al. 1992). The beginning and end of this glacial stage had a series of climate fluctuations.
	114 ⇓ 133	Eemian	Ipswichian	Sangamonian	Warm climate.
	134 ⇓	Saalian	Wolstonian	Illinoian	Glacial climate.

Two institutes provided radio echo systems to be used at Summit. The Technical University of Denmark (TUD) system was an airborne burst transmission system which was capable of

recording a reflection from the bedrock. The Forschungsstelle für Physikalische Glaziologie (FPG) provided two ground based systems: a single pulse 35 MHz system which was designed to get to a depth of 1000 metres, and a 35 MHz burst transmitter which was designed to image the bedrock (Hempel and Thyssen, 1992). The FPG mono pulse system is also the system that was used at Berkner, where it was retuned to 30 MHz.

7.2 The TUD Radio Echo system

This system used by Jacobel and Hodge (1995) at Summit was the TUD 60 MHz system (Skou and Sondergaard, 1976; Wright et al. 1989; Hodge et al. 1990; Jacobel, pers com). The data were collected during the summer of 1987. The area surveyed was a box of side 180 km centred on the summit of the Greenland icecap. The traces used in this thesis come from flight line N375, at a point 10 km along the flightline; this is 1.5 km south of the GRIP borehole. Hodge et al. (1990, pp 19) give a typical aircraft speed of 120 m s^{-1}. I have been unable to establish the altitude above the ice sheet that the plane was flying at, and whether it was flying at a constant height above the ice sheet or a constant height above sea level.

7.2.a The transmission

The antenna is four dipoles suspended a quarter of a wavelength beneath the starboard wing. The carrier frequency is 60 MHz with a frequency band width of 4 MHz and a peak transmitted power of 10 kW. The wavelet duration is 250 ns; this means about 15 periods are transmitted. If travelling in ice of density 917 kg m^{-3} at a speed of 1.68×10^{8}m s^{-1} the wavelet will have a length of 42 m. The transmission rate is 12.5 kHz which is one wavelet every 80 μs.

7.2.b The reception

From the antenna the returning signal goes through a transmit / receive (T/R) switch, then through a linear amplifier with a gain of 21 dB and a bandwidth of 20 MHz. While transmission is occurring this amplifier is suppressed by approximately 40 dB. This suppression is of a variable duration (in the range 4 to 14 μs in 1 μs steps) and variable decay in order to make it possible to reduce the very large echo from the surface of the ice (Skou and Sondergaard, 1976). This suggests to me that the first energy recorded in the receiver is the tail end of the suppression of the surface reflection.

After this there is a filter amplifier to select a 4 MHz bandwidth, centred on 60 MHz, followed by a logarithmic amplifier.

7.2.b.i Logarithmic Amplifier

This is a very common type of amplification applied to the returning radio echo for deep sounding systems. It is a useful amplifier as it is able to convert a wide range of input amplitudes, strong reflections from near the surface and weak reflections from near the bedrock, into a range that can be recorded by the system. The logarithmic amplifier is most effective at the central frequency of 60 MHz, its efficiency decreases as the frequency decreases and has halved at 34 MHz (Skou and Sondergaard, 1976). This frequency is called the 3dB bandwidth of the amplifier.

The input power (P_{in}) to a logarithmic amplifier is measured in dBm which is the logarithmic power with reference to 1 milli Watt, ie: ($10 \log_{10} (P_{in} / 1\ mW)$). The amplifier in the TUD radar can deal with an input range from -90 to +10 dBm. -80 dBm is input of 1×10^{-8} mW and gives an output of about 0.085 volts, +0 dBm is input of 1 mW and gives an output of about 1.530 volts (Skou and Sondergaard, 1976).

However with logarithmic amplifiers there are a number of bad side effects. Firstly, there is always noise from the receiver circuit and antenna at the input to the logarithmic amplifier. The logarithmic amplifier converts this random noise into a steady dc output. Typically there is a noise level of -80 dBm which gives a steady dc output of a fraction of a volt. Therefore any returning signal less than -80 dBm at the input to the logarithmic amplifier will not be detected even with averaging. Secondly, due to the electronics inside the logarithmic amplifiers, they convert an oscillating gated wavelet into a monopulse, as shown in figure 7.2 below. This means that the frequency content in the recorded trace is a result of the amplifier, not the frequency of the transmitted wavelet or the processes in the ground.

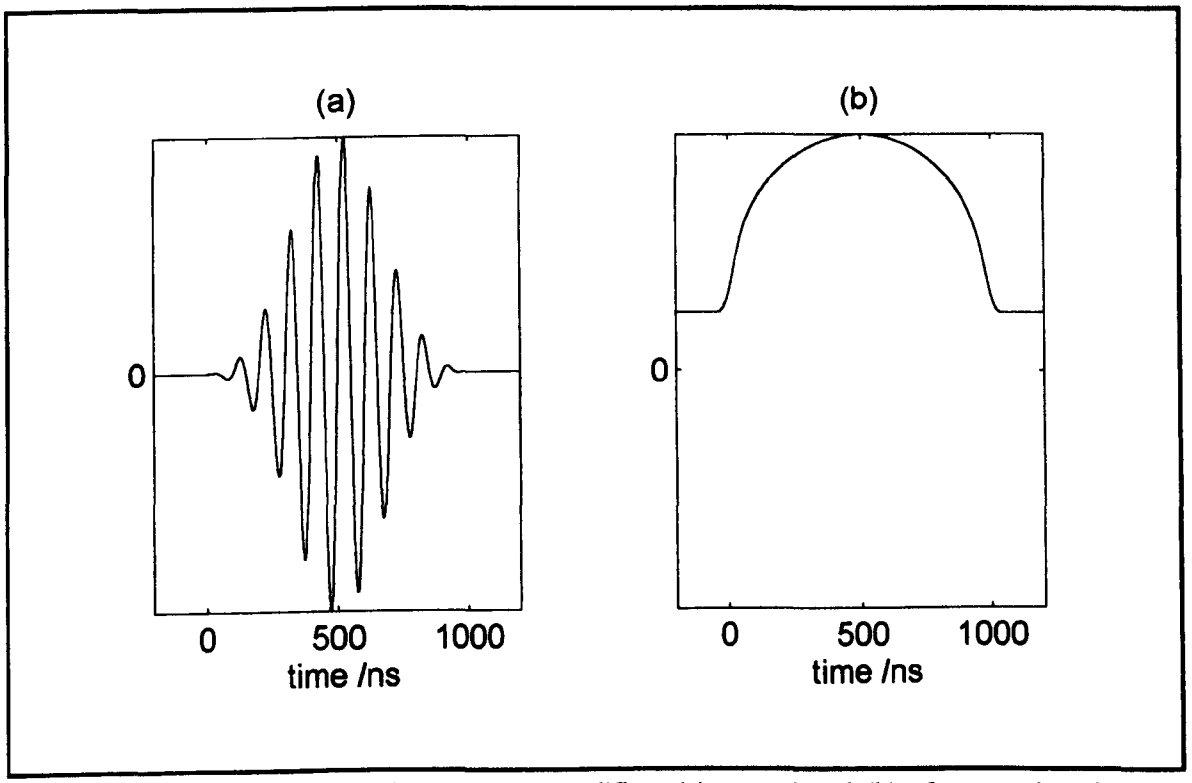

Figure 7.2 One effect of a logarithmic amplifier (a) raw signal (b) after passing through logarithmic amplifier. The vertical scale is arbitrary, there is a dc offset in the output signal.

Thirdly, a logarithmic amplifier typically has a rise time of 50 ns which imposes an additional filtering.

From the logarithmic amplifier on the TUD receiver there are two outputs; the first output is the direct A Scope form, the second output is derived from the first by analogue differentiation. The trace I have been supplied with is the differentiated one.

7.2.b.ii Differentiation

Differentiation of the returning trace can be done electronically in the circuits after the amplifier or digitally as part of the subsequent signal processing. The purpose is to reduce the dynamic range, sharpen edges and enhance features such as internal layers (Gudmandsen, 1975).

The differentiation removes any dc component in the data and also prevents any investigation of the decay that has occurred.

After the differentiation the digitisation electronics is attached (Wright et al. 1989). The digitisation system records the reflections after every second transmitted wavelet with a sample spacing of 40 ns (Nyquist frequency 12.5 MHz) for 2048 samples for a total record length of 81920 ns. The digitiser uses eight bits to digitise each point. From the digitiser the trace goes into a memory unit which sums using a 24 bit system. This memory unit stacks 512 of the captured traces then passes the total over a general purpose interface bus (GPIB) to the computer. The summed trace was being presented to the computer 12.2 times per second, but the computer was only able to read the output at a rate of about 8 times a second. This is despite all the computer code being written in assembly language for speed. Therefore the traces recorded by the system are at a horizontal spacing of 17 m of surface travel, (Jacobel and Hodge, 1995). In an earlier paper Wright et al. (1989) give the distance as 15 m. The sum from the stacking (all 24 bits) is written to a nine track tape. For the TUD system the system sensitivity is 218 dB.

The summation of the traces occurs after all the filtering. The dominant frequency in the traces at this point is of the order 10 MHz, with a period of 100 ns. This means that in order for one trace to be in anti phase with its neighbour it would need to be displaced by 50 ns with respect to its neighbour. This would correspond to a vertical movement of 15 m in a fraction of a second, which is improbable for the aircraft . However if the summation had been when the dominant frequency was still 60 MHz, then the necessary displacement would be 2.5 m which is possible.

7.2.c The Post Processing

Before producing figure 2 of Jacobel and Hodge (1995), which is displayed below, there are two further processing steps. First an additional 8 fold stacking, so that now each trace is 4096 returns, from a travel distance of 8×17 = 136 m. Then a differencing operation is used to enhance the contrast (Jacobel, pers com), where the new value z at position n is given by:

$$z(n) = \frac{z(n+1) - z(n-1)}{2} + \frac{z(n+2) - z(n-2)}{4} \qquad (7.1)$$

The resulting data, taken from figure 2 of Jacobel and Hodge (1995), are shown in figure 7.3 below:

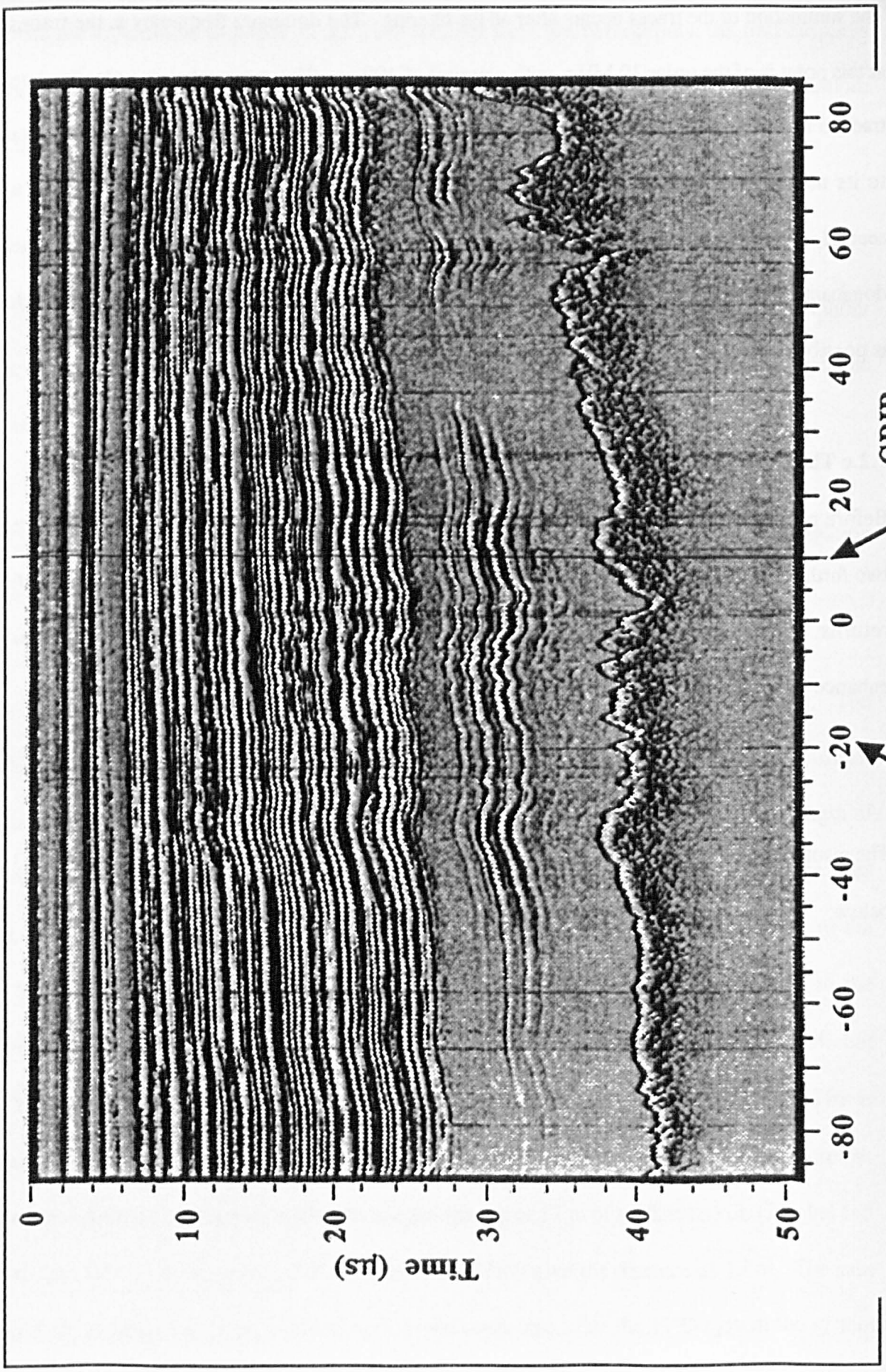

Figure 7.3 The TUD return from figure 2 of Jacobel and Hodge (1995), corresponding to flightline N375.

The surface is assigned to the reflection that curves across the figure starting at a t_{twtt} of just greater than 4 μs on the left hand axis and rising to about 3.5 μs at the closest point of approach to the GRIP drill site. The bedrock reflection is at 37.5 μs in this figure which implies a t_{twtt} of 34 μs.

The prominent break in the pattern of the internal layers that occurs half way down the record is thought to correspond to the Holocene-Wisconsin transition (see Table 7.2) (Jacobel and Hodge, 1995).

Displayed in figure 7.4.a below are the six traces from line N375 that have been provided by R.Jacobel. It is not certain whether the traces I have been supplied with have had the differencing operation (eqn 7.1) applied, though there is evidence in section 7.7.c that differencing has been applied. Also displayed in 7.4.b is the average of the six traces. The internal reflections are very continuous across the 6×136 m = 816 m of the track which is shown here.

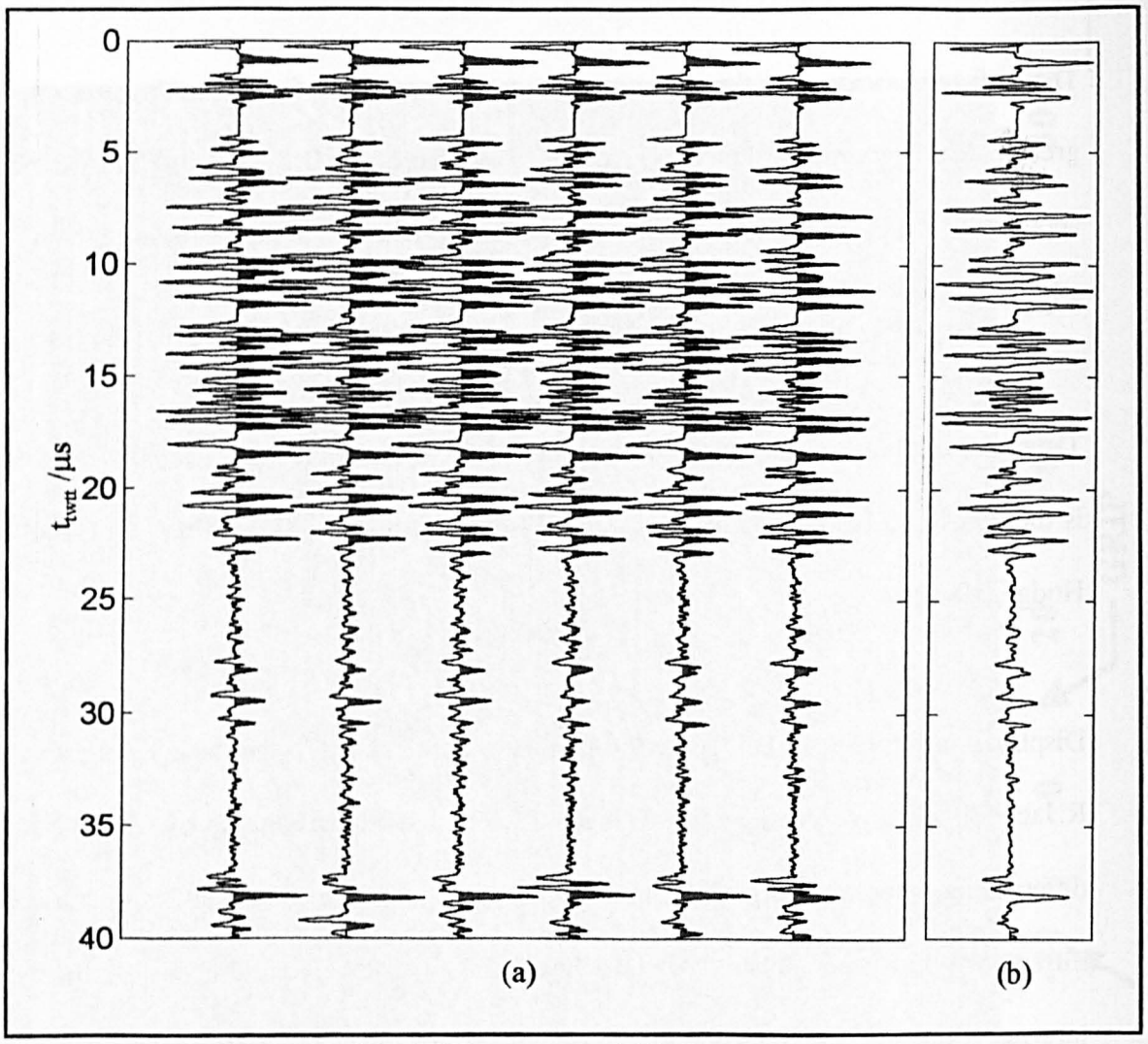

Figure 7.4 (a) Six traces of the TUD return, and (b) the average trace.

7.2.d Travel time

I am uncertain about the start time of the recording (or sweep) used at GRIP. Sometimes in the TUD system the sweep is started shortly before the transmitter is activated (Christensen et al. 1970). At the start the transmitted wavelet leaks into the receiver (via the T/R switch), a few microseconds later, dependent on the altitude, the echo from the surface appears. Somewhat later the attenuated echo from the bedrock peers out (Sondergaard and Skou, 1976).

Figure 7.5 below shows two portions of one of the provided traces: the topmost part (7.5.a) which will include the reflection from the snow surface and may (depending on the attenuation and the start of the recording) include the transmitted wavelet and (7.5.b) the reflection from the bedrock.

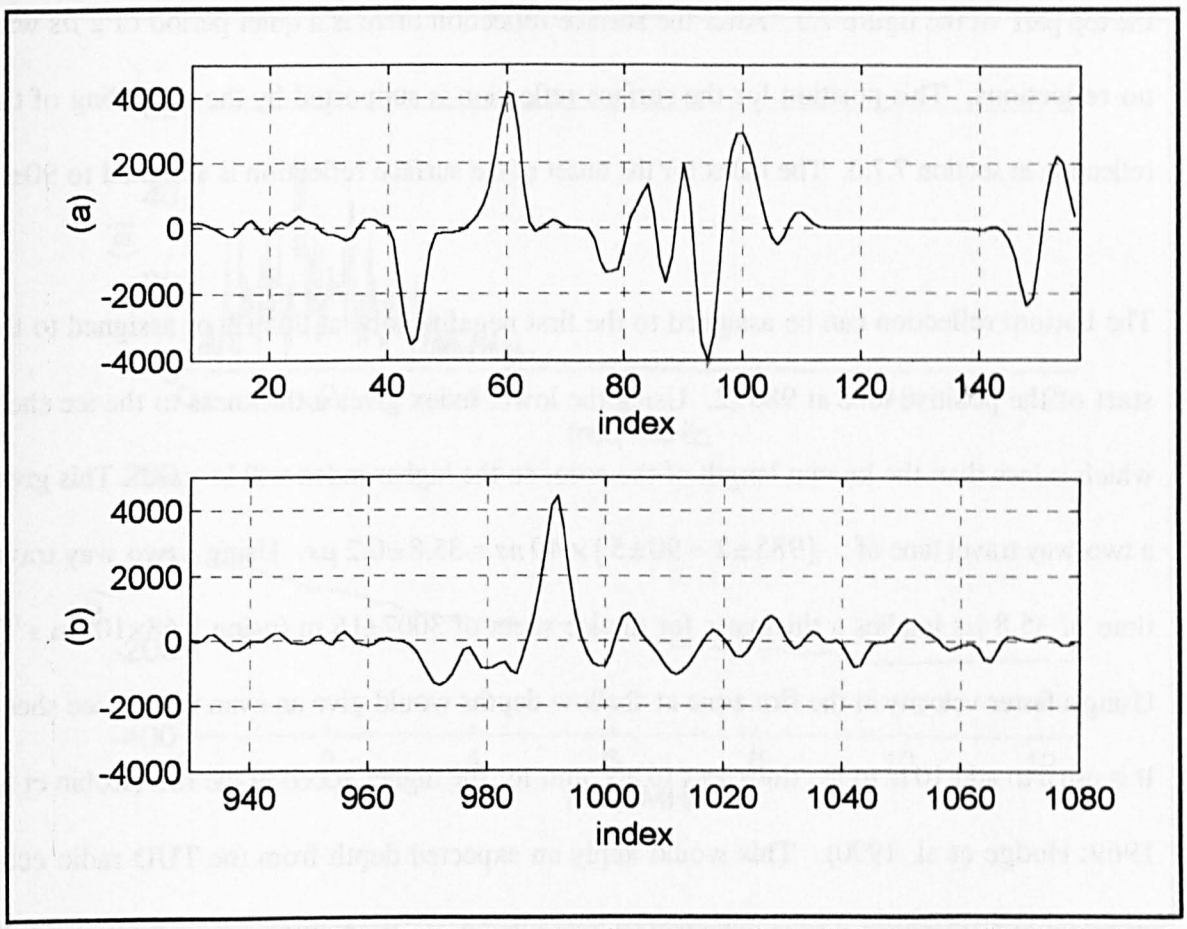

Figure 7.5 Portions of the TUD data: (a) the top portion of the trace, (b) the bedrock reflection

The surface and bedrock reflections are both at the interface from a lower to higher impedance material. Therefore the shape of the reflected wavelet should be the same. It would therefore be tempting to assign the surface reflection to the energy between indices 40 and 60. This would give it the same characteristic shape (an initial negative lobe and a subsequent positive lobe) seen in the bedrock reflection, although there is a surprising difference in the relative sizes

of the negative and positive lobes of the reflection from the bedrock.

However figure 7.3 has shown that the surface reflection is actually in the more complex reflection seen between indices 80 and 110. This energy is a combination of the surface reflection and another source of energy which can be seen as continuous horizontal lines across the top part of the figure 7.3. After the surface reflection there is a quiet period of 2 μs with no reflections. This position for the surface reflection is supported by the modelling of the reflection in section 7.7.d. The index for the onset of the surface reflection is assigned to 90±5.

The bottom reflection can be assigned to the first negative lobe at 965±2, or assigned to the start of the positive lobe at 985±2. Using the lower index gives a thickness to the ice sheet which is less than the known length of the core, so the higher index will be used. This gives a two-way travel time of: $(985\pm2 - 90\pm5)\times 40\,ns = 35.8\pm0.2\,\mu s$. Using a two way travel time of 35.8 μs implies a thickness for the ice sheet of 3007±16 m (using 1.68×10^{8} m s^{-1}). Using a faster velocity in the firn zone at shallow depths would give an even thicker ice sheet. It is usual to add 10 m to the thickness to account for the higher speed in the firn (Robin et al. 1969; Hodge et al. 1990). This would imply an expected depth from the TUD radio echo sounding of 3017±16 m. For comparison the measured depth to the top of the silty layer in the GRIP core was 3022.5 m, then there was 6 m of debris laden ice. The expected thickness of the silty ice is about 20 m which would give an ice sheet thickness at GRIP of 3042 m. Depending on the quantity of silt in the ice the reflection can be from the top of the silt layer or from the bedrock. It must be remembered that the GRIP borehole is 1.5 km north of the radar flightline N375. There is an expanded discussion on the accuracy of RES depth determination in Christensen et al. (1970, pp 9).

7.2.e Frequency content

In figure 7.6 below is shown the power spectrum and the unwrapped phase spectrum of the average trace in the TUD radar data. The model result will need to have the same power spectrum and phase spectrum to match the radio echo data. The Nyquist frequency is 12.5 MHz.

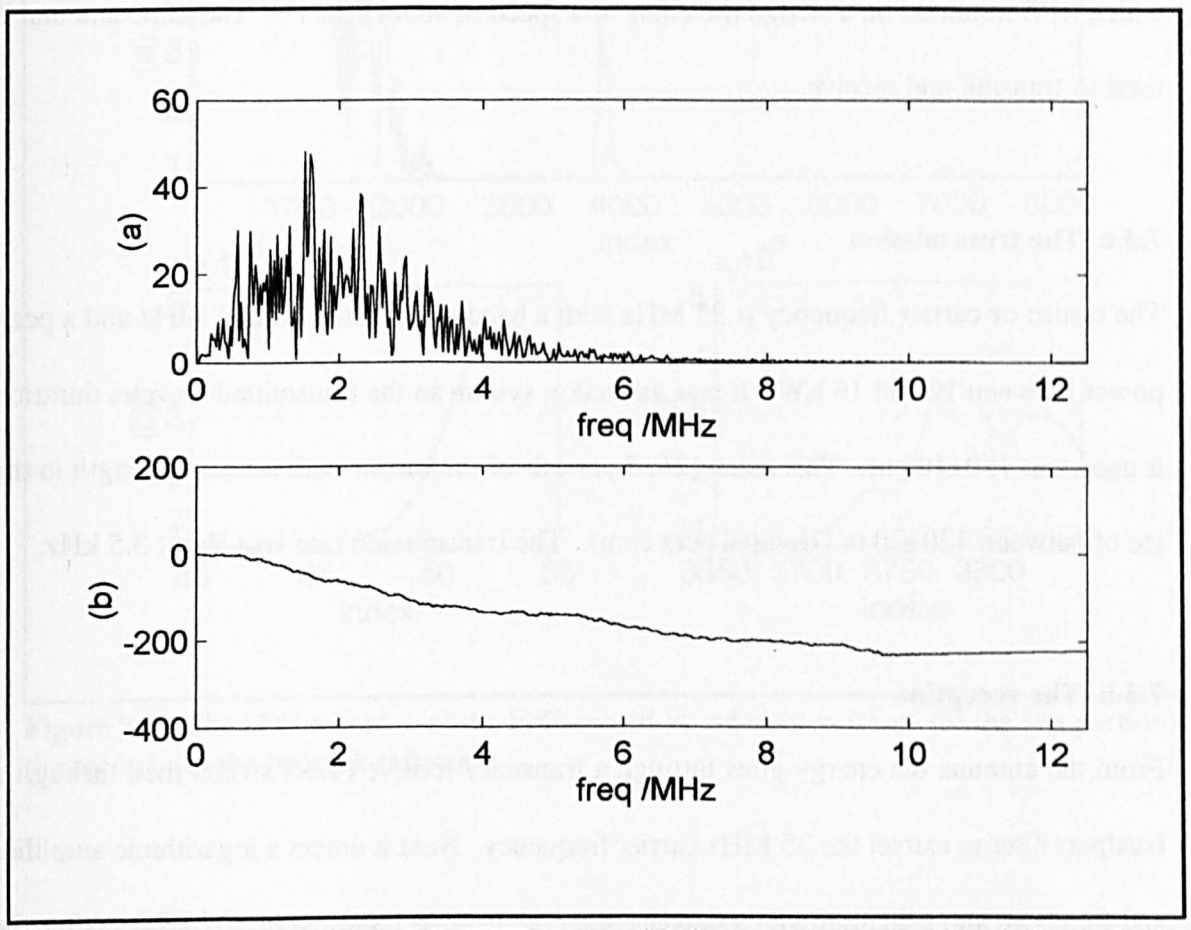

Figure 7.6 Frequency content of the TUD return. (a) the power spectrum in relative units (b) the unwrapped phase in radians.

The maximum in the power spectrum is at about 1.5 MHz, which is a period of 666 ns. This is not the duration of the transmitted wavelet (250 ns) which implies that some spreading has occurred, this is discussed further in section 7.7.b. In figure 7.6.b the unwrapped phase is displayed, unwrapping is explained in §4.7.c.i. In order to get an exact match to the RES data the model result will need to have the same magnitude and phase in the frequency domain.

7.3 The FPG burst pulse radio echo system

The Münster University team operated a radio echo system at GRIP. This was a burst transmitter designed to penetrate to a depth of 3000 metres. Due to the antenna resonating from the transmitted wavelet (recovery period) no reflections could be recorded from the first 1000 m (Hempel and Thyssen, 1992). The record was collected about 20 m from the borehole with a RES mounted on a sledge travelling at a speed of about 1 m s^{-1} . The same antenna is used to transmit and receive.

7.3.a The transmission

The centre or carrier frequency is 35 MHz with a bandwidth of the order 1 MHz and a peak power between 12 and 16 kW. It was an analog system so the transmitted wavelet duration is uncertain 750±100 ns. This means 26±5 periods of the carrier with a wavelet length in the ice of between 120±20 m (Hempel pers com). The transmission rate was about 3.5 kHz.

7.3.b The reception

From the antenna the energy goes through a transmit / receive (T/R) switch then through a bandpass filter to extract the 35 MHz carrier frequency. Next it enters a logarithmic amplifier and then goes into a digitiser with a sampling interval of 10 ns (Nyquist of 50 MHz). After the digitiser the traces are summed. The summation is of 2048 returns. As in the TUD the summation is after the filtering of the received trace.

7.3.c The post processing

L.Hempel has provided a trace in its raw form and in its form after processing. The raw trace will be looked at first to show the arrivals of the surface and bedrock reflections. In figure 7.7 below the entire raw trace is shown, below it are the top portion of the trace and the bedrock

reflection.

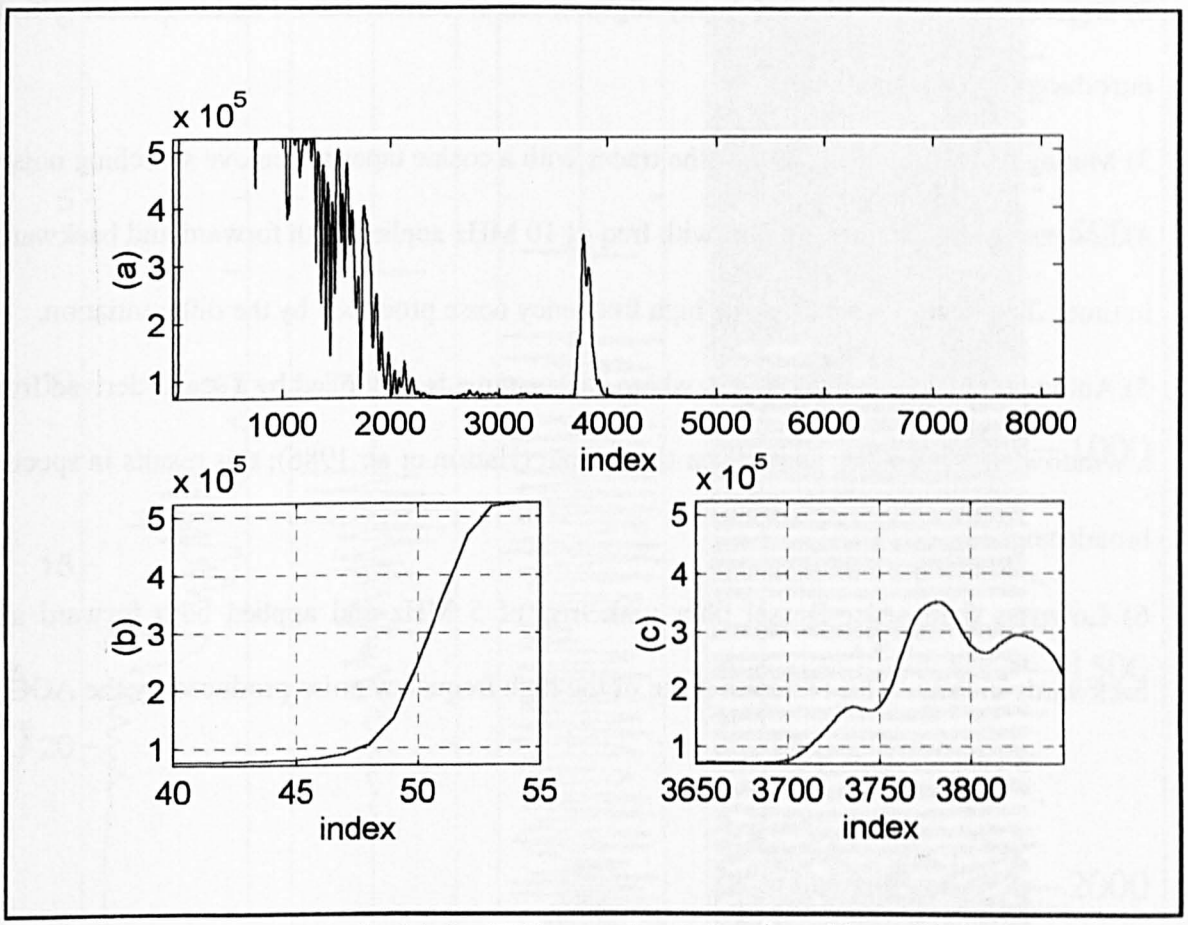

Figure 7.7 The FPG record. (a) the FPG record vs index Δt = 10 ns, (b) the top portion of the record, (c) the bedrock reflection.

I do not know when the sweep for the FPG trace started in relation to the transmitted wavelet. As the sledge rests on the surface it can be assumed that the surface reflection starts immediately the transmitted wavelet starts. Hempel and Thyssen (1992) calculate an ice thickness of 3050±26 m, which if they use the standard 10 m correction and a velocity of 1.68×10^8 m s^{-1} implies a t_{twtt} of 36.2 μs. This means that the top pick and the bottom pick are separated by 3620 indices; reasonable values would be 47 and 3667.

The following post processing was carried out by Hempel to obtain the wiggle plot form:

1) Shifting of traces to remove time shift due to cables etc.

2) Differentiation filter to sharpen any edges or features in the record and to remove offsets introduced by the amplifiers.

3) Muting of beginning and end of the traces with a cosine taper to remove switching noise.

4) Lowpass 6 th order Bessel filter with freq of 10 MHz applied both forward and backwards in time. This removes some of the high frequency noise produced by the differentiation.

5) Automatic Gain Control (AGC), where each sample is multiplied by a scalar derived from a window of 51 samples centred on the sample (Hatton et al. 1986); this results in spectral broadening.

6) Lowpass 6 th order Bessel filter with freq of 5 MHz and applied both forward and backwards in time. This removes some of the high frequency noise produced by the AGC.

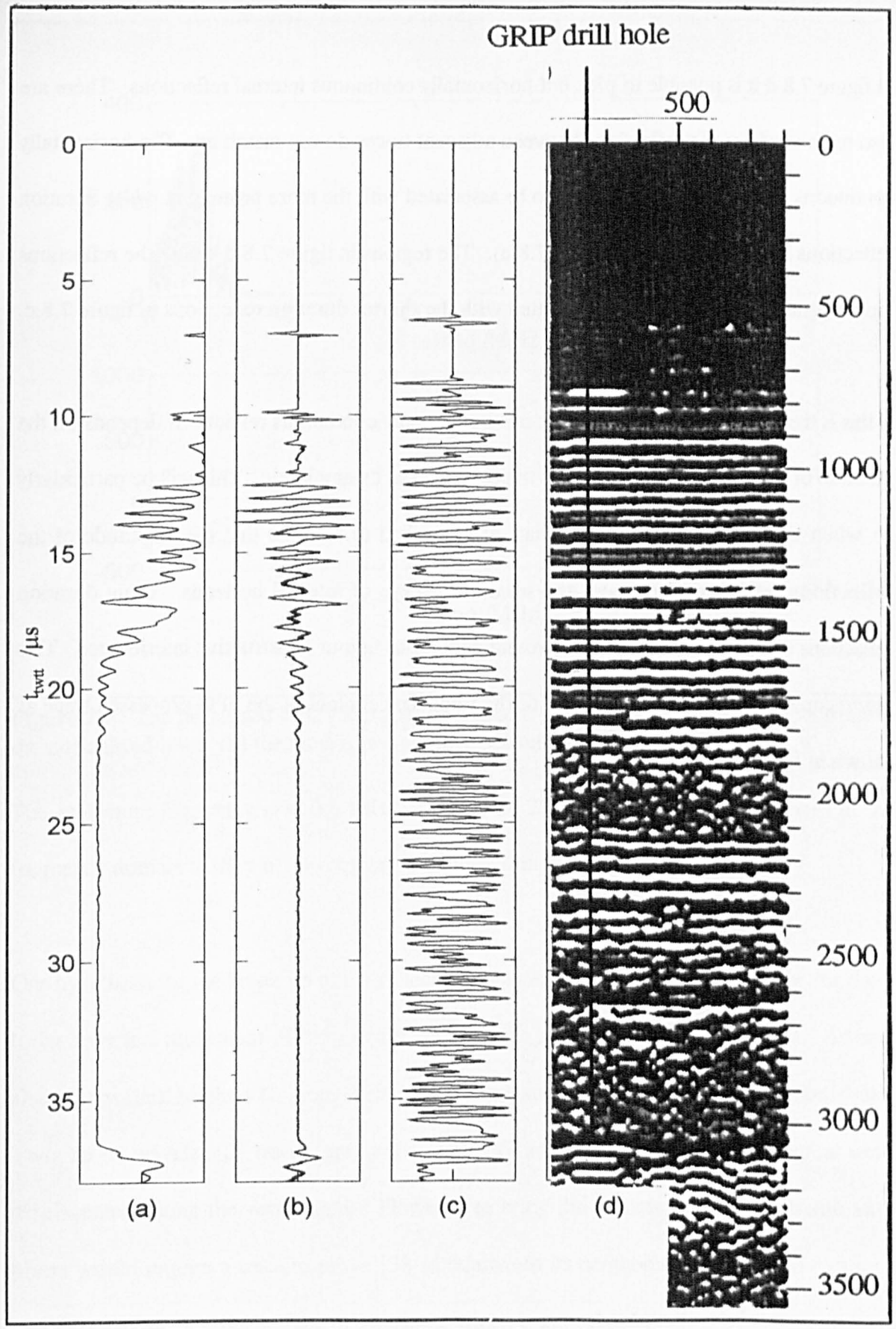

Figure 7.8 The FPG record. (a) the normalised raw form of the FPG record vs time, (b) the record vs time after simple single differentiation without any filtering. (c) the record vs time after the sophisticated processing by Hempel described above (d) the radio echo profile from Hempel and Thyssen (1992) on a depth scale in metres.

In figure 7.8.d it is possible to pick out horizontally continuous internal reflections. There are also regions where the reflections between adjacent traces do not match up. The horizontally continuous internal reflections appear to be associated with the more prominent wider duration reflections in the single trace (figure 7.8.c). The regions in figure 7.8.d where the reflections are not continuous appear to be associated with the shorter duration reflections in figure 7.8.c.

If this is the case then the ability to pick out horizontally continuous reflections depends on the duration of the internal reflection in the traces as well as its amplitude. This will be particularly so when the individual traces have had AGC applied to them so that the amplitude of the reflections no longer influences the selection by eye of internal horizons. Long duration reflections will be formed where the ground conditions favour constructive interference. This discussion now requires a knowledge of the frequency content of the FPG processed trace as shown in figure 7.9 below.

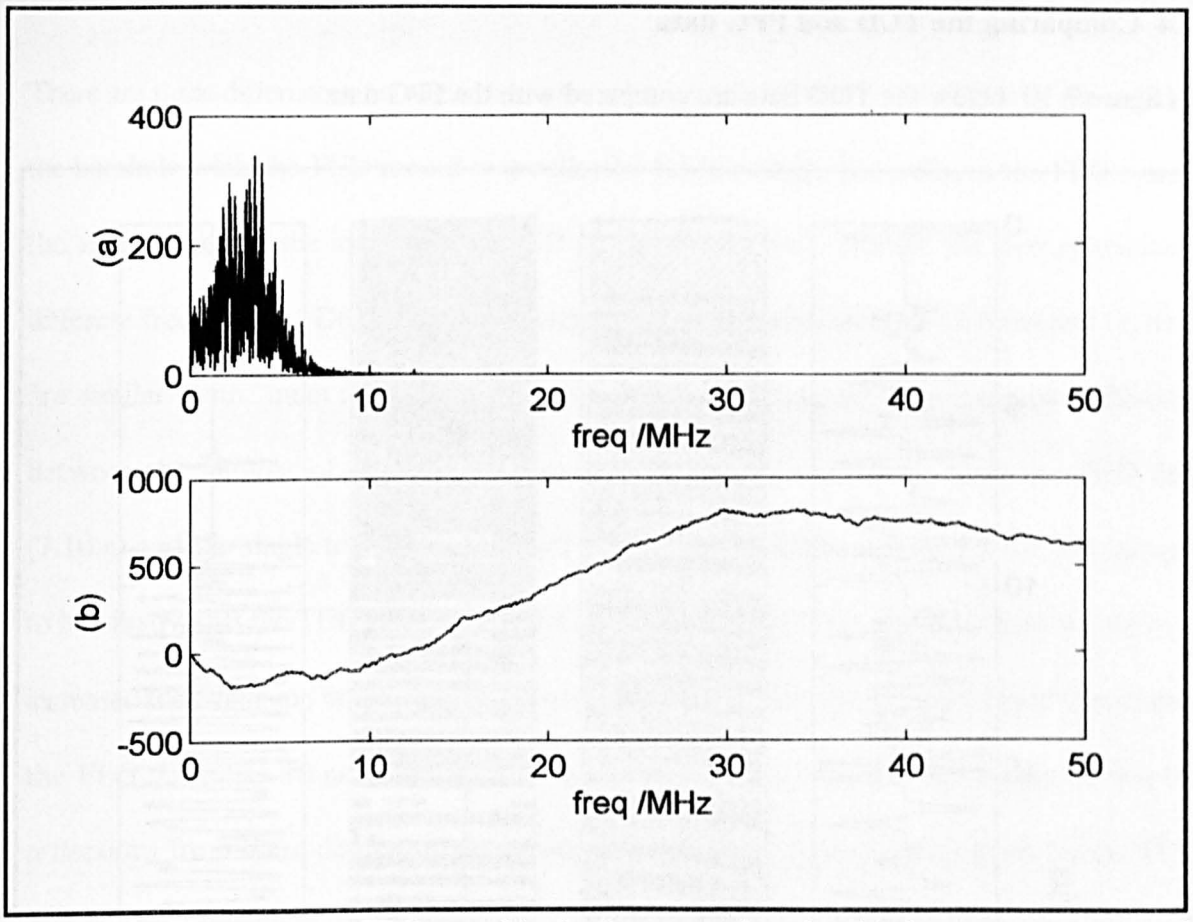

Figure 7.9 The processed FPG record in the frequency domain. (a) the power spectrum of the normalised trace (b) the unwrapped phase spectrum in radians.

The maximum frequency is at 3.6 MHz, a period of 277 ns. The unwrapped phase in the frequency domain is shown, unwrapping is explained in §4.7.c.i.

One hypothesis for the break up of the reflections between adjacent traces would be for there to be a vertical movement of the antenna between the reception of the two traces. A small change in vertical height is far more likely to bring two small wavelength traces into antiphase. Two large wavelength traces are more likely to interfere constructively after a small displacement along the vertical axis. However to bring the dominant wavelength into anti-phase would require a trace to move 138 ns relative to its neighbour. This would require a vertical movement at the surface of 38 metres which is improbable.

7.4 Comparing the TUD and FPG data

In figure 7.10 below the TUD data are compared with the FPG data.

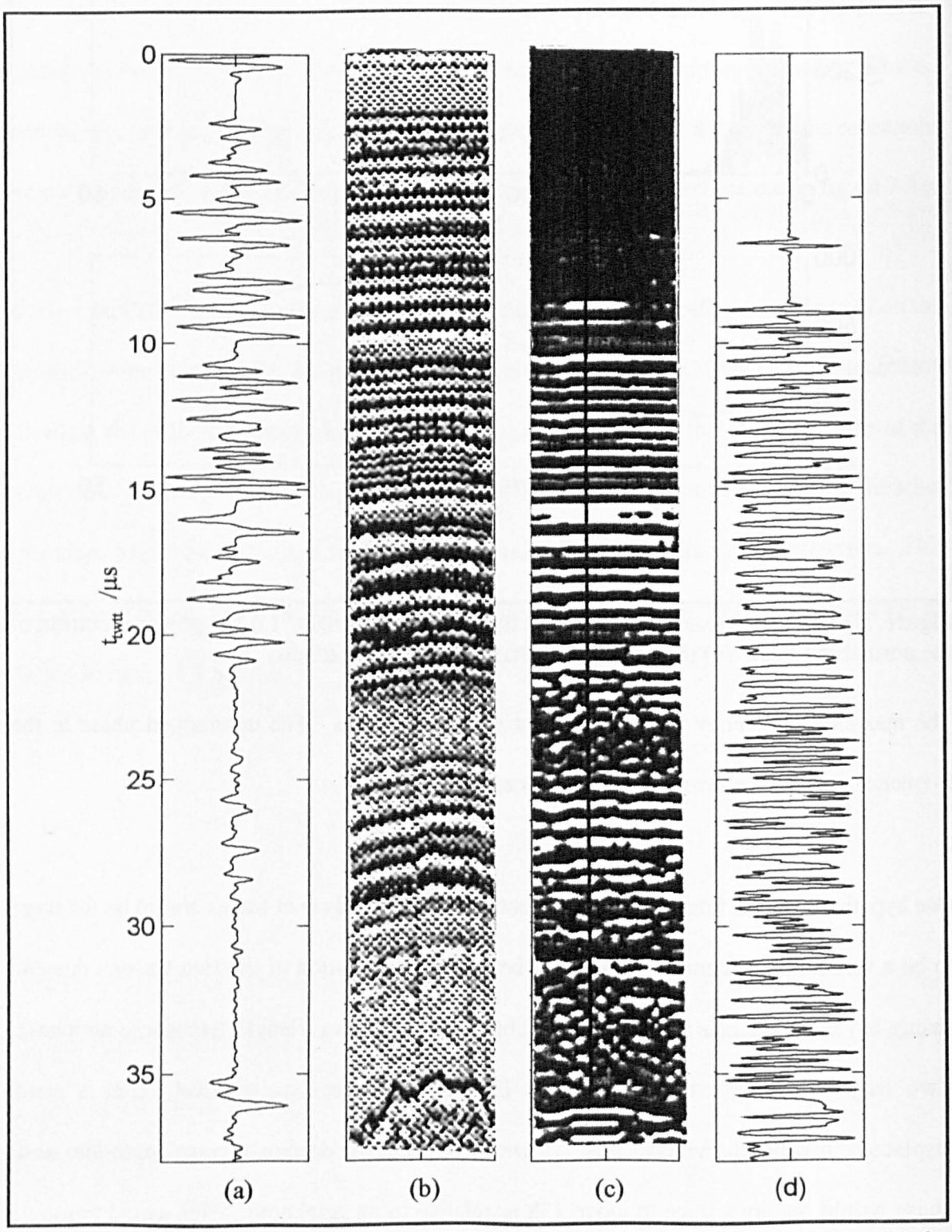

Figure 7.10 Comparing the TUD and FPG data (a) average TUD trace vs time, (b) the published TUD figure vs time (showing a 26 km wide section), (c) the published FPG figure vs depth (showing a 0.6 km wide section). (d) the provided FPG trace, processed by Hempel vs time. All the traces have been stretched to place the surface at the top of the figure and the bedrock at the bottom of the figure.

There are three differences between the radio echo systems: Firstly, the FPG was recorded at the borehole while the TUD record was collected 1.5 km away. Secondly, in the FPG system the antenna lies on the ice while the TUD system is airborne. Thirdly, the two systems use different frequencies. Despite these differences the radio echo sections (7.10.b) and (7.10.c) are similar, with "quiet regions" near 23 μs and 32 μs. However there is a great difference between the number of internal reflections visible on the single trace from the TUD data (7.10.a) and the single trace from the FPG data (7.10.d). Three reasons for this are thought to be: firstly, that the TUD has not had AGC applied to it; AGC on the TUD data would have increased the amplitude of the reflections in the low amplitude times ("quiet times"); secondly the FPG trace has 10 ns sampling, four times that of the TUD; thirdly, it may be that the reflections from these depths are not continuous and the long horizontal travel by the TUD during the summation may mean that when the traces are summed there is destructive interference in these regions. The TUD trace is the summation of 4096 returns over a distance of 138 m while the FPG trace is the summation of 2048 returns over a distance of order 1 metre. It is also possible that if the TUD system receives shorter duration reflections from these "quiet" regions and if the aeroplane is experiencing vertical displacement then it would be possible for destructive interference to occur.

It has been suggested that the absence of strong reflectors late in the TUD trace (summation of 4096 returns over a distance of 138 m) is due to the presence of folding near the base of the ice sheet. In that case there will be no continuous horizons from which reflections can occur. This then raises the problem of the many internal reflections seen in the FPG trace (summation of 2048 returns over 1 m). It may be that the reflections gathered within a horizontal distance of 1 m can stack constructively. However the reflections gathered within a horizontal distance

of 138 m stack destructively. This analysis, given time, could be extended to reveal details about the size of the folding in the ice sheet.

There is certainly scope for research into the effect on the positions and strength of the internal reflections and their horizontal continuity as a function of the amount of averaging of the traces. Such an investigation is not possible in this thesis due to the lack of radar data available.

7.5 The Ice Core

7.5.a The Drilling and Logging.

Drilling started in the summer of 1989 using the ISTUK drill system (Johnsen et al. 1994). The drilling fluid used was a hydrocarbon called D60 with a Chloro-Fluoro-Carbon densifier called F113 (Gundestrup et al. 1994). The combined liquid was denser than ice so that any ice chips produced floated. The drilling continued over the next three summers 1990 to 1992.

A fibreglass tube was used to case the borehole to a depth of 96 m. The core was brittle between 800 and 1300 m, coinciding with the upper limit of air hydrate formation. Silt was encountered at a depth of 3022.5; there followed 6 metres of debris laden basal ice. At this depth there was a vast increase in the force required to break off the cores. This force was breaking the cable. Therefore drilling stopped at a depth of 3028.65 m on 12th July, 1992.

The GRIP drill hole did not deviate more than 3^0 from the vertical (Johnsen et al. 1994) and less than one metre of core was lost in the drilling process (Dansgaard et al. 1993).

It is unknown what thickness of ice there may be between the base of the borehole and the

bedrock. Three other boreholes on the Greenland ice cap provide clues: at Camp Century there was 17 m of silt (Robin et al. 1969); at Dye 3 there was 25 m of silt (Gundestrup et al. 1984) and at GISP2 there was 13 m of silt (Gow et al. 1997). All three sites are shown on figure 7.1.

The core pieces recovered at GRIP had a diameter of about 10 cm and could be up to 2.5 metres long. Each recovered core was placed on a wooden tray and moved into the core buffer.

Table 7.3 Drilling progress (from Johnsen et al. 1994)

Period	Depth /m
25th June 1990 to 6th August 1990	surface to 769
4th June 1991 to 7th August 1991	769 to 2321
27th May 1992 to 12th July 1992	2321 to 3028

The cores were processed in a series of underground chambers on the site. The layout of the underground chambers is shown in figure 7.11.

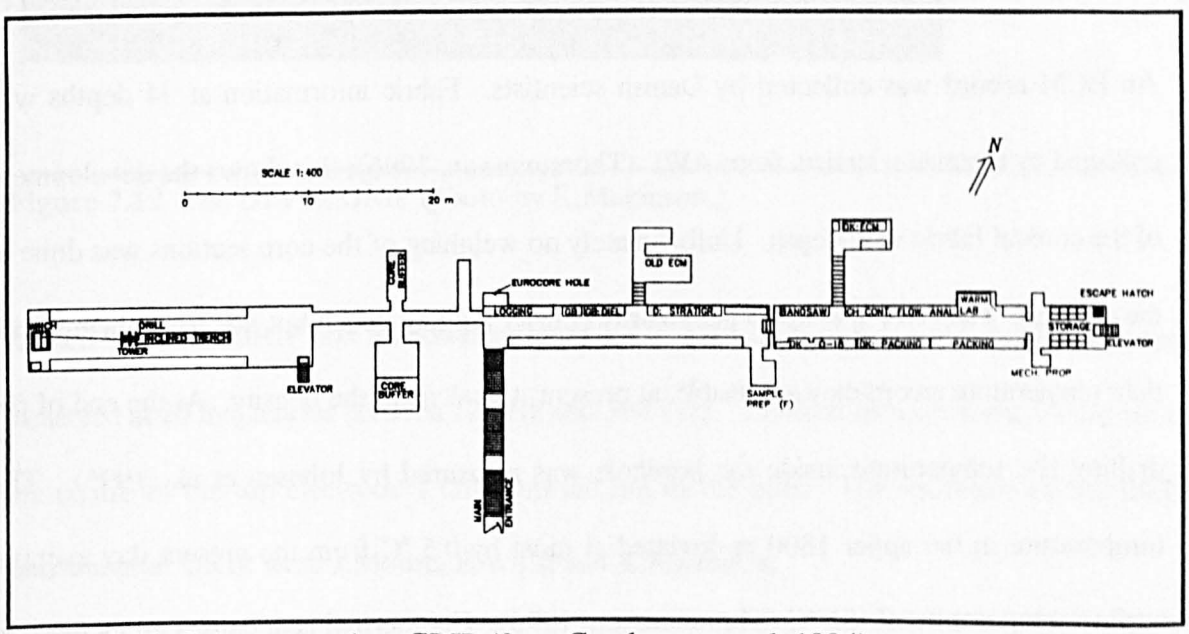

Figure 7.11 Science trench at GRIP (from Gundestrup et al. 1994)

Each core was taken from the core buffer and had a stratigraphic log done to it. This involved reassembling any broken pieces and drawing a pencil line down one side. The core was then passed on to the DEP. In the DEP the cores were processed before being cut into 55 cm lengths. The DEP records were labelled after the bag that the top of the core would go into.

Table 7.4 DEP processing progress

Summer Period	Position of the DEP in the processing trench	Bag Numbers Logged by DEP
1990	Core comes from buffer, gets stratigraphic log, then German 4 probe ECM, then DEP, then others.	G270 to G1272
1991	Core comes from buffer, gets stratigraphic log, then DEP, then others	G1277 to G1692 Then left out brittle zone, so jumped to do bags: G2304 to G4221
1992	Core comes from buffer, gets stratigraphic log, then into buffer (3-4 cores), then DEP, then others	First did the brittle zone G1696 to G2360 then G4148 to G5504

The shallowest measurement done by the DEP was at 137.98 m and the deepest measurement was at 3028.62 m.

An ECM record was collected by Danish scientists. Fabric information at 34 depths was collected by German scientists from AWI (Thorsteinsson, 1996); this shows the development of the conical fabric with depth. Unfortunately no weighing of the core sections was done at the drill site. The AWI operated a gamma ray density logging bench but due to problems with their temperature record they are unable, at present, to calculate the density. At the end of the drilling the temperature inside the borehole was measured by Johnsen et al. (1995). The temperature in the upper 1800 m deviated at most by 0.5 °C from the present day average surface temperature of -32 °C (Thorsteinsson, 1996). Geothermal heat causes an increase in

the temperature to -9°C as the base of the borehole is reached.

7.5.b The GRIP DEP

7.5.b.i The instrument

In the DEP used at GRIP the top electrode was split into one hundred and twenty 2 cm wide strips. For each measurement one top strip would be an "active" electrode while all the other top strips would be guard electrodes. Both the top and bottom electrodes were inside an

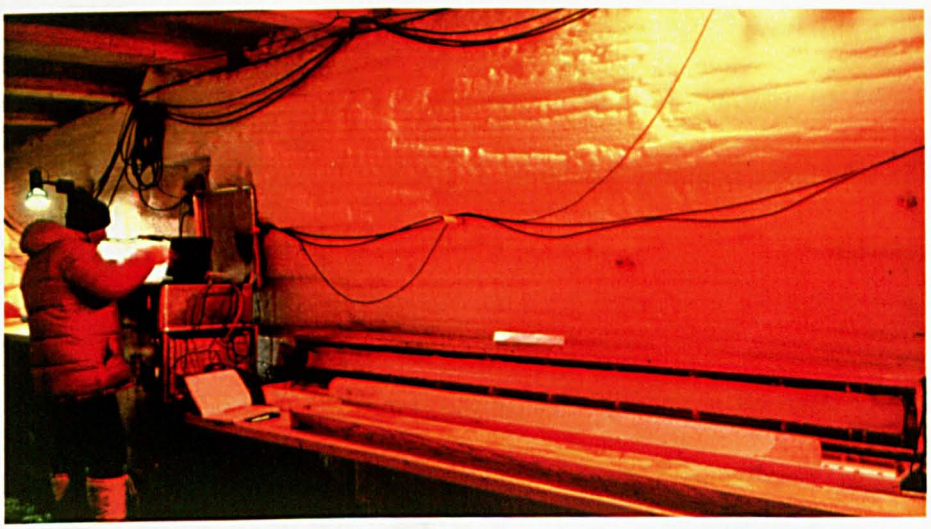

Figure 7.12 The DEP at GRIP (photo by K.Makinson.)

earthed box. The GRIP box is shown in figure 7.12. The conductance and capacitance were measured at 20 frequencies between 120 Hz and 300 kHz. The first measurement would have the centre of the top electrode 1 cm from the top of the core. The operators of the DEP instrument at GRIP were J.Moore, E.Wolff and K.Makinson.

7.5.b.ii The results

In figure 7.13 below are shown the capacitance and conductance measured on one length of core.

The temperature during logging was measured by thermistors inside the logging box and was stored in the header of the data files. Figure 7.14 below shows the range of temperatures recorded during the logging. The temperature varies between extremes of -8.669°C (while measuring core number 1147) and -27.17°C (while measuring core number 1739), but mainly lie in the range -15 to -25 °C.

7.5.b.iii Calculating the high frequency conductivity (σ_∞)

The processing used to extract the high frequency conductivity from the individual measurements of conductance is that of J.Moore. It involves fitting the measured data to a linearised Debye relation.

7.5.b.iv Temperature correcting the high frequency conductivity (σ_∞)

The value of σ_∞ calculated from the individual measurements depends on the temperature in the logging chamber during the measurements. The value of σ_∞ was corrected to a standard temperature of -15 °C using a similar process to that in section 6.6.d with equation 6.6. The temperature corrected value allows comparisons between measurements made on different days on different lengths of core.

During the 1991 season the DEP was near the front of the core processing line, see table 7.4. Therefore the core had not reached equilibrium temperature and the centre of the core was colder than the surface values measured by the thermistors in the DEP box. Therefore J.Moore

applied an additional temperature correction to the σ_∞ values determined for this field season.

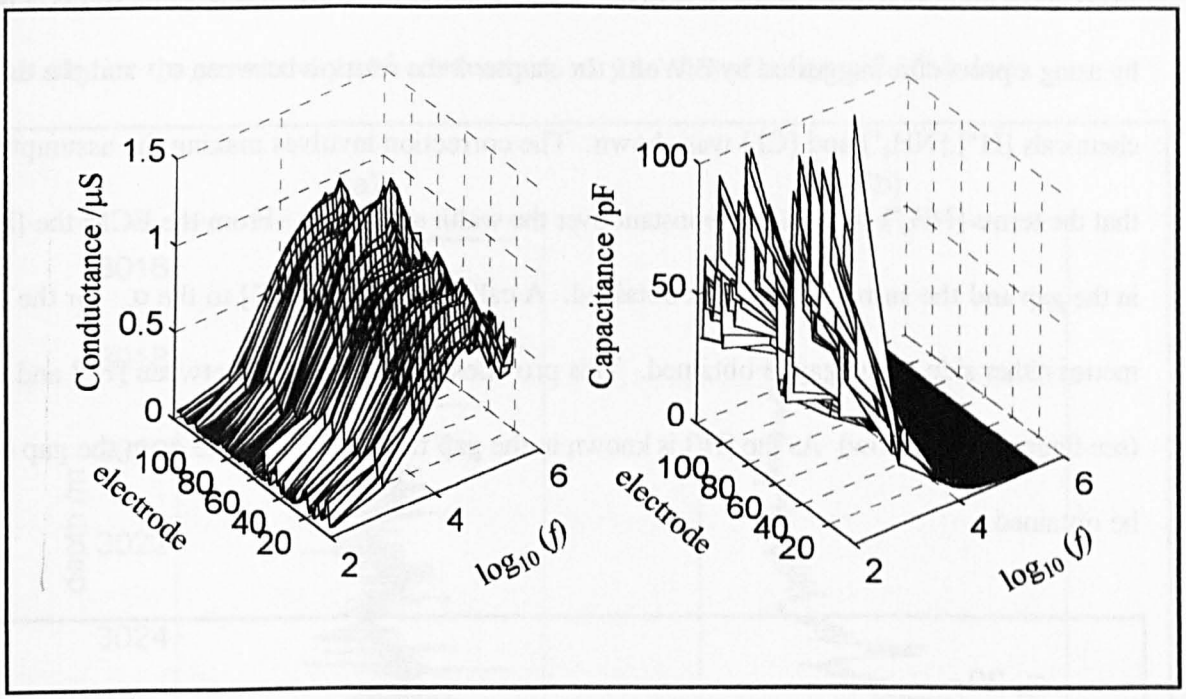

Figure 7.13 The values of conductance and capacitance for one length of the GRIP core.

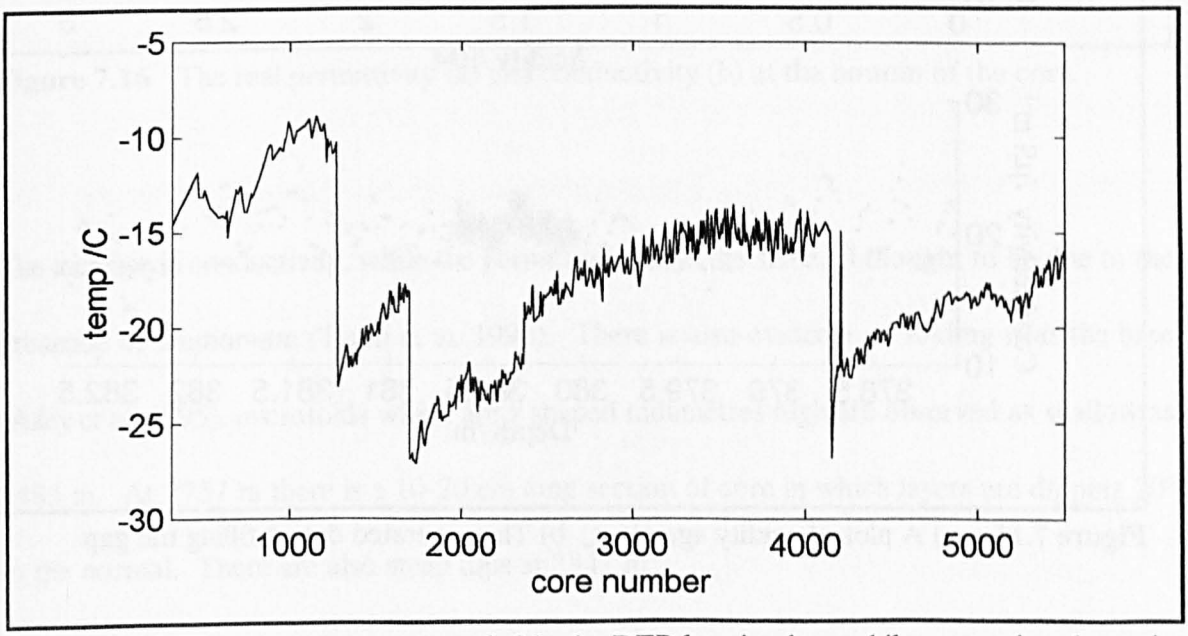

Figure 7.14 The temperatures recorded in the DEP logging box while measuring the entire core.

7.5.b.v Making a continuous record

There are a number of gaps in the high frequency conductivity record. These gaps can be filled by using a procedure suggested by E.Wolff. In chapter 3 the relation between σ_∞ and the three chemicals $[H^+]$,$[NH_4^+]$ and $[Cl^-]$ was shown. The correction involves making the assumption that the terms $[NH_4^+]$ and $[Cl^-]$ are constant over the width of the gap. From the ECM the $[H^+]$ in the gap and the surrounding ice is obtained. A calibration of the $[H^+]$ to the σ_∞ for the ten metres either side of the gap is obtained. This provides a linear relation between $[H^+]$ and σ_∞. (see figure 7.15.a below) As the $[H^+]$ is known in the gap this means that the σ_∞ in the gap can be obtained.

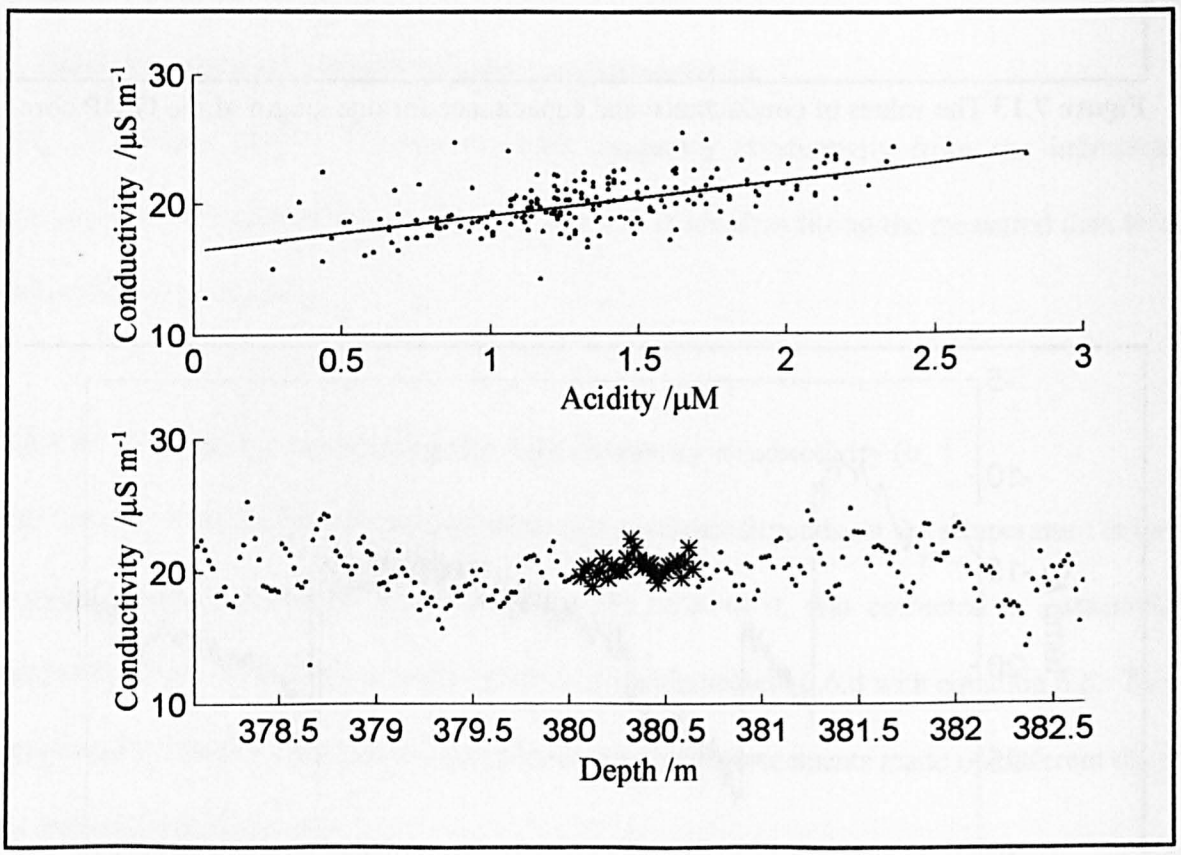

Figure 7.15 a) A plot of acidity against σ_∞ b) The generated data * filling the gap

7.5.b.vi The bottom part of the DEP record

At a depth of 3022.5 m the ice recovered started to contain silt. When the DEP is measuring the silty ice the permittivity and conductivity vary as shown in figure 7.16 below.

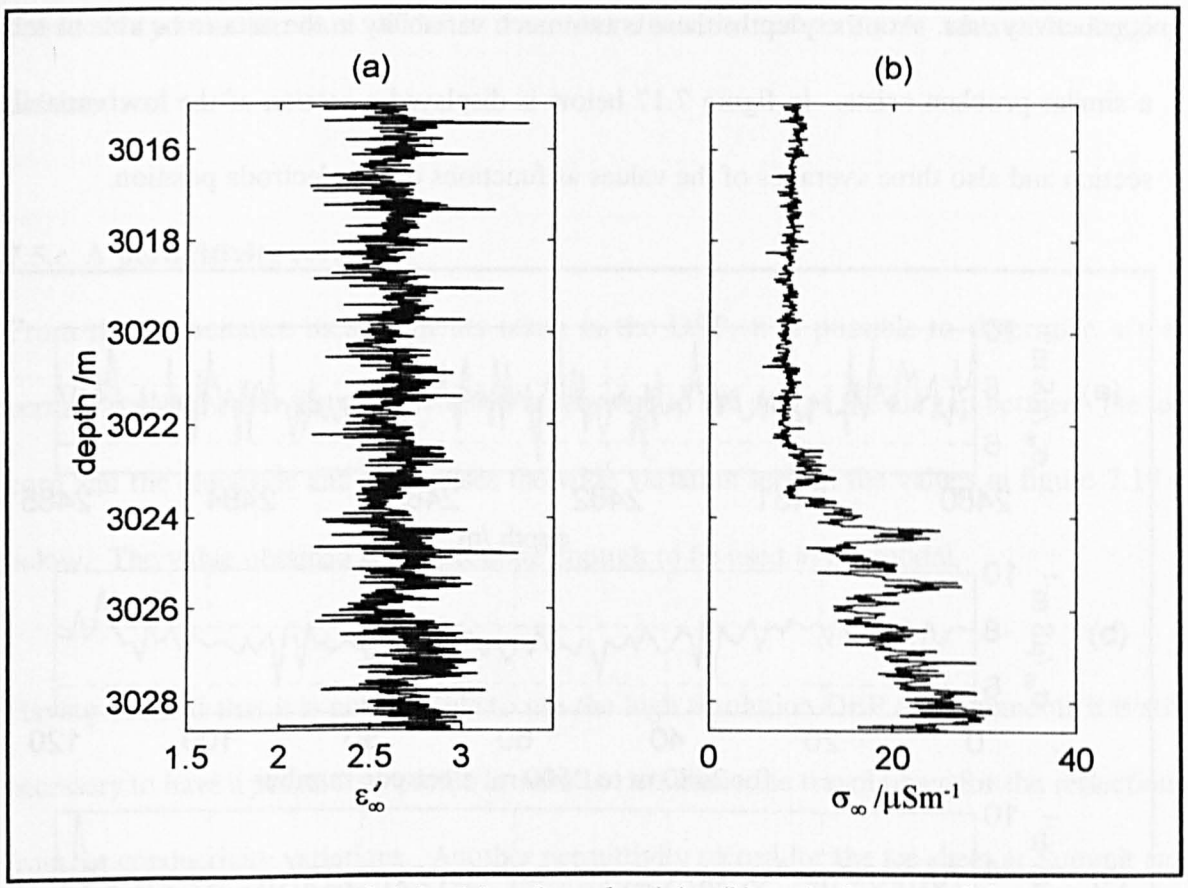

Figure 7.16 The real permittivity (a) and conductivity (b) at the bottom of the core.

The increase in conductivity, while the permittivity stays the same, is thought to be due to the presence of ammonium (Tison et al. 1998). There is also evidence of folding near the base (Alley et al. 1995), microfolds which are z shaped millimetres high are observed as shallow as 2483 m. At 2757 m there is a 10-20 cm long section of core in which layers are dipping 20° to the normal. There are also steep dips at 2847 m.

7.5.b.vii Periodicity in the DEP data

When looking at the low variability section between the depths of 2479 and 2532 m of the 1992 data Wolff et al. (1995) noticed a slight dependence on the electrode position for the conductivity data. At other depths there is too much variability in the data to be able to tell if a similar problem exists. In figure 7.17 below is displayed a section of the low variability section and also three averages of the values as functions of the electrode position.

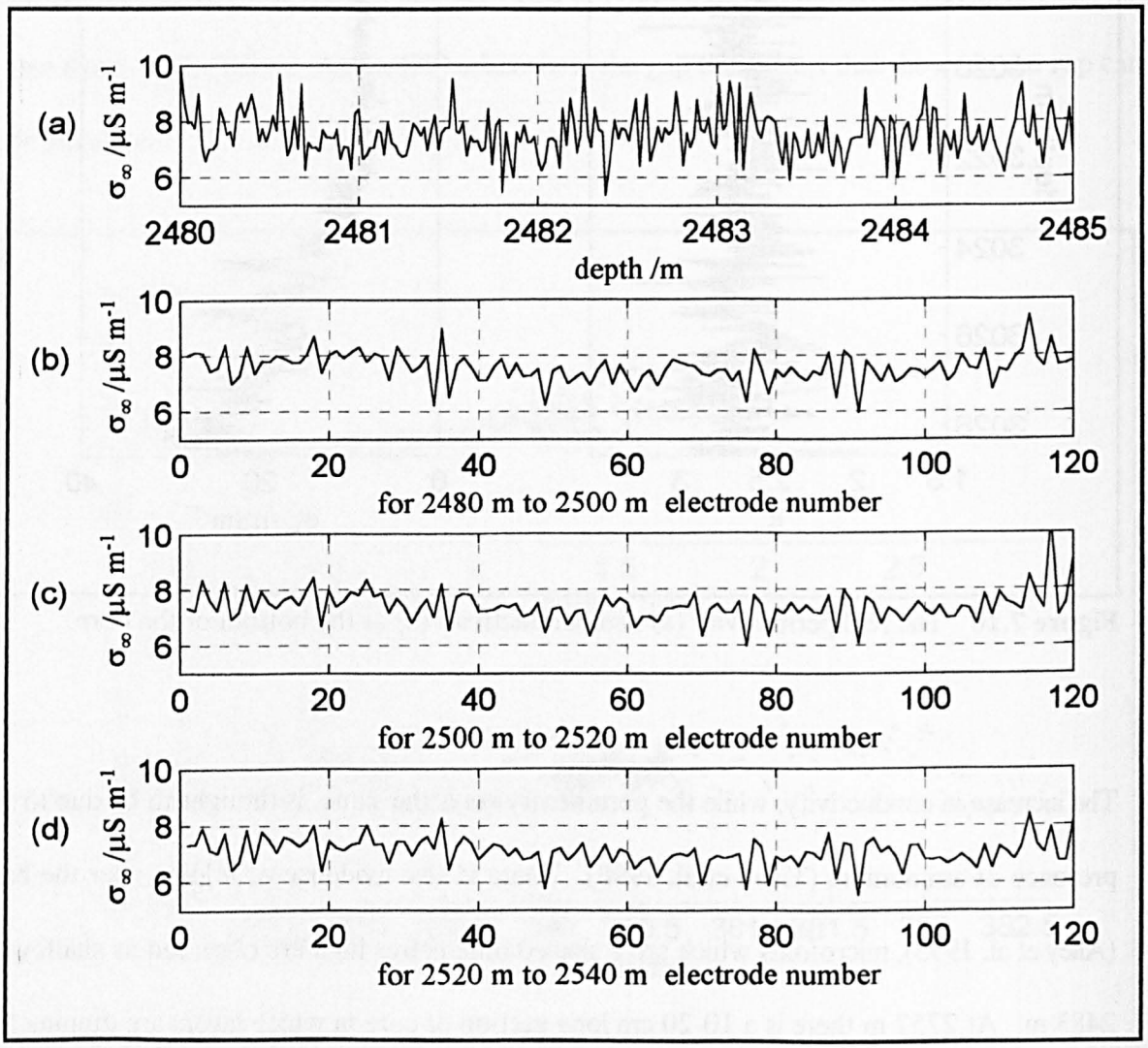

Figure 7.17 a) A low variation section of the DEP record. b) c) & d) The mean values measured at each electrode for three different 20 m long sections.

The mean values with electrode position do show a similarity over the three twenty metre long sections. This does imply a dependence on position and an additional uncertainty of order 1 μS m^{-1} in the σ_∞. and a periodicity of 2.4 m in the σ_∞.

7.5.b.viii Relating surface values to underground values

In order to convert the σ_∞ measured at the surface into the values at depth the same temperature correction is used as in the Berkner record (§6.6.d). This causes an increase in the conductivity near the base where it is warmer than the temperatures where the logging occurred.

7.5.c A permittivity record

From the capacitance measurements taken in the DEP, it is possible to determine a real permittivity. However the value obtained is sensitive to the size of the air gap between the ice core and the electrode and this causes the wide variation seen in the values in figure 7.19.c below. The value obtained is not accurate enough to be used in the model.

Having decided that it is not possible to use the high resolution DEP measurements it is still necessary to have a permittivity profile in order to determine the travel times for the reflections from the conductivity variations. Another permittivity record for the ice sheet at Summit can be obtained from the density record of the GISP2 core which was drilled about 30 km from the GRIP core (Gow et al. 1998). These are shown in table 7.5 below. The values are obtained by weighing the sample in isooctane then correcting to the temperature in the ground. The relative real permittivity at GISP2 varies between 3.14 and 3.16.

Table 7.5 Permittivity from GISP2

depth /m	density / kg m^{-3}	relative permittivity
250	914.1	3.141
500	919.0	3.156
1000	920.0	3.159
1500	920.5	3.160
2000	920.3	3.160
2250	919.7	3.158
2500	919.0	3.156
2750	918.0	3.153
3000	917.2	3.150

There is also a density record available from Site A, 70° 45′ N, 35° 57.5′ W which is 3145 m above sea level and about 170 km south of Summit (Alley and Koci, 1988). This record is shown in figure 7.18 below. From this density the permittivity can be calculated near the surface using the relation of Glen and Paren (1975) eqn 3.17 in chapter 3.

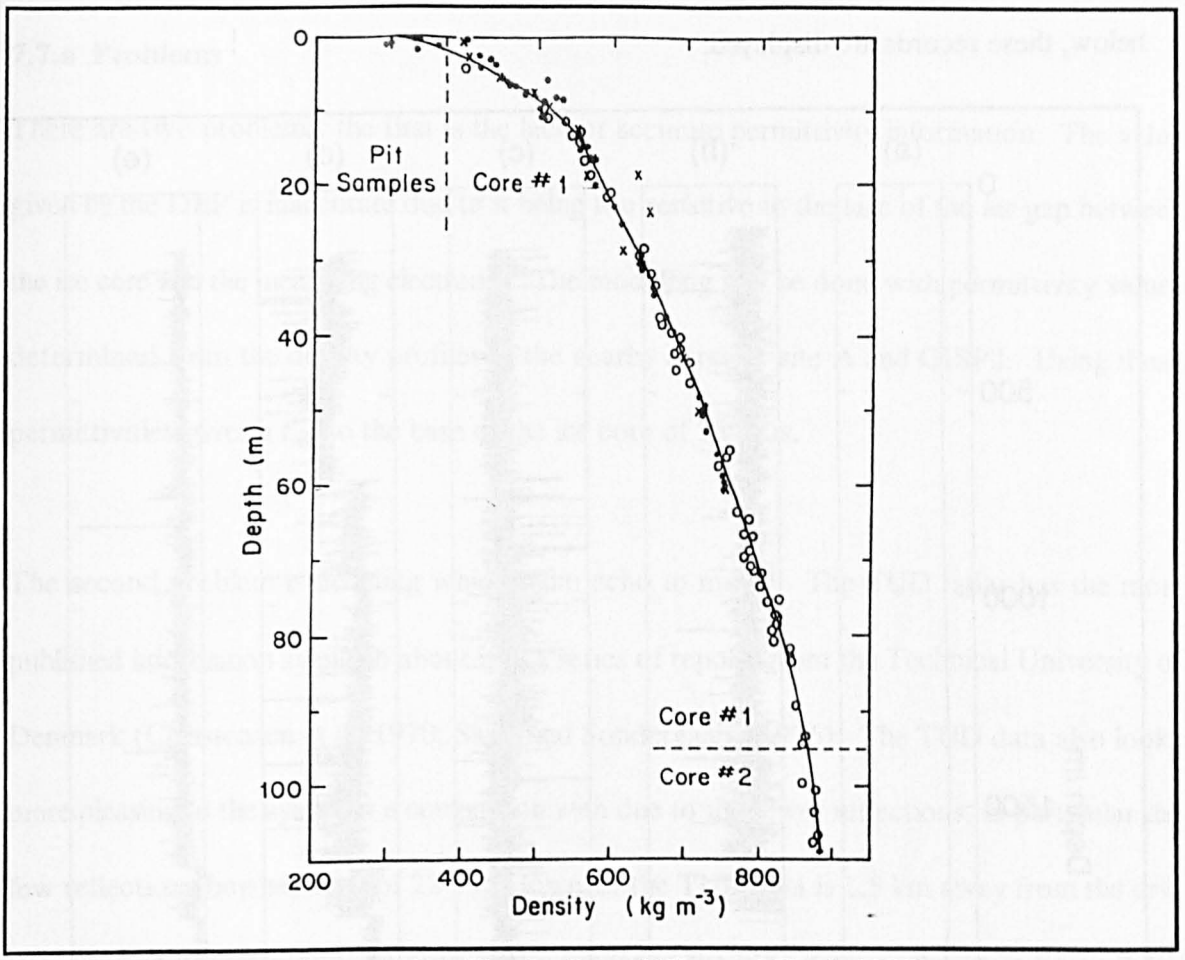

Figure 7.18 The density record at Site A , from (Alley and Koci, 1988).

7.6 Summary of ice core information for GRIP

In table 7.6 below is a summary of all the records available for GRIP.

Table 7.6 Information available

Variable		Depth range		Number of gaps in the record of a given size.		
		Top	Base	5 to 10 cm	0.5 to 1 m	5 to 10 m
DEP	σ_∞	148.045	3028.6	98	9	1
	ε_∞	148.045	3028.6	98	9	1
Borehole Temperature		0	3026.5	Assumed to be smooth function		
ECM		101.3	3022.2	6	2	0

Some of these gaps are due to degradation of the data on the magnetic disks. In figure 7.19 below, these records are displayed.

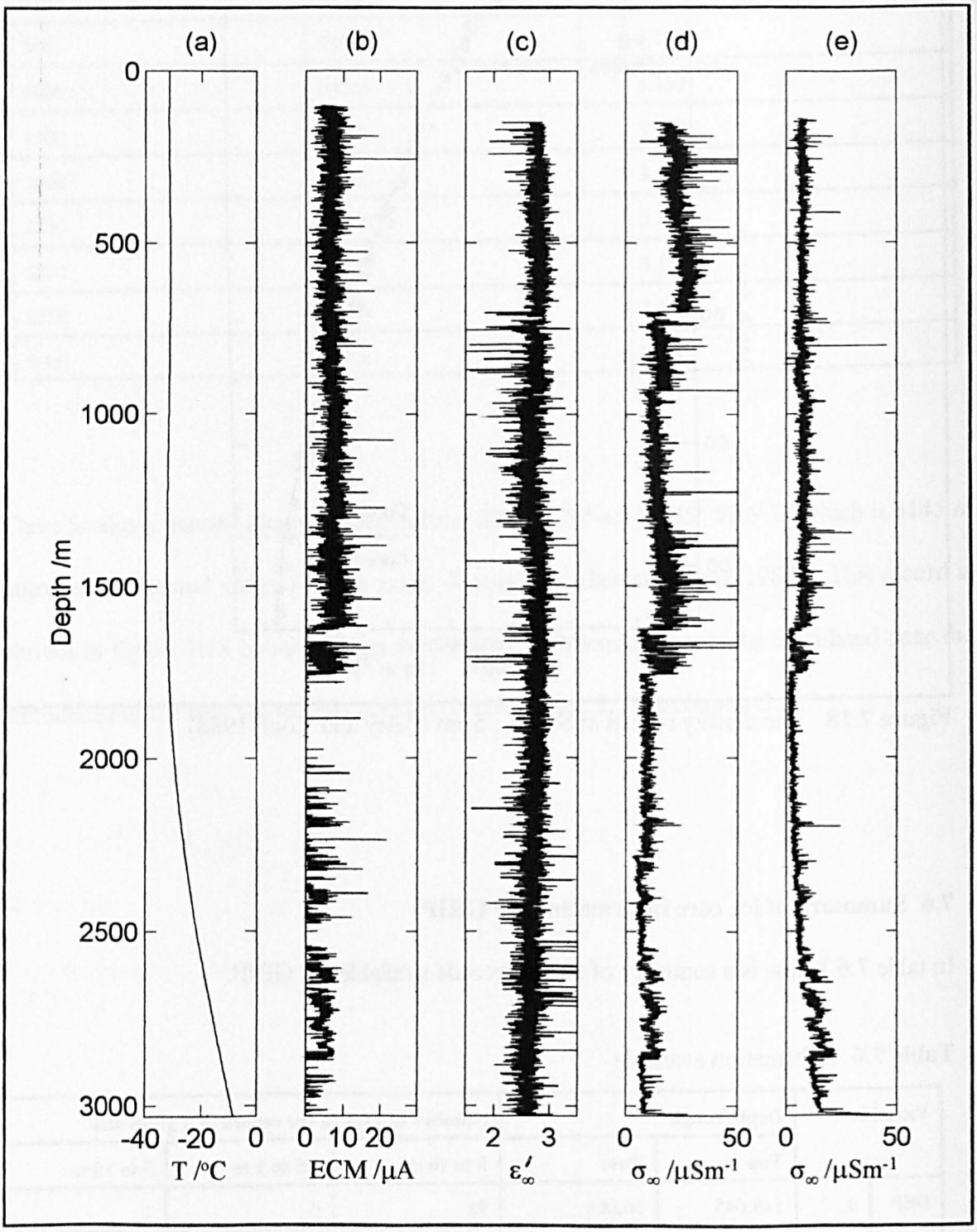

Figure 7.19 a) Borehole temperature, b) ECM (at -15 °C), c) $\varepsilon'_{r\infty}$ determined from the DEP measurements prior to any temperature correction, d) σ_∞ determined from DEP measurements prior to any temperature correction and e) σ_∞ at the ground temperature.

7.7 Modelling the Radio Echo

7.7.a Problems

There are two problems: the first is the lack of accurate permittivity information. The value given by the DEP is inaccurate due to it being too sensitive to the size of the air gap between the ice core and the measuring electrodes. The modelling will be done with permittivity values determined from the density profiles in the nearby cores of site A and GISP2. Using these permittivities gives a t_{twtt} to the base of the ice core of 35.8 μs.

The second problem is deciding which radio echo to model. The TUD radar has the most published information available about it in a series of reports from the Technical University of Denmark (Christensen et al. 1970; Skou and Sondergaard, 1976). The TUD data also looks more pleasing to the eye to do a comparison with due to the fewer reflections, in particular the few reflections beyond a t_{twtt} of 22 μs. However the TUD data is 1.5 km away from the drill site, though it does produce a profile very similar to the FPG data, as shown in figure 7.10. The FPG radar has no published information on it; most of the information I have has come from personal communication with L.Hempel. However there is a raw trace available for the FPG which should make it easier to model but matching up with such a raw trace will be very dependent on the correct modelling of spherical spreading which my models cannot do.

I have decided to do the comparison with the TUD radio echo mainly for the reason that it should be feasible to try to imitate the internal reflections at a t_{twtt} of 26 μs.

7.7.b A wavelet for the TUD radar

Two approaches will be looked at here to construct a TUD wavelet for the modelling. The first uses a totally artificial function to generate a 60 MHz wavelet with the correct characteristics. This will be called the "transmitted wavelet". In order to obtain the 4 MHz bandwidth an envelope is applied to the carrier monocycle wave which tapers off for the first and last quarter. This wavelet is shown in figure 7.20 below.

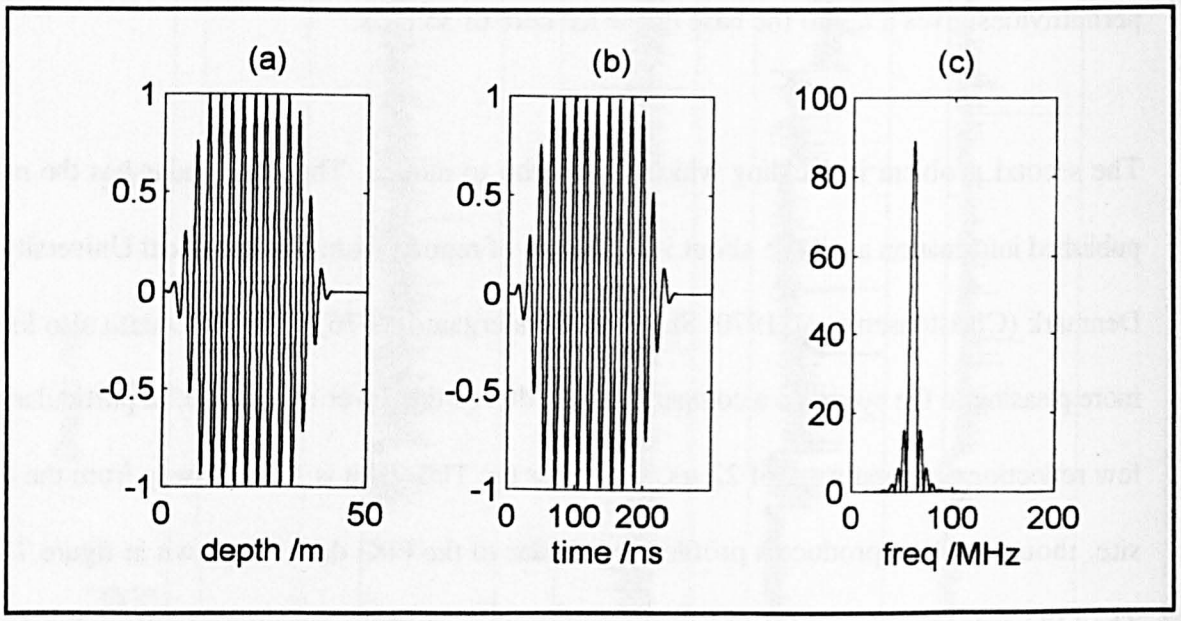

Figure 7.20 A wavelet for the TUD radar. a) as function of depth, b) as function of time, c) as frequency spectrum.

The second wavelet is generated from the TUD radar data using a zero phase function in a similar manner to that used in chapter six (§6.7.a.ii). This will be called the "zero phase wavelet" and can be thought of as the result of passing the transmitted wavelet through the ice sheet then through all the parts of the receiving system: linear amplifier, bandpass filter, logarithmic amplifier, differentiation, digitisation and finally differencing. In figure 7.21 below are shown the radar amplitude spectrum in the frequency domain, the smoothed amplitude spectrum and the resulting zero phase wavelet.

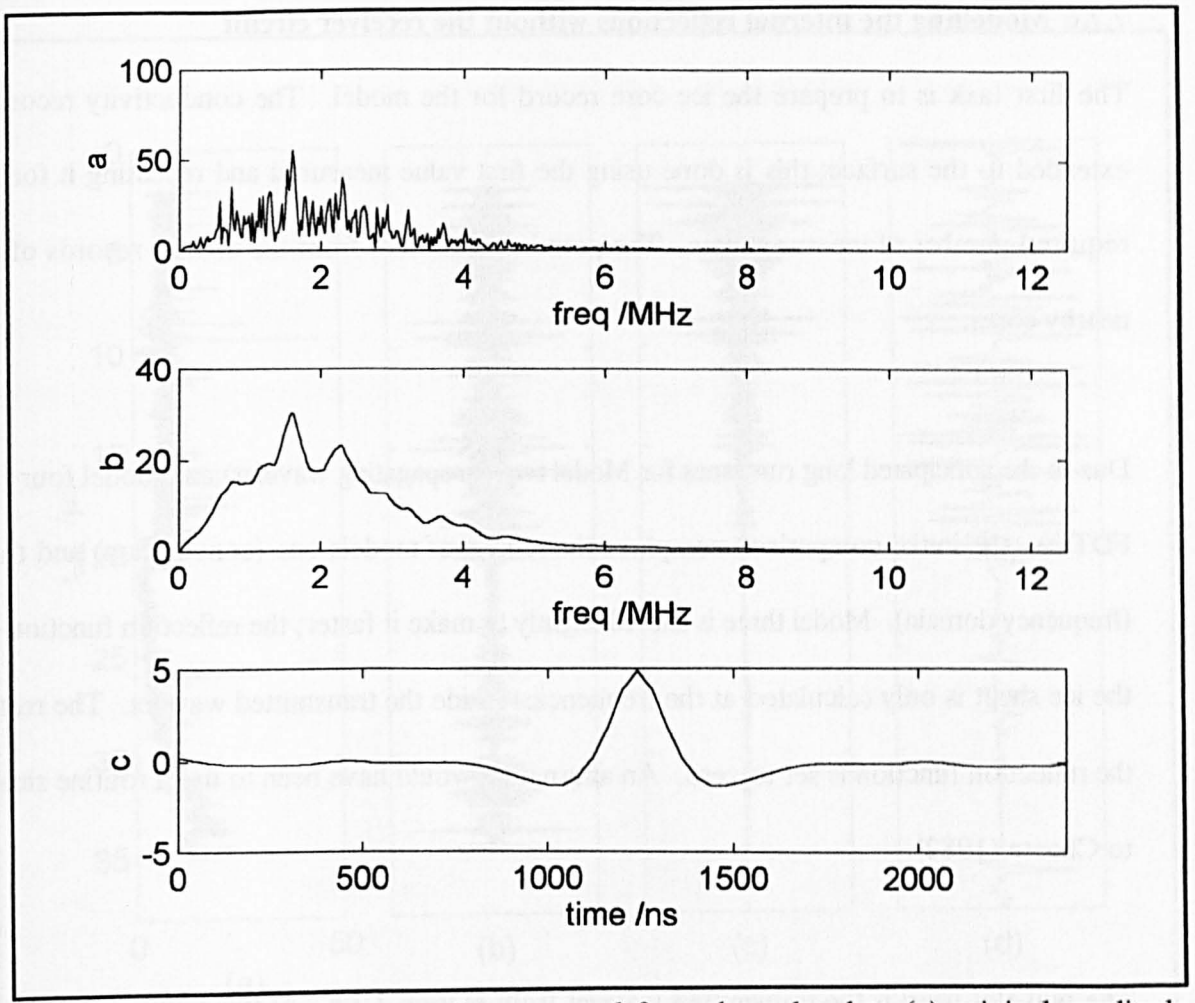

Figure 7.21 A zero phase wavelet generated from the radar data (a) original amplitude spectrum in the frequency domain (b) the smoothed amplitude spectrum, (c) the zero phase wavelet.

The zero phase wavelet has a duration greater than 500 ns. As the transmitted wavelet from the antenna has a duration of 250 ns this means that the wavelet energy has spread out during its journey to the recorder. It is not certain if the spreading has occurred during the transmission, in the ice sheet or in the receiver. If the spreading has occurred during the transmission or in the ice sheet it suggests that it may be necessary to do the modelling with a longer wavelet duration. If the spreading has occurred inside the receiver then the modelling of the reflections in the ice sheet should continue to be done with a 250 ns duration wavelet.

7.7.c Modelling the internal reflections without the receiver circuit

The first task is to prepare the ice core record for the model. The conductivity record is extended to the surface; this is done using the first value measured and repeating it for the required number of measurements. The permittivity comes from the density records of the nearby cores.

Due to the anticipated long run times for Model two (propagating wavelet) and model four (the FDTD), the initial comparison compares the results of models one (convolution) and three (frequency domain). Model three is altered slightly to make it faster; the reflection function for the ice sheet is only calculated at the frequencies inside the transmitted wavelet. The rest of the reflection function is set to zero. An alternative would have been to use a routine similar to Choate (1982).

The wavelet used is the transmitted wavelet from section 7.7.b. At this point no attempt is made to imitate the receiver circuit. In figure 7.22 below the conductivity has been converted from a depth scale to a t_{twtt} scale to allow easier comparison with the results. This conversion has been done using the permittivity profile of the model and the equations of section 5.3.b for a Goupillaud medium.

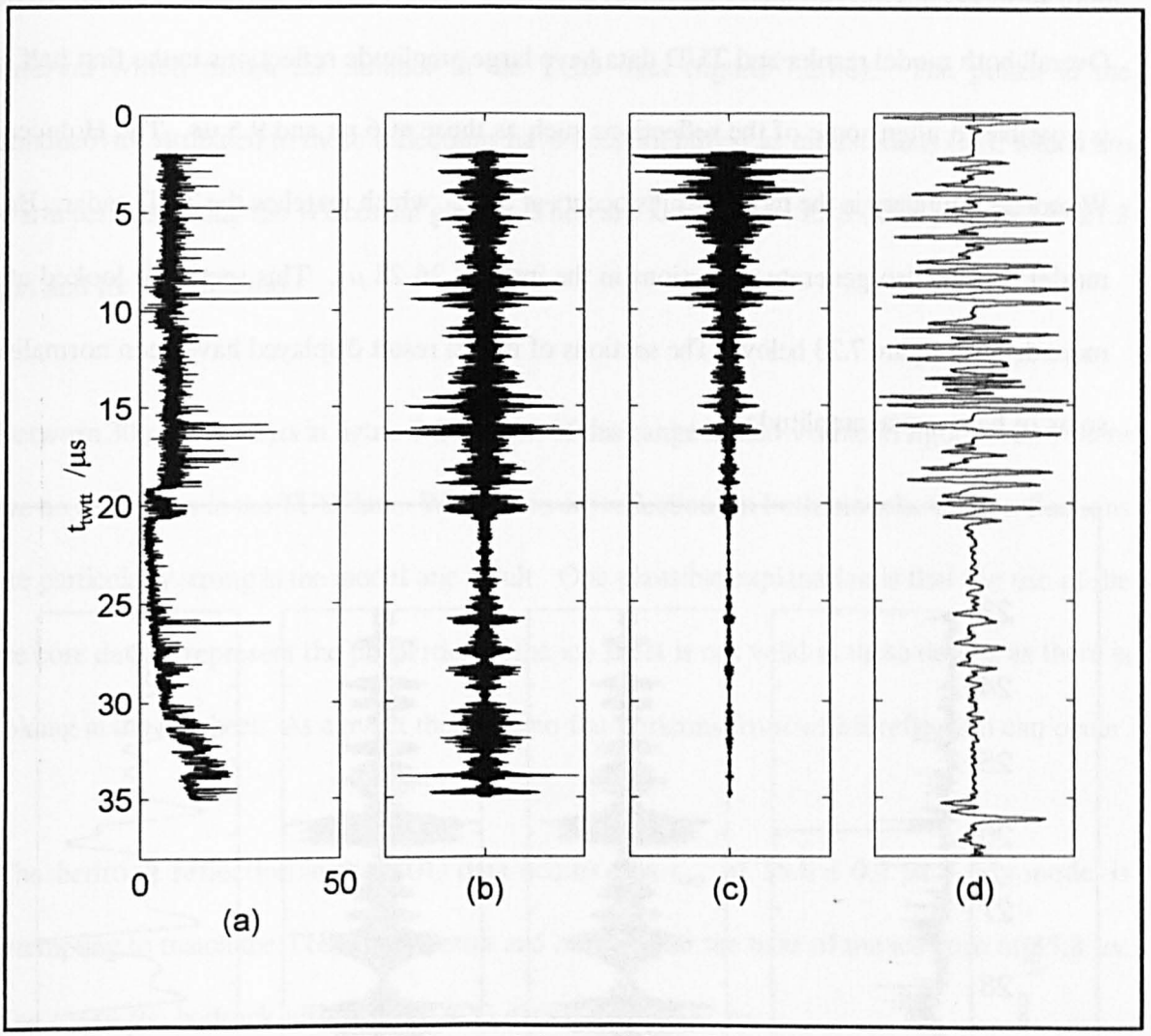

Figure 7.22 Comparing the TUD data and the model results (a) the conductivity record after conversion to a Goupillaud medium, (b) result of model one, (c) result of model three, (d) the average trace of the six TUD traces supplied.

Comparison of results from model one and model three

It can be seen in figure 7.22 that there is a noticeable difference in the results from model one and model three. The difference in the models is that model three includes absorption which is not included in model one. The absorption has reduced the amplitudes of the reflections from late travel times. Otherwise in the first half of the record the positions of the major reflections in the results from models one and three are the same. It is difficult to tell how similar the position of the reflections are in the second half as the results from model three are too weak.

Comparison of model results and TUD data

Overall both model results and TUD data have large amplitude reflections in the first half. It is possible to align some of the reflections such as those at 6 μs and 9.5 μs. The Holocene-Wisconsin boundary in the model results occurs at a t_{twtt} which matches the TUD radar. Both model results also generate reflections in the interval 26-28 μs. This section is looked at in more detail in figure 7.23 below. The sections of model result displayed have been normalised so as to have equal amplitude.

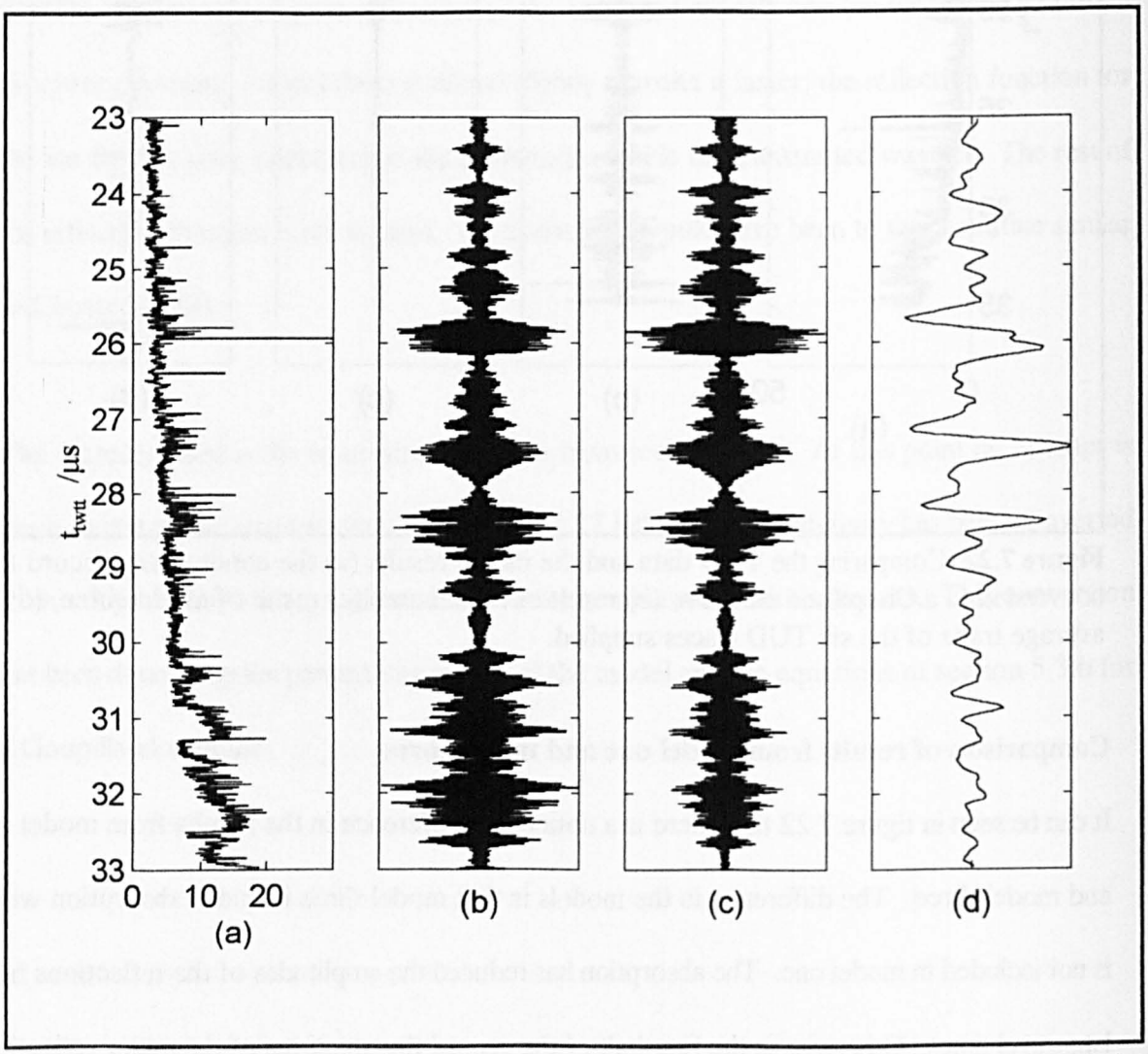

Figure 7.23 Comparing the lower interval of the TUD data and the model results (a) the conductivity record after conversion to a Goupillaud medium, (b) result of model one, (c) result of model three, (d) the average trace of the six TUD traces supplied.

In the model results (figure 7.23.b and 7.23.c) it is possible to pick out three reflections in this interval which match the number in the TUD data (figure 7.23.d). The peaks in the conductivity attributed to these reflections have been identified as interstadials (IS), which are warm periods during the Wisconsin glacial. They are identified as IS 8 (25.8 μs), IS 12 (27.3 μs) and IS 14 (28.3 μs).

Between 30 μs and 35 μs in figure 7.22 (a bit of this range is also visible in figure 7.23) there are no reflections in the TUD data. While there are reflections in both models, these reflections are particularly strong in the model one result. One plausible explanation is that the use of the ice core data to represent the properties of the ice sheet is not valid at these depths as there is folding in the ice sheet. As a result there are no flat horizons from which reflection can occur.

The bedrock reflection in the TUD data occurs at a t_{twtt} of 35.8 ± 0.2 μs . My model is attempting to match the TUD radar result and has a t_{twtt} to the base of the ice core of 35.8 μs. The t_{twtt} to the bedrock given by the FPG data is 36.2 ± 0.2 μs.

As there is no model two result it is not possible to examine the O'Doherty Anstey effect (O'Doherty and Anstey, 1971) as was done for the Berkner core (§5.7.c and §6.7.d).

Due to the similarity in the reflections generated by model one and model three only model one will be used for the rest of this chapter. In the next section an attempt is made to imitate the receiver electronics.

7.7.d Modelling surface reflection with the receiver circuit

In figure 7.4.a the surface reflection in one of the provided traces was shown. The surface reflection is a simple image of the transmitted wavelet after it has gone through the receiver. By feeding the transmitted wavelet into the receiver circuit a record similar to figure 7.4.a should be obtained. To recap the parts of the receiver circuit in the TUD radar are:

1) Transmit / Receive switch

2) Linear amplifier with a 20 MHz bandwidth

3) Filter amplifier (band pass) 4 MHz bandwidth centred on 60 MHz

4) Logarithmic amplifier

5) Differentiation

6) Digitisation, every 40 ns.

Then there is possible differencing which may have been applied to the trace.

Two receiver circuit models will be constructed: a simple receiver and a decay compensating receiver. The difference in the two circuit models is the way that they deal with the logarithmic amplifier. Both models exclude the initial bandpass filter from the circuit model as it was not possible to tune it accurately enough to avoid ringing in the time domain. Both circuit models give the same result for the surface reflection, see figure 7.24.

A simple receiver

This model does not attempt to imitate the amplification of the logarithmic amplifier, it only imitates its envelope generation effect. First the model result is normalised; then the magnitude of the Hilbert transform is taken to obtain the envelope; then this is filtered with a smoothing "box window" filter of duration 150 ns; it is differentiated, then resampled to 40 ns sample spacing. Then if required differencing according to equation 7.1 can be applied.

A decay compensating (or complex) receiver

This model attempts to imitate all of the components in the receiver circuit. This requires first supplying a decay to the model result. The model result is taken and normalised; then it is multiplied by a decay function of time (in μs) raised to the power -2 (the value used was tested in the range -0.1 to -3 with negligible difference in the receiver output); then it is converted into its magnitude; then a noise of value 1×10^{-8} is added; then it is converted into a dB value in the range 0 to -80; it enters the logarithmic amplifier using a linear equation $y = 0.018\ x + 1.53$ to give a value between 0.085 and 1.53. Finally, to replicate the smoothing effect of the logarithmic amplifier the result is smoothed with a 150 ns duration box window filter; it is differentiated; then resampled to 40 ns sample spacing. Then if required differencing according to equation 7.1 can be applied.

The model result obtained when using a 250 ns duration wavelet is shown in the figure below. In figure 7.24.a is the expected reflection, which is an image of the transmitted wavelet. Figure 7.24.b is the expected recorded signal after digitisation (both circuit models give the same result). Figure 7.24.c is what the reflection would look like after differencing and finally figure 7.24.d is the top portion of the provided trace.

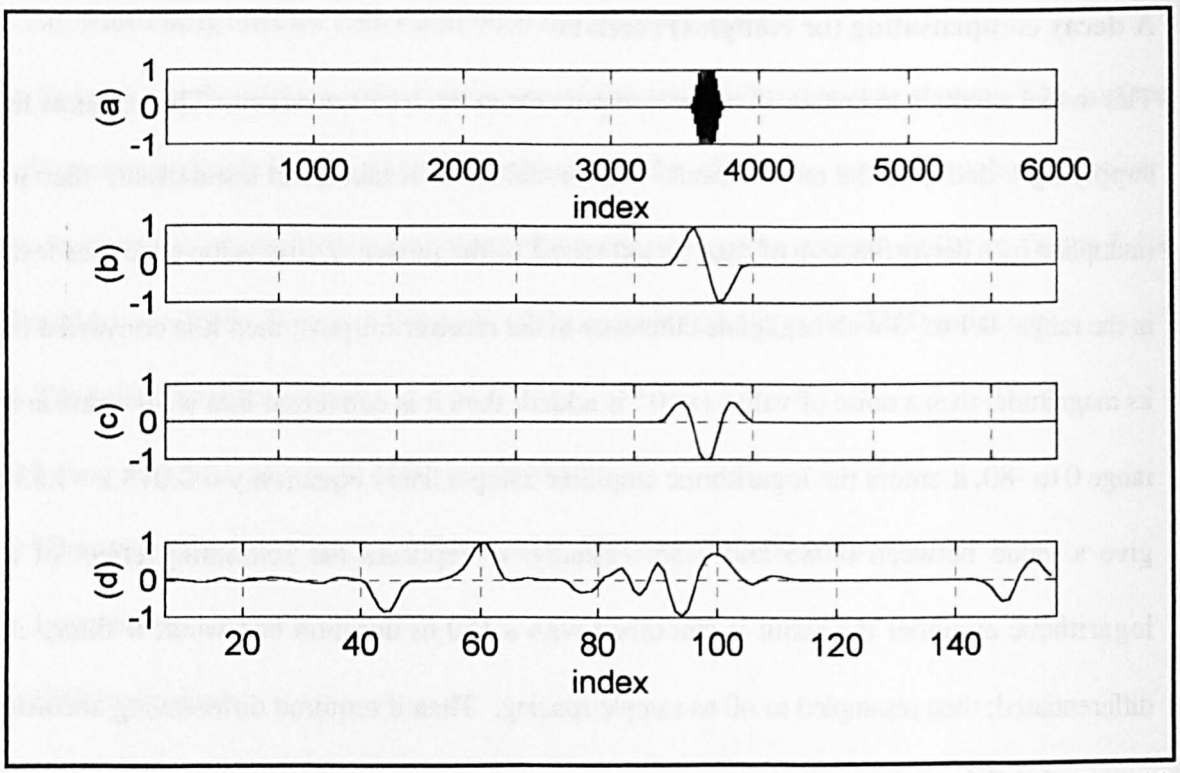

Figure 7.24 Comparing the TUD data and the model result (a) reflected 250 ns wavelet with $\Delta t = 1$ ns, (b) recorded wavelet shape with $\Delta t = 40$ ns, (c) wavelet after differencing operation (eqn 7.1) with $\Delta t = 40$ ns (d) top portion of TUD data, with $\Delta t = 40$ ns.

From a comparison of model results (7.24.b) and (7.24.c) with TUD data (7.24.d) it appears that (7.24.c) is the closest match to a reflection that may occur in (7.24.d) during the range of indices 80 to 110. Therefore it appears that the differencing operation (eqn 7.1) has been carried out on the traces.

A brief attempt has been made to model the bottom reflection. A variety of layer models were tried with the silt represented by a layer of increased conductivity (see figure 7.16) or a layer of increased permittivity. Such models give an initial lower amplitude reflection at the interface ice to silt followed by a subsequent higher amplitude reflection at the interface silt to bedrock. However none of the results was a successful match to the TUD data.

7.7.e Modelling the internal reflections with the receiver circuit

The results from model one in section 7.7.c is fed through the two receiver circuit models and the results compared with the TUD data. In figure 7.25 the entire record is compared.

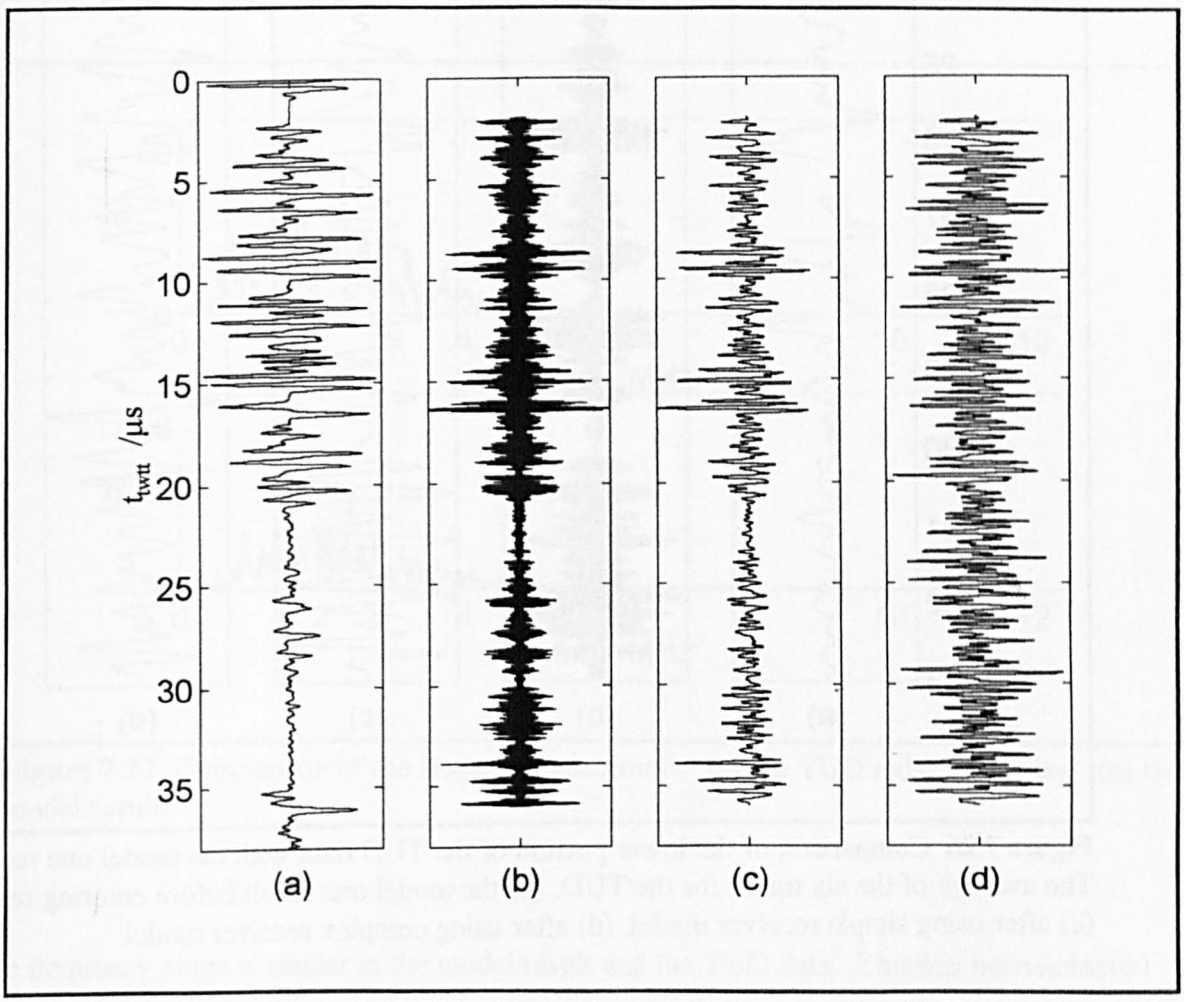

Figure 7.25 Comparison of the TUD data with the model one results (a) The average of the six supplied TUD traces, (b) model one result before entering receiver, (c) after using simple receiver model (d) after using complex receiver model.

The two receiver models have a different effect on the model result. The complex receiver increases the amplitude of the small reflections to produce a result with many more large amplitude reflections visible and it produced very similar results when model three was fed into it.

In order to compare the shape of the reflections the lower portion of the record is looked at in

figure 7.26 below.

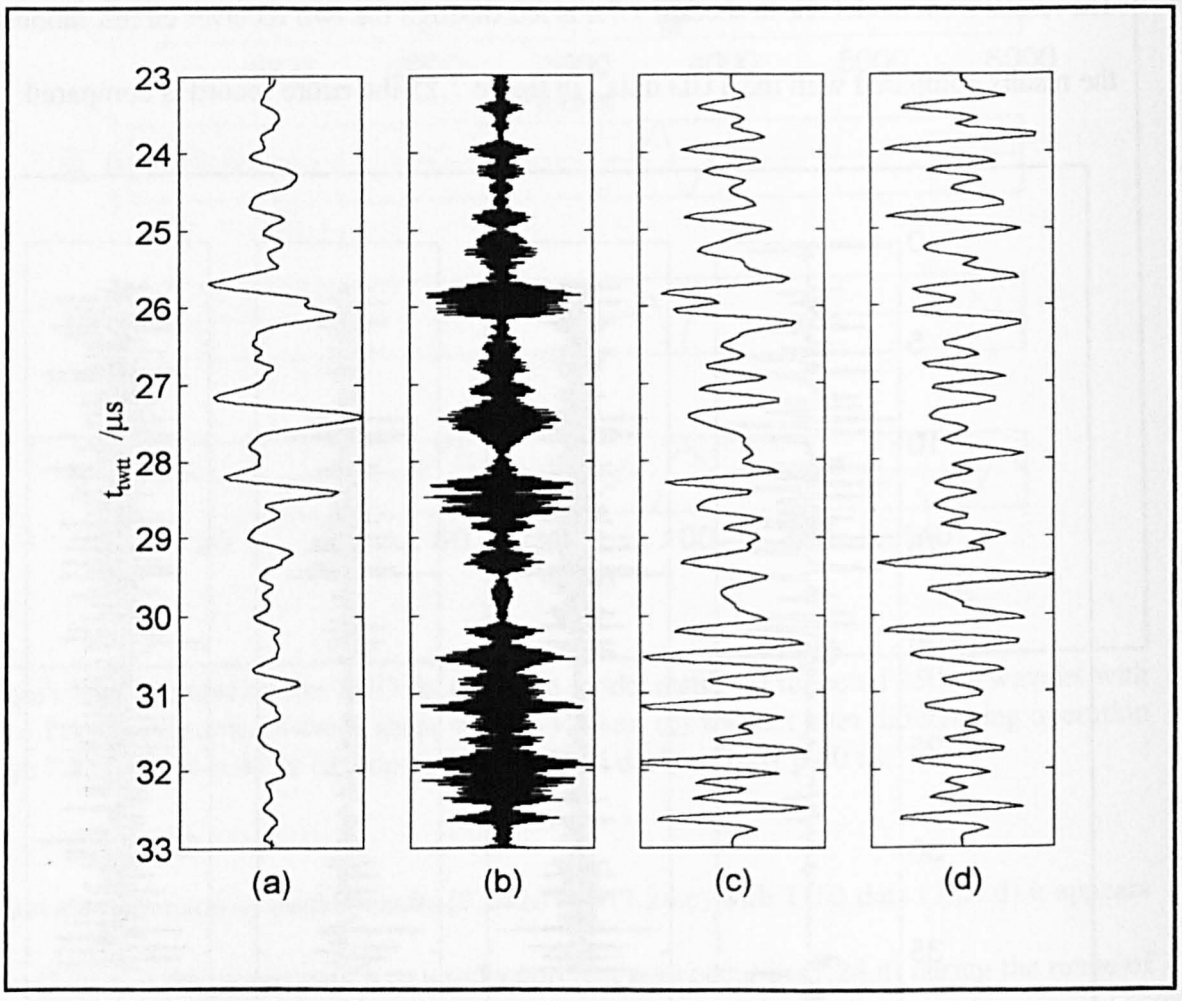

Figure 7.26 Comparison of the lower portion of the TUD data with the model one result (a) The average of the six traces for the TUD, (b) the model one result before entering receiver, (c) after using simple receiver model, (d) after using complex receiver model.

The receiver outputs are similar in shape but different in amplitude. Neither receiver model produces a match with the TUD radar. In attempts to improve the match between the output of the complex receiver and the TUD data a variety of decay curves in the range $t^{-0.1}$ to t^{-3} have been tried and the level of noise added has been altered from 0 to 10^{-5} . None of these alterations has affected the output of the complex receiver model.

7.7.e.i Comparison in the frequency domain

The result of model one after passing through the simple receiver circuit is compared with the TUD data. The comparison is made in figure 7.27 below. For both power spectrums the frequency range shown is from dc to the Nyquist frequency of 12.5 MHz.

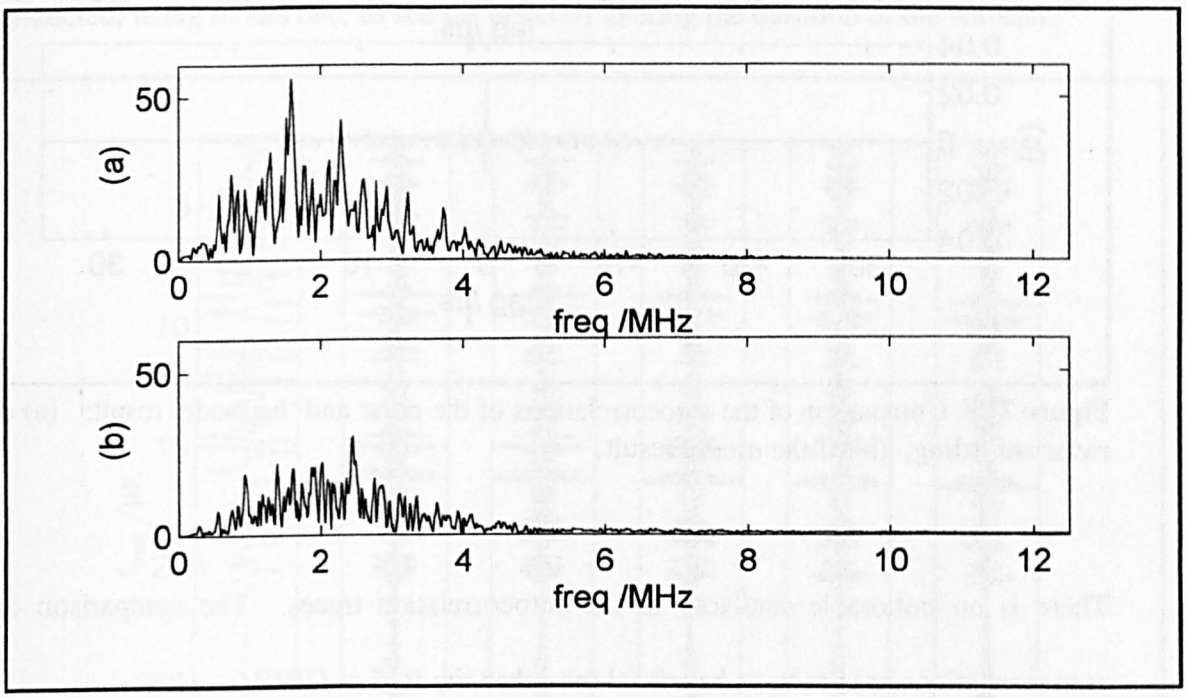

Figure 7.27 Comparison of the frequency spectrums: (a) the TUD radar recording, (b) the model result.

The frequency range is similar in the model result and the TUD data. This has been achieved by altering the filter duration in the model of the receiver circuit to its present value of 150 ns. There is less power overall (area under the curve) in the model result. This area could be increased by using a longer duration wavelet.

7.7.e.ii Comparison of the autocorrelations

The result of model one after passing through the simple receiver circuit is compared with the TUD data. The comparison is made for the autocorrelations and the results are compared in figure 7.28 below.

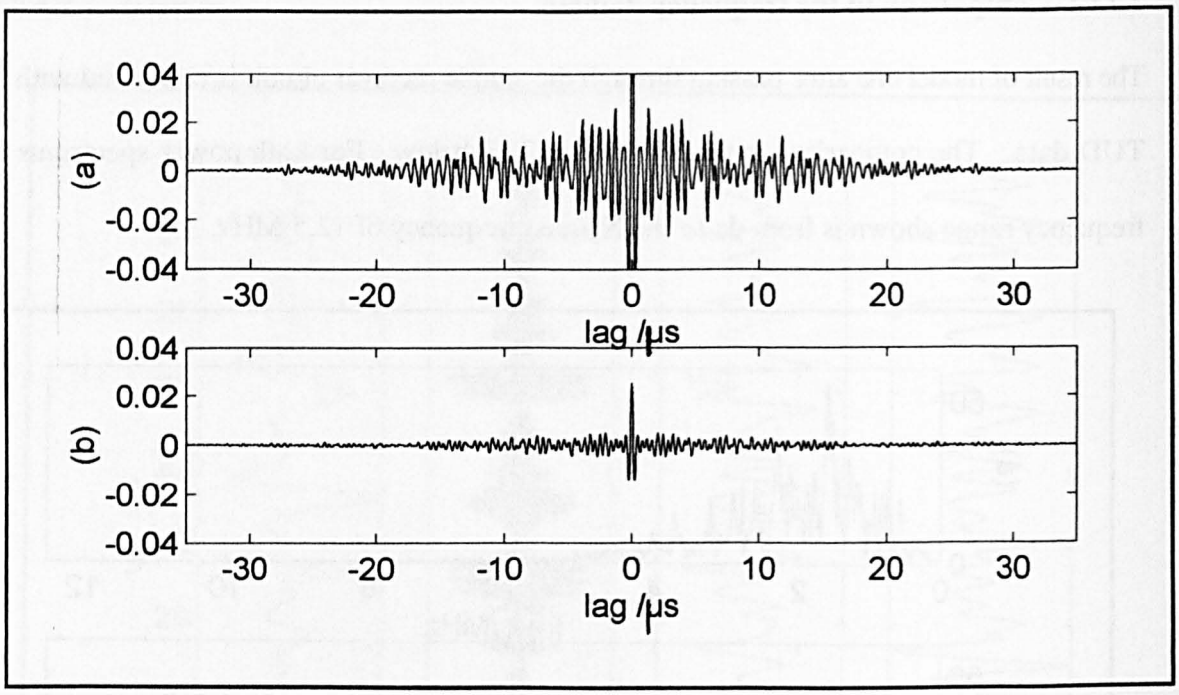

Figure 7.28 Comparison of the autocorrelations of the radar and the model result: (a) of the radar recording, (b) of the model result.

There is no noticeable similarity in the autocorrelation traces. The comparison of the autocorrelations has not been beneficial for either site B25 or GRIP.

The experiments in this section trying to imitate the receiver circuit have only been partially successful. The frequency content of the radar data can be achieved but the shapes of the reflections (their phase) cannot.

In the next few sections different parts of the model will be altered to see how this affects the model result. In many of these sections the model results will be presented raw without passing through the imitation receiver circuit. Due to the long run times for the models no attempt has been made to obtain a correlation surface as was done in section 6.8.c for Berkner.

7.7.f Altering the duration of the wavelet

Due to the long duration of the transmitted wavelet and the phase destroying characteristics of the receiver circuit it is anticipated that the model result will not be sensitive to alteration in the carrier frequency and phase of the transmitted wavelet. However an experiment was conducted, using model one, to see the effect of altering the duration of the wavelet.

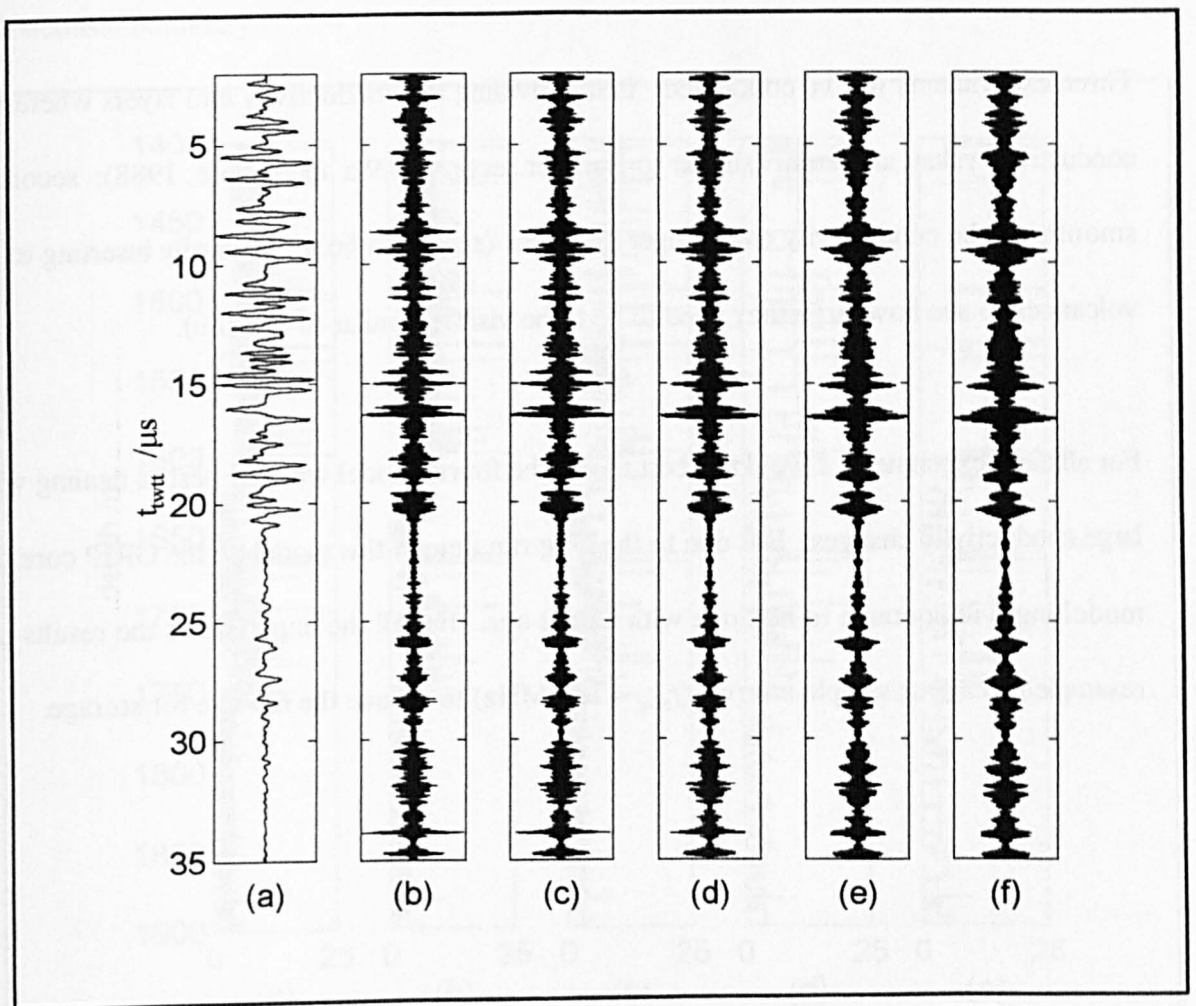

Figure 7.29 Altering the duration of the transmitted wavelet. (a) is the TUD data, then the wavelet duration used is (b) 200 ns (c) 250 ns (d) 300 ns (e) 400 ns (f) 500 ns

The result is similar for the wavelet durations 200 to 300 ns. The noticeable difference starts to occur between 400 ns (7.29.e) and 500 ns (7.29.f). There is some evidence from section 7.7.b (the zero phase wavelet) that the wavelet may be as long as 500 ns. This section shows that even if the transmitted wavelet were this long then it does not alter the t_{twtt} of the prominent internal reflections. The modelling will continue to be done with a 250 ns wavelet.

7.7.g Altering the conductivity of the ice sheet

When modelling the Berkner Island record, experiments were conducted to see if a better match between the model result and radar data could be obtained if the permittivity and conductivity of the ice core were altered, so that the ice sheet had a different permittivity and conductivity to the ice core. A similar investigation will be used here at the GRIP site.

Three experiments will be conducted: firstly dividing the conductivity into layers where the conductivity values are similar (similar to Berkner section §6.9.a and Moore, 1988); secondly smoothing the conductivity over longer distances (similar to §6.9.b); thirdly inserting extra volcanoes to see how large they need to be to be visible (similar to §6.10.b).

For all these experiments it would be best to use the fourth model which is best at dealing with large conductivity changes. But due to the long run time of this model on the GRIP core the modelling will continue to be done with model one. For all the experiments the results are resampled to a 5 ns sample interval (f_{Nyq} = 100 MHz) to reduce the file size for storage.

7.7.g.i Forming layers

In a similar manner to the procedure used previously for Berkner in section 6.9.a and Moore, (1988) the layering inside the ice sheet is calculated from the ice core data. In figure 7.30 below the layers become larger to the right as each layer can accommodate a greater variation in the conductivity. The example below comes from a section of core crossing the Holocene-Wisconsin boundary.

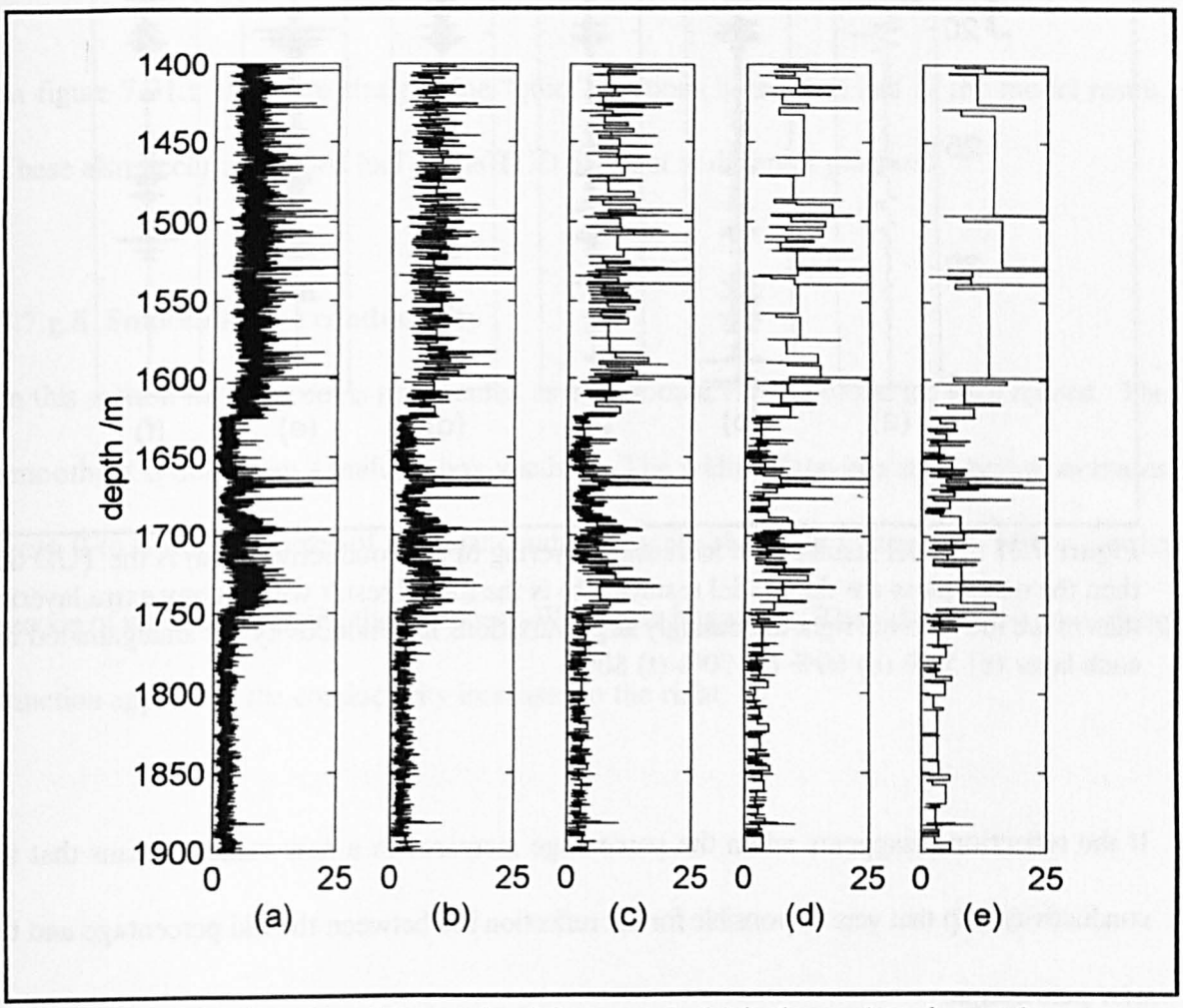

Figure 7.30 The alteration of the conductivity record. (a) is the unaltered core then as move to the right increasingly large variations in conductivity are amalgamated into each layer: (b) 50% (c) 60% (d) 70% (e) 80%.

Similar levels of amalgamation are used for the ice sheets used in the model to give the results shown in figure 7.31 below.

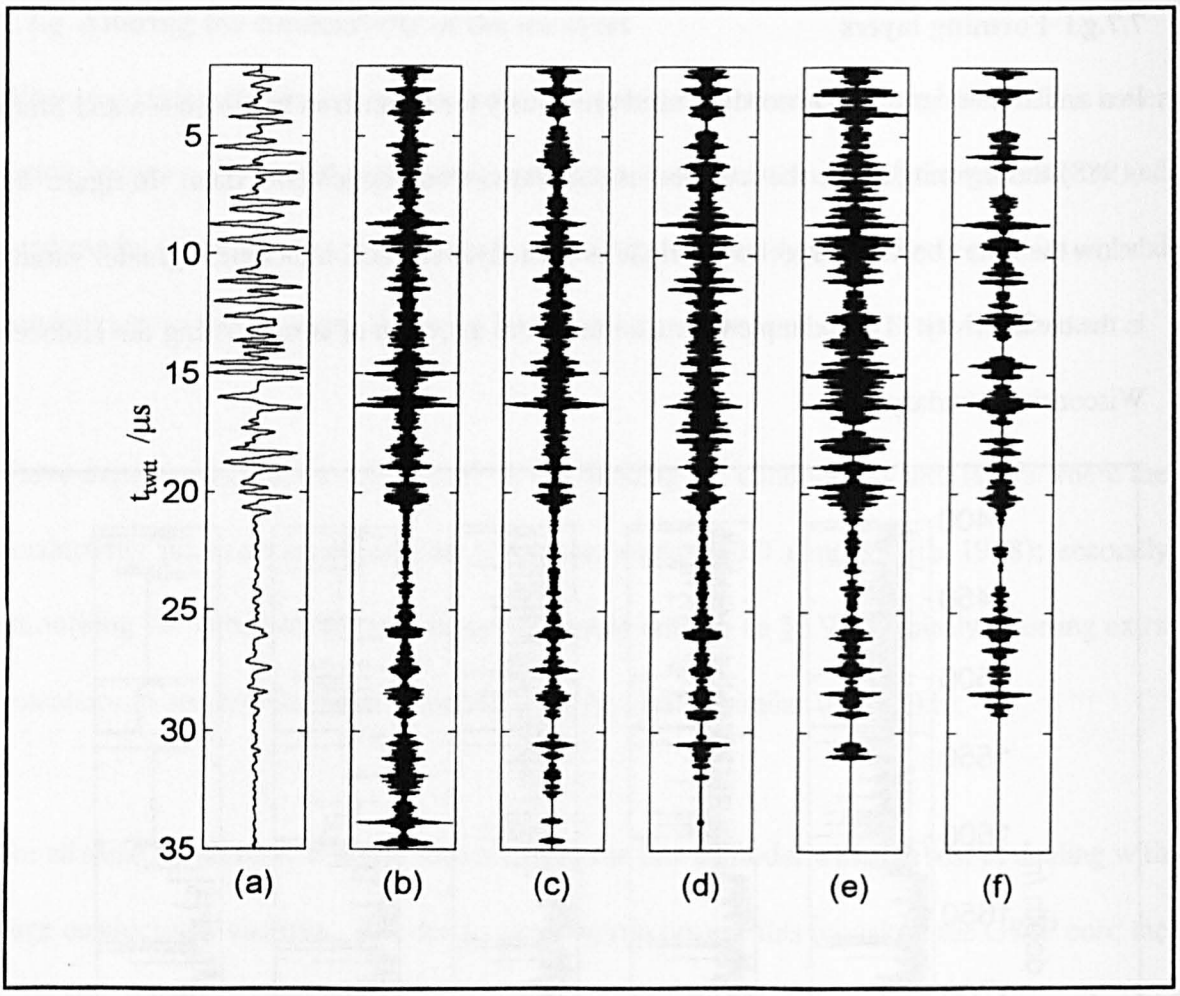

Figure 7.31 Model results with increasing layering of the conductivity. (a) is the TUD data then the other plots are the model results. (b) is the model result without any extra layering, then as we move to the right increasingly large variations in conductivity are amalgamated into each layer (c) 50% (d) 60% (e) 70% (f) 80%.

If the reflection disappears when the percentage increases to a new value it means that the conductivity step that was responsible for the reflection lies between the old percentage and the new percentage.

For a percentage of 50% (7.31.c) the reflections in the second half of the model result have altered from the original result (7.31.b). However it is only when the percentage rises to 70% (7.31.e) that the reflections in the top half of the record start to change. This suggests that the reflections in the top part of the model result are being mainly formed by conductivity steps of

between 60% and 70% while in the bottom half of the model result they are being caused by changes of 50% or less.

For the higher percentages there are very few reflections at late t_{twtt} this is a result of the algorithm forming the layers. Once a layer is initiated it requires a large change in the conductivity to start a new layer.

In figure 7.31.f there are straight line "quiet" portions in the first half of the model result. These also occur in the first half of the TUD data but at different positions.

7.7.g.ii Smoothing the conductivity

In this section the ice sheet is represented as a smoothed version of the ice core record. The smoothing is done with a uniform box window. The width of the box used below increases from 0 to 8 m. Examples of the final conductivity are shown in figure 7.32 below for the section of ice sheet crossing the Holocene-Wisconsin boundary. The width of the smoothing function applied to the conductivity increases to the right.

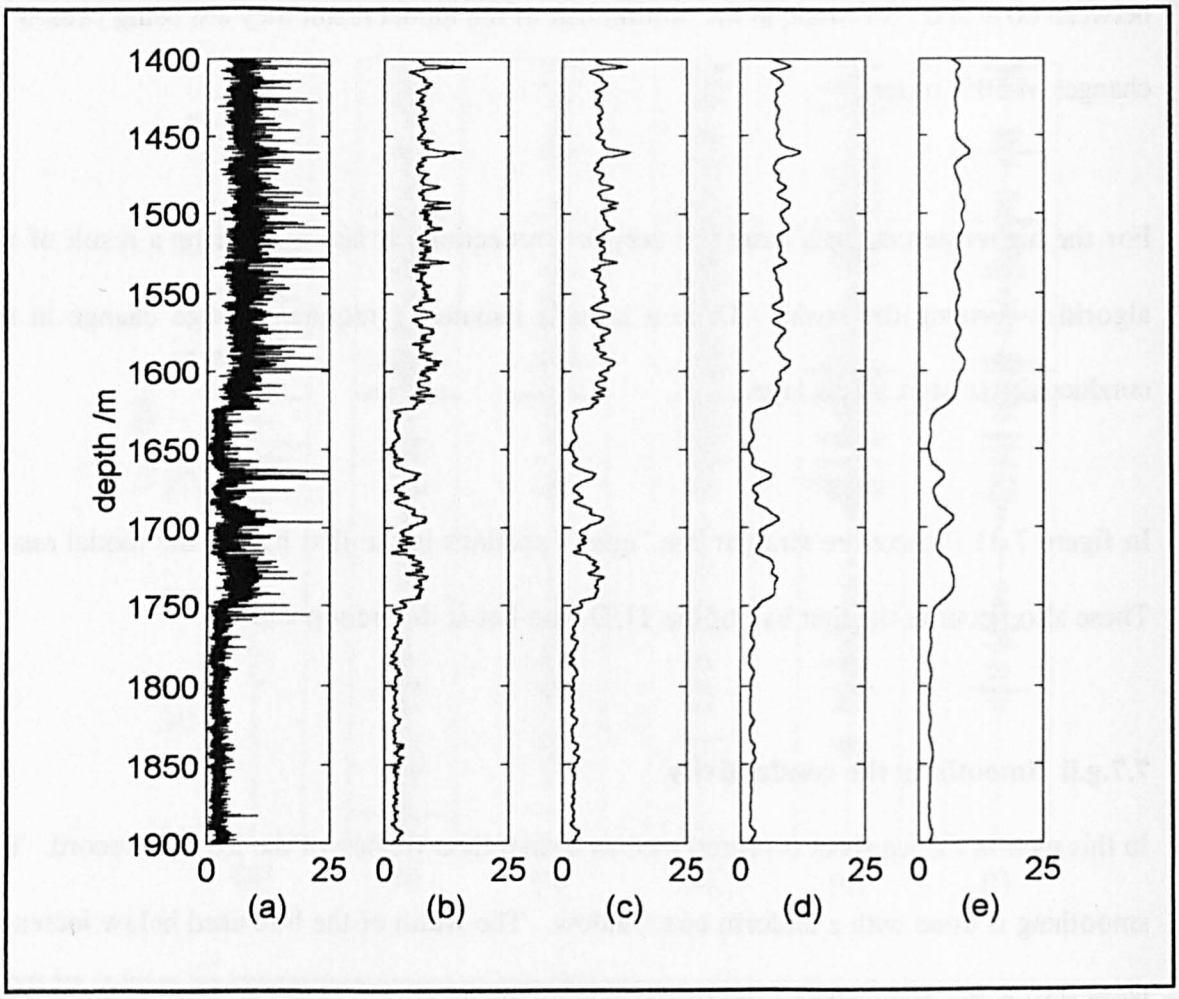

Figure 7.32 Smoothing the conductivity record, moving to the right increasingly wide smoothing functions are applied to the record. (a) is the unaltered record (b) 50 samples {1 m} (c) 100 samples {2 m} (d) 200 samples {4 m} (e) 400 samples {8 m}.

Similar smoothing windows are used in the model to give the results shown in figure 7.33 below.

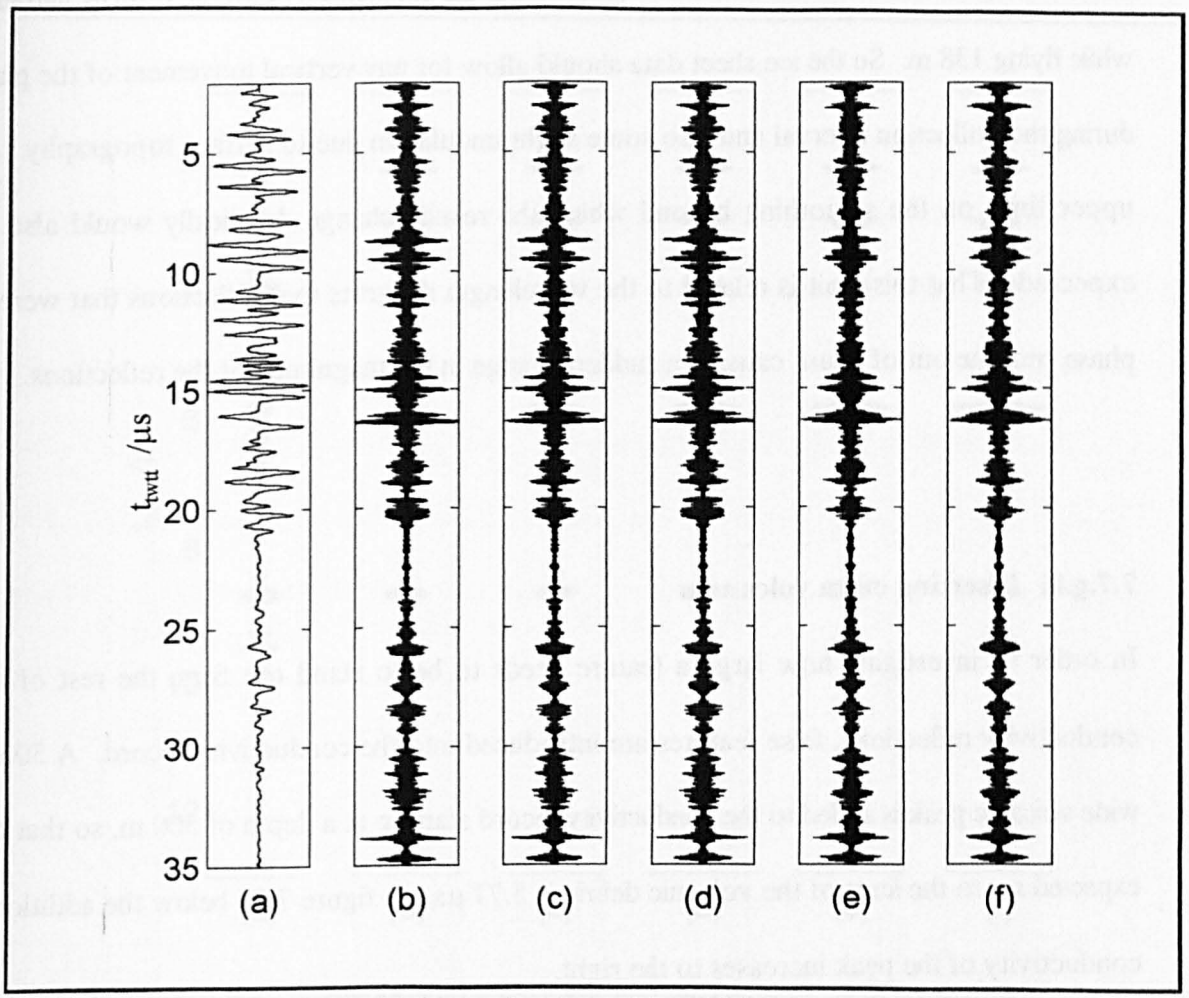

Figure 7.33 Model results with increasing smoothing of the conductivity. (a) TUD data (b) model result with no smoothing then as move to the right increasingly wide smoothing functions are applied (c) 50 samples {1 m} (d) 100 samples {2 m} (e) 200 samples {4 m} (f) 400 samples {8 m}

Small changes in the model result are noticeable as the smoothing increases from 2 m (7.33.d) to 4m (7.33.e). The changes are mostly in the second half of the result. The 60 MHz wavelet has a wavelength of 3 m so this change occurs after a smoothing length comparable with the wavelength. The change continues when the smoothing is increased from 4 m to 8 m. Smoothing the conductivity record has not improved the match between the model results and the TUD data.

Some smoothing of the ice sheet data (used in the model) in comparison to the ice core data

could be expected as the radio echo trace presented is the summation of all the returns gathered while flying 138 m. So the ice sheet data should allow for any vertical movement of the plane during the collection interval and also some slight undulation due to surface topography. An upper limit on the smoothing beyond which the results change drastically would also be expected. That this limit is related to the wavelength suggests that reflections that were in phase become out of phase causing a sudden change in the magnitude of the reflections.

7.7.g.iii Inserting extra volcanoes

In order to investigate how large a feature needs to be to stand out from the rest of the conductivity reflections, false features are introduced into the conductivity record. A 50 cm wide volcanic peak is added to the conductivity record starting at a depth of 500 m, so that the expected t_{twtt} to the start of the volcanic debris is 5.77 μs. In figure 7.34 below the additional conductivity of the peak increases to the right.

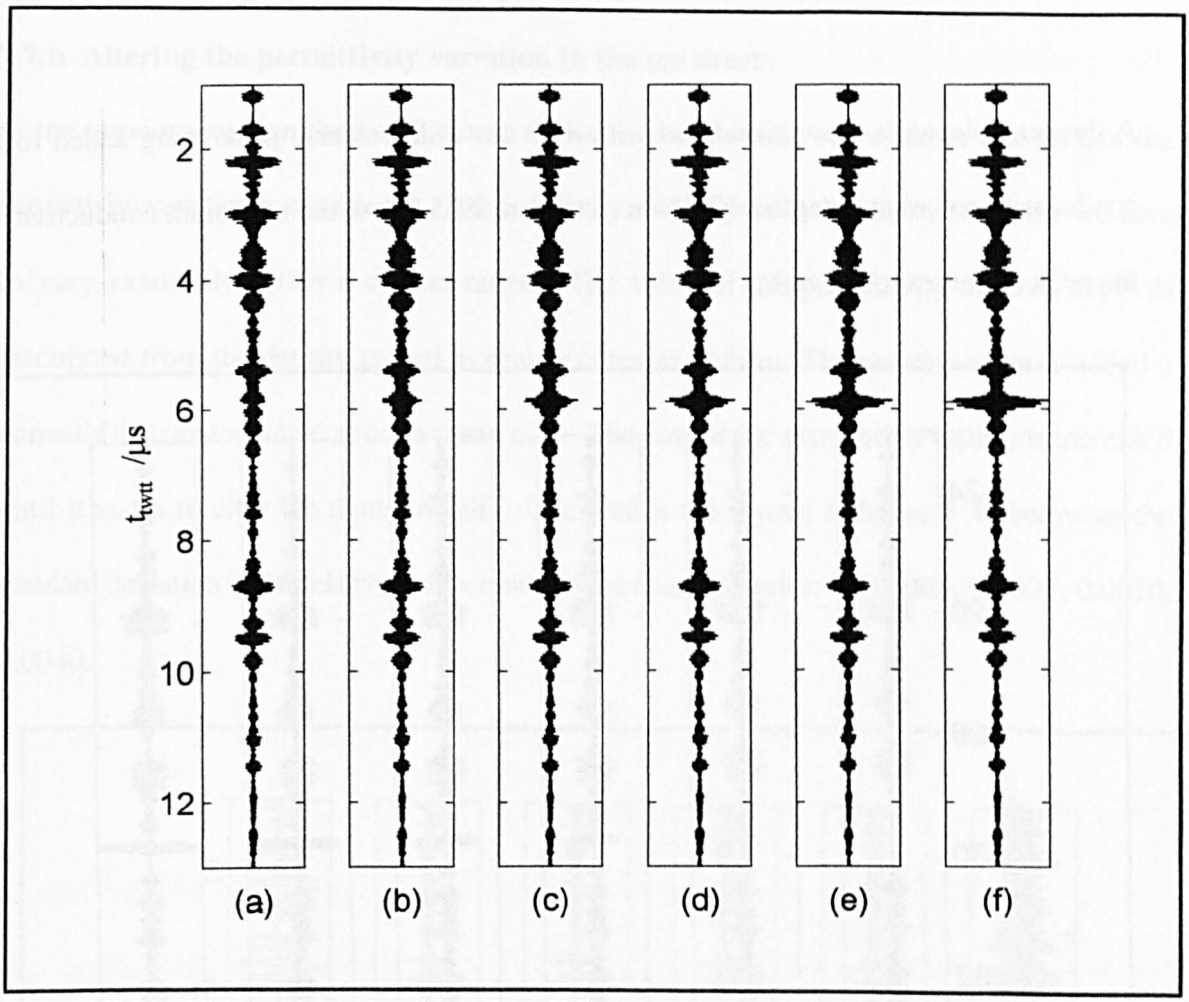

Figure 7.34 Effect of a volcanic peak at 500 m (expected t_{twtt} is 5.77 µs). (a) Without an added volcano, then the model results with an extra 50 cm wide volcano; as we move to the right the additional conductivity of the volcano increases (b) 10 µS m^{-1} (c) 20 µS m^{-1} (d) 30 µS m^{-1} (e) 40 µS m^{-1} (f) 50 µS m^{-1}.

The volcano is visible in the model result as a region of higher amplitude with the rise of the reflection starting at the expected time of about 5.8 µs. The amplitude of this region starts to rise above the envelope of the surrounding reflections at an additional conductivity of 30 µS m^{-1}. For comparison the volcanic peak in the conductivity due to the unknown volcano which erupted in 1269 AD has a peak conductivity of 40 µS m^{-1} and is at a depth of 187 m with an expected t_{twtt} of 2.1 µs. It is possible to identify a region of higher amplitude at this t_{twtt} . The Mt Thera volcano in the GRIP core (shown in figure 2.3) has a peak conductivity of 48 µS m^{-1} occurring at a depth of 736 m expected t_{twtt} of 8.6 µs. At this t_{twtt} there is a region of increased

amplitude though it is not as large as would be expected.

A deeper volcano is now considered with a 50 cm wide volcanic peak being added to the conductivity record at a depth of 2500 m. In figure 7.35 below the maximum conductivity of the peak increases to the right.

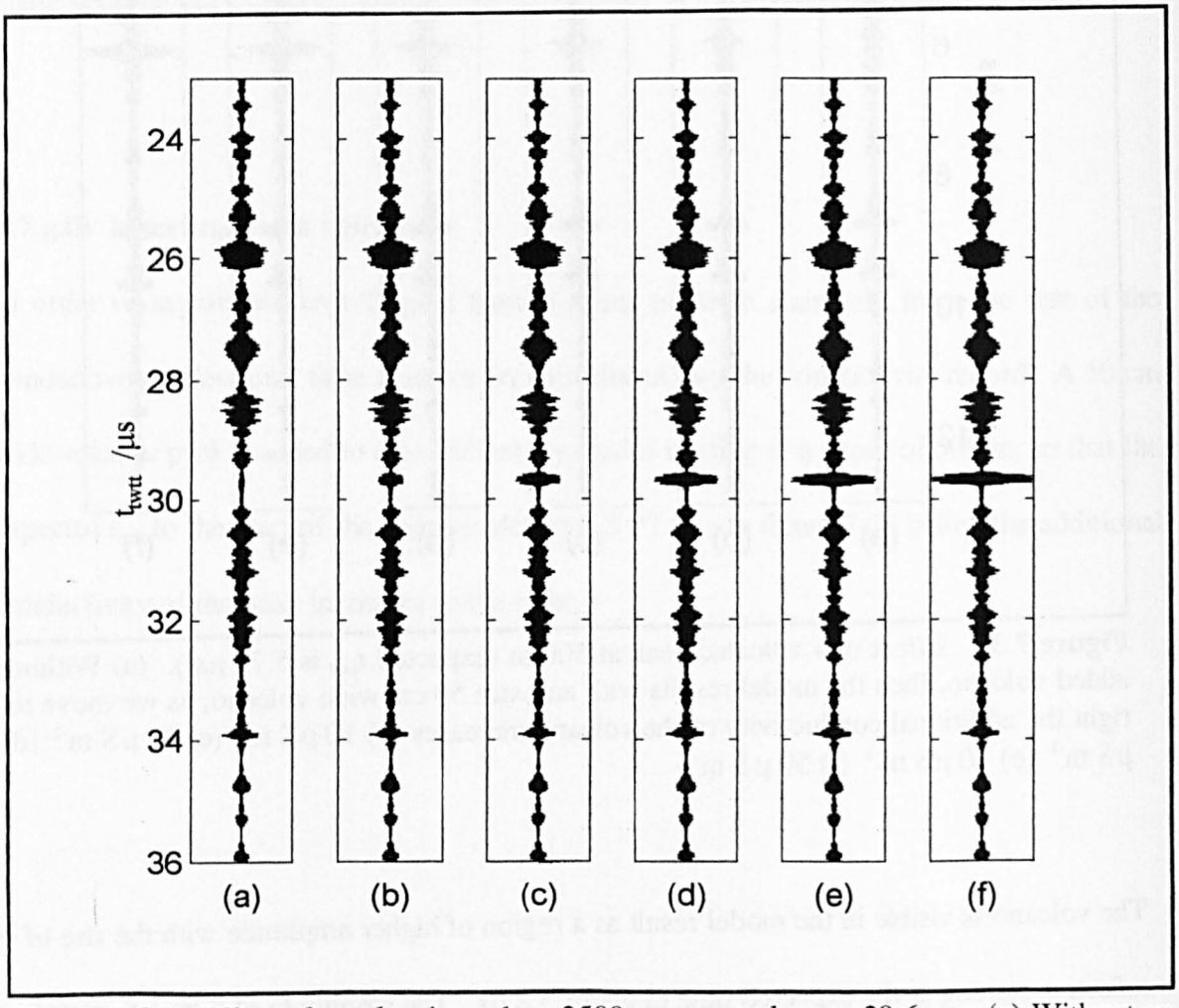

Figure 7.35 Effect of a volcanic peak at 2500 m expected t_{twtt} = 29.6 µs. (a) Without an added volcano, then the model results with an extra 50 cm wide volcano; as we move to the right the added conductivity of the volcano increases (b) 10 µS m^{-1} (c) 20 µS m^{-1}(d) 30 µS m^{-1} (e) 40 µS m^{-1} (f) 50 µS m^{-1}.

At this depth the volcano only needs to be an additional 10 µS m^{-1} above the rest of the conductivity record in order to stand out from the reflections caused by other variations in the conductivity. This experiment indicates that large discrete volcanic peaks do produce reflections that can be distinguished from the other conductivity variations in the core.

7.7.h Altering the permittivity variation in the ice sheet

In the previous section the conductivity variation was considered, while in this section the permittivity variation is considered. This is done by allowing the permittivity along the ice core to vary randomly within a certain range. The value of the permittivity at each depth is calculated from the density record in nearby cores as before. Then to this value is added a normally distributed value about a mean of 0. The size of the standard deviation is increased until it starts to alter the model results. The results are shown in figure 7.36 below as the standard deviation in the relative real permittivity increases in series: 0, 0.0001, 0.0005, 0.0010, 0.0040.

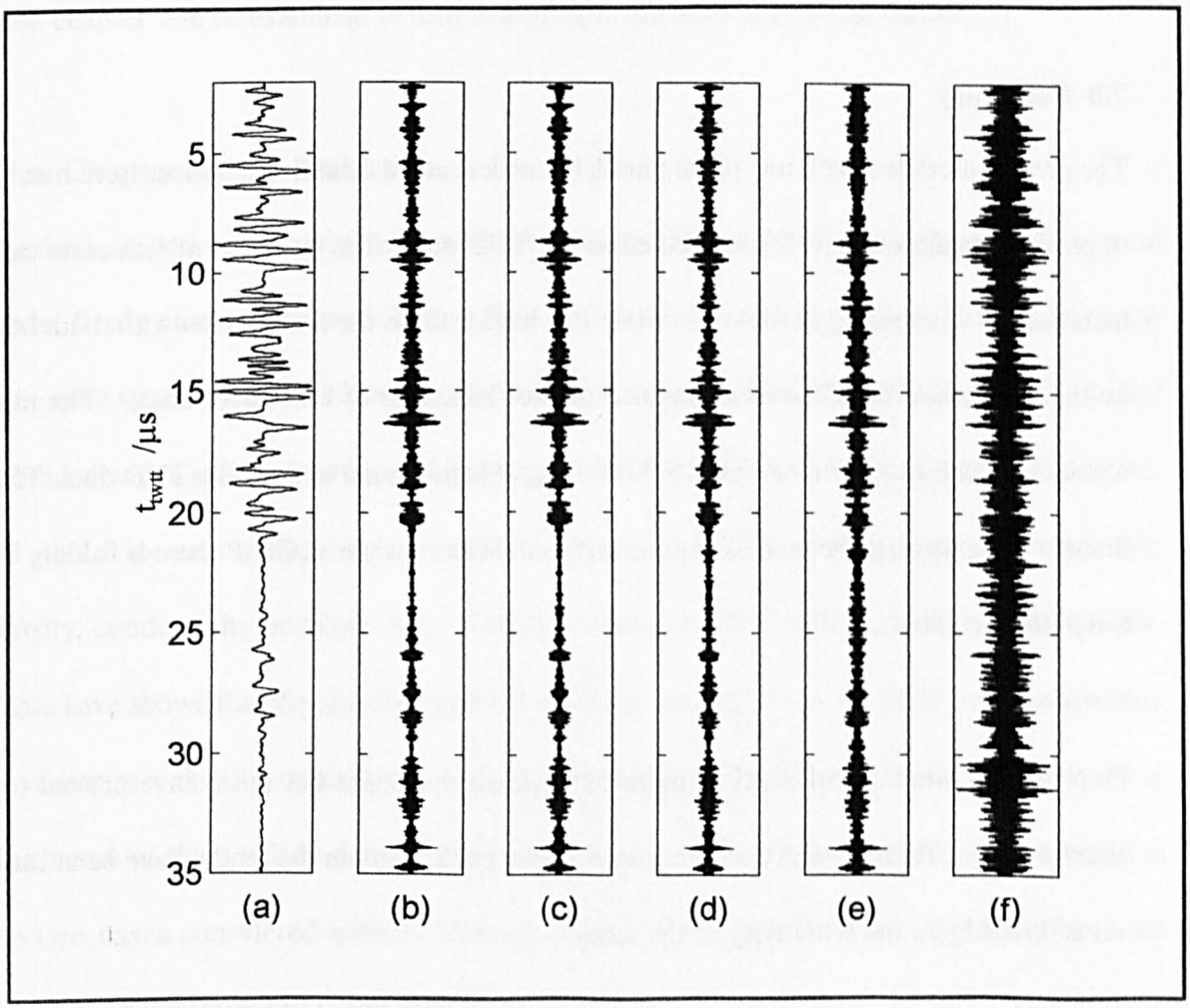

Figure 7.36 Comparison of the radio echo data (a) with model results (b) to (f). The model results are produced using a permittivity record which comes from the density of nearby cores, to the permittivity record is added a normally distributed random value with a standard deviation which increases to the right (b) 0 (c) 0.0001 (d) 0.0005 (e) 0.0010 (f) 0.0040.

For a standard deviation of 0.0005 (figure 7.36.d) (a standard deviation in the density of 0.15 kg m^{-3}) the conductivity reflections in the second half of the model result are only just starting to be disrupted by the appearance of additional reflections. However the conductivity reflections in the top half of the record are not affected by this level of variation in the permittivity. For a standard deviation of 0.0010 (figure 7.36.e) the second half reflections have been overridden by the reflections from the permittivity variations while the major reflections in the top half such as at 8 μs and 17 μs are still discernible. If the $\Delta\varepsilon'_{r\infty}$ is increased to 0.0040 (a standard deviation in the density of 1.2 kg m^{-3}) the result becomes unrecognisable.

7.8 Summary

The present models which use plane parallel wavelets and a stratified ice sheet have managed to produce results that give a good match to the TUD data. The positions of reflectors can be matched up when using model one, while it is harder to do the comparison with model three as the absorption has decreased the size of the reflections at late travel times. The model results produce reflections at late (> 30μs) t_{twtt} which are not seen in the TUD data. This is thought to be because the models assume horizontal layers while at GRIP there is folding deep inside the ice sheet.

Two models were constructed to imitate the receiver circuits but these have proved to be unsatisfactory. Then a variety of alterations to the parameters in the model have been carried out to investigate the sensitivity of the model.

CHAPTER 8

SUMMARY AND CONCLUSIONS

This chapter has five sections: firstly a summary of the previous chapters (§8.1); then a discussion on what has been learnt (§8.2); what has not been covered and how it may have affected the results (§8.3); a final discussion on isochrones and internal reflections (§8.4); and a conclusion (§8.5).

8.1 Summary

Each chapter will be examined in turn to highlight the main points and results.

8.1.a Chapter one: Introduction

The thesis started with a review of internal reflecting horizons (IRH). Four comparisons were made: firstly characteristics of IRH as functions of their position inside a glacier and as the radio echo system (RES) is changed; secondly a review of the many occasions a drill site has coincided with a radio echo survey and a comparison of the IRH and the ice core (appendix A). All of the ice core comparisons provide evidence for IRH occurring at depths where the density, conductivity or fabric vary. Thirdly, comparing IRH with electromagnetic models. These have shown that the observed power reflection coefficients of the IRH can be replicated by variations in density, conductivity and fabric though there is still debate about the depths at which each of these will be dominant. Fourthly, comparing IRH with glacier flow models, in the two cases considered authors have obtained a remarkable fit between the IRH and the calculated isochrones inside the glaciers.

8.1.b Chapter two: Cold Glaciers

There is a review of the density, chemical and fabric variations inside an ice sheet. There are many instances where the fabric can change suddenly; often these are associated with changes in the chemical impurity concentrations.

The density and conductivity profiles in the deep ice are caused by processes of seasonal accumulation and deposition on the surface. The subsequent snowfall buries the features keeping them in chronological order. Snow that fell at the same time is likely to be buried to the same depth. The density and conductivity features will not alter drastically once emplaced in the ice sheet. The fabric changes with depth and can alter with the stress and strain regime inside the ice.

8.1.c Chapter three: Permittivity of glacier ice

Due to the anisotropy in solid monocrystals of pure ice and the fabric in an ice sheet the permittivity and conductivity at each point inside the ice sheet is a second order tensor, which is frequency dependent. During this chapter some examples are given of the anisotropy in the electrical properties, but the bulk of the chapter treats the glacier ice as isotropic.

At the start of the chapter two models of the electrical behaviour of ice are examined: the Jaccard model and the Debye model. A distinction is made between pure solid monocrystalline ice typically used in laboratory studies and porous, multicrystalline, impure glacier ice. The variation in the high frequency permittivity and high frequency conductivity of glacier ice is examined over the range of conditions expected inside an ice sheet.

8.1.d Chapter four: Monochromatic waves

From Maxwell's equations the source free wave equation is obtained and this is solved using a negative separation constant and a positive time exponent. This leads to the various equations for: wavelength, impedance, phase velocity and absorption. These equations would have been different if a different separation constant and time exponent were used.

Then various types of reflection are considered. Care is taken with the geometry and the orientation of the fields, without which discussion of phase change on reflection is pointless. The reflection coefficient from single interfaces, from single layers and then from stacks of layers are all considered. The equations provided are only capable of considering interfaces between lossy dielectrics, not from pure dielectric to lossy dielectric (i.e. air to ice).

Lastly a comparison is made on a short section of core which can be considered as a stack of layers. The reflection coefficients calculated at the top of the stack are very similar irrespective of whether dispersive or non-dispersive permittivity and conductivity are used. Considering the accuracy of the available data it is sufficient to use the high frequency values for the permittivity and conductivity in the subsequent modelling.

8.1.e Chapter five: Wavelets

First there is a discussion of the rationale behind the adoption of a parallel layered one dimensional model in which the wavelet propagates normally to the layers. In order for a reflection to be related to a distinct depth and hence a distinct age and so be considered as an isochrone then a plane parallel model must be adequate.

Four models were then developed. Each uses the same geometry but considers the reflections

differently. Model one considers only the primary reflections without transmission losses and is calculated using convolution with a depth invariant wavelet (§5.3). Model two considers only the primary reflections with transmission losses and is calculated by considering the propagation of the wavelet and its reflection at each boundary (§5.4). Model three considers primary and multiple reflections with losses and is calculated by considering monochromatic waves in a frequency domain convolution (§5.5). Model four considers primary and multiple reflections with losses and a depth varying wavelet and is calculated using the finite difference time domain technique (§5.6). These models all give similar results for a short section of the Berkner core. There is evidence for an O'Doherty Anstey effect in ice sheets where the short peg leg multiples cause the primary reflections (in the results of models three and four) to be slightly delayed and slightly reinforced in comparison to the results of model two (only primary reflections with transmission losses).

The best model to use is probably model three (frequency domain) as it includes the absorption and the multiples. Both these effects are missing from model one and the multiples are missing from model two. The disadvantage of model four (FDTD) is the presence of the down going wavelet on the recording. In the way I have set up the FDTD it is also necessary to describe the wavelet in the space domain (see §5.6.d). The alternative would be to apply the time domain wavelet to a certain space point. It is also necessary to put in absorbing boundary conditions which are difficult to make perfect with the non-dispersive velocity. This means that low amplitude reflections are generated by the boundaries.

8.1.f Chapter six: Modelling the Berkner Island record

First there is a description of the process of acquiring the radio echo data and the ice core data. The ice core conductivity was collected using an instrument I built for the field season. The

ice core records from each bag are then connected to form a continuous record of the expected high frequency conductivity and high frequency permittivity inside the top hundred metres of the ice sheet. These ice core data together with an estimate of the transmitted radio echo wavelet are combined with the four models developed in chapter five. The model results are very similar. This implies a lack of importance of multiples and absorption for shallow depths.

A variety of parameters in the model are then altered to try to obtain a better match between the model result and the data. Changing the duration of the wavelet with 1, 2, 4 and 6 periods of the carrier showed that the longer duration wavelets produced a model result that had a better match to the radar data. The result was insensitive to small changes in the carrier frequency, allowing variation in the range 28 to 32 MHz without a change in the positions of the reflections. However 20 MHz and 40 MHz carrier frequencies produced very different reflections. A correlation coefficient surface was determined using a range of frequencies and durations for the wavelet. The best quantitative match between model result and data were on a ridge, but the match was still poor when looked at by eye.

In the above experiments the properties of the ice sheet were a replica of the properties of the ice core. In these subsequent experiments the properties of the ice sheet differ from those of the ice core. The first alteration was similar to that used by Moore (1988 b), where instead of using a layer in the ice sheet for each ice core measurement the ice sheet layers are thicker and incorporate all measurements within a certain percentage of each other. A new layer only occurs when there is a large alteration in the ice core measurement. The model result changes dramatically when the percentage increases from 2% to 5%, which shows that near to the surface many of the reflections are being caused by increases in the permittivity of less than 2%.

The second alteration is to smooth the ice core data using a filter. The model results (using a wavelet with a carrier frequency 30MHz (wavelength 6 m) and a length of 20 m) change when the smoothing increases from 1.6 to 3.2 m. The critical smoothing appears to be more comparable to half the wavelength of the wavelet than the length of the wavelet.

Finally the conductivity record is altered while the permittivity record remains unaltered. This shows that the conductivity has negligible effect for the shallowest hundred metres of the B25 core. Extra volcanoes are introduced and it is shown that a volcano at 10 m would need a maximum conductivity of 400 $\mu S\ m^{-1}$; while a volcano at 90 m would need a conductivity of about 60 $\mu S\ m^{-1}$ in order to be visible above the reflections generated by the permittivity variations. The actual volcanic peaks seen in this core and other cores are not this large so it is thought unlikely that any volcanic peak will have this required conductivity. Therefore reflections from volcanic horizons are not thought to be discernible above the reflections from permittivity variations in the top 100 m.

Lastly the Münster Model for the production of synthetic radargrams is described. This model was used to produce the paper Miners et al. (1997). It is a useful model in situations where there are insufficient computer resources to use any of the first four models.

8.1.g Chapter seven: Modelling the GRIP record

The chapter starts with a description of the collection of two radio echo data sets, one using the TUD system, the other using the FPG system. The two systems stack different numbers of traces collected over different horizontal distances before storage. However the previously published Z scope radar profiles have a similar general pattern (Jacobel and Hodge, 1995; Hempel and Thyssen, 1992).

The drilling and collection of an ice core from the site are then looked at. The processing and production of a high frequency conductivity record for the ice sheet are described. The permittivity record from the DEP has inaccuracies so the permittivity record for the modelling is taken from the density profiles of two adjacent ice cores.

The GRIP ice core has 1.4×10^5 measurements for conductivity, which means that the run times for using models two (propagating wavelet) and four (FDTD) were too long. Therefore the modelling was done with models one (depth invariant convolution) and three (frequency domain). These give different results at late t_{twtt} which is attributed to the absorption in the third model. However the positions of the major reflections match quite well. Two additional models are constructed in an attempt to match the receiver circuit in the TUD radar but neither is satisfactory.

The rest of the chapter is involved with the alteration of the parameters entering the models in order to try to improve the match. First, different wavelet lengths are used, showing that variation between 200 ns and 300 ns makes little difference to the result. Secondly, the number of layers inside the ice sheet is decreased and it is found that the model result alters when the percentage change in the conductivity at the boundaries is beyond 50%. Thirdly, the conductivity record is smoothed and it is found that the model result alters when the smoothing distance increases beyond 4 m. Fourthly, volcanoes are inserted into the ice sheet and it is found that a conductivity of 40 μS m^{-1} above the normal variation is necessary to have a noticeable reflection at 500 m, while a conductivity of 10 μS m^{-1} above the normal variation is necessary at a depth of 2500 m. Both these values are possible from the volcanoes seen in the ice core, so it is expected that a number of the reflections seen in the radar data are caused by single large volcanic layers. Finally normally distributed relative real permittivity noise with

a standard deviation of $\Delta\varepsilon'_{r\infty}$ is added to the existing permittivity record. Once $\Delta\varepsilon'_{r\infty}$ exceeds 0.0005 ($\Delta\rho$ of 0.15 kg m^{-3}) the reflections in the interval 22 to 35 μs are masked and once $\Delta\varepsilon'_{r\infty}$ exceeds 0.004 ($\Delta\rho$ of 1.2 kg m^{-3}) the reflections in the top half of the record are masked.

8.2 What has been learnt

8.2.a Usefulness of a plane parallel wavelet model in a stratified ice sheet

The plane parallel wavelet model has proved useful for the GRIP modelling. The positions of the major reflections seen in the TUD data are replicated in the model result. However the model result has not reproduced the radar data for the Berkner drillsite. This can be attributed to many causes: the importance of spherical spreading near the surface, not having a clear idea of the source wavelet and possibly due to the distance between the source and receiver. Which of these is the primary culprit has not been established.

The model result for Berkner is very sensitive to the duration of the wavelet and the percentage amalgamation used when layering. The GRIP result is not sensitive to the wavelet or the percentage layering.

8.2.b The importance of multiples

For the Berkner models the multiples had no importance but for the GRIP model it was not possible to establish this. I expect most future modelling (which will include three dimensions or fabric) will be of the FDTD type so will include multiples. There is evidence of an O'Doherty Anstey effect (O'Doherty and Anstey, 1971) in the propagation of electromagnetic waves in ice sheets, where the short peg leg multiples delay and reinforce the primary reflections.

8.2.c Comparing the variation in permittivity with conductivity.

It has always been thought that the internal reflections originating at shallow depths were caused by variations in density. The most recent publication to quantify the depth at which density variations ceased to be important was Moore (1988 a). He decided that above 250 m density variations caused IRH while below 250 m conductivity variations caused IRH. This changeover depth will depend on the densification rate at a site, which itself is dependent on factors such as the annual temperature and accumulation.

In the Berkner core the density variations were responsible for all the reflections in the top 100 m. Variations in the density, caused by changes in porosity, are still easily measured towards the bottom of the data I have been supplied with and this is shown in figure 8.1 below.

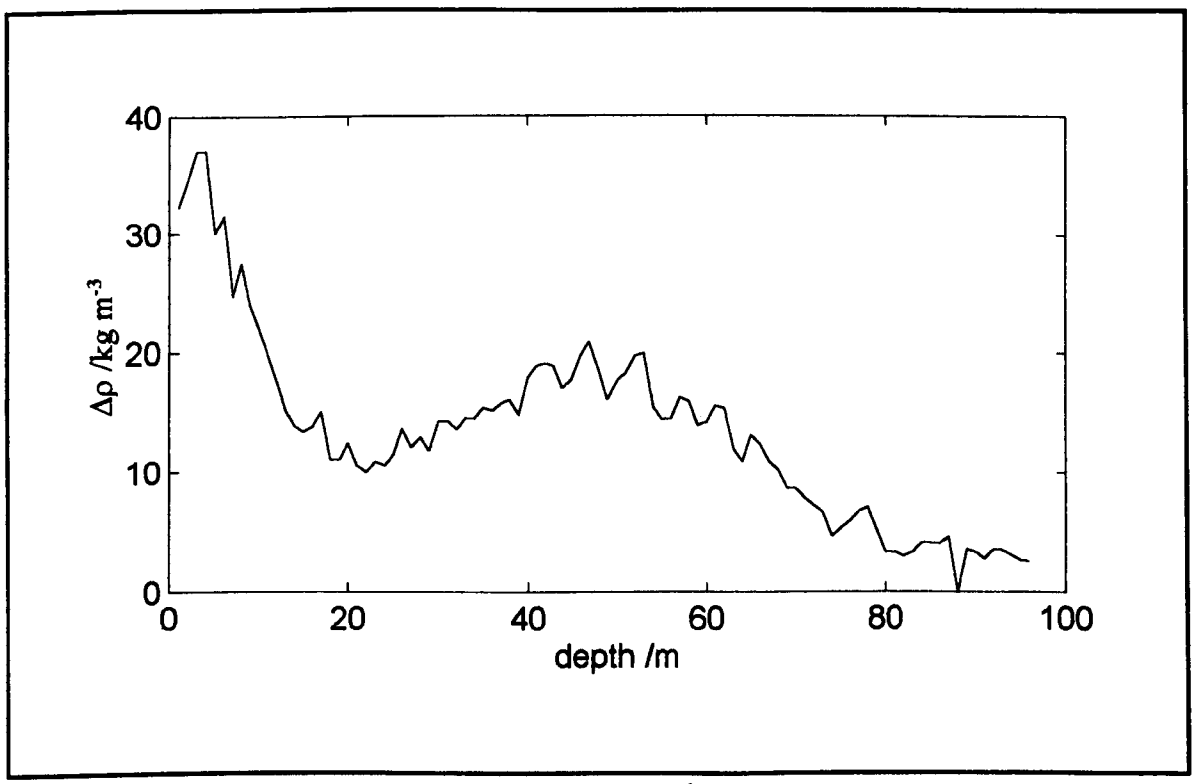

Figure 8.1 The standard deviation in density (kg m^{-3}) in 2 m portions of the B25 core.

At pore close off at a depth of 51 m the standard deviation in density ($\Delta\rho$) is 20 kg m^{-3} corresponding to a standard deviation in the normally distributed high frequency relative real

permittivity ($\Delta\varepsilon'_{r\infty}$) of 0.06. At a depth of 98 m $\Delta\rho$ is about 2.5 kg m^{-3} corresponding to a $\Delta\varepsilon'_{r\infty}$ of 0.008. In the GRIP chapter it was shown that the reflections in the lower half of the record are drowned out when $\Delta\varepsilon'_{r\infty}$ is 0.0005 while the reflections in the top half are drowned out when $\Delta\varepsilon'_{r\infty}$ is 0.004 ($\Delta\rho$ = 1.2 kg m^{-3}). This experiment could be improved to narrow down the noise level at which reflections are drowned out. It would be possible to model the standard deviation in density with depth and determine at which depth the conductivity reflections would be visible.

More simply, consider the reflection from a volcanic layer as given in figure 5.10 of section 5.7.b.ii with a reflected maximum amplitude of 1×10^{-4} for an incident maximum amplitude of 1. Consider the situation at the base of the measured density available for the B25 core, for instance at 98 m where there is an 80mm thick layer of density 888 kg m^{-3} surrounded by ice of density 896 kg m^{-3}. At this depth such a feature will produce a reflected wavelet with a maximum absolute amplitude of 5.7×10^{4}, for an incident maximum amplitude of 1. Future work could calculate how the density will increase in the layer and the surrounding ice using the densification model of Salamatin and Lipenkov (1993). This would give the depth at which the reflection from such a density feature would match the reflection from the volcano.

8.2.d The frequency dependence of the reflection coefficient

Fujita and Mae (1994) considered the reflection from interfaces and concluded that r_{AF} at an interface with only a permittivity change will be independent of frequency, while r_{AF} at an interface with a conductivity change will be inversely related to frequency (Fujita and Mae 1994, pp 84). They reach this conclusion by using the first order approximation of Paren, which was shown to be a good approximation in section 4.5.f , and an assumption that the loss

tangent is zero before the acidic ice (in order to obtain their equation 9 on pp 83).

An example of the frequency dependence of the power reflection coefficient is shown in figure 8.2 below. Consider the interface between ice with $\varepsilon'_{r\infty} = 3$ and $\sigma_{\infty} = 10\ \mu S\ m^{-1}$ to ice with $\varepsilon'_{r\infty} = 3$ and $\sigma_{\infty} = 20\ \mu S\ m^{-1}$. The line shown is the power reflection coefficient calculated using the equation of Paren (eqn 4.29).

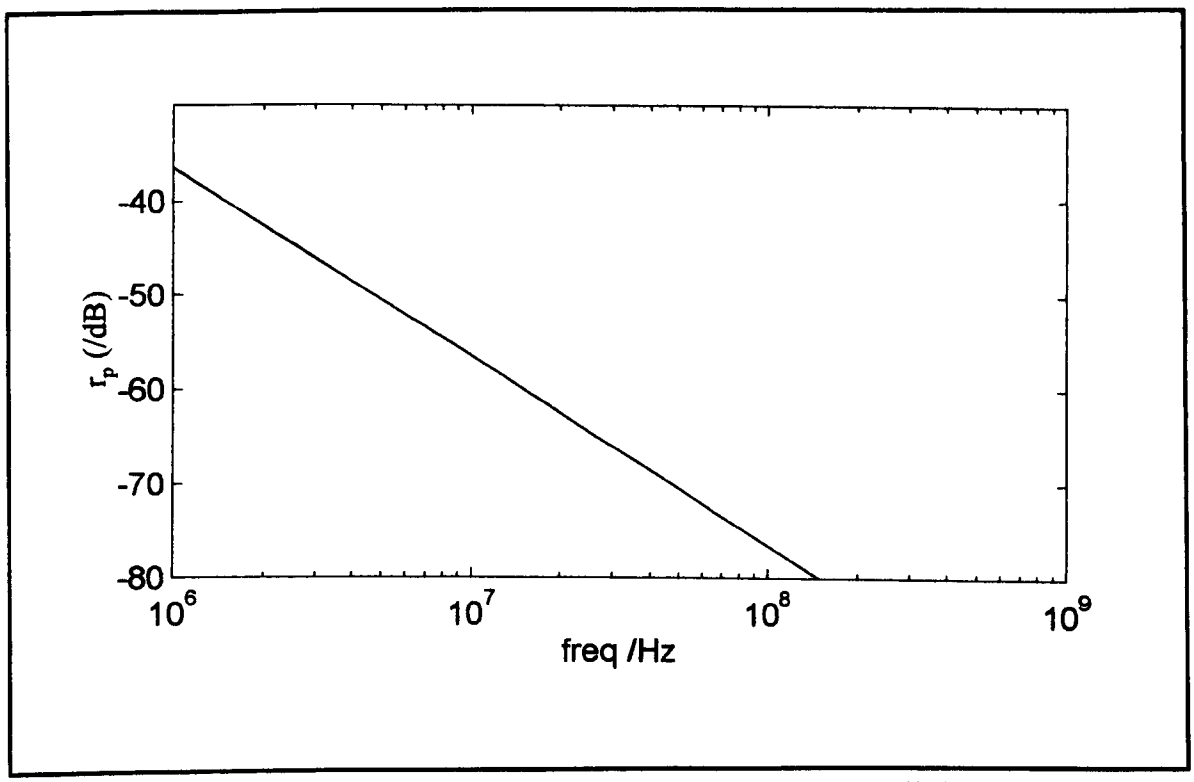

Figure 8.2 The frequency dependence of the power reflection coefficient at an interface between ice of different properties calculated using the equation of Paren (eqn 4.29). top ice is: $\varepsilon'_{r\infty} = 3$ and $\sigma_{\infty} = 10\ \mu S\ m^{-1}$ and bottom ice is: $\varepsilon'_{r\infty} = 3$ and $\sigma_{\infty} = 20\ \mu S\ m^{-1}$.

Fujita and Mae (1994) propose doing radio-echo sounding using two wavelets with different carrier frequencies. For each of the wavelets the amplitudes of the internal reflections are measured. If the amplitude of the internal reflection differs with each wavelet it will imply that the reflection was from a variation in the conductivity. When doing this experiment care will need to be taken as the interference effect will change so that constructive interference can

increase the size of reflections. This has been shown in table 1.6 and section 6.8.b.

8.2.e The importance of the RES data

There is a difference in the characteristics and number of reflections visible on the processed TUD and FPG traces provided for GRIP. However the general large scale features in the two published Z scope radar profiles match up well. This observation from GRIP that the single processed traces can differ while the Z scopes are similar has implications for the Berkner modelling. It may mean that the trace that was provided for the Berkner modelling may also be different from what would be seen on a Z scope display. Unfortunately the Z scope data was not available for the Berkner site.

It would have been nice to have had many radio echo traces for each site to be able to investigate the effect of averaging and combining traces on the positions and strength of the IRH.

It is worth reiterating a previously known fact, which will become important as scientists start to use increasingly higher resolution GPR systems: if summing adjacent traces over a long travel distance then it is important that low pass filtering has occurred before summation. For example, if using a 500 MHz carrier frequency system then the displacement between adjacent measurements need only be 0.2 m before the traces are in antiphase.

8.3 What has not been covered?

An expanded title for this section would be what has not been covered, how important was its omission and what could be done to include it in the future. The three areas that will be considered are polarisation, three dimensional modelling and the modelling of Z scope data.

8.3.a Polarisation

For ice sheets the reflected electromagnetic waves have different polarisations to the incident electromagnetic waves. This polarisation of the reflections has been attributed to many causes (§1.4.e.i). Hargreaves (1977, 1978) concluded that it was the anisotropy of the ice that was causing the birefringence. Due to the hexagonal crystal lattice the electrical properties of a single crystal will have different values parallel and perpendicular to the basal plane. To consider the propagation of electromagnetic waves through such anisotropic crystals requires a knowledge of a field called crystal optics. The characteristic equations take on the forms: $\boldsymbol{D} = \underline{\underline{\varepsilon}}\,\boldsymbol{E} + \boldsymbol{P}$ and $\boldsymbol{J} = \underline{\underline{\sigma}}\,\boldsymbol{E}$. where the double underline indicates a second order tensor. For single ice crystals the permittivity and conductivity have the form:

$$\underline{\underline{\varepsilon'}} = \begin{pmatrix} a & 0 & 0 \\ 0 & a & 0 \\ 0 & 0 & b \end{pmatrix} \qquad \underline{\underline{\sigma}} = \begin{pmatrix} a & 0 & 0 \\ 0 & a & 0 \\ 0 & 0 & b \end{pmatrix}$$

An EM wave travelling parallel to the c axis is transmitted normally. A ray incident from any other direction is split into two waves. This property is called birefringence. In an ice sheet there are many crystals arranged together so the macroscopic permittivity and conductivity tensors depend on the number of crystals orientated in the different directions (the fabric).

First consider single crystals; the anisotropy in the real permittivity at radio frequencies has been determined by many authors. Some of the results are given in the table 8.1 below:

Table 8.1 Observed anisotropy in $\varepsilon'_{r\infty}$ in single ice (Ih) crystals at high frequencies

Author	Frequencies (Hz)	Anisotropy
Johari and Charrette (1975)	35×10^6 and 60×10^6	less than 1%.
Johari (1976)	0.5×10^6 to 100×10^6	less than 1 ± 0.3 %
Johari and Jones (1978)	0.5 to 0.2×10^6	less than 0.5%.
Fujita et al. (1993)	9.7×10^9	1.2 ± 0.2 %.
Matsuoka et al. (1997 a, b)	3.9×10^{10}	1.07 ± 0.02%

The anisotropy in the conductivity has been measured by fewer authors; Ruepp's values (from Paren, 1970 and Hobbs, 1974 pp 96) give an anisotropy of between 9% and 18% at 300 kHz, (also see also Ruepp, 1973). Measurements at 1 MHz on the anisotropy in the imaginary permittivity give a value of 20% (Matsuoka et al. 1997 a, pp 5). Any future research considering the anisotropy in the conductivity will need to consider which of the conductivity tensors the DEP measures.

Secondly consider that in ice sheets the ice crystals are collected together in a polycrystalline fabric. This fabric describes how the orientation of the individual crystals varies. Matsuoka et al. (1998) measured the dielectric properties of a polycrystalline sample from Dome Fuji. They used a disc of diameter 50 mm and thickness 3.5 mm with the disc surface parallel to the vertical. From their measurement technique they deduce an anisotropy in the dielectric constant of 0.0104 ± 0.0004 at a temperature of 233 K. This is a percentage of about 0.3% which is a third of the anisotropy of a single crystal.

It is possible to calculate the tensor permittivity if given the fabric of a polycrystalline sample

(Hargreaves,1977,1978). Hargreaves limited himself to considering the real permittivity. So if each single crystal has a real permittivity given in its principal axis by:

$$\varepsilon' = \begin{pmatrix} a & 0 & 0 \\ 0 & a & 0 \\ 0 & 0 & b \end{pmatrix}$$

Then for a conical distribution of these crystals defined by a probability function:

$$\rho = constant, \quad \theta < \theta_0$$
$$\rho = 0, \quad \theta > \theta_0$$

The real permittivity is given by:

$$\varepsilon' = \begin{pmatrix} c & 0 & 0 \\ 0 & c & 0 \\ 0 & 0 & d \end{pmatrix}$$

where

$$c = a + \frac{(b-a)\left[(1-\cos\theta_0)-\frac{1}{3}(1-\cos^3\theta_0)\right]}{2(1-\cos\theta_0)}$$
$$d = a + \frac{\frac{1}{3}(b-a)(1-\cos^3\theta_0)}{(1-\cos\theta_0)}$$

Using this relation it is possible to consider the possible changes in the real permittivity as the fabric alters. Consider a typical solid ice monocrystal which has real permittivities measured parallel and perpendicular to the axis (Fujita et al. 1993):

$\|C$ $\quad a = 3.189 \pm 0.006 \qquad \perp C \quad b = 3.152 \pm 0.003$

Then the real permittivity tensor for various conical angles is given below:

For a random fabric near the surface:

$$\varepsilon'\left(\theta_0 = 90^0\right) = \begin{pmatrix} 3.1767 & 0 & 0 \\ 0 & 3.1767 & 0 \\ 0 & 0 & 3.1767 \end{pmatrix}$$

At deeper depth with some orientation:

$$\varepsilon'\left(\theta_0 = 45^0\right) = \begin{pmatrix} 3.1841 & 0 & 0 \\ 0 & 3.1841 & 0 \\ 0 & 0 & 3.1618 \end{pmatrix}$$

At great depth with strong fabric:

$$\varepsilon'\left(\theta_0 = 10^0\right) = \begin{pmatrix} 3.1887 & 0 & 0 \\ 0 & 3.1887 & 0 \\ 0 & 0 & 3.1526 \end{pmatrix}$$

The above tensors give an indication of the permittivity variation. A sudden change from a random fabric (90^0) to a strong conical fabric (10^0), such as was observed to happen at 2006 m in the Byrd core (Section 2.9 and Gow and Williamson, 1976), could give a change in the permittivity tensor of:

$$\Delta\varepsilon' = \begin{pmatrix} -0.012 & 0 & 0 \\ 0 & -0.012 & 0 \\ 0 & 0 & +0.024 \end{pmatrix}$$

It can be seen that the variation between the tensor elements is large in comparison to many of

the permittivity variations considered in previous sections such as §5.7.b.iv and §7.7.h. However the amplitude of the reflections that would be generated can only be determined by using models. Previous authors (Clough, 1977; Ackley and Keliher, 1979; Fujita and Mae, 1994) approximated the fabric change as a step change in the permittivity and considered only monochromatic waves. A better estimate of the expected reflection would be obtained by using finite difference time domain models which could model the propagation and reflection of electromagnetic wavelets from a stack of layers in which the fabric varied in each layer (Schneider and Hudson, 1993; Lin et al. 1993).

The final point that needs to be made is that often in ice cores the fabric changes are associated with changes in the chemistry. It may be that the depths in the ice core where the DEP measures large changes in the conductivity are also depths where there are sudden changes in the fabric. To examine this properly requires fabric measurements at a finer depth resolution than has previously been done.

8.3.b Three dimensional effects

There are many three dimensional effects that are missing from the one dimensional model used in this thesis. These include the spherical spreading from the antenna, which leads to the Fresnel zones, the refraction of the waves towards the vertical as they travel down and the polar diagrams of the antennas. These polar diagrams consider how the antenna radiates energy at different angles to the vertical. The one dimensional model is also unable to model the return from an offset source and receiver. Because of this it was necessary to apply a NMO correction to the Berkner radar data (§6.2.c.ii).

While three dimensional modelling could be done with Bessel functions, considering the

propagation of waves in homogeneous spaces, there is more flexibility if a FDTD grid is used (Kunz and Luebbers, 1993; Wang and Hohmann, 1993). However three dimensional FDTD grids would require a lot of computer memory unless it is shown that smoothing of the ground data can be done in three dimensional models as it has proved possible to do for the one dimensional models used here in §6.9.b and §7.7.g.ii. A FDTD grid would allow horizontal inhomogeneities to be introduced. This would also allow modelling to consider reflections from diffuse (rough) surfaces. Previously diffuse surface reflections have had their statistical properties considered by Harrison (1972). It is also now becoming possible to construct FDTD models which consider frequency dependent materials (Bergmann et al. 1998).

Three dimensional effects are most important for modelling shallower cores. For deeper depths refraction decreases the spherical spread of the radio wave. This may be one explanation why the present one dimensional model is successful for the GRIP core but not successful for the Berkner core.

8.3.c Modelling Z scope RES data

Z scope RES are the two dimensional sections obtained as a radar system traverses across a glacier. It is upon such sections that IRH are most visible and discernible, as has been discussed in section 7.4 where the TUD and FPG data are compared. Also most of the interesting phenomena associated with IRH such as the horizontal fading, the deformation of layers over smooth bedrock and the uparching of layers below domes are only visible on Z scope data (see table 1.3). All the modelling in this thesis has been restricted to A scope data.

In order to model Z scope data it would be necessary to do a series of synthetic radargrams along a section. This would require a series of ice cores which would be very labour intensive,

though it could be done with ten metre cores and a very high frequency GPR. But then as the modelling becomes shallower it becomes increasingly necessary to use a 3D model, although it would only be necessary to use the density data in an isotropic model. Alternatively it would be possible to use ice core data generated from a glacier flow model. Such a glacier flow model would need to reproduce the annual density variations inside an ice sheet which are responsible for reflections near the surface.

8.4 Internal Reflecting Horizons and Isochrones

8.4.a What causes a reflection?

The electromagnetic wavelet is spreading out in three dimensions into the ice sheet. Its motion through the glacier is governed by the permittivity and conductivity tensor at each point. The permittivity and conductivity tensors at a point are determined by the porosity, pressure, temperature, chemical impurity content and fabric. Whenever there is an abrupt change in either of the electrical tensors a portion of the electromagnetic energy will be reflected. The permittivity tensor is most likely to alter abruptly due to a change in the porosity or fabric of the ice. The conductivity tensor is most likely to alter abruptly due to a change in the impurities, porosity or fabric.

At Berkner the reflections are caused by changes in the permittivity which is changing with the porosity. There are no large changes in the permittivity that can be matched up with individual reflections in the radar data. Volcanoes would have required a huge peak conductivity to stand out: 400 μS m^{-1} at 10 m and 100 μS m^{-1} at 90 m.

At GRIP there are abrupt changes in the conductivity, and the depths of these changes match

up with reflections seen in the radar data. The conductivity measured by the DEP may be partly influenced by the fabric of the ice. However, at the Holocene-Wisconsin boundary where the conductivity has its most noticeable change there is no change in the fabric (Thorsteinsson, 1996, pp 110).

8.4.b The reflecting boundary

The energy arriving back at the antenna at any given instant $t_{twtt\,1}$ has been reflected back from the area that the front of the propagating wavelet occupied at time: $t_{twtt\,1}/2$. The propagating front of the wavelet will spread out in the ice sheet. This front is a function of the antenna diagram when the antenna is on the surface of the ice sheet (West and Demarest, 1987).

8.4.b.i Near the surface of the ice sheet

Near the surface of the ice sheet the propagating front of the wavelet is spherical. If a spherical boundary is causing the reflection then a one dimensional model is not adequate and the energy arriving back at the antenna has come from different depths and cannot be considered to have been reflected from ice of the same age.

Consider a large permittivity step at a depth z_1. This step produces a reflection coefficient that dominates over the reflections within a wavelength in either direction for normally incident wavelets. But once the normally incident rays have propagated deeper than z_1 the non-normal rays will still be striking the step at z_1 . The reflections from these non-normal rays will produce reflected energy that travels back to the antenna and may dominate over the normal reflections from below z_1. These non-normal reflections will put a long tail onto the initial normal reflection. The returning energy will be spread out over a longer duration, so it is more likely to experience interference from other reflections and also causes the problem of selecting

the start of the reflection out of the noise.

As there are many permittivity variations near the surface there will be energy returned from a range of depths. This energy will interfere and it is not possible to assign energy at any particular instance in the returning radar data to a particular depth.

8.4.b.ii Deep inside the ice

Deep inside the ice sheet refraction will have bent the spreading electromagnetic wavelet's energy so that the energy is now travelling vertically downwards. This means that the front of the spreading wavelet is at the same depth at a given time and it is appropriate to use a one dimensional model. A reflection can now be related to a single feature inside the ice, the two-way travel time of the reflection is related to the depth of the feature and the reflection can be considered to be an isochrone.

8.4.b.iii At intermediate depths

There is a depth range inside the ice sheet where the refraction has started to pull the rays of the EM wave to the vertical, but it is still not appropriate to consider a one dimensional model. There are still reflections returning to the antenna from non-normal reflections.

If the non-normal reflections were returning from specular (plane) surfaces then Snell's law would be applicable and the reflection coefficient would decrease as the angle of incidence increased. However it is probably more appropriate to consider the ice sheet as a material where the electrical tensors change with depth. The most abrupt changes will be seen by a ray travelling vertically downwards. The non-normal rays experience less abrupt changes in the electrical tensors therefore the reflections from these non-normal rays are weaker. This

argument has been used previously in section 5.2.

For the reflection at a given t_{twtt} to be identifiable as a reflection from a feature in the ice core it will need to be stronger than the sum of all the non-normal reflections. The size of the permittivity step required to cause the initial normal reflection to dominate is a function of the other interfaces that are being illuminated at the same time, the horizontal continuity of the step and the horizontal nature of the downwards propagating wavelet.

8.4.c What are isochrones?

For an ice core an age can be assigned to a depth with a precision which depends on the accumulation rate at the site and the processes during deposition such as the action of the wind on the surface moving around features such as sastrugi and snow barchans. Of secondary importance is the slight diffusion of water molecules during the densification in the firn.

Once an age has been assigned to a feature in a single ice core the feature needs to be extendable over a wide area in order to be considered as an isochrone. Volcanoes and climate changes produce features that extend horizontally over many kilometres. Volcanoes are found in many ice cores across Antarctica (Moore et al. 1991). Climate changes cause changes in the chemical impurities arriving at the surface of the ice sheet so that the signal extends for long distances.

The depth of features is expected to vary in two cores drilled adjacent to each other. This is a result of slight changes in the deposition processes. Most glacier flow models will not include such small scale effects. In glacier flow models the depth of an isochrone will change very gradually due to changes in the accumulation at the surface or the stress inside the glacier.

The present positions of isochrones inside a glacier are a result of many different contributions.

1) Temporal changes in quantity of annual accumulation.

2) Geographical changes in the quantity of annual accumulation.

3) Temporal changes in the movement inside the glacier.

4) Geographical changes in the movement of the glacier.

The glacier flow modellers who originally placed the ice sheet isochrones close to internal reflections had to make assumptions about some of these processes.

8.4.d When is an internal reflection an isochrone?

Robin et al. (1969) introduced a distinction between the reflections near the surface which had a diffuse (rough) behaviour and the reflections at depth which appeared to originate from specular (smooth) surfaces. The deep reflections were weak, and on Z scope data formed stratified, continuous reflections. It was these deep reflections that Robin et al. hypothesised could be isochrones.

The Berkner reflections are certainly stratified and continuous as seen on the published figure (Steinhage and Blindow, 1995 and figure 6.6). As the Berkner reflections are from close to the surface they are strong reflections. However, from a single trace it is not possible to establish the diffuse nature of the reflections. To establish the diffuse nature would require the data from the common midpoint gather made at B25 in order to see how the brightness/position of the internal reflections alter as the distance between the transmitting antenna and receiving antenna increases. Therefore the Berkner reflections are not candidates for being isochrones.

The reflections deep inside the GRIP core are certainly weak, stratified and continuous on the published profiles, and they can certainly be considered as isochrones.

In order for an internal reflection on Z scope data to be an isochrone the reflection needs to be reflecting from the same feature inside the ice sheet. The feature inside the ice sheet needs to be large enough to stand out from the interference effects of other variations in the electrical tensors above and below. In such a case the energy returning to the antenna at time t can be considered to have been caused by a reflection at a single depth z. If an internal reflection can be modelled using a one dimensional plane wave model the internal reflection is an isochrone.

8.5 Conclusion

The original question was: can it be assumed that the ice causing each weak stratified internal reflection fell as snow at the same time?

The answer is that this is true for deep reflections but not necessarily for shallow reflections with the cut off point between the two left indistinct but the present limits are lower than 100 m and probably higher than 1000 m. The exact place will depend on the antenna system and the properties of the ice sheet at a site.

The rationale for this conclusion is that for the GRIP core the present parallel layered one dimensional model is adequate since it places reflections from large scale climatic events that have a wide area spread. Consider the Holocene-Wisconsin boundary where the reflection is seen in the TUD data and is seen in the model result. The conductivity change is due to climate change and the climate change will affect the rest of the ice sheet, so that the reflection is an isochrone.

For shallow reflections the spherical spreading of the wavelet is important. The energy arriving back at the receiver at a given two-way travel time originates from a range of depths spread over an arc. There are many permittivity changes causing reflections which leads to interference and it is not possible to associate the reflected energy with a single depth feature. In order to understand more about shallow reflections three dimensional modelling will be necessary.

APPENDIX 1: Comparison of Internal reflections and Ice cores

Table A1.1 Polar ice cores and RES data from the same site, 1973 to 1982

Paper	Site	length of core /m (year, drilled)	Radar System	Observation	Conclusion of Authors
1975 Gudmandsen	Greenland (Camp Century)	1387 (1966)	TUD	IRH in the upper part of the core from the end of the last glaciation to the present.	IRH related to the climatic variation.
1977 Clough	Antarctica (Byrd)	2164	50 MHz burst pulse (SPRI Mk 2) (1970) Analog receiver	13 IRH identified	IRH in the uppermost kilometre due to density variations.
1978 Gudmandsen and Overgaard	Greenland (Camp Century) (North Central)	100	4 nsec pulse operated by H. A. Lessow		IRH match layers of high conductivity
	Greenland (Crete)	400	TUD		
1979 Ackley and Keliher	Antarctica (Cape Folger)	324 (1969)	35 MHz burst pulse (1967), 100 MHz burst pulse (1973), Receiver: A scope with accuracy ±15 m	Two IRH show up on both RES surveys.	IRH are due to variations in primarily density and secondarily bubble size.
1980 Hammer	Greenland (Crete)	400	TUD	Four IRH are within ±5 m of volcanic eruptions	IRH can be due to volcanic horizons.
1981a,b Millar	Many Antarctic and Greenland sites		Data from many different systems, SPRI and TUD	All observations have a lack of IRH during the Wisconsin period.	IRH can be due to volcanic horizons. In the Wisconsin the acidity is neutralised by calcium dust
1982 Millar	Greenland (Crete)	400	TUD		IRH can be due to volcanic horizons

Table A1.2 Polar ice cores and RES data from the same site, 1985 to present.

Paper	Site	length of core /m (year drilled)	Radar System	Observation	Conclusion of Authors
1985 Nishio and Ohmae	Mizuho Plateau (Antarctica)	130	300 MHz (3 ns pulse) 500 MHz (2 ns pulse) Recording returns from shallower than 25 m	Measure specific conductivity and density	
1987 Yoshida et al.	Mizuho Station (Antarctica)	700	179 MHz, ground based system with digital recording	5 cm thick volcanic ash layer in the ice, gives a 20 dB reflection	
1993 Fujita and Mae	Antarctica (Mizuho)	700	179 MHz, ground based with transmit & receiving antenna parallel	Strongest reflection when antenna orientated parallel or perpendicular to the flowline.	IRH equally likely to be produced by ice fabric variation as density variation.
1992 Hempel and Thyssen	Greenland (GRIP & GISP)	GRIP (3028) GISP	Two systems a 35 MHz mono cycle transmitter and a 35 MHz conventional burst transmitter, Digital recording	Depth interval without any IRH corresponds to Wisconsin ice.	
1994 Blindow	Antarctica (FRIS)	B13 (240 m) B15	40 MHz monocycle transmitter (1989), with digital recording	No IRH in the marine ice.	IRH correlate well with zones of increased conductivity.
1995 Jacobel and Hodge	Greenland (GRIP & GISP)	GRIP (3028) GISP	TUD radar but with digital recording	Many IRH in the Holocene ice, few in the alkaline Wisconsin ice.	

APPENDIX 2. The Fast Fourier Transform (FFT)

The description that follows comes from chapter 11 of Brigham (1974). A different number range is used compared to that in chapter 5.

Analysis equation

$$\tilde{F}(p) = \sum_{n=0}^{N-1} E_0(n) W^{p\,n}$$

where $W = e^{-\left(\frac{2\pi i}{N}\right)}$

The fast Fourier transform is a rapid (more efficient) way to calculate the discrete Fourier transform in the case where N is 2 raised to an integer power. It is desirable to represent the integers n and p as binary numbers, so if N = 4 then: $n = (n_1, n_0) = 00, 01, 10, 11$ and $p = (p_1, p_0) = 00, 01, 10, 11$ so $p = 2p_1 + p_0$ therefore the analysis equation is rewritten as:

Analysis equation

$$\tilde{F}(p_1, p_0) = \sum_{n_0=0}^{1} \sum_{n_1=0}^{1} E_0(n_1, n_0) W^{(2p_1+p_0)(2n_1+n_0)}$$

The W term can be multiplied out as shown below:

$$\begin{aligned} W^{(2p_1+p_0)(2n_1+n_0)} &= W^{(2p_1+p_0)2n_1} W^{(2p_1+p_0)n_0} \\ &= \left[W^{4p_1n_1}\right] W^{2p_0n_1} W^{(2p_1+p_0)n_0} \\ &= \left[\left(e^{\frac{-2\pi i}{N}}\right)^{4p_1n_1}\right] W^{2p_0n_1} W^{(2p_1+p_0)n_0} \\ &= \left[1^{p_1n_1}\right] W^{2p_0n_1} W^{(2p_1+p_0)n_0} \\ &= W^{2p_0n_1} W^{(2p_1+p_0)n_0} \end{aligned}$$

So that the analysis equation is:

Analysis equation

$$\tilde{F}(p_1, p_0) = \sum_{n_0=0}^{1} \left[\sum_{n_1=0}^{1} E_0(n_1, n_0) W^{2p_0n_1}\right] W^{(2p_1+p_0)n_0}$$

The inner summation can be rewritten as:

$$E_1(p_0, n_0) = \sum_{n_1=0}^{1} E_0(n_1, n_0) W^{2 p_0 n_1}$$

Determining the term $E_1(p_0, n_0)$ due to the inner summation in the form of a matrix gives:

$$\begin{bmatrix} E_1(0,0) \\ E_1(0,1) \\ E_1(1,0) \\ E_1(1,1) \end{bmatrix} = \begin{bmatrix} 1 & 0 & W^0 & 0 \\ 0 & 1 & 0 & W^0 \\ 1 & 0 & W^2 & 0 \\ 0 & 1 & 0 & W^2 \end{bmatrix} \begin{bmatrix} E_0(0,0) \\ E_0(0,1) \\ E_0(1,0) \\ E_0(1,1) \end{bmatrix}$$

Where W^0 is unity, and $W^0 = -W^2$ (when N = 4). The outer summation is determined in a similar manner:

$$E_2(p_0, p_1) = \sum_{n_0=0}^{1} E_1(p_0, n_0) W^{(2p_1 + p_0) n_0}$$

where:

$$\begin{bmatrix} E_2(0,0) \\ E_2(0,1) \\ E_2(1,0) \\ E_2(1,1) \end{bmatrix} = \begin{bmatrix} 1 & W^0 & 0 & 0 \\ 1 & W^2 & 0 & 0 \\ 0 & 0 & 1 & W^1 \\ 0 & 0 & 1 & W^3 \end{bmatrix} \begin{bmatrix} E_1(0,0) \\ E_1(0,1) \\ E_1(1,0) \\ E_1(1,1) \end{bmatrix}$$

The final step is to alter the bit order of the result of the outer sum $\tilde{F}(p_1, p_0) = E_2(p_0, p_1)$. To calculate this Fourier transform (for $N = 2^y = 4$, where y = 2) as a discrete Fourier transform would require N^2 (16) complex multiplications and (N)(N-1) (12) complex additions. By using the FFT only Ny/2 (4) complex multiplications and Ny (8) complex additions are required. There are many other formulations available for calculating FFTs.

APPENDIX 3. Electrical Conductivity Measurement (ECM)

This instrument was designed by Hammer (1980). First a sharp microtome knife is used to cut a flat surface on the side of the core. This is to remove any ice that has been in contact with the drill fluid and to obtain a flat surface which needs to be about 20 mm wide. Then two sharp brass electrodes separated by a distance of about 10 mm and a potential difference of about 1000 Volts are scratched along the surface at a speed of between 20 and 1000 mm s^{-1}. In the BAS instrument a speed of 40 mm s^{-1} is used.

For stationary electrodes (disregarding the first 10 ms) the current keeps constant for 0.1 to 0.5 seconds (T) then decreases exponentially with a half life of the order of a second to give a final steady current. The electrodes need to spend less than time T in one place and this gives a recommended minimum speed. At any slower speeds then the measured current will fall off.

The current flow between the tips is measured. This current is related to the dc conductivity of the ice. The resolution of this instrument is roughly a few mm. The degree to which the current represents the bulk properties of the ice is determined by the thickness of the quasi-liquid layer and the flow of charge in the surface and the bulk (Schwander et al. 1983).

In polar ice conduction at dc is almost entirely controlled by the concentration of strong acid in the ice. There is no ECM response to even a vast excess of salt. Large ammonium peaks correspond to drops in the ECM but this is assumed to be due to the neutralising of the acid (Moore et al. 1994).

The current reading may be converted into the acidity using a calibration curve of μA and μequivalents of hydroxonium ions. The concentrations are derived from pH measurements on

melted samples (Hammer, 1980).

$$[H+] = (1.2 + 0.017\ i^2)\ \mu\text{equiv. } H^+/\text{kg}$$

or $$[H+] = (0.045\ i^{1.73})\ \mu\text{equiv. } H^+/\text{kg}$$

The current is sensitive to the temperature, so Hammer (1980) corrects the ECM to a temperature of -14 °C using an activation energy of 0.23 eV (22 kJ mol^{-1}). Other workers use different activation energies and final temperatures.

APPENDIX 4: Dielectric Profiling (DEP)

There are a number of different methods of measuring dielectric properties as functions of frequency, a field that has been called Impedance spectroscopy (Macdonald, 1987) or Dielectric spectroscopy (Craig, 1995). For descriptions of various methods see (Field, 1954; Grant et al. 1978; Blythe, 1979). A good description of many different bridge systems can be found in Hall (1971).

Background

The air capacitance (C_{air}) and conductance (G_{air}) is determined between two electrodes. The ice sample is then placed between the electrodes and the capacitance (C_{raw}) and conductance (G_{raw}) measured at one or more frequencies. The conductivity (σ) and permittivity (ε) at a given frequency are calculated using the equations below:

$$\sigma = \frac{\varepsilon_0 \left(G_{raw} - G_{air} \right)}{C_{air}} \qquad \varepsilon = \frac{\varepsilon_0 G_{raw}}{G_{air}}$$

The conductivity and permittivity are those of the combined air and ice that lies between the electrodes.

Sources of Error

1) Leakage and strays. We have a problem in that we are measuring a piece of ice with a large resistance (so that there is a temptation for leakage currents) and a small capacitance (so there is a temptation for stray capacitances to be significant). The way to avoid these leakage currents and stray capacitances is by a shield or guard. The shield is put at the same potential as the detector arm. This means that any current that leaks onto the guard before any of the

components will not leak back into the circuit at the detector. Any current flow shielding is in place so that any capacitance between the parts of the measuring circuit and the shield/ guard will not affect the detector.

2) Fringe capacitance. For any sample between two electrodes there is a capacitance that goes through the air between the electrodes. When the ice is inserted, the middle capacitance increases but the edge capacitance stays the same.

3) Surface conductivity. When dealing with ice for temperatures warmer then -25 °C there is considerable surface conductivity (Petrenko, 1993). This means that the conductivity is higher near the surface than the centre. These higher surface currents should be avoided in the measurement.

4) The ice-air composite. The results of AC measurements are the real parts of the conductance and capacitance at various frequencies. But these values are for a finite size sample of ice sandwiched between two layers of air. There are a number of mechanisms that mean that the permittivity values of this composite system are not those of the bulk ice. The problem is that ice is a proton conductor and it exchanges charge poorly with electron conducting metal electrodes. This effect is worsened if there are air gaps at the interface between the electrodes and the ice. The build up of charge at the interface is called Space Charge Polarisation (SCP), (also called interfacial or electrode polarisation). This is the fourth type of polarisation after dipolar, ionic and electronic. There are two common ways to tackle this: Firstly try to ensure as good a contact as possible, striving for the ideal of an "Ohmic" electrode. This is done by having a supply of protons at the electrodes. This has been tried with proton doped electrodes or by using a Hydrogen rich atmosphere (Petrenko, 1993).

Secondly suppress all charge exchange by inserting layers of loss free dielectric between the metal contacts and the ice. This approach is called blocking electrodes and it is now the most common approach when measuring ice samples.

Three terminal measurement, Transformer Ratio arm bridge measurement

This is the type of measurement used by Paren (1970) when using parallel plate electrodes to measure disc shaped ice samples. He used a General Radio 1620 which covers the frequency range 50 Hz to 10 kHz. Ratio arm bridges have a high (HI) terminal, high voltage but low impedance output of the transformer, and a Low (LO) terminal, low voltage and high impedance. When the bridge is balanced there is no voltage from LO to the ground (G). This G terminal can then be used for the shielding. The guards used by Paren were concentric rings surrounding the electrode plates. Subsequently Reynolds (1983) and Moore (1988 a) used similar apparatus.

There are a couple of international standards available for the permittivity measurement of flat samples: British Standard BS 7663 and American Society of Testing Materials D 150.

Four terminal measurement, Frequency sweeping multibridge

This is the device designed by Moore and Paren (1987). The ice core is laid on its side and placed between two curved electrodes. A Wayne Kerr 6425 AC bridge circuit is used to measure the impedance over the frequency range 20 Hz to 300 kHz. The guard electrodes are curved plates that lie adjacent to one of the measurement electrodes. There have been publications which examine the air capacitance of such systems (Moore, 1988 a; Wilhelms 1996; Wilhelms et al. 1998). However there is a need for far more research into understanding the distribution of the fields when ice is between the curved plates and the need for shielding.

The smaller the width of the electrodes used for the measurement the smaller the value measured which leads to an increase in the error. A balance needs to be struck between the desired resolution and the desired accuracy. By using more accurate bridges and improving the control on the field lines inside the ice a finer resolution is possible.

Moore et al. (1990, pp 195) found it satisfactory to use the dielectric parameters of the composite system alone to relate to the chemical stratigraphy. At 100 kHz the conductivity of the composite system is within a few percent of that intrinsic to the ice, and approximates well to the conductivity of ice in the radar sounding MHz frequency range.

APPENDIX 5: The error in the Berkner measurement

The measurement by the Wayne Kerr frequency sweeping multi-bridge will have an error associated with it. This error can be quite large due to the difficulty of trying to measure a very small capacitance (pF) in the presence of a large resistance (MΩ).

Assumptions

The first assumption is that the Wayne Kerr has had time to warm up. During the first hour after turning on there can be drift in the measurement due to temperature changes inside the instrument. The measurements is then made at a position x and at a frequency f. It is assumed that x and f are exact. One volt and normal speed are used on the Wayne Kerr for the measurement and the Wayne Kerr is trimmed at the measurement frequency for open circuit and short circuit corrections.

Initial acquisition errors

The values in the Wayne Kerr manual are absolute percentages so that the manufacturers are fairly certain that the actual value will be within the percentage of that quoted. Therefore the rest of this analysis uses percentages not standard deviations. This is a disadvantage as most of the statistics that deals with the combination of measured quantities in calculations and the error in the product uses standard deviations.

Other points raised in discussion with the support staff at Wayne Kerr are:

1) "The newer manufacturers are starting to introduce statistics into their accuracy quotes, but that Wayne Kerr had been around for a long time and still used the traditional method."

2) Accuracy can be a lot worse if measuring at a harmonic of AC so good idea to avoid 25/30

Hz, 50 / 60 Hz, 100/120 Hz. If you have to use them, use a slow measurement speed.

3) The areas off the marked charts, that I am using for the high and low frequency measurements, are unknown, and there may be sudden jumps in the accuracy levels. You could test with a constant performance substance such as polystyrene.

4) The measurement of a conductance and capacitance in parallel means that you need to consider the ability of the analyser to measure a small conductance current in the presence of a capacitance current. The chart to use for the accuracy of the conductance depends on the value of Q. $Q = \omega C_p R_p$

for $0<Q<0.1$ use raw table page 2.8 Wayne Kerr manual

for $0.1< Q<1$ use table page 2.8 Wayne Kerr manual and multiply by factor 1+Q

for $1<Q$ use Q accuracy chart

Measurement of air capacitance

The air capacitance used is the average of the values measured for air over a range of frequencies.

$$C_{air} = \frac{1}{n}\sum_{i=1}^{n} C_{air\,i}$$

This means that the error in the average value will depend on the error in each of the values used in the calculation of the average. The errors in the air capacitance measurements at a range of frequencies are shown in the table below. As the error increases at the higher and lower frequencies it is usual to confine the measurement to the middle frequency range of the Wayne Kerr in order to get more precise values. These values are given as if a capacitance only measurement mode is used for the measurement.

Table Berkner Air Capacitance

Frequency	**Value C**	**Precision % value off table page 2-10 Wayne Kerr manual**
20 Hz	380 fF	0.5
1 kHz	380 fF	0.05
300 kHz	380 fF	0.5

Table Berkner Ice Measurement

Freq	**ω**	**Quantity**	**Value**	**Conductance Precision %**	**Capacitance Precision %**
50 kHz	3.14×10^5	G	500 nS	Using table on page 2-8 Wayne Kerr manual then multiplying by 1+Q 0.8 %	Using table on page 2-10 Wayne Kerr manual then multiplying by 1+D 0.8%
		R	2 MΩ		
		C	1 pF		
		D	1.6		
		Q	0.6		

Conductivity

The conductivity is given by the equation:

$$\sigma = \frac{\varepsilon_0 \left(G_{raw} - G_{air} \right)}{C_{air}}$$

The error percentage in the calculated conductivity depends on the error in G_{raw} and C_{air} (the value of G_{air} should be close to zero). Taking into consideration the percentage errors in these quantities the percentage error in the 50 kHz conductivity is slightly less than 1% when measuring the Berkner ice core using a 15 mm wide top electrode.

APPENDIX 6: The Berkner Bench

The logging bench has a motorised carriage to move the tools for each run across the top of the ice core. The ice core does not move but the tool used can be changed. This gives the following advantages:

****Improved acquisition for the individual tools:

With this new bench the ECM is moved at a set speed (40 mm s^{-1}) which is an improvement over the variable speed when the tool was moved by hand. The signal is immediately recorded on a computer rather than on the graph paper of previous seasons.

J.Moore's HRDEP system showed the viability of a small top electrode with a large base electrode to act as a signal source. The HRDEP system had the top electrode moved by hand which may lead to an inaccurate position when used by an inexperienced operator. The other problem was that the movement of the top electrode was continuous, while the Wayne Kerr 6425 Multibridge (WK) takes four measurements in order to produce one value; so the problem would have been that these four measurements were not occurring over the same piece of ice. The new bench has the top electrode stationary as it takes the four measurements. The other problem with the use of a relay driven system (GRIP Box) is that there is some variability of the measurement dependent on the measuring position that can not at the moment be explained.

****Improved comparison:

As the core is not moved between the stratigraphy, ECM and DEP then the three records are easier to compare.

****Improved expansion capacity:

It is now far easier to alter the DEP electrode size and sample spacing than on previous systems. If the need arises for future expansion to a two metre (or longer) system, ie: for a deep drilling project, then only four parts need to be altered: three hardware components (the base plate, base electrode and extruded slide); the fourth alteration is a few parameters in the computer software. The end blocks, motor, tools and carriage will all remain the same.

Parts of the Berkner Bench

The slide (produced by the company Time and Precision) is mounted on an aluminium sheet. At one end of the slide is the motor to drive it. On the other end of the slide is a digital potentiometer that provides the position information. The motor is controlled by a PDX15.

The bench is controlled by a Toshiba T5200/100 with a 20 MHz Intel 386 microprocessor, bought by J.Moore after seeing it in use by other nations. This computer was running a Turbo Pascal program; this was the language used previously by J.Moore and is the software for the card drivers in the Toshiba. There are two cards in the Toshiba, these are:
Firstly a PC30B card for input and output of signals. Secondly a General Purpose Interface Board (GPIB) a PC1A using IEEE protocol for communication with the WK.

PREPARATION OF THE BENCH FOR A FIELD SEASON

In the UK

Change the RAM configuration of the T5200/100 from desk to acquire mode using batch program dtoa.bat (atod.bat returns it back from acquire to desk). In the acquire mode there are reserved areas of the RAM memory for the transfer of variables to the cards.

Run the program accuracy.pas while still in the UK. This requires a high accuracy capacitor and tests the WK to see if recalibration is necessary. Before the Berkner field season WK

number 064 was sent away for calibration to: Farnell Instruments (Technical Service Dept), Sandbeck Way, Wetherby, West Yorkshire, 581961 (cost £125).

Use the backpack system to get a complete backup of the hard disk of the T5200.

Get a computer prediction of the depth to date relationship at the site. This will give you an idea of where to look for volcanoes during the logging.

Decide in the UK what sort of resolution data is required for the ECM and DEP. On Berkner I used a 15 mm wide electrode, a sample separation of 10 mm and the 'normal' measurement speed on the WK. All of these could be altered.

In the field.

Construct a large underground cave (a chain saw is very useful) for the logging. This allows the cores to be stored in the same area as the apparatus. On Berkner it took 2 days to build this. (It is advisable to watch your back as the snow blocks are passed out of the chamber!) Site the generator away from the logging area as it emits pollutants. Run wires from the generator to the logging equipment on wires strung between bamboo canes (connect using cable ties). If the cables lie on the snow surface they will melt into the snow then ice over and will not be removable at the end of the field season.

Assemble the bench

All the cables between the various parts are labelled. Where a cable meets a socket, if possible screw the connection together. This will save you much time later on looking for mysterious intermittent faults that turn out to be due to loose connections.

From the computer:

The COM 1 port connects via a 9 way D to the motor controller PDX15

The PC30B connects via a 50 way D to the ECM box.

The PC1A (GPIB) card connects via a IEEE wire to the WK.

From the WK:

The brown and red (current return) sockets connect via a coaxial T socket to the top electrode. The yellow and orange (signal source) sockets connect via a T socket to the bottom electrode. After connecting the chosen top electrode between the guard electrodes it is worth while using a multimeter on the coaxial plug to check that a short circuit has not occurred between the central pin and the outside.

From the ECM box:

There is a coaxial to the ECM tool and a 9 way D to the potentiometer.

From the PDX15

There is a special cable to go to the motor. If in the field it is a good idea to cover the connecting plug with a plastic bag to avoid snow working its way into the connection. Try to have this connection easily accessible in case it becomes necessary to break the connection quickly if the slide is driven up to the end.

Initial chores

Run some test programs to ensure that the various bits of the bench work. The program testslid.pas can be used to test the movement control of the carriage. The program testwkerr.pas can be used to test the IEEE connection to the WK. The program testcurr.pas can be used to test the ECM line.

****Trimming the Wayne Kerr.

Before operation it is necessary to do the open circuit (O/C) and short circuit (S/C) trims on the Wayne Kerr Multibridge.

O/C. Move the top electrode as far away as possible from the bottom electrode and press trigger.

S/C. Use a piece of wire to connect the top and bottom electrodes, some of the anodised layer has been scratched away at the end of the bottom electrode, use the screw attaching the top electrode.

****Recording the stray conductance and capacitance.

Set up with the top and bottom electrodes separated by the diameter of the core. For the BAS drill this is 106 mm. For a Polar ICe coring Office shallow drill (PICO) this is 76 mm. Then run the program strays.pas which records the two values on the hard disc in the file c:\data\cur\stray.dat. The conductance value should be close to zero. The capacitance value will be that for air: for a 15 mm electrode about 340 fF; for a 5 mm electrode about 180 fF.

****In most cases the drilling will start at a certain depth below the present day snow surface. It is necessary to record this parameter in the program unit globals.pas. Try to establish one depth scale for the core, hopefully with depth zero being the snow surface on the day that drilling starts.

****Alter the place site name and label for the computer records in unit globals.pas

**** Form a directory on the hard disc for the logging files to go to eg: c:\data\b25\

**** Alter the form of the record in C:\data\cur\going.dat so that it reads:

site
bag number
0 (this is the number of samples in the strat log)
0 (this is the number of samples in the first ECM run)
0 (this is the number of samples in the second ecm run)
0 (this is the number of samples in the DEP log)

Have a blank disc available.

OPERATION

The main program is c:\tp\berkner\acquire.bas. After each operation Stratigraphy, DEP and ECM, the data are saved from the RAM to the hard disc in the c:\data\cur directory. This is because there was often a failure of the instrument or power when in the field. This would make it unnecessary to start to log the core from scratch.

In the morning, in the field, before breakfast the generator was started and all the logging equipment was switched on. It was important that the equipment had time to warm up in the morning, since if cold the WK gives inconsistent readings and the T5200 can be damaged. I had heater pads spread around the instruments, and left them for at least half an hour. I found it useful to use a temperature probe tucked beneath the T5200. The one time I tried to write or read from the hard disc when the T5200 was still cold I ended up having to reformat the hard disc then reload all the software from floppies.

Before logging

The recovered core is left to reach the room temperature. (If the logging is being done in the UK cold room this means that adjusting the room temperature to -15 °C immediately prior to taking the measurement is a bad idea, as the temperature in the centre of the core will be lower.) The core bag is removed from the cardboard tube, and weighed. Then it is placed on

the bottom electrode. There is a spacer to put at the bottom of the core to ensure that the bottom electrode extends beyond the bottom of the core. At the start the tool holder should be at the bottom of the core, in the space next to the motor.

Stratigraphy

Given the option of a full log or just the length. If the full log is chosen then the operator drives the tips of the tool down the core stopping at any interesting features. Possible features are: break in core: b, clear ice layer: i, hoar crystal layer: h, radiation crust: r, wind crust: w, separate fragments: s. I tended to avoid doing a full strat log towards the end of the Berkner season due to the time involved. I chose the option of simply recording the length of the core in the program. Then the positions of the breaks are noted in a log book and added later to the data file.

DEP

Put the top electrode on the holder and drive it to the top, so that the centre of the top electrode lies above the top of the core. The spacing of the measurements is controlled by parameters in program unit Globals.pas. The axis of the graph is set by the two parameters range and base. These are initially set when the program first runs then updated whenever the viewgraph function is used.

Potential between plate electrodes: 1 Volt
Top plate electrode width: 15 mm, 10 mm and 5 mm available.
Bottom plate electrode length: 1500 mm
Measurement frequency: 50 kHz
Intended sample separation: 10 mm
Actual sample separation: 9 - 11 mm

The DEP conductance was stored as a value in nano-siemens, but in order to be able to compare with the values given by J.Moore in previous publications the effect of the geometry needs to be removed to give a conductivity value in micro-siemens per metre. This is done

using the values recorded by the program strays.pas for the air capacitance.

ECM

The surface of the ice core is planed off with a microtome, then brushed clean. This is only necessary for the deeper cores when the ice is hard. For soft firn cores it is possible to push the tips into the core to reach fresh ice. There is a holder available which can support the microtome to the carriage to allow a fixed cutting depth, or to allow the microtome to cut just in front of the ECM tips.

In this instrument the motor dragged the ECM tips along the surface at 40 mm s^{-1} towards the bottom of the core. It was often necessary for both operators to help hold the pieces of ice on the bottom electrode as the tips ran along the core. Usually two ECM runs were done for the first few runs in the morning or in the afternoon in order to check repeatability. Two ECM runs were also done if the electrode tips lifted off the ice during the first run. Despite initial worries, the large metal electrode below the core had no noticeable effect on the ECM measurement. The precision of the ECM current measurement was about ± 1 μA.

Potential between scratch electrodes: 1500 Volts
Separation of scratch electrodes: 10 mm
Speed of scratch electrodes over the ice: 40 mm s^{-1}
Intended sample separation: 2 mm
Actual sample separation: 2 to 5 mm

Extras

At the end of the logging extra information is requested: temperature in room, temperature on the ice surface. (These need only be exact if the data is going to be used quantitatively to correct the values to a standard - 15 °C.). As the conductivity of ice is sensitive to temperature, two temperatures were measured and recorded on the computer with the DEP

measurements. These were the air temperature in the pit 50 cm above the bench surface and another using a pad sensor pressed up against the end of the ice. The original intention had been to drill a hole in the body of the core and insert a probe to get the temperature in the centre. The surface and centre temperatures would differ if the core had not yet reached equilibrium with the surroundings. But this was vetoed by the glacio-chemists as they feared that this would introduce contamination into the centre of the core. Another consideration is that such a measurement would probably have required too much time in the field. During the Berkner season the temperature in the chamber varied between -11.9 and -18.0 °C.

Finally the mass of the ice core is recorded. Then the program constructs a file on the hard drive of the computer in the chosen directory. It then checks the space available on the disc. in the A drive. Compares this with the size of the file. If sufficient space exists then the file is copied to the floppy disc.

It takes about 20 to 30 minutes to do each bag.

APPENDIX 7: The wavelet modelling programs written in IDL

This is one example of the programs used to model the wavelet propagation

Main Program Wavelet.pro which calls functions which are listed in subsequent pages.

```
PRINT,' '
PRINT,' WAVELET MODELLING '
PRINT,' '

display = 1
dofdtd  = 1
doconv  = 1
doprop  = 1
dofreq  = 1
time    = 1

SET_Plot, 'X'
; produce a backing store for all graphics
DEVICE, retain = 2

; Constants
cmu0  = 12.5663706144E-7          ; permeability of a vacuum
ce0   = 8.85418782E-12            ; permittivity of a vacuum
cf    = 50E6                      ;carrier frequency of the wavelet being used

;*************************
; Read in a file of ground properties
;*************************
Get_LUN, lun              ; get a free logical unit number
file   = DIALOG_PICKFILE(/READ, PATH='data', FILTER = '*.dat')
PRINT, ' Reading in file : ',file

dz     = 0D               ;set to scalar type
var1   = 0                ;set to a scaler type

OpenR,   lun, file
ReadF,   lun, dz
ReadF,   lun, var1

array  = FLTARR(3,var1)       ;set to an array type

ReadF,   lun, array
Free_LUN, lun

PRINT, ' Size of array is: ',SIZE(array)
indepth = Reform(array[0,*])
inepsil = ce0*Reform(array[1,*])
insigma = Reform(array[2,*])
PRINT, ' Number of depth steps  ',N_ELEMENTS(indepth)
PRINT, ' minimum depth          ',MIN(indepth)
PRINT, ' maximum depth          ',MAX(indepth)

;*************************
; Calculate dt
;*************************
vmax   = 2E8
dt     = 0.5*dz/vmax

PRINT, ' the depth step is = ',dz
PRINT, ' the time step  is = ',dt

mcore     = SIZE(indepth, /N_ELEMENTS)
length    = FLOOR((indepth[mcore-1]-indepth[0])/dz)
moddepth  = indepth[0]+dz*LINDGEN(length+1)  ;+1 as starts at zero

epsil     = INTERPOL(inepsil,indepth,moddepth)
sigma     = INTERPOL(insigma,indepth,moddepth)


;*********************************
; Define wavelet
;*********************************
```

```
E1              = billwavz(dz,dt,50E6,epsil[0]/ce0,0)
mwave           = SIZE(E1,/N_ELEMENTS)
PRINT,' Length of wave in dz steps (mwave)  = ',mwave
PRINT,' Length of wave in metres        = ',mwave*dz,' m'

mcore           = N_ELEMENTS(epsil)

;*********************************
; define epsilf  f for fdtd
;*********************************
epsilf                  = DBLARR(mcore+mwave)
epsilf[0:mwave-1]       = epsil[0]
epsilf[mwave:(mwave+mcore-1)] = epsil

sigmaf                  = DBLARR(mcore+mwave)
sigmaf[0:mwave-1]       = sigma[0]
sigmaf[mwave:(mwave+mcore-1)] = sigma

mcore                   = N_ELEMENTS(epsilf)

; determine indicies for core
; use imaginary as could be sig or epsil that change
kf                      = COMPLEX(epsilf,sigmaf)
m1                      = mwave
a                       = WHERE(kf NE kf[0])
m2                      = MIN(a)
a                       = WHERE(kf NE kf[mcore-1])
m3                      = MAX(a)+10
PRINT,' m1 = ', m1,'  m2= ', m2,'  m3 = ',m3
PRINT,' thickness = ',dz*(MAX(a)-m2)

;PRINT, sigmaf[m2-2:m2+1]

Ebig                    = DBLARR(mcore)
Ebig(0:mwave-1)         = E1

; ************************
; The initial conditions
; ************************
show  = 1
if (show EQ 1) THEN BEGIN
 Window, /Free
 !P.MULTI = [0,1,3]
 PLOT, epsilf/ce0, YTITLE= 'epsil/ceo'
 !P.MULTI = [2,1,3]
 PLOT, sigmaf, YTITLE= 'sigma'
 !P.MULTI = [1,1,3]
 PLOT, Ebig, YTITLE= 'E field'
ENDIF

; ****************************************
; determine expected reflection time
; ****************************************
; velocity in medium infront of layer
cv1         = 3E8/SQRT(epsilf[0]/ce0)

; velocity in ice core section
cvmean      = 3E8/SQRT(MEAN(epsilf(m2:m3)/ce0))

; time for wavelet to pass the start
tt1         = ((m1-1)*dz)/cv1

; time for wavelet to travel to first boundary
tt2         = ((m2-m1)*dz)/cv1

; time for wavelet to travel through medium
tt3         = ((m3-m2)*dz)/cvmean

; decide on number of time steps
ttime       = tt1+2*tt2+2*tt3
ntime       = 0L  ; set up as long integer
ntime       = 1+ROUND(ttime/dt)

; decide on expected time of first return
firstrtn    = 2*tt2
finalrtn    = 2*tt2+2*tt3+tt1

PRINT,' '
```

```
PRINT,' Expected travel time to feature  = ',tt1/1E-9,' ns'
PRINT,' Expected first return at         = ',firstrtn/1E-9,' ns'
PRINT,' Expected final return at         = ',finalrtn/1E-9,' ns'
PRINT,' Decided on a record duration of  = ',ttime/1E-9, ' ns'
PRINT,' This means having number of steps = ',ntime


IF (dofdtd EQ 1) THEN BEGIN
 ; ********************************
 PRINT, ' Do FDTD '
 ; ********************************
 IF time EQ 1 THEN T1 = SYSTIME(1)
 recfdtd  = fdtd(dt,dz,Ebig,epsilf,sigmaf,m1,ntime,0)
 IF time EQ 1 THEN BEGIN
  T2 = SYSTIME(1)
  PRINT,'  it took ',T2-T1,' seconds'
 ENDIF

 ; ********************************
 ; create an FDTD file
 ; ********************************
 array    = DBLARR(2,N_ELEMENTS(recfdtd[1,*]))
 array[0,*] = recfdtd[0,*]
 array[1,*] = recfdtd[1,*]

 Get_LUN, lun
 OpenW,   lun, 'mmfdtd.dat'
 PrintF,  lun, N_ELEMENTS(recfdtd[1,*])
 PrintF,  lun, array
 Free_LUN, lun

ENDIF ELSE BEGIN

 ; ************************************
 PRINT, ' Read in fdtd file '
 ; ************************************
 Get_LUN, lun              ; get a free logical unit number
 var1   = 0L               ; set to a scaler type

 OpenR,   lun, 'mmfdtd.dat'
 ReadF,   lun, var1

 array  = DBLARR(2,var1)   ;set to an array type

 ReadF,   lun, array
 Free_LUN, lun

 recfdtd   = DBLARR(2,var1)
 recfdtd[0,*] = Reform(array[0,*])
 recfdtd[1,*] = Reform(array[1,*])

ENDELSE

index   = Where(recfdtd[0,*] GT firstrtn AND recfdtd[0,*] LT finalrtn)
fdtdt   = recfdtd[0,index]
fdtde   = recfdtd[1,index]

IF (display EQ 1) THEN BEGIN
 Window, /Free
 !P.MULTI = 0
 label  = 'FDTD at posn '+ STRING(m1)
 PLOT, fdtdt/1E-9, fdtde, TITLE=label, XTITLE=' time /ns'
ENDIF
PRINT,'  FDTD maximum is ',MAX(fdtde,ind),' at time ',fdtdt[ind]/1E-9,' ns'
PRINT,'  FDTD minimum is ',MIN(fdtde,ind),' at time ',fdtdt[ind]/1E-9,' ns'


;STOP


; ***************************
; Extract the time wavelet
; ***************************
a1              = CEIL(((1.00D*mwave*dz)/cv1)/dt)
a2              = CEIL(((1.25D*mwave*dz)/cv1)/dt)
lend            = a2-a1
decrease          = ((lend-1.0D)-DINDGEN(lend))/(lend-1.0D)
```

```
;print, ' decrease(0) = ',decrease(0)
;print, ' decrease(',lend-1,') = ',decrease(lend-1)

E1              = DINDGEN(a1+lend)
len             = a1+1
first           = LINDGEN(len)
E1[first]         = recfdtd[1,first]
last            = a1+1L+LINDGEN(lend)
E1[last]          = decrease*recfdtd[1,last]


IF (display Eq 1) THEN BEGIN
 WINDOW, /free
 !P.MULTI = 0
 PLOT, E1, TITLE='E1 from FDTD'
ENDIF


; reduced epsil and sigma for time records
repsil  = epsilf(m1:mcore-1)
rsigma  = sigmaf(m1:mcore-1)

IF (doconv EQ 1) THEN BEGIN
 ; ********************************
 PRINT, ' Do Convolution '
 ; ********************************
 IF time EQ 1 THEN T1 = SYSTIME(1)
 recconv  = propone(dt,dz,E1,repsil,rsigma,0)
 IF time EQ 1 THEN BEGIN
  T2 = SYSTIME(1)
  PRINT,'  it took ',T2-T1,' seconds'
 ENDIF

 ; ********************************
 ; create an conv file
 ; ********************************
 array     = DBLARR(2,N_ELEMENTS(recconv[1,*]))
 array[0,*]  = recconv[0,*]
 array[1,*]  = recconv[1,*]

 Get_LUN,  lun
 OpenW,   lun, 'mmconv.dat'
 PrintF,  lun, N_ELEMENTS(recconv[1,*])
 PrintF,  lun, array
 Free_LUN, lun

ENDIF ELSE BEGIN

 ; ************************************
 PRINT, ' Read in conv file '
 ; ************************************
 Get_LUN, lun              ; get a free logical unit number
 var1    = 0L              ; set to a scaler type

 OpenR,   lun, 'mmconv.dat'
 ReadF,   lun, var1

 array   = DBLARR(2,var1)    ;set to an array type

 ReadF,   lun, array
 Free_LUN, lun

 recconv     = DBLARR(2,var1)
 recconv[0,*] = Reform(array[0,*])
 recconv[1,*] = Reform(array[1,*])

ENDELSE

index   = Where(recconv[0,*] GT firstrtn AND recconv[0,*] LT finalrtn)
convt   = recconv[0,index]
conve   = recconv[1,index]

IF (display EQ 1) THEN BEGIN
 Window, /Free
 !P.MULTI = 0;
 PLOT, convt/1E-9, conve, TITLE='Convolution', XTITLE=' time /ns'
ENDIF
PRINT,'  Conv maximum is ',MAX(conve,ind),' at time ',convt[ind]/1E-9,' ns'
```

```
PRINT,'  Conv minimum is ',MIN(conve,ind),' at time ',convt[ind]/1E-9,' ns'


; pad out the wavelet to sufficient length
mwave          = SIZE(E1, /N_ELEMENTS)
Elong          = DBLARR(ntime)
Elong[0:mwave-1] = E1

show = 0
IF (show EQ 1) THEN BEGIN
 WINDOW, /free
 !P.MULTI = 0
 PLOT, Elong, TITLE='Elong into prop'
ENDIF

IF (doprop EQ 1) THEN BEGIN
 ; ********************************
 PRINT, ' Do propagating wavelet '
 ; ********************************
 IF time EQ 1 THEN T1 = SYSTIME(1)
 recprop  = proptwo(dt,dz,Elong,repsil,rsigma,0)
 IF time EQ 1 THEN BEGIN
  T2 = SYSTIME(1)
  PRINT,'  it took ',T2-T1,' seconds'
 ENDIF

 ; ********************************
 ; create an prop file
 ; ********************************
 array     = DBLARR(2,N_ELEMENTS(recprop[1,*]))
 array[0,*]  = recprop[0,*]
 array[1,*]  = recprop[1,*]

 Get_LUN,  lun
 OpenW,   lun, 'mmprop.dat'
 PrintF,  lun, N_ELEMENTS(recprop[1,*])
 PrintF,  lun, array
 Free_LUN, lun

ENDIF ELSE BEGIN

 ; ************************************
 PRINT, ' Read in prop file '
 ; ************************************
 Get_LUN, lun              ; get a free logical unit number
 var1   = 0L             ; set to a scaler type

 OpenR,   lun, 'mmprop.dat'
 ReadF,   lun, var1

 array   = DBLARR(2,var1)    ;set to an array type

 ReadF,   lun, array
 Free_LUN, lun

 recprop    = DBLARR(2,var1)
 recprop[0,*] = Reform(array[0,*])
 recprop[1,*] = Reform(array[1,*])

ENDELSE

index   = Where(recprop[0,*] GT firstrtn AND recprop[0,*] LT finalrtn)
propt   = recprop[0,index]
prope   = recprop[1,index]

IF (display EQ 1) THEN BEGIN
 Window, /Free
 !P.MULTI = 0;
 PLOT, propt/1E-9, prope, TITLE='Reflected propagating wavelet', XTITLE=' time /ns'
ENDIF
PRINT,'  Prop maximum is ',MAX(prope,ind),' at time ',propt[ind]/1E-9,' ns'
PRINT,'  Prop minimum is ',MIN(prope,ind),' at time ',propt[ind]/1E-9,' ns'


IF (dofreq EQ 1) THEN BEGIN
 ; ********************************
 PRINT, ' Do Frequency '
 ; ********************************
```

```
IF time EQ 1 THEN T1 = SYSTIME(1)
recfreq = freq(dt,dz,Elong,repsil,rsigma,0)
IF time EQ 1 THEN BEGIN
  T2 = SYSTIME(1)
  PRINT,'  it took ',T2-T1,' seconds'
ENDIF


; ******************************
; create a freq file
; ******************************
array     = DBLARR(2,N_ELEMENTS(recfreq[1,*]))
array[0,*] = recfreq[0,*]
array[1,*] = recfreq[1,*]

Get_LUN, lun
OpenW,   lun, 'mmfreq.dat'
PrintF,  lun, N_ELEMENTS(recfreq[1,*])
PrintF,  lun, array
Free_LUN, lun

ENDIF ELSE BEGIN

; ************************************
PRINT, ' Read in freq file '
; ************************************
Get_LUN, lun              ; get a free logical unit number
var1   = 0L               ; set to a scaler type

OpenR,   lun, 'mmfreq.dat'
ReadF,   lun, var1

array  = DBLARR(2,var1)    ;set to an array type

ReadF,   lun, array
Free_LUN, lun

recfreq    = DBLARR(2,var1)
recfreq[0,*] = Reform(array[0,*])
recfreq[1,*] = Reform(array[1,*])

ENDELSE

index  = Where(recfreq[0,*] GT firstrtn AND recfreq[0,*] LT finalrtn)
freqt  = recfreq[0,index]
freqe  = recfreq[1,index]

IF (display EQ 1) THEN BEGIN
 Window, /Free
 !P.MULTI = 0;
 PLOT, freqt/1E-9, freqe, TITLE='Frequency Domain', XTITLE=' time /ns'
ENDIF
PRINT,'  Freq maximum is ',MAX(freqe,ind),' at time ',freqt[ind]/1E-9,' ns'
PRINT,'  Freq minimum is ',MIN(freqe,ind),' at time ',freqt[ind]/1E-9,' ns'


; ********************************
PRINT, ' Setting up the output array '
; ********************************; round to nearest nanosecond
finalrtn  = 1E-9*FLOOR(finalrtn/1E-9)
firstrtn  = 1E-9*CEIL(firstrtn/1E-9)
duration  = finalrtn-firstrtn
time      = firstrtn+1E-9*DINDGEN(floor(duration/1E-9))

array     = DBLARR(5,N_ELEMENTS(time))
array[0,*] = time
array[1,*] = interpol(recconv[1,*],recconv[0,*],time)
array[2,*] = interpol(recprop[1,*],recprop[0,*],time)
array[3,*] = interpol(recfreq[1,*],recfreq[0,*],time)
array[4,*] = interpol(recfdtd[1,*],recfdtd[0,*],time)

; ********************************
PRINT, ' Display '
; ********************************
lim    = [min(array[*,*]), max(array[*,*])]
Window, /Free
!P.MULTI = [0,4,1]
PLOT, time, array[1,*], YRANGE = lim
```

```
!P.MULTI = [3,4,1]
PLOT, time, array[2,*], YRANGE = lim
!P.MULTI = [2,4,1]
PLOT, time, array[3,*], YRANGE = lim
!P.MULTI = [1,4,1]
PLOT, time, array[4,*], YRANGE = lim


; create a file
STRPUT, file, '.out', RSTRPOS(file, '.')
PRINT, ' Destination file is ', file
Get_LUN, lun
OpenW,  lun, file
PrintF,  lun, array
Free_LUN, lun


STOP
END
```

FUNCTION billwavz.pro

```
FUNCTION billwavz, dz, dt, cf, ce1, display
;
; OUTPUTS
;   gives the E field
;   for a monopulse in
;   the space domain
;

cmu0          = 12.5663706144E-7
ce0           = 8.8541878E-12

if (display EQ 1) THEN BEGIN
 PRINT, ' '
 PRINT, ' billwavz dt  = ', dt
 PRINT, ' billwavz dz  = ', dz
ENDIF
cw            = 2*!PI*cf
ck1           = FLOAT(SQRT(cmu0*ce1*ce0*(cw^2)))
clam          = (2*!PI)/ck1
wn1           = CEIL(clam/dz)

E1            = DBLARR(2*wn1)
wave          = HANNING(wn1)*(-1.0D)*SIN(ck1*dz*FINDGEN(wn1))
wave          = wave/MAX(wave)
sites         = CEIL(wn1/2)+INDGEN(wn1)
E1(sites)     = wave

IF (display EQ 1) THEN PRINT, ' billwavz length E1 = ',SIZE(E1, /N_ELEMENTS)

Return, E1
END
```

FUNCTION fdtd.pro

```
FUNCTION fdtd, dt, dz, E1, epsil, sigma, rec1p, ntime, display

; Finite Difference model
;   given an initial electric field in the space domain
;   gives the time records of E for ntime steps
;   at position rec1p
;
; Constants
cmu0       = 12.5663706144E-7
ce0        = 8.85418782E-12

; Check the dt and dz in Courant condition
vmax       = 3E8/SQRT((MIN(epsil)/ce0))
idealdt    = (6.0D/7.0D)*dz/vmax
IF (dt GT idealdt) THEN BEGIN
 PRINT, ' **** ERROR YOUR dt = ',dt, ' IDEAL dt = ',idealdt,' ****'
 PRINT, ' **** ERROR vmax   = ',vmax
```

```
 STOP
ENDIF

mcore     = DOUBLE(N_ELEMENTS(epsil))

; generate a manetic field
ce1       = epsil[0]/ce0
H1        = billwavh(dz,dt,E1,ce1,0);


IF (display EQ 1) THEN BEGIN
 PRINT,''
 PRINT,'  billfdtd starting at  ', SYSTIME(0)
 PRINT,'  billfdtd length mcore ', mcore
 PRINT,'  billfdtd length H1    ', SIZE(H1, /N_ELEMENTS)
 PRINT,'  billfdtd length E1    ', SIZE(E1, /N_ELEMENTS)

 ;*************************
 ; The display graph
 ;*************************
 magni   = 0.2D;
 Window, /free
 !P.MULTI = 0
 PLOT, E1, YTITLE = '1',YRANGE = [+magni, -magni]
ENDIF

;*************************
; The records and constants are set up
;*************************

record1   = DBLARR(ntime)
record1[0] = E1[rec1p]

; constants used in fdtd calculation
cc1 = DOUBLE(REPLICATE(1.0,mcore-2)-(dt*sigma(1:mcore-2))/epsil(1:mcore-2))
cc2 = DOUBLE((dt*REPLICATE(1.0,mcore-2))/(dz*epsil(1:mcore-2)))
cc3 = DOUBLE((dt/(dz*cmu0)));

IF (display EQ 1) THEN BEGIN
 PRINT,'  billfdtd length cc1 = ', SIZE(cc1, /N_ELEMENTS)
 PRINT,'  billfdtd length cc2 = ', SIZE(cc2, /N_ELEMENTS)
 PRINT,'  billfdtd length cc3 = ', SIZE(cc3, /N_ELEMENTS)
ENDIF

; boundary velocities
cv1       = 3E8/SQRT(epsil(0)/ce0)
cv2       = 3E8/SQRT(epsil(mcore-1)/ce0)

Eold      = E1
Hold      = H1

Enew      = DBLARR(mcore)
Hnew      = DBLARR(mcore-1)

;*************************
; The fdtd loop is started
;*************************

divfact   = ROUND(ntime/10.0)

;IF (display AND (ntime GT 20000)) THEN PRINT,'  billfdtd starting at  ', SYSTIME(0)
FOR pp = 1L, ntime-1 DO BEGIN
 IF ((pp MOD divfact)EQ 0)OR(pp LT 3) THEN BEGIN
  PRINT,'  billfdtd doing loop ',pp,' of ',ntime-1
 ENDIF

 ; For E do main values
 Enew[1:mcore-2] = (cc1*Eold[1:mcore-2])-(cc2*(Hold[1:mcore-2]-Hold[0:mcore-3]))

 ; For E do edge values
 Enew[0]     = Eold[1]+((cv1*dt-dz)/(cv1*dt+dz))*(Enew[1]-Eold[0])
 Enew[mcore-1]= Eold[mcore-2]+((dz-cv2*dt)/(dz+cv2*dt))*(Eold[mcore-1]-Enew[mcore-2])

 ; Check E record values
 a  = FINITE(Enew)
 b  = N_ELEMENTS(Enew)
 IF (TOTAL(a) NE b) THEN BEGIN
  PRINT,' **** FDTD ERROR AT POSITION ',pp,' **** '
```

```
  STOP
 ENDIF

 record1[pp]    = Enew[rec1p]

 ; For H do values
 Hnew          = Hold - cc3*(Enew[1:mcore-1]-Enew[0:mcore-2])

 IF (display EQ 1) THEN BEGIN
  PLOT, Enew, YTITLE = STRING(pp), YRANGE = [-magni,+magni]
  ;WAIT, 0.02
 ENDIF

 Eold = Enew
 Hold = Hnew

ENDFOR


;IF (ntime GT 20000) THEN PRINT, '  billfdtd ending at ', SYSTIME(0)

IF (display EQ 1) THEN BEGIN
 PRINT, '  billfdtd ntime = ',ntime,'  divfact = ',divfact
 PRINT, '  billfdtd ending at ', SYSTIME(0)
ENDIF

; prepare output
array      = DBLARR(2,ntime);
array[0,*]  = dt*DINDGEN(ntime)
array[1,*]  = record1

RETURN, array
END
```

FUNCTION propone.pro

```
FUNCTION propone, dt, dz, E1, epsil, sigma, display
;
; Propagating wavelet one
;     without absorption or transmission losses
;     where the E1 is the time record
;     at the first position epsil[0]
;

cmu0     = 12.5663706144E-7
ce0      = 8.8541878E-12

; ***************************
; Form Goupillaud medium
; ***************************
mcore        = DOUBLE(N_ELEMENTS(epsil))
vint         = DBLARR(mcore)
twttm        = DBLARR(mcore)

IF MIN(epsil) EQ MAX(epsil) THEN BEGIN
 if (display EQ 1) THEN PRINT, '  billconv simple Goupillaud '
 vint         = 3.0E8/SQRT(epsil[0]/ce0)
 twttm         = 2.0*dz*DINDGEN(mcore)/vint
ENDIF ELSE  BEGIN
 if (display EQ 1) THEN PRINT, '  billconv tortuous Goupillaud  '
 vint         = 3.0E8/SQRT(epsil/ce0)
 twttl        = DBLARR(mcore)
 twttl        = dz/vint

 a            = 0L  ; needs to be long integer for loop!
 a            = MIN(WHERE(twttl NE twttl[0])) ; where feature starts
 twttm[0:a-1]   = REPLICATE(twttl[0],a)+2*twttl[0]*LINDGEN(a)
 ;PRINT, twttl[0:2]
 ;PRINT, twttm[0:2]
 ;PRINT, ''

 FOR pp = a, mcore-1 DO BEGIN   ; needs to be long integer for loop!
  twttm[pp] = twttl[pp]+twttl[pp-1]+twttm[pp-1]
 ENDFOR
 ;PRINT, a-3+INDGEN(6)
```

```
 ;PRINT, twttl[a-3:a+2]
 ;PRINT, twttm[a-3:a+2]
 ;STOP

ENDELSE

; find travel time for first reflection
; use complex as feature may be either epsil or sigma
kf          = COMPLEX(epsil,sigma)
loco        = MIN(Where( kf NE kf[0]))
travel      = twttm[loco]

if (display EQ 1) THEN BEGIN
 PRINT, ' '
 PRINT, '  billconv minimum goupillaud = ',MIN(twttm)/1E-9, ' ns'
 PRINT, '  billconv maximum goupillaud = ',MAX(twttm)/1E-9, ' ns'
 PRINT, '  billconv twtt to interface  = ',travel/1E-9, ' ns'
 PRINT, '  billconv number of twttm    = ',SIZE(twttm, /N_ELEMENTS)
ENDIF

dtconv      = MIN(twttm[1:mcore-2]-twttm[0:mcore-3])

if (display EQ 1) THEN BEGIN
 PRINT, '  billconv previous sampling  = ',dt/1E-9, ' ns'
 PRINT, '  billconv convolut sampling  = ',dtconv/1E-9, ' ns'
ENDIF

;dtconv   = dt
numlayer  = FLOOR((MAX(twttm)-MIN(twttm))/dtconv)
twttg     = MIN(twttm)+dtconv*DINDGEN(numlayer)

;PRINT, N_ELEMENTS(twttm)
;PRINT, N_ELEMENTS(epsil)
;PRINT, N_ELEMENTS(sigma)
;PRINT, N_ELEMENTS(twttg)

epsilg    = INTERPOL(epsil,twttm,twttg)
sigmag    = INTERPOL(sigma,twttm,twttg)
gcore     = SIZE(epsilg, /N_ELEMENTS)

; ***************************
; Consider the wavelet
; ***************************
; put to same sample spacing
mwave     = DOUBLE(N_ELEMENTS(E1))
E1t       = dt*DINDGEN(mwave)
Econvt    = dtconv*DINDGEN(ROUND(MAX(E1t)/dtconv))

;PRINT, N_ELEMENTS(E1)
;PRINT, N_ELEMENTS(E1t)
;PRINT, N_ELEMENTS(Econvt)

Econv     = INTERPOL(E1,E1t,Econvt)

Eff       = billfreq(dtconv,Econv,0)
; Eff is a complex array!
; Eff pads out the wavelet

qm        = DOUBLE(N_ELEMENTS(Eff[0,*]))  ;length of new wavelet
posit     = 1.0+DINDGEN(qm/2.0)           ; range: 1 to qm/2 (ie not dc!)
negat     = (qm/2.0-2.0)-DINDGEN(qm/2.0-1.0)   ; negat is used on posit!!
beyond    = ((qm/2.0)+1.0)+DINDGEN(qm/2.0-1.0)

IF (display EQ 1) THEN BEGIN
 PRINT, '  billconv qm   = ',qm
 PRINT, '  billconv size posit = ',SIZE(posit, /N_ELEMENTS)
 PRINT, '  billconv size negat = ',SIZE(negat, /N_ELEMENTS)
ENDIF

; determine the frequency in the positive range
dft1      = Eff[2,posit]
freqs     = FLOAT(Eff[1,posit])
wfreqs    = 2.0*!PI*freqs
nfreqs    = DOUBLE(N_ELEMENTS(wfreqs))

; determine the central frequency
Ebig      = MAX(ABS(Eff(2,0:qm/2)),index)
fcent     = FLOAT(Eff(1,index))        ;real centre freqency of new wavelet
```

```
wcent       = 2.0*!PI*fcent

if (display EQ 1) THEN BEGIN
 PRINT,'  billconv wavelet length   = ',qm
 Window, /Free
 PLOT, FLOAT(Eff(0,*)), TITLE=' wavelet used in conv'
ENDIF

; ***************************
; Form Reflection series
; ***************************
k      = SQRT(DCOMPLEX((cmu0*(wcent^2)*epsilg),(-cmu0*wcent*sigmag)))
arr    = (k[0:gcore-2]-k[1:gcore-1])/(k[0:gcore-2]+k[1:gcore-1])

; select which interfaces to do
needed   =  WHERE(ABS(arr)>0)


; ***************************
; Prepare for loop
; ***************************
waves  = DBLARR(gcore+qm)
mwaves  = N_ELEMENTS(waves)
pm     =  N_ELEMENTS(needed)

IF (display EQ 1) THEN BEGIN
 PRINT, '  billconv number of interfaces = ',pm
 ;PRINT, '  billconv needed = ',needed
ENDIF

divfact = ROUND(pm/10.0)

IF (display EQ 1) THEN PRINT, ''
FOR nn =  0L, pm-1 DO BEGIN
 IF ((nn MOD divfact)EQ 0)OR(nn LT 2) THEN BEGIN
  display = 1
  IF (display EQ 1) THEN PRINT, '  propone doing loop ',nn,' of ',pm-1
 ENDIF

 pp  = needed[nn] ; the interface that needs doing

 ; do reflection coefficient
 ;PRINT, pp
 ;PRINT, epsilg[pp:pp+1]
 ;PRINT, sigmag[pp:pp+1]

 ktop = SQRT(DCOMPLEX((cmu0*(wfreqs^2)*epsilg[pp]),(-cmu0*wfreqs*sigmag[pp])))
 kbot = SQRT(DCOMPLEX((cmu0*(wfreqs^2)*epsilg[pp+1]),(-cmu0*wfreqs*sigmag[pp+1])))
 rr  = (ktop-kbot)/(ktop+kbot)

 ; determine analytic
 dftres          = rr*Eff[2,posit]
 dftall          = DCOMPLEXARR(qm)
 dftall[0]       = 0.0D
 dftall[posit]   = dftres
 dftall[beyond]  = CONJ(dftres[negat])

 ; do inverse fft
 wavv            = DOUBLE(FFT(dftall,+1))
 ;PRINT, MAX(ABS(WAVV))
 waves[pp+1:pp+qm]  = waves[pp+1:pp+qm]+wavv
ENDFOR

; ***************************
; Output the record and the time
; ***************************

time    = dtconv*DINDGEN(mwaves)

array   = DBLARR(2,mwaves)
array[0,*] = time
array[1,*] = waves

RETURN, array
END
```

FUNCTION proptwo.pro

```
FUNCTION proptwo, dt, dz, E1, epsil, sigma, display
;
; Propagating wavelet
;     with transmission loss and absorption
;     where the E1 is the time record
;     at the first position epsil[0]
;

cmu0     = 12.5663706144E-7
ce0      = 8.8541878E-12
i        = DCOMPLEX(0,1)

;****************************
; Consider the wavelet
;****************************
mwaves       = N_ELEMENTS(E1)
Eff          = billfreq(dt,E1,0)
; Eff is a double precision complex array

; Only consider the positive range
qm           = DOUBLE(N_ELEMENTS(Eff[0,*]))
posit        = 1.0+DINDGEN(qm/2.0)              ; range: 1 to qm/2 (ie not dc!)
negat        = (qm/2.0-2.0)-DINDGEN(qm/2.0-1.0)   ; negat is used on posit!!
beyond       = ((qm/2.0)+1.0)+DINDGEN(qm/2.0-1.0)

; determine the frequency in the positive range
dft1         = Eff[2,posit]
freqs        = FLOAT(Eff[1,posit])
wfreqs       = 2.0*!PI*freqs
nfreqs       = DOUBLE(N_ELEMENTS(wfreqs))

; determine the central frequency
Ebig         = MAX(ABS(Eff(2,0:qm/2)),index)
fcent        = FLOAT(Eff(1,index))          ;real centre freqency of new wavelet
wcent        = 2.0*!PI*fcent


if (display EQ 1) THEN BEGIN
  PRINT,'  billpro qm           = ',qm
  PRINT,'  billpro number of freqs = ',nfreqs
  PRINT,'  billpro SIZE of wfreqs  = ',SIZE(wfreqs, /DIMENSIONS)
  PRINT,'  billpro fcent         = ',fcent/1E6,'  MHz'
  PRINT,'  billpro size posit    = ',SIZE(posit, /N_ELEMENTS)
  PRINT,'  billpro size negat    = ',SIZE(negat, /N_ELEMENTS)
ENDIF


;*********************************
;  Consider the ground
;*********************************
mcore    = DOUBLE(N_ELEMENTS(epsil))
k        = SQRT(DCOMPLEX((cmu0*(wcent^2)*epsil),(-cmu0*wcent*sigma)))
rr       = (k[0:mcore-2]-k[1:mcore-1])/(k[0:mcore-2]+k[1:mcore-1])

; select which interfaces to do
a        = ABS(rr) GT 0
needed   = WHERE(a)

;****************************
; Fourier transform at each boundary and paste
;****************************
waves    = DBLARR(mwaves)
pm       = MAX(needed)

;display = 0
IF (display EQ 1) THEN BEGIN
  PRINT,'  billpro number of interfaces   = ',N_ELEMENTS(needed)
  ;PRINT,'  billpro needed (the interfaces) = ',needed
ENDIF

divfact = ROUND(pm/5.0)

IF (display EQ 1) THEN PRINT,''

kold  = SQRT(DCOMPLEX((cmu0*(wfreqs^2)*epsil[0]),(-cmu0*wfreqs*sigma[0])))
```

```
Fnow = dft1
; Fnow is the spectrum just before a boundary
; Fnow is two way travel spectrum!!

FOR nn = 1L, max(needed) DO BEGIN
 IF ((nn MOD divfact)EQ 0)OR(nn LT 3) THEN BEGIN
  PRINT, '  billpro doing loop ',nn+1,' of ',pm
 ENDIF

 know = SQRT(DCOMPLEX((cmu0*(wfreqs^2)*epsil[nn]),(-cmu0*wfreqs*sigma[nn])))
 Fnow = Fnow*((2*know)/(kold+know))*((2*kold)/(kold+know))*EXP(-i*2*dz*know)

 ;*******************************************
 ; If just above a reflection boundary then calculate the reflection
 ;*******************************************
 ;PRINT, nn
 ;PRINT, needed
 a = WHERE(nn EQ needed,COUNT)
 ;PRINT, COUNT
 ;PRINT, SIZE(COUNT)
 IF COUNT EQ 1 THEN BEGIN
  ;PRINT, nn, needed
  ;PRINT, epsil[nn-1:nn+1]
  ;PRINT, sigma[nn-1:nn+1]
klow = SQRT(DCOMPLEX((cmu0*(wfreqs^2)*epsil[nn+1]),(-cmu0*wfreqs*sigma[nn+1])))
rr   = (know-klow)/(know+klow)
  Fgrnd = rr*Fnow

  ;*************************************
  ; Convert back to time domain
  ;*************************************
  dftall          = DCOMPLEXARR(qm)
  dftall[0]       = 0.0D
  dftall[posit]   = Fgrnd
  dftall[beyond]  = CONJ(Fgrnd[negat])
  wavv            = DOUBLE(FFT(dftall,+1))
  waves           = waves+wavv
 ENDIF

 kold = know
ENDFOR

;*****************************
; Output the record and the time
;*****************************

time    = dt*DINDGEN(mwaves)
array   = DBLARR(2,mwaves)
array[0,*] = time
array[1,*] = waves

RETURN, array
END
```

FUNCTION freq.pro

```
FUNCTION freq, dt, dz, E1, epsil, sigma, display
;
;  Frequency Domain calculation
;     where E1 is the time record
;     split into monochromatic waves
;     model each wave then recombine
;

cmu0        = 12.566370E-7
ce0         = 8.8541878E-12

;*********************************
;  Consider the wavelet
;*********************************
Eff         = billfreq(dt,E1,display)
; Eff is a double precision complex array

; Only consider the positive range
qm          = N_ELEMENTS(Eff[0,*])
```

```
posit       = 1.0+DINDGEN(qm/2.0)              ; range: 1 to qm/2 (ie not dc!)
negat       = (qm/2.0-2.0)-DINDGEN(qm/2.0-1.0)   ; negat is used on posit!!
beyond      = ((qm/2.0)+1.0)+DINDGEN(qm/2.0-1.0)

dft1        = Eff[2,posit]
freqs       = FLOAT(Eff[1,posit])
wfreqs      = 2.0*!PI*freqs
nfreqs      = DOUBLE(N_ELEMENTS(wfreqs))

display = 0
if (display EQ 1) THEN BEGIN
 PRINT,'  billfreq qm            = ',qm
 PRINT,'  billfreq number of freqs = ',nfreqs
 PRINT,'  billfreq SIZE of wfreqs  = ',SIZE(wfreqs, /DIMENSIONS)
ENDIF
display = 0

; ********************************
;  Consider the ground
; ********************************
mcore         = DOUBLE(N_ELEMENTS(epsil))

; ********************************
; Do the bottom layer
; ********************************

kneed  = SQRT(DCOMPLEX((cmu0*epsil[mcore-1]*wfreqs^2),(-cmu0*wfreqs*sigma[mcore-1])))
zbulk  = (cmu0*wfreqs)/kneed
zsurfo = zbulk  ;o for old

; ********************************
; Loop over other layers
; ********************************

divfact   = ROUND(mcore/5.0)


FOR nn = 0L, mcore-2 DO BEGIN
 IF ((nn MOD divfact) EQ 0)OR(nn LT 3) THEN BEGIN
  PRINT,'  billfreq doing loop ',nn,' of ',mcore-2
 ENDIF

 pp    = (mcore-2)-nn

 kneed  = SQRT(DCOMPLEX((cmu0*epsil[pp]*wfreqs^2),(-cmu0*wfreqs*sigma[pp])))
 zbulk  = (cmu0*wfreqs)/kneed

 i     = DCOMPLEX(0,1)
 a     = SIN(dz*kneed)/COS(dz*kneed) ; IDL does not do COMPLEX tangents
 up    = zsurfo+(i*zbulk*a)
 down  = zbulk+(i*zsurfo*a)
 zsurf = zbulk*(up/down)
 zsurfo = zsurf
ENDFOR

rimpe   = (zsurfo-zbulk)/(zsurfo+zbulk)
dft2    = dft1*rimpe

;PRINT,''
;FOR pp = 0,4 DO BEGIN
;  PRINT,'f(',freqs[pp]/1E6,') r dft2= ',FLOAT(dft2[pp]),' i dft2= ',IMAGINARY(dft2[pp])
;ENDFOR

dftall          = DCOMPLEXARR(qm)
dftall[0]       = COMPLEX(0D,0D)
dftall[posit]     = dft2
dftall[beyond]    = CONJ(dft2[negat])
dft2            = 0
posit = 0
beyond = 0

time            = dt*DINDGEN(qm)
wavv             = FLOAT(FFT(dftall,+1))

array           = DBLARR(2,qm)
array[0,*]       = time
array[1,*]       = wavv
```

```
RETURN, array
END
```

FUNCTION billfreq.pro

```
FUNCTION billfreq, dt, E1, display
;
; OUTPUTS
;   gives a complex array which conmtains:
;   1) the padded E
;   2) the frequencies
;   3) the complex frequency components
;   for entering E1
;

; ***********************************
; Pad the record
; ***********************************
n           = DOUBLE(N_ELEMENTS(E1))
qm          = (2.0)^CEIL(ALOG10(n)/ALOG10(2.0))

if (display EQ 1) THEN BEGIN
 PRINT, ' '
 PRINT, ' billfreq original length n  = ', n
 PRINT, ' billfreq padded length   qm = ', qm
ENDIF

E2          = DBLARR(qm)
E2(0:n-1)       = E1


; ***********************************
; Determine the Nyquist
; ***********************************
f_nyq       = 1.0/(2.0*dt)
f_need      = f_nyq*(2.0/qm)*FINDGEN(qm)

if (display EQ 1) THEN BEGIN
 PRINT, ' billfreq f_nyq    = ',f_nyq
 PRINT, ' billfreq f_need(0) = ',f_need(0)
 PRINT, ' billfreq f_need(1) = ',f_need(1)
ENDIF

; ***********************************
; Discrete Fourier Transform
; ***********************************
dft         = fft(E2)

if (display EQ 1) THEN BEGIN
 PRINT, ' '
 PRINT, ' billfreq  0th dft  = ',dft(0)
 PRINT, ' billfreq  1st dft  = ',dft(1)
 PRINT, ' billfreq  2nd dft  = ',dft(2)
 PRINT, ' billfreq  3rd dft  = ',dft(3)
 PRINT, ' .... '
 PRINT, ' billfreq  (qm/2)-2 = ',dft((qm/2)-2)
 PRINT, ' billfreq  (qm/2)-1 = ',dft((qm/2)-1)
 PRINT, ' billfreq  (qm/2)   = ',dft((qm/2))
 PRINT, ' billfreq  (qm/2)+1 = ',dft((qm/2)+1)
 PRINT, ' billfreq  (qm/2)+2 = ',dft((qm/2)+2)
 PRINT, ' .... '
 PRINT, ' billfreq  qm-2     = ',dft(qm-2)
 PRINT, ' billfreq  qm-1     = ',dft(qm-1)


 posit          = 1.0+INDGEN(qm/2.0)          ; range: 1 to qm/2 (ie not dc!)
 negat          = (qm/2.0-2.0)-INDGEN(qm/2.0-1.0)  ; negat is used on posit!!
 beyond           = ((qm/2.0)+1.0)+INDGEN(qm/2.0-1.0)

 sp                     = SIZE(posit, /N_ELEMENTS)
 PRINT, '  billfreq SIZE posit     = ',sp
 PRINT, '  billfreq posit[0]       = ',posit[0]
 PRINT, '  billfreq posit[',sp-1,' ]  = ',posit[sp-1]
 sn                     = SIZE(negat, /N_ELEMENTS)
 PRINT, '  billfreq SIZE negat     = ',sn
 PRINT, '  billfreq negat[0]       = ',negat[0]
 PRINT, '  billfreq negat[',sn-1,' ]  = ',negat[sn-1]
 sb                     = SIZE(beyond, /N_ELEMENTS)
```

```
  PRINT, '  billfreq SIZE beyond     = ',sb
  PRINT, '  billfreq beyond[0]       = ',beyond[0]
  PRINT, '  billfreq beyond[',sb-1,' ]  = ',beyond[sb-1]

  dft1              = dft[posit]
  rebuild           = DCOMPLEXARR(qm)
  rebuild[0]        = 0
  rebuild[posit]    = dft1
  rebuild[beyond]   = CONJ(dft1[negat])

  Window, /Free
  !P.MULTI = [0,1,5]
  PLOT, E1
  !P.MULTI = [4,1,5]
  PLOT, ABS(dft)
  !P.MULTI = [3,1,5]
  PLOT, FFT(dft,+1)
  !P.MULTI = [2,1,5]
  PLOT, FLOAT(FFT(dft,+1))
  !P.MULTI = [1,1,5]
  PLOT, FLOAT(FFT(rebuild,+1))

ENDIF

f_comp          = ABS(dft[0:qm/2])
if (display EQ 1) THEN BEGIN
  PRINT, ' '
  PRINT, ' billfreq f_comp(0) = ',f_comp(0)
  PRINT, ' billfreq f_comp(1) = ',f_comp(1)
ENDIF

array           = DCOMPLEXARR(3, qm)
array[0,*]      = E2
array[1,*]      = f_need
array[2,*]      = dft

RETURN, array
END
```

REFERENCES

Ackley S.F. and Keliher T.E., **1979**. Ice sheet internal radio-echo reflections and associated physical property changes with depth. *Journal of Geophysical Research*, vol 84, no B10, pp 5675-5680.

Addison J.R., **1975**. Electrical properties of saline ice at 1 kHz down to -150 °C. *Journal of Applied Physics*, vol 46, no 2, pp 513-522.

Addison J.R., **1969**. Electrical properties of saline ice. *Journal of Applied Physics*, vol 40, no 8, pp 3105-3114.

Alley R.B., Perepezko J.H. and Bentley C.R., **1986 a**. Grain Growth in Polar ice: I. Theory. *Journal of Glaciology*, vol 32, no 112, pp 415-424.

Alley R.B., Perepezko J.H. and Bentley C.R., **1986 b**. Grain Growth in Polar ice: II. Application. *Journal of Glaciology*, vol 32, no 112, pp 425-433.

Alley R.B., and Koci B.R., **1988**. Ice core analysis at Site A., Greenland: preliminary results. *Annals of Glaciology*, vol 10, pp 1-4.

Alley R.B., Gow A.J., Johnsen S.J., Kipfstuhl J., Meese D.A. and Thorsteinsson Th., **1995**. Comparison of deep ice cores. *Nature*, vol 373, pp 393-394.

Ambach W. and Denoth A., **1980**. The dielectric properties of snow: A study versus liquid water content. *Proceedings of the NASA workshop on the Microwave Remote Sensing of Snowpack Properties*, Fort Collins, Colorado, USA, 20-22 May.

American Society of Testing Materials, **1995**. Standard test methods for AC loss Characteristics and Permittivity (Dielectric constant) of solid electrical insulation. D150-95.

Alvarez R., **1973**. Complex dielectric permittivity in rocks: a method for its measurement and analysis. *Geophysics*, vol 38, no 5, pp 920-940.

Bailey J.T., Evans S. and Robin G. de Q., **1964**. Radio Echo Sounding of Polar ice sheets. *Nature*, vol 204, no 4957, pp 420-421.

Bales R.C. and Wolff E.W., **1995**. Interpreting natural climate signals in Ice Cores. *EOS*, vol 76, no 47.

Bamber J.L., **1987**. Radio Echo Sounding Studies of Svalbard Glaciers. PhD thesis, Scott Polar Research Institute, University of Cambridge, UK.

Baranov V. and Kunetz G., **1960**. Film synthetique avec reflexions multiples; theorie et calcul pratique. *Geophysical Prospecting*, vol 8, pp 315-325.

Barnola J.M., Pimienta P., Raynaud D. and Korotkevich Y.S., **1991**. CO_2 climate relationship as deduced from the Vostok ice core: a re-examination based on new measurements and on a re-evaluation of the air dating. *Tellus*, vol 43B, pp 83-90.

Bennett J.M. and Bennet H.E., **1978**. Polarisation, Chapter 10 in *Handbook of Optics*, Editors: Driscoll W.G. and Vaughan W., Optical Society of America, McGraw-Hill, New York, USA.

Bentley C.R., **1964**. The structure of Antarctica and its ice cover. In: *Research in Geophysics. Vol 2*, Massachussetts Institute of Technology, USA, pp 335-389.

Bergmann T., Robertsson J.O.A. and Holliger K., **1996**. Numerical properties of staggered finite difference solutions of Maxwell's equations for ground penetrating radar modelling. *Geophysical Research Letters*, vol 23, no 1, pp 45-48.

Bergmann T., Robertsson J.O.A. and Holliger K., **1998**. Finite Difference modelling of electromagnetic wave

propagation in dispersive and attenuating media. *Geophysics*, vol 63, no 3, pp 856-867.

Bernal J.D. and Fowler R.H., **1933**. A theory of water and ionic solution, with particular reference to hydrogen and hydroxyl ions. *Journal of Chemical Physics*. vol 1, pp 515-548.

Berry M.V., **1973**. The statistical properties of echos diffracted from rough surfaces. *Philosophical transactions of the Royal Society Series A*, vol 273, pp 613-654.

Berry M.V., **1975**. Theory of Radio Echos from Glacier beds. *Journal of Glaciology*, vol 15, no 73, pp 65-74.

Berryman L.H., Goupilaud P.L. and Waters K.H., **1958**. Reflections from Multiple Transition Layers. *Geophysics*, vol 13, no 2, pp 223-243.

Bjerrum N., **1951**. Structure and properties of ice I. The position of the hydrogen atoms and the zero-point entropy of ice. *K.danske Vidensk. Selsk. Skr*, vol 27, pp 1-56.

Blindow N., **1994 a**. The central part of the Filchner-Ronne ice shelf Antarctica: internal structures revealed by 40 MHz monopulse RES, *Annals of Glaciology*, vol 20, pp 365-371.

Blindow N., **1994 b**. Reflection amplitudes of 40-MHz monopulse radioecho sounding: correlation with ice core data and ice dynamics. *Filchner Ronne Ice Shelf Programme, Report No. 8*, Alfred-Wegener-Institute for Polar and Marine Research, Bremerhaven, Germany.

Blythe A.R., **1979**. *Electrical properties of Polymers*. Cambridge University Press, Cambridge, U.K.

Bogorodsky V., Trepov G.V. and Federov B.A., **1970**. On measuring dielectric properties of glaciers in the field. *Proceedings of the international meeting on Radioglaciology* Lyngby, Denmark, May 1970, pp20-31, Editor: Gudmanndsen P.

Bogorodsky V.V., Bentley C.R. and Gudmandsen P.E., **1985**. *Radioglaciology*. translated from 1983 book: Radioglyatziologiya by Chebotareva V., D.Reidel Publishing company, Dordrecht, Holland.

Boned C. and Barbier A., **1973**. A study of the change with time of the dielectric properties of polycrystalline ice. *Physics and Chemistry of Ice*. Editors: Whalley E. et al., Royal Society of Canada, Ottawa, Canada.

Born M. and Wolff E., **1975**. *Principles of Optics*. Electromagnetic Theory of propagation, interference and diffraction of light. Oxford University Press, Oxford, UK.

Brigham E.O., **1974**. *The fast Fourier Transform*. Prentice-Hall, Englewood Cliffs, New Jersey, USA.

British Standard Association, **1993**. *Determination of Permittivity and dissipation factor of electrical insulating material in sheet or tubular form*. BS 7663.

Budden K.G., **1985**. *The propagation of radio waves*. Cambridge University Press, Cambridge, UK.

Camplin G.C. and Glen J.W., **1973**. The dielectric properties of HF doped single crystals of ice. *Physics and Chemistry of Ice*. Editors: Whalley E. et al., Royal Society of Canada, Ottawa, Canada.

Camplin, G.C., Glen J.W. and Paren J.G., **1978**. Theoretical models for interpreting the dielectric behaviour of HF doped ice. *Journal of Glaciology*, vol 21, no 85, pp 123-141.

Chan, R.K., Davidson D.W. and Whalley E., **1965**. Effect of pressure on the dielectric properties of ice. *Journal of Chemical Physics*, vol 43, pp 2376-2383.

Chew W.C., **1990**. *Waves and Fields in Inhomogeneous Media*. Van Nostrand Reinhold, New York, USA.

Choate W.C., **1982**. A fast algorithm for normal incidence seismograms. *Geophysics*, vol 47, no 2, pp 196-205.

Christensen E.L., Gundestrupt N., Nilsson E. and Gudmandsen P., **1970**. *Radioglaciology 60 MHz radar*, Technical University of Denmark Electromagnetics Institute, report R 77.

Claerbout J.F., **1976**. *Fundamentals of Geophysical data processing.* McGraw-Hill, New York, USA.

Clarke D. and Grainger J.F., **1971**. *Polarised light and Optical measurement.* Monographs in Natural Philosophy, vol 35, Pergammon Press, Oxford, UK.

Clarke G.K.C., Cross G.M. and Benson C.S., **1989**. Radar Imaging of Glaciovolcanic stratigraphy, Mount Wrangell caldera, Alaska: Interpretation model and results. *Journal of Geophysical Research,* vol 94, no B6, pp 7237-7249.

Clough J.W. and Bentley C.R., **1970**. *Measurements of electromagnetic wave velocity in the East Antarctic ice sheet.* ISAGE, Publication number 86.

Clough J.W., **1974**. *Propagation of radio waves in the Antarctic ice sheet.* PhD thesis, University of Wisconsin. USA.

Clough J.W., **1977**. Radio Echo sounding, reflections from internal layers in ice sheets. *Journal of Glaciology,* vol 18, no 78, pp 3-14.

Corr H., Moore J.C. and Nicholls K.W., **1993**. Radar absorption due to impurities in Antarctic ice. *Geophysical Research Letters,* vol 20, no 11, pp 1071-1074.

Craig D.Q.M., **1995**. *Dielectric Analysis of Pharmaceutical systems.* The Taylor and Francis series in Pharmaceutical sciences, Publisher: Taylor and Francis, London, UK. 232p.

Crook A.W., **1948**. The reflection and transmission of light by any system of parallel isotropic films. *Journal of the Optical Society of America,* vol 38, no 11, pp 954-964.

Cumming W.A., **1952**. The dielectric properties of Ice and Snow at 3.2 centimeters. *Journal of Applied Physics,* vol 23, no 7, pp 768-773.

Daniels D.J., **1996**. *Surface penetrating Radar.* IEE Radar, Sonar, Navigation and Avionics, series 6, Short Run Press Ltd, Exeter, UK.

Dansgaard W., Johnsen S.J., Clausen H.B., Dahl-Jensen D., Gundestrup N.S., Hammer C.U., Hvidberg C.S., Steffensen J.P., Sveinbjornsdottir, Jouzel J. and Bond G., **1993**. Evidence for general instability of past climate from a 250 kyr ice-core record. *Nature,* vol 364, no 6434, pp 218-220.

Darayan S., Shattuck D.P., Shen L.C. and Liu R.C., **1996**. Measurement of dielectric constant and conductivity of samples using guarded electrodes. *Radio Science,* vol 31, no 6, pp 1417-1426.

Davis J.L. and Annan A.P., **1989**. Ground penetrating radar for high resolution mapping of soil and rock stratigraphy. *Geophysical Prospecting,* vol 37, pp 531-551.

Debye P., **1929**. *Polar molecules,* pp 172, Chemical Catalog Company, New York, USA.

Dennison A.T., **1960**. An introduction to synthetic seismograms techniques. *Geophysical Prospecting,* vol 8, no 2, pp 231-241.

Dobrin M.B. and Savit C.H., **1988**. *Introduction to Geophysical Prospecting.* McGraw Hill Book Company, Singapore.

Engheta N., Papas C.H. and Elachi C., **1982**. Radiation patterns of interfacial dipole antennas. *Radio Science,* vol 17, no 6, pp 1557-1556.

Evans S., **1965**. Dielectric properties of ice and snow - a review. *Journal of Glaciology,* vol 5, no 42, pp 773-792.

Evans S., **1966**. Progress report on Radio Echo Sounding. *The Polar Record,* vol 13, no 85, pp 413-420.

Evans S. and Smith B.M.E., **1969**. A radioecho equipment for depth sounding in polar ice sheets. *Journal of Scientific Instruments (Journal of Physics E),* Series 2, vol 2, pp 131-136.

Feynmann R.P., Leighton R.B. and Sands M., **1963**. *The Feynman lectures on Physics.* Publishers: Addison-Wesley, Reading, Mass., USA.

Field R.F., **1954**. Permittivity. *Dielectric Materials and Applications*, Editor: A. von Hippel, Cambridge, Mass., Technology Press of M.I.T. USA, 438p.

Fitzgerald W.J. and Paren J.G., **1975**. The dielectric properties of Antarctic ice. *Journal of Glaciology*, vol 15, no 73, pp 39-48.

Fitzgerald W.J., Glen J.W. and Paren J.G., **1977**. Are the anomalous dielectric properties of polar ice due to impurities? *International symposium on isotopes and impurities in snow and ice*, Grenoble, August 28-30, 1975, pp 3-8.

Fletcher N.H, **1970**. *The Chemical Physics of Ice.* Cambridge University Press, Cambridge, UK.

Fujita S. and Mae S., **1993**. Relation between ice sheet internal radio-echo reflections and ice fabric at Mizuho Station, Antarctica. *Annals of Glaciology*, vol 17, pp 269-275.

Fujita S. and Mae S., **1994**. Causes and nature of ice sheet radio-echo internal reflections estimated from the dielectric properties of ice. *Annals of Glaciology*, vol 20, pp 80-86.

Fujita S., Mae S. and Matsuoka T., **1993**. Dielectric anisotropy in ice Ih at 9.7 GHz. *Annals of Glaciology*, vol 17, pp 276-280.

Gary M., McAfee Jr. R. and Wolf C.L., **1974**. *Glossary of Geology.* American Geological Institute, Washington DC., USA.

Georgio E.F. and Kumar P., **1994**. *Wavelets in Geophysics.* Academic Press, San Diego, USA.

Gerland S., **1993**. Zerstorungsfreie hochauflosende Dichteuntersuchungen mariner sedimente, *Berichte zur Polarforshung 123/93*, Alfred Wegener Institute, Bremerhaven, Germany.

Gerland S., Kipfstuhl S., Graf, W. and Minikin, A., **1994**. Non-destructive high resolution density measurements of the B15 ice core. *Filchner Ronne Ice Shelf Programme, Report No. 8.* Editor: Oerter H., Publishers: Alfred-Wegener-Institute for Polar and Marine Research, Bremerhaven, Germany.

Gerland S., Oerter H., Kipfstuhl J., Wilhelms F., Frenzel A., Miners W.D., Mulvaney R. and Peel D., **1996**. Continuous Density Measurements on the Ice Core B25 from Berkner Island, Antarctica. *Filchner Ronne Ice Shelf Programme, Report No. 10.* Editor: Oerter H., Publishers: Alfred-Wegener-Institute for Polar and Marine Research, Bremerhaven, Germany.

Ginzburg V.L., **1961**. *Propagation of electromagnetic waves in plasma.* Gordon and Breach, New York, USA.

Glen J.W. and Paren J.G., **1975**. The electric properties of snow and ice. *Journal of Glaciology*, vol 15, no 73, pp 15-38.

Goodman R.H., **1975**. Radio Echo Sounding on temperate glaciers. *Journal of Glaciology*, vol 14, no 70, pp 57-69.

Goodman D., **1994**. Ground penetrating radar simulation in engineering and archaeology. *Geophysics*, vol 59, no 2, pp224-232.

Gough S.R. and Davidson D.W., **1973**. Dielectric properties of Clathrate ices. *Physics and Chemistry of Ice.* Editors: Whalley E. et al., Royal Society of Canada, Ottawa, Canada.

Gough S.R., Hawkins R.E., Morris B. and Davidson D.W., **1973**. Dielectric properties of some Clathrate Hydrates of structure II. *The Journal of Physical Chemistry*, vol 77, no 25, pp 2969-2976.

Goupillaud P.L., **1961**. An approach to inverse filtering of near-surface layer effects from seismic records. *Geophysics*, vol 16, no 6, pp 754-760.

Gow A.J., **1968**. Bubbles and bubble pressures in Antarctic glacier ice. *Journal of Glaciology*, vol 7, no 50, pp 167-182.

Gow A.J., **1969**. On the rates of growth of grains and crystals in South Polar firn. *Journal of Glaciology*, vol 8, no 53, pp 241-252.

Gow A.J., **1970**. Deep core studies of the crystal structure and fabrics of Antarctic glacier ice. *CRREL research report* 282.

Gow A.J. and Williamson T., **1976**. Rheological implications of the internal structure and crystal fabrics of the West Antarctic ice sheet as revealed by deep core drilling at Byrd Station. Cold Regions Research and Engineering Laboratory (CRREL) Report 76-35.

Gow A.J., Meese D.A., Alley R.B., Fitzpatrick J.J., Anandakrishnan S., Woods G.A. and Elder B.C., **1997**. Physical and Structural properties of the Greenland Ice Sheet Project, ice core: A review. *Journal of Geophysical Research*, vol 102, no C12, pp 26559-26575.

Granicher H., **1969**. Evaluation of Dielectric dispersion behaviour. *Physics of Ice*. Proceedings of the third international symposium on the Physics of Ice held in Munich Sept 9-14 1968. Editor N.Riehl.

Grant E.H., Sheppard R.J. and South G.P., **1978**. *Dielectric behaviour of biological solutions*. Oxford University Press, Oxford, UK.

Gross G.W., **1967**. *Some effects of trace inorganics on the ice-water system*. Internal report, New Mexico Institute of Mining and Technology, USA.

Gross G.W. and Johnson J., **1983**. The layered capacitor method for dielectric bridge measurements. Data analysis and interpretation of fluoride doped ice. *IEEE Transactions on Electrical Insulation*, vol EI-18, no 5, pp 485-497.

Gross G.W. and McGehee R.M., **1988**. The layered-capacitor method for bridge measurements of conductive dielectrics. II New algorithum for inversion and parameter fitting. *IEEE Transactions on Electrical Insulation*, vol 23, no 3, pp 387-396.

Gross G.W., Hayslip I.C. and Hoy R.N., **1980**. Dielectric relaxation spectrum of ice measured with linear blocking layer. *Geophysics*, vol 45, no 5, pp 914 - 927.

Gundestrup N.S., Johnsen S.J. and Reeh N., **1984**. ISTUK a deep ice core drill system. *Second International Symposium on Ice Drilling Technology*, August 30 - Sept 1, 1982, Calgary Canada, Special Report 84-34, U.S. Army Corps of Engineers, Cold Regions Research and Engineering Laboratory, Hanover, New Hampshire, USA.

Gudmandsen P., **1975**. Layer echos in polar ice sheets. *Journal of Glaciology*, vol 15, no 73, pp 95-101.

Gudmandsen P., **1976**. Studies of ice by means of radio echo sounding. Contribution to Colston Symposium on: *Remote sensing of the terrestrial environment*. Held in Bristol April 1976. Published in a report by Electromagnetics Institute, Technical University Denmark.

Gudmandsen P. and Overgaard. S., **1978**. Establishment of time horizons in Polar ice sheets by means of RES. Presented at the: *Nordic Symposium on Climate Change and related problems*. Copenhagen 24-28th April 1978. Published in a report by Electromagnetics Institute, Technical University Denmark.

Gundestrup N.S., Steffensen J.P. and Schwander J., **1994**. The GRIP deep drilling camp. *Mem. Natl. Inst. Polar Research*, Special Issue 49, pp 358 - 371.

Hall H.P., **1971**. Impedence Measurement. *Electronic Measurements and Instrumentation*, Inter University Electronics Series, vol 12, McGraw Hill.

Hall J.S. and Wolff E.W., **1998**. Causes of Seasonal and Daily variations in aerosol sea-salt concentrations at a coastal Antarctic Station. *Atmospheric Environment*, vol 32, no 21, pp 3669-3677.

Hammer C.U., **1980**. Acidity of polar ice cores in relation to absolute dating, past volcanism, and radio echos. *Journal of Glaciology*, vol 25, pp 359-372.

Hammer C.U., **1989**. Dating by Seasonal Variations and reference horizons. *The Environmental record in Glaciers and Ice Sheets*. Editors: Oeschger H. and Langway C.C., Dhalem Workshop Report.

Hamran S-E. and Aarholt E., **1993**. Glacier study using wavenumber domain synthetic aperture radar. *Radio Science*, vol 28, no 4, pp 559-570.

Hargreaves N.D., **1977**. The polarisation of radio signals in radio echo sounding of ice sheets. *J.Phys,D. Applied Phys*, vol 10, pp 1285-1304.

Hargreaves N.D., **1978**. The Radio frequency birefringence of Polar ice. *Journal of Glaciology*, vol 21, no 85, pp 301-313.

Harrison C.H., **1972**. *Radio propagation effects in glaciers*. PhD thesis, Scott Polar Research Institute, University of Cambridge, Cambridge, UK.

Harrison, C.H., **1973**. Radio Echo Sounding of Horizontal layers in ice. *Journal of Glaciology*, vol 12, no 66, pp 383-397.

Hatton L., Worthington, M.H. and Makin J., **1986**. *Seismic Data processing: Theory and Practice*. Blackwell Scientific Publications, Oxford, UK.

Hecht E., **1987**. *Optics*. 2nd Edition, Publishers:Addison Wesley.

Hempel L. and Thyssen F., **1992**. Deep Radio echo soundings in the vicinity of GRIP and GISP2 drill sites, Greenland. *Polarforshung*, vol 62, no 1, pp 11-16.

Herron S.L. and Langway C.C., **1982**. A comparison of ice fabrics and textures at Camp Century, Greenland and Byrd Station, Antarctica. *Annals of Glaciology*, vol 3, pp 118-124.

Hobbs P.V., **1974**. *Ice Physics*. Clarendon Press, Oxford, UK.

Hodge S.M., Wright D.L., Bradley J.A., Jacobel R.W., Skou N. and Vaughan B., **1990**. Determination of the surface and bed topography in central Greenland. *Journal of Glaciology*, vol 36, no 122, pp 17-30.

Hondoh T., Anzai H., Goto A., Mae S., Higashi A. and Langway C.C., **1990**. The crystallographic structure of the natural air-hydrate in Greenland Dye-3 deep ice core. *Journal Incl. Phenom. Mol Recogn. Chem.*, vol 8, pp 17-24.

Hubmann M., **1978**. Effect of pressure on the dielectric properties of ice Ih single crystals doped with NH_3 and HF. *Journal of Glaciology*, vol 21, no 85, pp 161-172.

Humbel F., Jona F. and Scherrer P., **1953**. Anisotropie der Dielektrizitats Konstante des Eises. *Helv.Phys.Acta*, vol 26, pp 17-32.

Itagaki K., **1987**. Dielectric properties of strained ice. 1: effect of plastic straining. *Journal de Physique*; 48(colloque C1, supplement au no 3): pp 143-147.

Jaccard C., **1959**. Etude theorique et experimentale des properties electriques de la glace. *Helv phys Acta*, vol 32, pp 89-128.

Jaccard C., **1963**. Thermoelectric effects in ice crystals I, Theory of the steady state, *Phys. Condens. Mater.* vol 1, pp 143-151.

Jaccard C., **1964**. Thermodynamics of irreversible processes applied to ice. *Phys. Condens. Mater.* vol 3, pp 99-118.

Jacka T.H., **1984**. Laboratory studies on relationships between crystal size and flow rate. *Cold Regions Science and*

Technology, vol 8, pp 261-268.

Jackson J.D., **1975**. *Classical Electrodynamics*. 2nd Edition, Publishers: John Wiley & Sons, New York, USA.

Jacobel R.W. and Hodge S.M., **1995**. Radar internal layers from the Greenland summit. *Geophysical Research letters*, vol 22, no 5, pp 587-590.

Jacobel R.W., Glades A.M., Gottschling D.L., Hodge S.M. and Wright D.L., **1993**. Interpretation of radar detected internal layer folding in West Antarctic ice streams. *Journal of Glaciology*, vol 39, no 133, pp 528-537.

Jacobsson R., **1966**. Light reflection from films of continuously varying refractive index. *Progress in Optics, vol 5*, Editor Wolff E.

Jezek C.J. and Roeloffs E.A., **1983**. Measurements of Radar wave speeds in polar glaciers using down-hole radar target technique. *Cold Regions Science and Technology*, vol 8, no 2, pp 199-208.

Jiracek G.R., **1967**. *Radio sounding of Antarctic Ice*. Research Report 67-1, Geophys. and Polar Res. Center, University of Wisconsin-Madison, USA.

Johari G.P., **1976**. The dielectric properties of H_2O and D_2O ice Ih at MHz frequencies. *Journal of Chemical Physics*, vol 64, no 10, pp 3998-4005.

Johari G.P., **1981**. The spectrum of ice. *Contemporary Physics*, vol 22, no 6, pp 613-642.

Johari G.P. and Charette P.A., **1975**. The permittivity and attenuation in polycrystalline and single crystal ice Ih at 35 and 60 MHz. *Journal of Glaciology*, vol 14, no 71, pp 293-303.

Johari G.P. and Jones S.J., **1978**. The orientation polarisation in hexagonal ice parallel and perpendicular to the c-axis. *Journal of Glaciology*, vol 21, no 85, pp 259-276.

Johnsen S.J., **1977**. Stable isotope homogenization of polar firn and ice. *Isotopes and Impurities in snow and ice*. International Association of Hydrological Sciences publication number 118, Grenoble, pp 210-219.

Johnsen S.J., Clausen H.B., Dansgaard W., Fuhrer K., Gundestrup N., Hammer C.U., Iversen P., Jouzel J., Stauffer B. and Steffensen J.P., **1992**. Irregular glacial interstadials recorded in a new Greenland ice core. *Nature*, vol 359, pp 311-313.

Johnsen S.J., Gundestrup N.S., Hansen S.B., Schwander J. and Rufli H., **1994**. The New improved version of the ISTUK ice core drill. *Mem Natl Inst. Polar Research Special Issue* 49, pp 9-23.

Johnsen S.J., Dahl-Jensen D., Dansgaard W. and Gundestrup N., **1995**. Greenland palaeotemperatures derived from GRIP bore hole temperature and ice core isotope profiles. *Tellus*, vol 47B, pp 624-629.

Jokat W. and Oerter H., **1997**. The Expedition ANTARKTIS-X11 of RV "Polarstern" in 1995 Report of leg ANT-X11/3. *Berichte zur Polarforschung, Report No. 219*. Alfred-Wegener-Institute for Polar and Marine Research, Bremerhaven, Germany.

Jonscher A.K., **1983**. *Dielectric relaxation in solids*. Chelsea Dielectrics Press, London, UK.

Kelly K.R., Ward R.W., Treitel S. and Alford R.M., **1976**. Synthetic Seismograms, a finite difference approach. *Geophysics*, vol 41, no 1, pp 2-27.

Kimura T., **1983**. Preliminary experiments of snow density meter by gamma-ray scattering (in Japanese with English summary). *Journal Japanese Soc Snow and Ice*, vol 45, no 3, pp 119-124.

Kraus J.D., **1988**. *Antennas*. 2nd Edition, McGraw-Hill, New York, USA.

Kohler J., Moore J.C., Kennett M., Engeset R. and Elvehoy H., **1997**. Using ground penetrating radar to image previous years' summer surfaces for mass-balance measurements. *Annals of Glaciology*, vol 24, pp 355-360.

Kotlyakov V.M. and Smolyarova N.A., **1990**. *Dictionary of Glaciology.* Elsevier, Amsterdam., Netherlands.

Kovacs A., Gow A.J. and Morey R.M., **1995**. The in-situ dielectric constant of polar firn revisited. *Cold Regions Science and Technology,* vol 23, no 3, pp 245-256.

Kumai M., **1976**. Identification of nuclei and concentrations of chemical species in snow crystals sampled at the South Pole. *J.Atmos. Science,* vol 33, pp 833-841.

Kunz K.S. and Luebbers R.J., **1993**. *The finite difference time domain method for electromagnetics.* CRC press, London, UK.

Landauer R., **1978**. Electrical Conductivity in Inhomogeneous Media. *Electrical Transport and Optical Properties in Inhomogeneous Media,* American Institute of Physics Conference Proceedings 40, Ohio State University, 1977, Editors: Garland J.C. and Tanner D.B.

Langway C.C., **1958**. Bubble pressures in Greenland glacier ice. *Union Geodeique et Geophysique Internationale Association Internationale d'Hydrologie Scientifique,* Symposium Chamonix, 16-24 Sept, pp 336-349.

Langway C.C., **1967**. *Stratigraphic Analysis of a deep ice core from Greenland.* Research Report 77, Cold Regions Research and Engineering Laboratory, Hanover, New Hampshire, USA.

Lanzario-Mancilla O. and Gomez-Trevino E., **1996**. Synthetic radargrams from electrical conductivity and magnetic permeability variations. *Journal of Applied Geophysics,* vol 34, pp 283-290.

Legrand M., Angelis M.D., Staffelbach T., Neftel A. and Stauffer B. **1992**. Large perturbations of Ammonium and organic acids content in the summit Greenland ice core. Fingerprint from forest fires? *Geophysical Research Letters,* vol 19, no 5, pp 473-475.

Lin M-S., Lin C-M., Wu R-B. and Chen C.H., **1993**. Transient propagation in anisotropic laminated composites. *IEEE transactions on Electromagnetic compatibility,* vol 35, no 3, pp 357-365.

Lock G.S.H., **1990**. *The growth and decay of Ice.* Cambridge University Press. Cambridge, UK.

Loius C., Jouzel J. and Raynaud D., **1992**. The Ice core record: past archive of the climate and signpost to the future. *Philosophical Transactions of the Royal Society of London* Series B, vol 338, pp 227-234.

Luebbers R.J., Kunz K.S. and Chamberlin K.A., **1990**. An interactive demonstration of electromagnetic wave propagation using time domain finite differences. *IEEE transactions on education,* vol 33, no 1, pp 60-68.

Maccagnan M. and Duval P., **1982**. Electrical behaviour of Antarctic ice and Radio Echo Layers in Ice sheets. *Annals of Glaciology,* vol 3, pp 195-198.

Macdonald J.R., **1987**. *Impedance Spectroscopy.* John Wiley and Sons, New York, USA.

Maeno H., Fujita S., Kamiyama K., Motoyama H., Furukawa T. and Uratsuka S., **1995**. Relation between surface ice flow and anisotropic internal radio echos in the East Queen Maud land ice sheet Antarctica. *Proc NIPR Symp. Polar Meteorol. Glaciol.,* vol 9, pp 76-86.

Martinerie P., Raynaud D., Etheridge D.M., Barnola J.M. and Mazaudier D., **1992**. Physical and climatic parameters which influence the air content in polar ice. *Earth Planet Sci. Lett.,* vol 112, pp 1-13.

Matsuoka T., Fujita S. and Mae S., **1996**. Effect of temperature on dielectric properties of ice in the range 5-39 GHz. *Journal of Applied Physics,* vol 80, no 10, pp 5884-5890.

Matsuoka T., Fujita S., Morishima S. and Mae S., **1997 a**. Precise measurement of dielectric anisotropy in ice Ih at 39 GHz. *Journal of Applied Physics,* vol 81, no 5, pp 1-5.

MatsuokaT., Fujita S. and Mae S., **1997 b**. Dielectric properties of ice containing ionic impurities at Microwave frequencies. In: Proceedings of the conference on the Physics and Chemistry of Ice, 1996. *Journal of Physical Chemistry B.,* vol 101, no 32, pp 6219-6222.

Matsuoka T., Mae S., Fukazawa H., Fujita S. and Watanabe O., **1998**. Microwave dielectric properties of the ice core from Dome Fuji, Antarctica. *Geophysical Research Letters*, vol 25, no 10, pp 1573-1576.

Mayenski P.A. and Legrand M.R., **1990**. Recent increases in nitrate concentrations of Antarctic Snow. *Nature*, vol 346, no 6281, pp 258-260.

Mayenski P.A., Lyons W.B., Spencer M.J., Twichler M.S., Buck C.F. and Whitlow S., **1990**. An ice core record of atmospheric response to anthropogenic sulphate and nitrate. *Nature*, vol 346, no 6284, pp 554-555.

Mickleson A.R., **1992**. *Physical Optics*. Van Nostrand Reinhold, New York, USA.

Millar S.L., **1973**. The Clathrate Hydrates - Their Nature and Occurrence. *Physics and Chemistry of Ice*. Editors: Whalley E. et al., Royal Society of Canada, Ottawa, Canada.

Millar D.H.M., **1981 a**. *Radio-echo layering in polar ice sheets*. PhD thesis, Scott Polar Research Institute. University of Cambridge, Cambridge, UK.

Millar D.H.M., **1981 b**. Radio-echo layering in polar ice sheets and past volcanic activity. *Nature*, vol 292, pp 441-443.

Millar D.H.M., **1982**. Acidity levels in ice sheets from radio echo-sounding. *Annals of Glaciology*, vol 3, pp 199-203.

Miners W.D. and Mulvaney R., **1995**. Electrical logging and initial dating of the ice cores from Berkner 94/95. In: *Filchner Ronne Ice Shelf Programme, Report No. 9*. Editor: Oerter H., Publishers: Alfred-Wegener-Institute for Polar and Marine Research, Bremerhaven, Germany.

Miners W.D., Peel, D.A. and Mulvaney R., **1996**. Using DEP and ECM to produce a chronology at Berkner. *Filchner Ronne Ice Shelf Programme, Report No. 10*. Editor: Oerter H., Publishers: Alfred-Wegener-Institute for Polar and Marine Research, Bremerhaven, Germany.

Miners, W.D., Hildebrand A., Gerland S., Blindow N., Steinhage D. and Wolff E.W., **1997**. Forward modelling of the Internal Layers in Radio Echo Sounding using Electrical and Density Measurements from Ice Cores. Proceedings of the conference on the Physics and Chemistry of Ice, 1996. *Journal of Physical Chemistry*, Series B, vol 101, no 32, pp 6201-6204.

Miners W.D., Blindow, N. and Gerland S., **1998**, Modeling a ground penetrating radar record by using ice core data to produce a synthetic radargram. *Proceedings of the seventh international conference on ground penetrating radar*, University of Kansas, USA. Editor: Plumb R.

Moore J.C., **1988 a**. *Geophysical aspects of ice core drilling in Antarctica*. PhD Thesis, Council of National Academic Awards, British Antarctic Survey, Cambridge, UK.

Moore J.C., **1988 b**. Dielectric variability of a 130 m Antarctic ice core: Implications for radar sounding. *Annals of Glaciology*, vol 11, pp 95-99.

Moore J.C., Paren J.G. and Mulvaney R., **1990**. Chemical evidence in Polar ice cores from dielectric profiling. *Annals of Glaciology*, vol 14, pp 195-198.

Moore J.C., **1993**. High resolution dielectric profiling of ice cores. *Journal of Glaciology*, vol 39, no 132, pp 245-248.

Moore J.C. and Paren J.G., **1987**. A new technique for dielectric logging of Antarctic ice cores. *Journal de Physique*, Tome 48 (Mar Supl. 3), pp C1-155-160.

Moore J.C., Narita H. and Maeno N., **1991**. A continuous 770 year record of volcanic activity from East Antarctica. *Journal of Geophysical Research*, vol 96, no D9, pp 17353-17359.

Moore J.C., Wolff E.W., Hammer C.U. and Clausen H.B., **1992 a**. The chemical basis for the electrical stratigraphy of ice. *Journal of Geophysical Research*, vol 97, pp 1887-1896.

Moore J.C., Paren J.G. and Oerter H., **1992 b**. Sea salt dependent electrical conduction in polar ice. *Journal of Geophysical Research*, vol 97, pp 19803-19812.

Moore J.C., Wolff E.W., Clausen H.B., Hammer C.U., Legrand M.R. and Fuher K., **1994**. Electrical response of the Summit-Greenland ice core to ammonium, sulphuric acid and hydrochloric acid. *Geophysical Research Letters*, vol 21, no 7. pp 565-568.

Morgan V.I., **1972**. Oxygen Isotope Evidence for bottom freezing on the Amery Ice Shelf. *Nature*, vol 238, pp 393-394.

Mulvaney R., **1995**. The Berkner Island Ice core project: report and some initial results. *Filchner Ronne Ice Shelf Programme, Report No. 9*. Editor: Oerter H., Publishers: Alfred-Wegener-Institute for Polar and Marine Research, Bremerhaven, Germany.

Mulvaney R. and Wolff E.W., **1994**. Spatial variability of the major chemistry of the Antarctic ice sheet. *Annals of Glaciology*, vol 20, pp 440-447.

Mulvaney R., Wolff E.W. and Oates K., **1988**. Sulphuric acid at grain boundaries in Antarctic ice. *Nature*, vol 331, no 6153, pp 247-249.

Mulvaney R., Pasteur E.C., Graf W., Minikin A., Arrowsmith C., Oerter H., Peel D.A., Miners W.D. and Holman N., **1996**. The Berkner Island Project: isotopic and chemical trends in the ice core data. *Filchner Ronne Ice Shelf Programme, Report No. 10*. Editor: Oerter H., Publishers: Alfred-Wegener-Institute for Polar and Marine Research, Bremerhaven, Germany.

Mur G., **1981**. Absorbing boundary conditions for finite-difference approximation of the time domain electromagnetic field equations. *IEEE Trans Electromagnetic Compatability*, vol EMC-23, pp 1073-1077.

Nagle J., **1974**. Dielectric constant of ice. *Journal of Chemistry and Physics*, vol 61, pp 883-888.

Nakawo M., **1986**. Volume expansion of a 413.5 m Mizuho core after its recovery. *Mem Natl Inst Polar Res.*, Spec Issue 45, pp 78-85.

Neftel A., Beer J., Oeschger H., Zuercher F. and Finkel R.C., **1985**. Sulphate and nitrate concentrations in snow from south Greenland 1895-1978. *Nature*, vol 314, pp 611-613.

Nghiem S.V., Kwok R., Kong J.A., Shin R.T., Arcone S.A. and Gow A.J., **1996**. An electrothermodynamic model with distributed properties for effective permittivities of sea ice. *Radio Science*, vol 31, no 2, pp 297-311.

Nicollin F. and Kofman W., **1994**. Ground Penetrating Radar sounding of a temperate glacier, modelling of a multilayer medium. *Geophysical Prospecting*, vol 42, pp 715-734.

Nielsen P.H., **1978**, Calculation of synthetic reflection seismograms in the frequency domain. *Geophysical prospecting*, vol 26, pp 399-406.

Nishio F. and Ohmae H., **1985**. Internal radio echo reflections of polar snow covers in relation to acidic layers and density fluctuations. *Annals of Glaciology*, vol 6, pp 289-291.

Noll G., **1978**. Influence of the rate of deformation on the electric properties of ice monocrystals. *Journal of Glaciology*, vol 21, no 85, pp 277-289.

Nye J.F., **1955**. *Physical Properties of Crystals*. Clarendon Press, Oxford, UK.

Nyfors E., **1982**. *On the dielectric properties of dry snow in the 800 mHz to 13 GHz region*. Report S. 135, Radio Laboratory, Helsinki University of Technology, Finland.

O'Doherty R.F. and Anstey N.A., **1971**. Reflections on amplitudes. *Geophysical Prospecting*, vol 19, pp 430-458.

Oerter H., **1997**. Berkner Island. *The Expedition ANTARKTIS-X11 of RV "Polarstern" in 1995 Report of leg*

ANT-X11/3. Editors: Jokat W. and Oerter H., Berichte zur Polarforschung Report No. 219: pp 113-132. Publishers: Alfred-Wegener-Institute for Polar and Marine Research, Bremerhaven, Germany.

Oliver B.M. and Cage J.M., **1971**. *Electronic measurements and instrumentation*, Inter-University Electronics Series, vol 12, McGraw-Hill Book Company.

Oswald G.K.A., **1975**. Investigation of Sub-ice bedrock characteristics by Radio-Echo sounding. *Journal of Glaciology*, vol 15, no 73, pp 75- 87.

Pao H.Y., Dvorak S.L. and Dudley D.G., **1996**. The effects of neglecting displacement currents when studying transient wave propagation in the Earth. *IEEE Transactions on Antennas and Propagation*, vol 44, no 9, pp 1259-1265.

Paren J.G., **1970**. *Dielectric properties of ice* , PhD thesis, University of Cambridge, Cambridge, England.

Paren J.G., **1973**. The electrical behaviour of Polar glaciers. *Physics and Chemistry of Ice*. Editors: Whalley E. et al., Royal Society of Canada, Ottawa, Canada.

Paren J.G., **1981**. Reflection coefficient at a dielectric interface. *Journal of Glaciology*, vol 27, no 95, pp 203-204.

Paren J.G. and Walker J.C.F., **1971**. Influence of limited solubility on the electrical and mechanical properties of ice. *Nature, Physical Science*, vol 230, no 12, pp 77-79.

Paren J.G. and Robin G. de Q., **1975**. Internal reflections in polar ice sheets. *Journal of Glaciology*, vol 14, no 71, pp 251- 259.

Paren J.G. and Glen J.W., **1978**. Electrical properties of finely divided ice. *Journal of Glaciology*, vol 21, no 85, pp 173-192.

Parkhomenko, **1967**. *Electrical Properties of Rocks*. Translated by G.V.Keller, Plenium Press New York, USA.

Pasteur E.C., **1996**. *Biogenic Sulphur in Antarctic Ice Cores*. PhD thesis, University of East Anglia, UK.

Paterson W.S.B., **1994**. *The Physics of Glaciers*. Elsevier Science Ltd, Oxford, UK.

Pauer F., Kipfstuhl J. and Kuhs W.F., **1995**. Raman spectroscopic study on the nitrogen/oxygen ratio in natural ice clathrates in the GRIP core. *Geophysical Research Letters*, vol 22, no 8, pg 969-971.

Peel D.A., **1992**. Paleoclimatology. Merely the tip of the ice core. *Nature*, vol 359, no 6393, pp 274-275.

Peterson R.A., Fillippone W.R. and Coker F.B., **1955**. The synthesis of seismograms from well log data. *Geophysics*, vol 20, no 3, pp 516-538.

Petrenko V.F. and Ryzhkin I.A., **1984**. Dielectric properties of ice in the presence of space charge. *Physica Status Solidi(b)*, vol 121, pp 421-427.

Petrenko V.F., **1993**. Electrical properties of Ice. *Cold Regions Research and Engineering laboratory, Special report 93-20*.

Plumb R.G., **1998**. *Proceedings of the Seventh international conference on Ground Penetrating Radar*, University of Kansas, Lawrence, Kansas, USA, May 27 to 30th.

Priou A., **1992**. Dielectric properties of Heterogeneous Materials, *Progress in Electromagnetics Research*, vol 6, Elsevier.

Rees W.G. and Donovan R.E., **1992**. Refraction correction for radio echo sounding of large ice masses. *Journal of Glaciology*, vol 38, no 129, pp 302-308.

Reynolds J.M., **1983**. *Geophysical studies of the ice of the Antarctic Peninsula*. PhD thesis, Cambridge University, Cambridge, UK.

Reynolds J.M., **1985**. Dielectric behaviour of firn and ice from the Antarctic peninsular, Antarctica. *Journal of Glaciology*, vol 31, no 109, pp 253-262.

Richardson C., Aarholt E., Hamran S-E., Holmlund P. and Isaksson E., **1997**. Spatial distribution of snow in western Dronning Maud Land, East Antarctica, mapped by a ground-based snow radar. *Journal of Geophysical Research*, vol 102, no B9, pp 20343-20353.

Ricker N., **1940**. The form and nature of seismic wavelets and the structure of seismograms. *Geophysics*, vol 5, pp 348-366.

Ricker N., **1953**. The form and laws of the propagation of seismic wavelets. *Geophysics*, vol 18, pp 10-40.

Ritz C., **1989**. Interpretation of the temperature profile measured at Vostok, East Antarctica. *Annals of Glaciology*, vol 12, pp 138-144.

Robin G. de Q. and Millar D.H.M., **1982**. Flow of Ice Sheets in the vicinity of subglacial peaks. *Annals of Glaciology*, vol 3, pp 290-294.

Robin G. de Q., Evans S. and Bailey J.T., **1969**. Interpretation of Radio echo sounding in Polar Ice sheets. *Philosophical Transactions of the Royal Society of London, Ser A*, vol 265, no 1166, pp 437-505.

Robin G. de Q., Drewry D.J. and Meldrum D.T., **1977**. International studies of ice sheet and bedrock. *Philosophical Transactions of the Royal Society of London B.*, vol 279 pp 185-196.

Robinson E.A., **1968**. Basic equations for synthetic seismograms using the z transform approach. *Geophysics*, vol 33, no 3, pp 521-523.

Robinson E.A. and Treitel S., **1980**. *Geophysical Signal Analysis*. Prentice-Hall Inc., Englewood Cliffs, New Jersey, USA.

Robinson E.A., **1985**. Seismic time invariant convolutional model. *Geophysics*, vol 50, no 12, pp 2742-2752.

Ruepp R., **1973**. Electrical properties of ice Ih single crystals. *Physics and Chemistry of Ice*. Editors: Whalley E. et al., Royal Society of Canada, Ottawa, Canada.

Salamatin A.N. and Lipenkov V.Y., **1993**. Theoretical studies on densification and relaxation of bubbly glacier ice. *Antarctic Record*, vol 37, no 3, pp 265-276.

Sandhäger H., **1995**. Review of the Munster airborne radio-echo sounding data set: marine ice beneath Filchner-Schelfeis; bottom reflectivity and internal structures of Berkner Island. *Filchner Ronne Ice Shelf Programme, Report No. 9*. Editor: Oerter H., Publishers: Alfred-Wegener-Institute for Polar and Marine Research, Bremerhaven, Germany.

Scaife B.K.P., **1989**. *Principles of Dielectrics*. Monographs on the Physics and Chemistry of Materials. Clarendon Press, Oxford, UK.

Schneider J. and Hudson S., **1993**. The finite difference time domain method applied to anisotropic material. *IEEE Transactions on Antennas and Propagation*, vol 41, no 7, pp 994-999.

Schwan and Maczuk, **1960**. Effect of electrode size on polarisation and stray capacitance. *Rev Scientific Instruments*, vol 31, no 59.

Schwander J., **1989**. The transformation of Snow to Ice and Occlusion of gases. *The Environmental record in Glaciers and Ice Sheets*. Editors: Oeschger H. and Langway C.C., Dhalem Workshop Report.

Schwander J., **1996**. Gas Diffusion in Firn. *Nato ASI series I 43, Chemical exchange between the Atmosphere and Polar Snow*. Editors: Wolff E. and Bales R.C.

Schwander J. and Stauffer B., **1984**. Age difference between polar ice and air trapped in its bubbles. *Nature*, vol 311, pp 45-47.

Schwander J., Neftel A., Oeschger H. and Stauffer B., **1983**. Measurements of direct current conductivity on ice samples for climatological applications. *Journal of Physical Chemistry*, vol 87, no 21, pp 4157-4160.

Schwander J., Barnola J.M., Andrie C., Leuenberger M., Ludin A., Raynaud D. and Stauffer B., **1993**. The age of the air in the firn and the ice at Summit, Greenland. *Journal of Geophysical Research*, vol 98, no D2, pp 2831-2838.

Schytt V., **1968**. The inner structure of the ice shelf at Maudheim as shown by core drilling. *Norwegian-British Antarctic Expedition, 1949-1952*, Scientific Results 4, Glaciology 2, Norsk Polarinstitutt, Oslo, pp 115-151.

Seligman G. (**1939** 1st edt), (**1980** 3rd edt), *Snow Structure and Ski Fields*, Printed by Foister and Jagg, Publisher: International Glaciological Society, Cambridge, UK.

Sengbush R.L., Lawrence P.L. and McDonal F.J., **1961**. Interpretation of synthetic seismograms. *Geophysics*, vol 26, no 2, pp 138-157.

Shabtaie S. and Bentley C.R., **1994**. Unified theory of electrical conduction in firn and ice: Site percolation and conduction in snow and firn. *Journal of Geophysical Research*, vol 99, no B10, pp 19757-19769.

Sihvola A.H., Nyfors E. and Tiuri M., **1985**. Mixing formulae and experimental results for the dielectric constant of snow. *Journal of Glaciology*, vol 31, no 108, pp 163-170.

Sihvola A.H. and Lindell I.V., **1992**. Polarizability modelling of Heterogeneous Media. Chapter 3 in: *Dielectric Properties of Heterogeneous Materials, Progress in Electromagnetics research book 6 (PIERS 6)*, Editor: Priou A., Toulouse, France.

Shoji H. and Langway C.C., **1982**. Air Hydrate inclusions in fresh ice core. *Nature*, vol 298, pp 548-550.

Shoji H. and Langway C.C., **1989**. Physical Property reference horizons. *The environmental record in Glaciers and Ice Sheets*. Editors Oeschger H. and Langway C.C. pp 161-175.

Sivaprasad K. and Lessow H.A., **1976**. *Investigation of layering in ice*. Electromagnetics Institute, Technical University Denmark, Internal Report 103.

Skou N. and Sondergaard F., **1976**. *Radioglaciology A 60 MHz ice sounder system*. Electromagnetics Institute, Technical University Denmark, Internal Report 169.

Skolnik M.I., **1970**. *Radar Handbook*. McGraw-Hill, New York, USA.

Smith B.M.E and Evans S., **1972**. Radio Echo sounding: absorption and scattering by water inclusions and ice lenses. *Journal of Glaciology*, vol 11, no 61, pp 133-146.

Sondergaard F., **1975**. *Radioglaciology Surface Soundings near DYE-3*. Electromagnetics Institute, Technical University Denmark, Internal Report 258.

Sondergaard F. and Skou N., **1976**. *Radioglaciology side looking radar imaging and depth soundings of ice at 300 MHz*. Electromagnetics Institute, Technical University Denmark, Internal Report 170.

Staelin D.H., Morgenthaler A.W. and Kong J.A., **1994**. *Electromagnetic Waves*. Prentice Hall International Inc.

Stauffer B.R., **1989**. Dating of ice by radioactive isotopes. *The Environmental Record in Glaciers and Ice Sheets*. Editors: Oeschger H. and Langway C.C.

Steel W.H., **1983**. *Interferometry*. 2nd Edition, Cambridge University Press, Cambridge, UK.

Steinhage D. and Blindow N., **1995**. First results of short pulse radio echo sounding on the top of Berkner Island. *Filchner Ronne Ice Shelf Programme, Report No. 9*. Editor: Oerter H., Publishers: Alfred-Wegener-Institute for Polar and Marine Research, Bremerhaven, Germany.

Stiles W.H. and Ulaby F.T., **1981**. Dielectric properties of snow. *Workshop on the properties of Snow.* Editors: Brown R.L., Colbeck S.C. and Young R.N., U.S.Army Cold Regions Research and Engineering Laboratory. Special Report 82-18.

Stock J. **1993**. Vorwartsmodellierung von EMR-spuren mit Bohrkerndaten vom Filchner Ronne Schelfeis, Antarktis. Diplomarbeit im fach Geophysik, Institut fur Geophysik, Westfalische Wilhelms-Universitat, Münster, Germany.

Stratton J.A., **1941**. *Electromagnetic Theory.* 3rd Edition, McGraw-Hill, New York, USA.

Taubenberger R., **1973**. Ageing effects of electric properties of ice Ih single crystals. *Physics and Chemistry of Ice.* Editors: Whalley E. et al., Royal Society of Canada, Ottawa, Canada.

Taubenberger R., Hubmann M. and Granicher H., **1973**. Effect of hydrostatic pressure on the dielectric properties of Ice Ih single crystals. *Physics and Chemistry of Ice.* Editors: Whalley E. et al., Royal Society of Canada, Ottawa, Canada.

Thorsteinsson T., **1996**. Textures and Fabrics in the GRIP ice core, in relation to climate history and ice deformation. *Reports on Polar Research no 205,* Alfred Wegener Institute.

Tison J.L., Souchez R., Wolff E.W., Moore J.C., Legrand M.R. and deAngelis M., **1998**. Is periglacial biota responsible for enhanced dielectric response in basal ice from the Greenland Ice core Project core? *Journal of Geophysical Research-Atmospheres*, vol 103, no D15, pp 18885-18894.

Treitel S. and Robinson E.A., **1966**. Seismic wave propagation in layered media in terms of communication theory. *Geophysics*, vol 16, no 1, pp 17-32.

Trorey A.W., **1962**. Theoretical seismograms with frequency and depth dependent absorption. *Geophysics*, vol 27, no 6, pp 766-785.

Turner G., **1992**. GPR and the effects of conductivity. *Exploration Geophysics*, vol 23, pp 381-385.

Ulaby F.T., Moore R.K. and Fung A.K., **1986**. Dielectric constant of Snow. *Microwave Remote Sensing, Vol 3, Appendix E.6.* From Theory to Application. Artech House Inc.

Vainshtein L.A., **1976**. Propagation of Pulses. *Soviet Physics*, Usp 19, pp 189-205.

von Hippel A., Knoll D.B. and Westphal W.B., **1971**. Transfer of Protons through pure Ice, in single crystals. Polarisation spectra of ice Ih. *The Journal of Chemical Physics*, vol 54, no 1, pp 134-144.

von Hippel A., Mykolajewycz R., Runck H. and Westphal W.B., **1972**. Dielectric and Mechanical response of Ice 1h Single crystals and its interpretation. *The Journal of Chemical Physics*, vol 57, no 6, pp 2560-2571.

Wagenbach D., Graf W., Minikin A., Trfzer U., Oerter H., Kifstuhl J. and Blindow N., **1994**. Reconnaissance of Chemical and isotope firn properties on top of Berkner Island Antarctica. *Annals of Glaciology*, vol 20, pp 307-312.

Wait J.R., **1958**. Transmission and reflection of electromagnetic waves in the presence of stratified media. *Journal of Research of the National Bureau of Standards*, vol 61, no 3, pp 205-232.

Wait J.R., **1996**. *Electromagnetic waves in stratified media.* Institute of Electrical and Electronics Engineers, Classic Reprint Series, Oxford University Press, Oxford, UK.

Walford M.E.R., **1964**. Radio Echo Sounding through an ice sheet. *Nature*, vol 204, no 4956, pp 317-319.

Walford M.E.R., **1968**. Field measurements of dielectric absorption in Antarctic ice and snow at very high frequencies. *Journal of Glaciology*, vol 7, no 49, pp 89-94.

Wang T. and Hohmann G.W., **1993**. A finite difference, time domain solution for three dimentional electromagnetic modeling. *Geophysics*, vol 58, no 6, pp 797-809.

Warren S.G., **1984**. Optical constants of ice from ultraviolet to the microwave. *Applied Optics*, vol 23, no 8, pp 1206-1225.

Watts R.D. and England A.W., **1976**. Radio Echo sounding of temperate glaciers ice properties and sounder design criteria. *Journal of Glaciology*, vol 17, no 75, pp 39-48.

West J.C. and Demarest K.R., **1987**. The radiation characteristics of an arbitrary antenna positioned on a polar ice sheet. *Geophysics*, vol 52, no 12, pp 1689-1696.

Westphal W.B. and Iglesias J., **1970**. *Dielectric measurements on high-temperature materials*. Technical Report AFML-TR-70-138, Laboratory of Insulation Research, Massachusetts Institute of Technology, Cambridge, Massachusetts, USA.

Whillans I.M., **1976**. Radio echo layers and the recent stability of the West Antarctic ice sheet. *Nature*, vol 264, no 11, pp 152-155.

Whillans I.M. and Johnsen S.J., **1983**. Longitudinal variations in Glacial flow: Theory and Test using data from the Byrd Station strain network Antarctica. *Journal of Glaciology*, vol 29, no 101, pp 78-97.

Widess M.B., **1973**. How thin is a thin bed? *Geophysics*, vo. 38, no 6, pp 1176-1180.

Wilhelms F., **1996**. Measuring the conductivity and density of ice cores. *Reports on Polar research*. Alfred Wegener Institute, Bremerhaven, no 191.

Wilhelms F., Kipfstuhl J., Miller H., Heinloth K. and Firestone J., **1998**. Precise dielectric profiling of ice cores: a new device with improved guarding and its theory. *Journal of Glaciology*, vol 44, no 146, pp 171-174.

Wolff A., **1937**. The reflection of elastic waves from transition layers of variable velocity. *Geophysics*, vol 2, pp 357-363.

Wolff E.W. and Paren J.G., **1984**. A two phase model of electrical conduction in polar ice sheets. *Journal of Geophysical Research*, vol 89, no B11, pp 9433-9438.

Wolff E.W., Moore J.C., Clausen H.B., Hammer C.U., Kipfstuhl J. and Fuhrer K., **1995**. Long term changes in the acid and salt concentrations of the Greenland Ice Core project ice core from electrical stratigraphy. *Journal of Geophysical Research*, vol 100, no D8, pp 16249-16263.

Wolff E.W. and Bales R.C., **1996**. *Processes of Chemical Exchange between the atmosphere and Polar snow*. Proceedings of the NATO Advanced research workshop, NATO ASI series I, vol 43.

Wolff E.W., Miners W.D., Moore J.C. and Paren J.G., **1997**. Factors controlling the Electrical conductivity of Ice from the Polar regions - A summary. Proceedings of the conference on the Physics and Chemistry of Ice, 1996. *Journal of Physical Chemistry*, Series B, vol 101, no 32, pp 6090-6094.

Woodcock N.H., **1977**. Specification of fabric shapes using an eigenvalue method. *Geological Society of America Bulletin*, vol 88, pp 1231-1236.

Wright D.L., Bradley J.A. and Hodge S.M., **1989**. Use of a New High speed Digital Data Acquisition System in Airborne Ice Sounding. *IEEE Transactions on Geoscience and Remote sensing*, vol 27, no 5, pp 561-567.

Wright D.L., Hodge S.M., Bradley J.A., Grover T.P. and Jacobel R.W., **1990**. A digital low frequency surface profiling radar system. *Journal of Glaciology*, vol 36, no 122, pp 112-121.

Wuenschel P.C., **1960**. Seismogram synthesis including multiples and transmission coefficients. *Geophysics*, vol 15, no 1, pp 106-129.

Yee K.S., **1966**. Numerical Solution of initial Boundary value problems involving Maxwell's equations in isotropic media. *IEEE Transactions on Antennas and Propagation*, vol 14, no 3, pp 302-307.

Yoshida M., Yamashita K. and Mae S., **1987**. Bottom topography and internal layers in East Dronning Maud Land,

East Antarctica, from 179 MHz radio echo-sounding. *Annals of Glaciology*, vol 9, pp 221-224.

Zheludev I S., **1971**. *Physics of Crystalline Dielectrics Vol 1 and Vol 2*. Plenium Press, New York, USA.